Soap bubbles for large-scale PIV

Generation, control and tracing accuracy

Engler Faleiros, David

DOI
10.4233/uuid:c579128f-9e96-4e9e-9997-6ce9486e1e25

Publication date
2021

Document Version
Final published version

Citation (APA)
Engler Faleiros, D. (2021). *Soap bubbles for large-scale PIV: Generation, control and tracing accuracy*. [Dissertation (TU Delft), Delft University of Technology]. https://doi.org/10.4233/uuid:c579128f-9e96-4e9e-9997-6ce9486e1e25

SOAP BUBBLES FOR LARGE-SCALE PIV

Generation, control and tracing accuracy

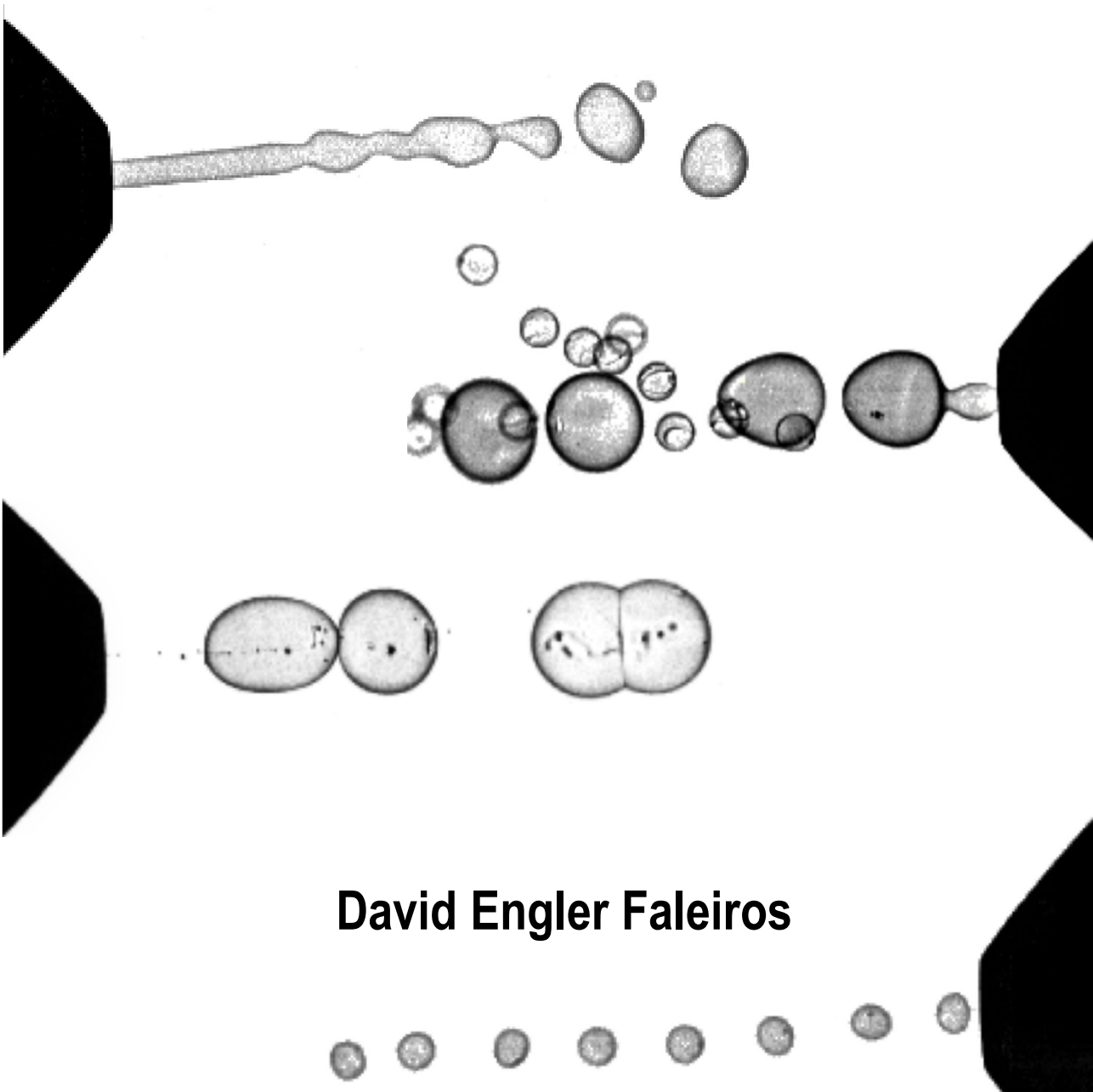

David Engler Faleiros

Soap bubbles for large-scale PIV

Generation, control and tracing accuracy

Soap bubbles for large-scale PIV

Generation, control and tracing accuracy

Dissertation

for the purpose of obtaining the degree of doctor
at Delft University of Technology
by the authority of the Rector Magnificus, Prof.dr.ir. T.H.J.J. van der Hagen,
chair of the Board for Doctorates
to be defended publicly on
Monday 10, May 2021 at 17:30 o'clock

by

David ENGLER FALEIROS

Master of Science in Sustainable Energy Technology,
University of Twente, the Netherlands
born in Franca, Brazil

This dissertation has been approved by the promotor.

Composition of the doctoral committee:

Rector Magnificus,	chairperson
Prof.dr. F. Scarano,	Delft University of Technology, promotor
Dr. A. Sciacchitano,	Delft University of Technology, copromotor

Independent members:

Prof.dr.-ing.habil. M. Raffel,	German Aerospace Center (DLR), Germany
Prof.dr.ir. J. Westerweel,	Delft University of Technology
Prof.dr. S. Ghaemi,	University of Alberta, Canada
M.Sc. U. Dierksheide,	LaVision GmbH, Germany
Prof.dr.ir L.L.M. Veldhuis,	Delft University of Technology, reserve member

Other members:

Ir. M. Tuinstra,	Royal Netherlands Aerospace Centre (NLR), daily supervisor

Keywords: neutrally buoyant tracers, helium-filled soap bubbles, large-scale PIV, aerodynamics

Printed by: Rijnja Repro

Front & Back Cover by: D.E. Faleiros

ISBN 978-94-6366-404-2

An electronic version of this dissertation is available at
http://repository.tudelft.nl/.

It doesn't matter how beautiful your theory is, it doesn't matter how smart you are. If it doesn't agree with experiment, it's wrong.

Richard P. Feynman

SUMMARY

Particle Image Velocimetry (PIV) relies upon the introduction of particle tracers that scatter sufficient light and follow the flow accurately. The use of submillimetre helium-filled soap bubbles (HFSB) as flow tracers for PIV is investigated for the purpose of enabling velocity measurements in large-scale industrial wind tunnels.

That soap bubbles reflect more light than scattered by small liquid droplets or solid particles, allowing larger volumes to be illuminated, is a long known fact and has caught the attention of aerodynamicists since the 1930s. The difficulty encountered during initial efforts on using soap bubbles for accurate measurements revolves around the lack of control during the generation of these tracers, and the failure in presenting evidence that they could accurately follow the flow. Proof of concept that HFSB could be used for accurate flow measurements in wind tunnels was presented in the year that preceded the beginning of this work.

In this thesis, the generation and control of HFSB and their tracing fidelity are studied through a series of experiments and simulations, bringing large-scale PIV using HFSB to the technology maturity level required for industrial measurements.

High-speed shadowgraphy at the bubble generator exit revealed the main *regimes of bubble generation*. A regular, periodic and controlled generation bubbles of monodisperse size distribution, namely, the *bubbling regime*, was obtained by properly tuning of the input flow rates. The relation of the later with the bubble size and production rate was also obtained from these visualizations.

Measurements of the HFSB velocity in the stagnation region ahead of a cylinder, obtained with Particle Tracking Velocimetry (PTV), relative to the flow velocity (*slip velocity*) were used to retrieve the HFSB *time response* and the ratio of helium to soap flow rates that satisfy the *neutral*

buoyancy condition, in which the soap bubble density equals that of the surrounding air flow.

Simulations of the particle motion in a rectilinear oscillatory flow was used to quantify the importance of the unsteady forces acting on a particle and to derive empirical relations for estimating the HFSB slip velocity in flows where the unsteady forces are relevant. In this case, the particle slip velocity is shown to depend on three parameters: the *particle Reynolds number*, the *ratio of particle-to-fluid density* and the *flow time-scale*. These cannot be combined into a single non-dimensional *Stokes number*. The validity of the empirical relations were extended for the analysis of the slip velocity of a particle travelling around an object. Based on the later, a method for deriving the density of a nearly-neutrally-buoyant particle that comprises the effects of unsteady forces and allows mismatch of acceleration between the particle and the flow was described.

The tools developed for slip velocity analysis using the simulations were applied to assess experimental data from large-scale PIV measurements performed at the Low-Speed Tunnel (LST) of the German-Dutch Wind Tunnels (DNW). The experiments were realized in the flow around an airfoil of 70 cm chord at free stream velocity up to 70 m/s, reaching a chord-based Reynolds number of 3.2 million. PIV measurements using HFSB at this speed and Reynolds number were unprecedented. The results have indicated variations of the bubble density (20-30%) occurring post-generation.

The tracing fidelity of HFSB in wall-bounded turbulence is investigated by comparing measurements in a turbulent-boundary layer of the mean velocity and Reynolds stress profiles, with those obtained with micrometre oil droplets (reference) and submillimetre air-filled soap bubbles (AFSB). The results have shown that the statistics of the first and second moments of velocity are well captured by all three investigated tracers, even by the heavier-than-air AFSB, which were shown to be poor

tracers in the stagnation of a cylinder. Mechanisms of preferential concentration in turbulence were attributed as the cause of the better traceability observed.

The thesis is concluded with a successful industrial application in the Large Low-Speed Facility (LLF) of DNW (9.5×9.5 m^2 test section) around a *tiltrotor aircraft* in three flight modes, *hover*, *transition* and *cruise*, and tunnel speeds up to 60 m/s. The bubbles were introduced into the flow using a 3×3 m^2 seeding rake, containing 400 bubble generators. The PIV measurements were performed in *stereoscopic* configuration in a field-of-view of 1.1×1.1 m^2.

SAMENVATTING

Particle Image Velocimetry (PIV) is gebaseerd op de introductie van deeltjes die voldoende licht verstrooien en de stroom nauwkeurig volgen. Het gebruik van sub-millimeter helium gevulde zeepbellen (HFSB) als stroomtracers voor PIV wordt onderzocht om snelheidsmetingen in grootschalige industriële windtunnels mogelijk te maken.

Dat zeepbellen meer licht reflecteren dan verstrooid door kleine vloeistofdruppeltjes of vaste deeltjes, waardoor grotere volumes kunnen worden belicht, is een al lang bekend feit en heeft sinds de jaren dertig de aandacht van aerodynamica-onderzoekers getrokken. De moeilijkheid die werd ondervonden tijdens de eerste pogingen om zeepbellen te gebruiken voor nauwkeurige metingen, heeft te maken met het gebrek aan controle tijdens hun generatie, en het mislukken om bewijs te leveren dat ze de stroom nauwkeurig konden volgen. Het bewijs van het concept dat HFSB kan worden gebruikt voor nauwkeurige stromingsmetingen in windtunnels werd gepresenteerd in het jaar voorafgaand aan het begin van dit werk.

In dit proefschrift worden de generatie en controle van HFSB en hun traceerbaarheid bestudeerd door middel van een reeks experimenten en simulaties, waardoor grootschalige PIV met behulp van HFSB op het technologisch volwassenheidsniveau wordt gebracht dat vereist is voor industriële metingen.

High-speed shadowgraphy bij de uitgang van de bellen generator onthulde de belangrijkste *regimes voor het genereren van bellen*. Een regelmatige, periodieke en gecontroleerde generatie van bellen met een monodisperse grootteverdeling, namelijk het *bubbling regime*, werd verkregen door het correct afstemmen van de ingangsstroomsnelheden. De relatie van de laatste met de belgrootte en productiesnelheid werd ook verkregen uit deze visualisaties.

Metingen van de HFSB-snelheid in het stagnatiegebied voor een cilinder, verkregen met Particle Tracking Velocimetry (PTV), ten opzichte van de stroomsnelheid (*slipsnelheid*) werden gebruikt om de HFSB-tijdsrespons en de verhouding van helium- tot zeepstroomsnelheid te achterhalen die voldoen aan de toestand van *neutraal drijfvermogen*, waarbij de dichtheid van de zeepbel gelijk is aan die van de omringende luchtstroom.

Simulaties van de deeltjesbeweging in een rechtlijnige oscillerende stroom werden gebruikt om het belang van de instationaire krachten die op een deeltje inwerken te kwantificeren en om empirische relaties af te leiden voor het schatten van de HFSB-slipsnelheid in stromen waar de instationaire krachten relevant zijn. In dit geval blijkt dat de slipsnelheid van de deeltjes afhangt van drie parameters: het *deeltjes-Reynoldsgetal*, de *dichtheidsverhouding tussen de zeepbel en het medium* en de *stromingstijdschaal* (genormaliseerd met de viskeuze tijdschaal). Deze kunnen niet worden gecombineerd tot een enkel niet-dimensionaal *Stokes-getal*. De geldigheid van de empirische relaties werd uitgebreid voor de analyse van de slipsnelheid van een deeltje dat rond een object beweegt. Op basis van dat laatste werd een methode beschreven om de dichtheid van een bijna neutraal drijvend deeltje af te leiden dat de effecten van instationaire krachten omvat en een verkeerde combinatie van de versnelling tussen het deeltje en de stroom toelaat.

De tools die zijn ontwikkeld voor slip-snelheidsanalyse met behulp van de simulaties, werden toegepast om experimentele gegevens te beoordelen van grootschalige PIV-metingen uitgevoerd in de Low-Speed Tunnel (LST) van de Duits-Nederlandse windtunnels (DNW). De experimenten werden uitgevoerd in de stroming rond een aerodynamisch profiel van een koord van 70 cm met een vrije stroomsnelheid tot 70 m/s, waarbij een op koorden gebaseerd Reynoldsgetal van 3,2 miljoen werd bereikt. PIV-metingen met HFSB bij deze snelheid en het Reynoldsgetal

waren nog niet eerder gedaan. De resultaten hebben variaties laten zien in de beldichtheid (20-30%) die na generatie optreden.

De traceerbaarheid van HFSB in wand-gebonden turbulentie wordt onderzocht door metingen in een turbulente grenslaag van de gemiddelde snelheid en Reynolds stressprofielen te vergelijken met metingen die verkregen zijn met micrometer oliedruppeltjes (referentie) en sub-millimeter lucht-gevulde zeepbellen (AFSB). De resultaten hebben aangetoond dat de statistieken van de gemiddelde snelheid en de turbulentie schommelingen goed worden vastgelegd door alle drie de onderzochte tracers, zelfs door de zwaarder-dan-lucht AFSB, die slechte tracers bleken te zijn bij de stagnatie van een cilinder. Mechanismen van preferentiële concentratie in turbulente stromingen werden toegeschreven als de oorzaak van de waargenomen betere traceerbaarheid.

Het proefschrift wordt afgesloten met een succesvolle industriële toepassing in de Large Low-Speed Facility (LLF) van DNW (9,5 x 9,5 m^2 testgedeelte) rond een tilt-rotor vliegtuig in drie vliegmodi, *standvlucht*, *overgang* en *kruisvlucht*, en tunnelsnelheden tot 60m/s. De bellen werden in de stroom gebracht met behulp van een systeem (3×3 m^2) met daarin 400 bellengeneratoren. De PIV-metingen werden uitgevoerd in stereoscopische configuratie in een gezichtsveld van 1,1 x 1,1 m^2.

TABLE OF CONTENTS

1

INTRODUCTION

1.1 Background

1.1.1 Flow measurement techniques: a brief history

Through the course of human history, the search of a deeper understanding of fluid dynamics is often associated with technological progress and pushed forward by our intrinsic desire to explore, making possible navigation, aviation and space exploration. If fluid dynamics knowledge began with Greek philosophy (Aristotle 384-322 B.C., Archimedes 287-212 B.C.), it only really took off during the Renaissance (Anderson, 2010), with perhaps the first flow visualizations of turbulent flows being recorded on the impressive drawings of Leonardo da Vinci (1452-1519). Most of our breakthroughs, however, only took place when empirical data started to be methodically acquired with proper instrumentation.

One of the most important instruments for measuring flow velocity is the Pitot tube, invented by Henry Pitot in 1732. By the time he had to use empirical relations to obtain velocity from the stagnation and static pressures. Bernoulli's equation, derived by Euler, only came about 20 years later (Anderson, 2010). Nowadays, there are several pointwise velocimetry techniques for fluid dynamics experimentation, such as hot-wire anemometry (HWA)—traced back to the beginning of the 20th century (1909-1914) and attributed to several authors (see Comte-Bellot

1976)—and laser Doppler velocimetry (LDV), first demonstrated by Yeh and Cummins in 1964.

Pointwise measurements, however, cannot provide information on velocity gradients, vorticity and instantaneous flow patterns. Multi-point quantitative information can be obtained for instance, through assembling arrays of hot-wires or five-hole probes. However, this approach is seldom practiced due to the technical complexity, blockage of the flow and inability to measure flow reversal.

Photography was introduced as a tool for scientific investigation in fluid dynamics by the end of the 19th century, offering the potential to capture the dynamics of unsteady flows. Initially, photography was mainly used for flow visualization. Some of the pioneering contributions to streakline visualizations at the time were performed by Ludwig Mach and Étienne-Jules Marey (figure 1-1, Hoffmann, 2013), followed by Friedrich Ahlborn and Ludwig Prandtl in the beginning of the 20th

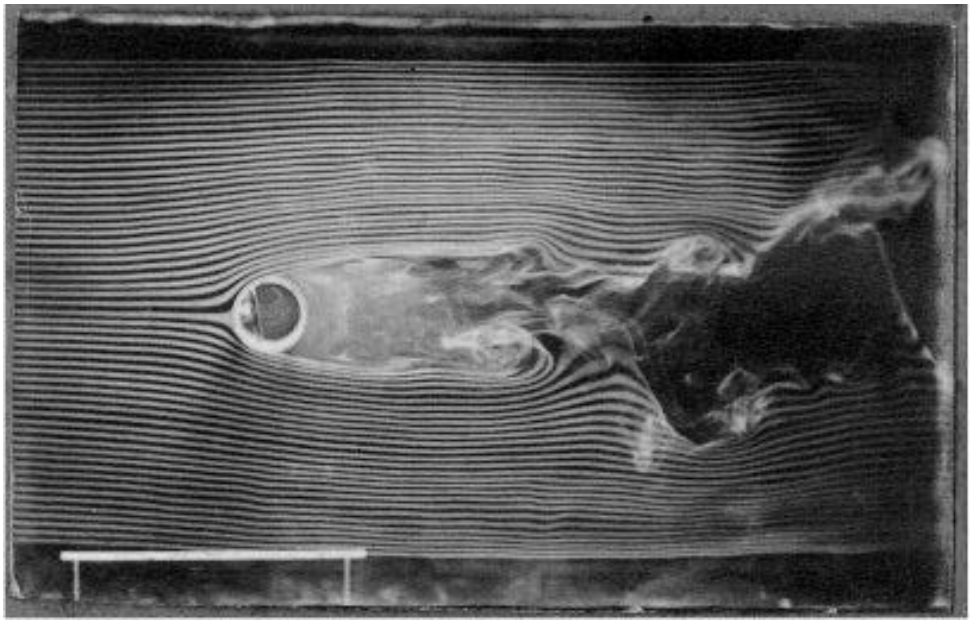

Figure 1-1. Photography of streaklines around a cylinder by Étienne-Jules Marey ca. 1901 (reproduced from Hoffmann, 2013).

century (see reviews from Hinterwaldner 2015 and Willert et al. 2019). Unfortunately, when wind tunnels became regular tools for aerodynamic research in the development of the first aircrafts a few years later, flow visualization had no place in the laboratories, which were mostly concerned in obtaining quantitative data for drag and lift through balance measurements (Hoffmann, 2013).

In fact, quantitative information of the flow through photography was obtained as early as 1917 by Nayler and Frazier (as cited by Adrian, 2009) to study the unsteady flow around a cylinder. They identified and tracked particle images through 80 consecutive frames (figure 1-2) using the oldest tools known to man—their own eyes and hands. Thus, particle tracking velocimetry (PTV) exists for almost as long as aviation itself, however, the cumbersome work of manually processing the photographs meant PTV would have to wait further advancements in digitalization of

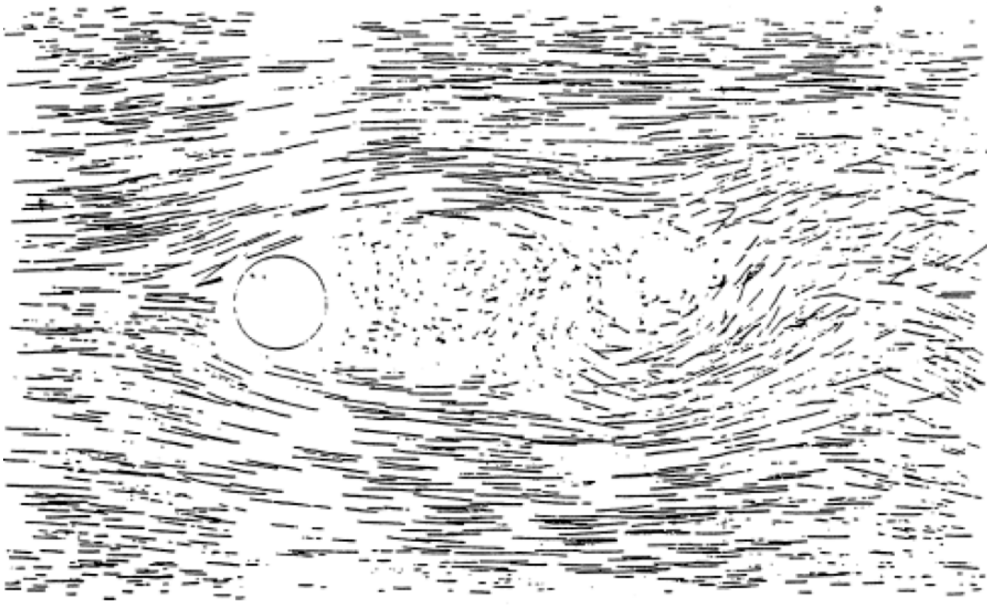

Figure 1-2. Streaks formed after manually reconstructing trajectories obtained with particle tracking velocimetry performed through 80 consecutive frames made using cinematography by Nayler and Frazier, 1917 (reproduced from Adrian, 2009).

images and automation of processing, before it would become a practical tool. Advancements in this direction appeared in the end of the seventies as, for instance, in the work of Elkins et al. (1977), who developed an automated algorithm for processing stereoscopic PTV data. In the same year, laser speckle velocimetry (LSV) was developed by three different research groups, and benefitted abundantly from the works of Roland Meynart (1979-1983, see Adrian, 2005). In fact, the developments of LSV formed the basis of particle image velocimetry (PIV). The term PIV, however, appeared for the first time in two contemporaneous publications by Pickering and Halliwell (1984) and Adrian (1984). In the latter, a distinction between LSV and PIV is given, based on the source density—a quantity proportional to the particle concentration and cross-sectional area. Basically, LSV can only be applied when the source density is much greater than one, meaning that many particle images overlap, allowing speckle patterns to exist. Instead, PIV is used when the particle concentration is sufficiently low, allowing distinct identification of particle images.

1.1.2 Particle Image Velocimetry

Particle image velocimetry (PIV) is a non-intrusive optical technique of flow velocity measurement that can capture simultaneously information from about 10^3-10^5 flow points with sufficient resolution, yielding instantaneous flow vorticity and rate of strain (Westerweel et al. 2013). The technique involves the measurement of the spatial displacement of particles, artificially introduced into the flow, within a brief time interval that is fixed by the measurement apparatus—usually defined by the time in between different pulses of the illumination source. The particles are usually illuminated by a pulsed laser, with pulses of very short duration (about 10 ns), “freezing” the image of the particles, which are captured in at least two time instants by the recording device (see chapter 0 for details). Particles must follow the flow, yielding an accurate representation of the flow behaviour, and scatter sufficient light, for the

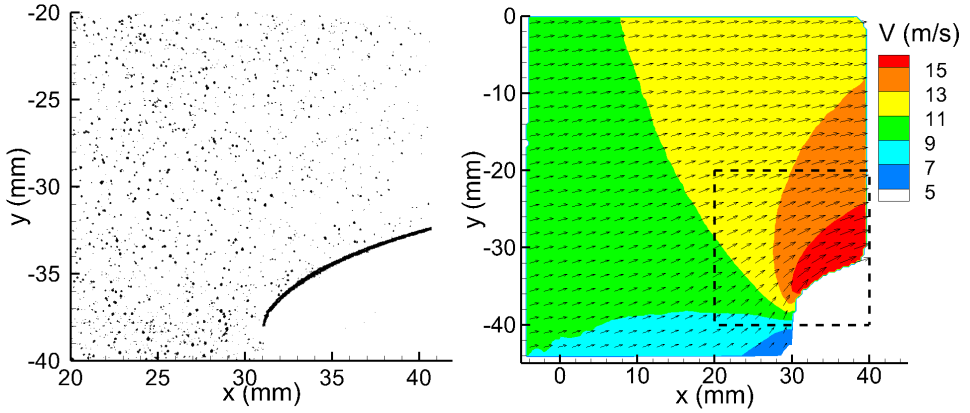

Figure 1-3. Example of a PIV measurement around an airfoil leading edge (LE) immersed in the air stream at 10 m/s, using micrometre Di-Ethyl-Hexyl-Sebacat (DEHS) particles. Left) Particle images recorded at a single time instant (zoomed view for clarity, see dashed square on the tight image). Right) Average velocity vectors after cross-correlation analysis of 100 image pairs (showing 1 every 5×5 vectors).

distinct identification of their images in the recording device. An example of a raw PIV image and resulting velocity field is shown in figure 1-3.

The choice of particles for PIV is therefore a vital task, in which experimentalists face a trade-off: small particles follow better the flow, but larger particles offer better optical properties (Melling, 1997). Conventional PIV particles are usually produced from solid or liquid materials much denser than air, e.g. oil and water droplets, and typically in the micrometre range—heavy particles larger than three micrometres tend to lag behind the flow, resulting in incorrect velocity measurements (Melling, 1997). However, because the amount of light scattered by a particle scales with its cross-sectional area (Adrian and Yao, 1985), when dealing with three-dimensional measurements, the domain achieved with microparticles seldom exceeds 100 cm^3 (Scarano 2013).

1.1.3 Large-scale PIV

When considering experiments at scales relevant for industrial aerodynamics, the setup of the PIV system becomes more challenging than in a small research laboratory. For instance, in the work of De Gregorio et al. (2010), where PIV measurements with DEHS micrometre particles have been performed around a helicopter with a four-bladed rotor of 4.2 m diameter (figure 1-4), the list of equipment amounted to: five Nd:YAG lasers (280 mJ per pulse), four 4-Mpx cameras with motorized Scheimpflug adapters and four mechanical traversing systems. The main reason for this extensive list of equipment is that micrometre particles do not scatter sufficient light for the illumination of large volumes, requiring, in this case, illumination from both sides and the division of the domain in several measurement planes.

Although the previous example is an impressive demonstration of a large-scale PIV measurement, it illustrates why the technique has been

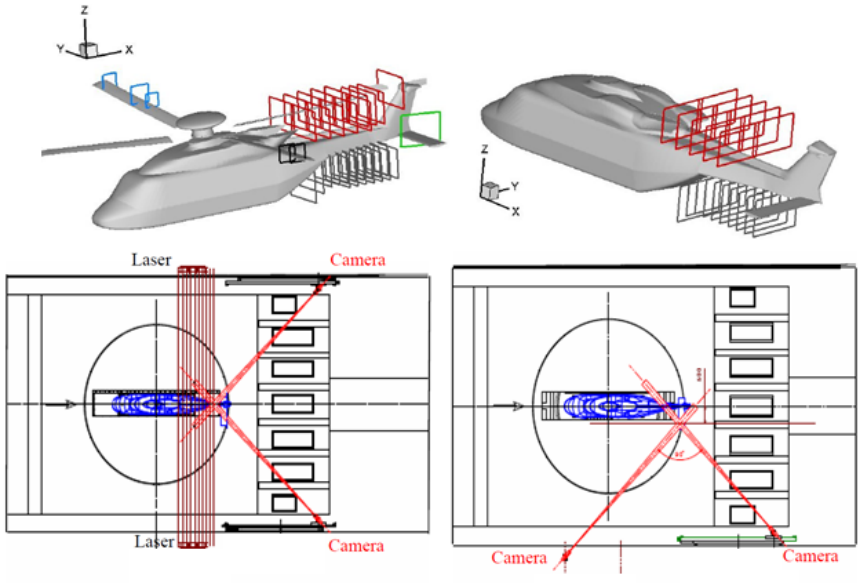

Figure 1-4 Example of industrial PIV measurement using a traversing system (reproduced from Gregorio, 2010).

usually associated, in the industrial environment, with complex and time-consuming setups. If sufficiently bright particles had been available, the illumination could have been realized using a single laser and the imaging with a single camera system (of at least three cameras), where the entire volume could have been captured at once (as long as optical access is not blocked along the lines-of-sight or lines-of-illumination).

In comparison to micrometre particles, submillimetre helium-filled soap bubbles (HFSB, Hale et al. 1969, Bosbach et al. 2009) scatter 10,000 times more light (Caridi, 2018). Consequently, larger regions of the flow can be illuminated with the same laser power. Planar PIV measurements using HFSB can be realized at meter-scale (e.g. the flow in an aircraft cabin mock-up, figure 1-5, Bosbach et al. 2009). Measurement volumes obtained with micrometre particles and HFSB are

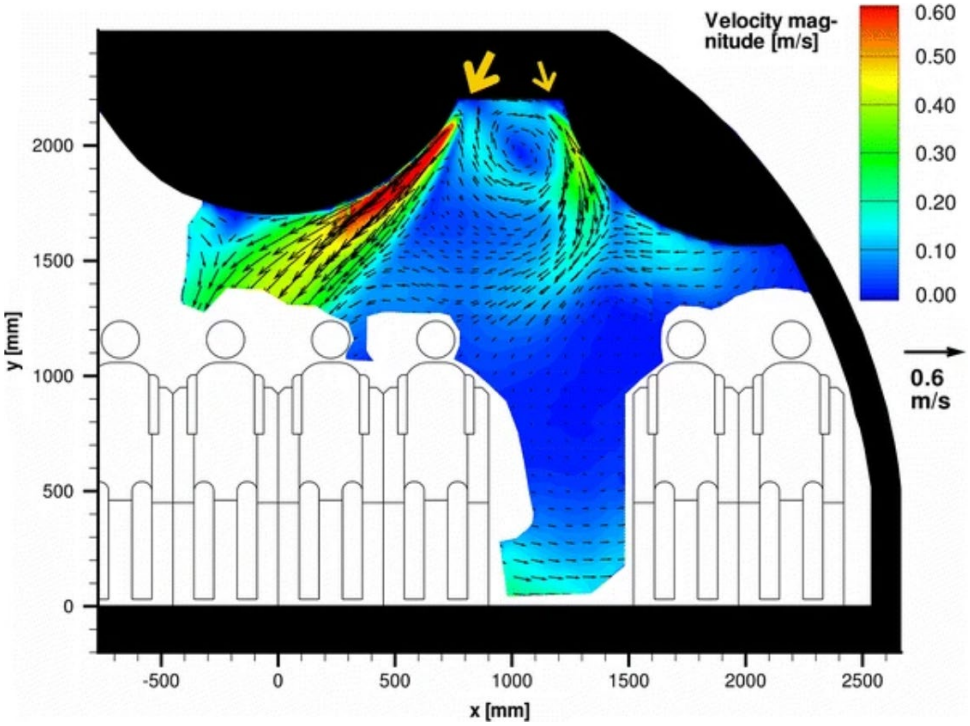

Figure 1-5. Planar PIV measurement in an aircraft cabin mock-up using helium-filled soap bubbles. Reproduced from Bosbach et al. 2009.

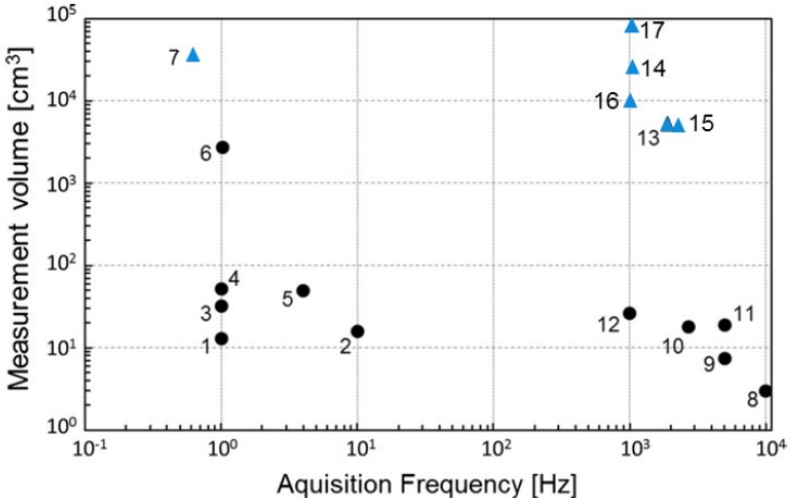

Figure 1-7 PIV measurement volume in airflows with conventional micrometre seeding (black circles) and submillimetre HFSB (blue triangles). 1. Elsinga et al. (2006); 2. Humble et al. (2009); 3. Atkinson et al. (2011); 4. Schröder et al. (2011); 5. Staack et al. (2010); 6. Fukuchi (2012); 7. Kühn et al.(2011); 8. Pröbsting et al. (2013); 9. Violato et al. (2011); 10. Ghaemi and Scarano (2011); 11. Schröder et al. (2009a); 12. Michaelis et al. (2012); 13. Scarano et al. (2015); 14. Caridi et al. (2016); 15. Schneiders et al. (2016); 16. Frigate experiment, Caridi (2018); 17 Huhn et al. (2017). Figure reproduced from Caridi (2018).

compared in figure 1-6 (reproduced from Caridi, 2018). For instance, at 1 kHz, micrometre particles are restricted to volumes of $O(10)$ cm³, while measurements with HFSB reach $O(10{,}000)$ cm³.

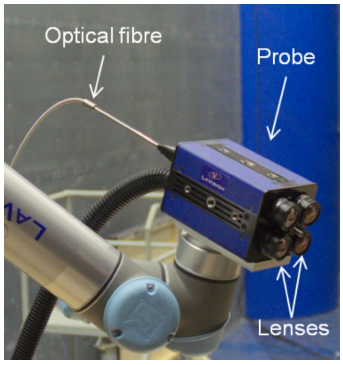

Figure 1-6. The CVV system: 4 cameras, 1 optical fibre. Reproduced from Jux et al. 2018.

1.1.4 Robotics PIV

The use of robotics for stereoscopic (Michaux et al. 2018) and volumetric PIV (Schneiders et al. 2018, Jux et al. 2018) have introduced additional flexibility for PIV measurements. The robot's arm six

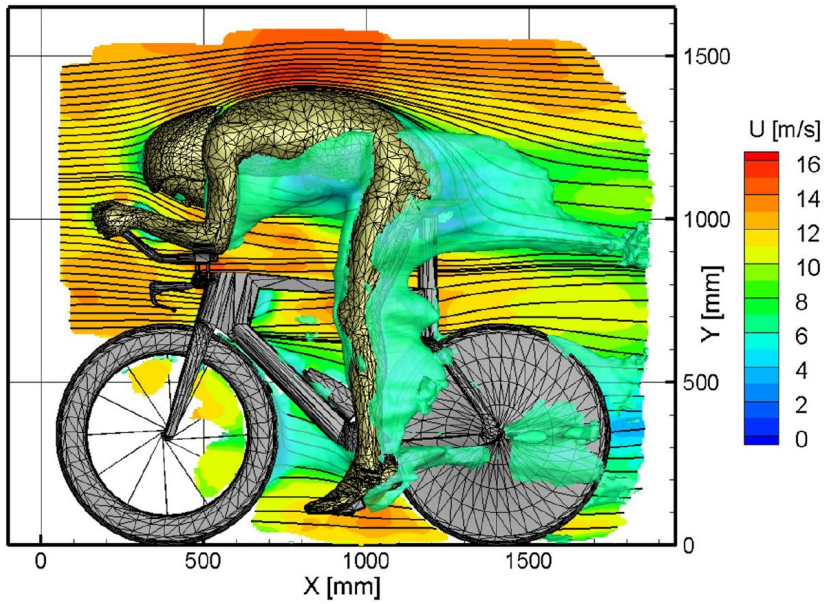

Figure 1-8. Velocity field measured around a full-scale cyclist model using the CVV system. Reproduced from Jux et al. 2018.

degrees of freedom enables measurements involving difficult optical access or the need to rotate the laser sheet with the model.

The coaxial volumetric velocimetry CVV (Schneiders et al. 2018, Jux et al. 2018) combines a compact volumetric PIV system (figure 1-7) with HFSB to perform time-resolved measurements in a volume of about 15 litres (Jux et al. 2018). With a single calibration, Jux et al. (2018) measured the velocity field in a volume of 2.2 m^3 around a full-scale cyclist model (figure 1-8) by combining measurements from 450 positions.

1.1.5 PIV for CFD validation

Computational fluid dynamics (CFD) plays an instrumental role in many industrial applications, contributing to the design and analysis of aircrafts, helicopters, automobiles, trucks, boats, wind turbines and wind farms (Spalart and Venkatakrishnan, 2016). However, in spite of continuous advances in computer technology, direct numerical

simulation (DNS) resolution in turbulent flows is still unattainable for most aeronautical applications (Favier, 2010). Therefore, CFD predictions must rely on methods that include the modelling of turbulence, such as the Reynolds-averaged Navier-Stokes (RANS). Although RANS can deal with a variety of flow regimes and configurations, more complex flows require the assessment of the uncertainties, and experimental validation.

Currently, CFD and wind tunnel tests are used in a complementary interactive process. As CFD advances it requires more sophisticated techniques for experimental validation. Nowadays there are several techniques that are capable of delivering data with minimal intrusiveness (Schröder et al. 2009b), such as: pressure sensitive paint (PSP, McLachlan and Bell 1995) for surface pressure data, image pattern correlation technique (IPCT, Kirmse 2016) for capturing the model

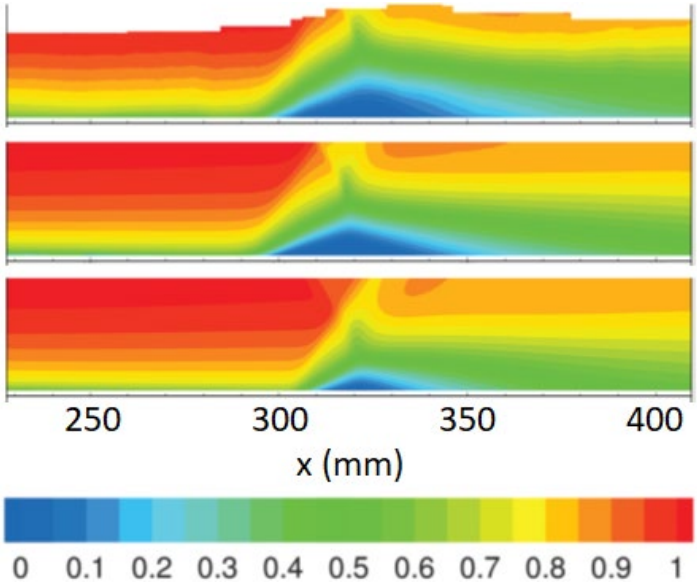

Figure 1-9. CFD validation of shock wave-boundary layer interaction. From top to bottom: PIV experiment; RANS simulation using the Spalart-Allmaras (SA) turbulence model; RANS simulation using the k-ϵ turbulence model. Colour contours represent streamwise velocity. Reproduced from DeBonis et al. (2012).

surface deformation, background oriented Schlieren (BOS, Raffel 2015) for detecting density gradients at shocks and vortex lines, LDV for point-wise time-resolved spectral information (or the more intrusive HWA), and PIV for analysis of instantaneous velocity fields and derived flow and statistic quantities (e.g. CFD validation of shock wave-boundary layer interaction, figure 1-9, DeBonis et al. 2012).

1.2 Research motivation

Until recently, PIV has been associated with complex time-consuming setups, restricted to measurements on planes and in small volumes, and mostly applied for laboratory research. The introduction of HFSB potentially enables instantaneous velocity measurements in large volumes in a time-efficient manner. PIV, thus, becomes a promising technology for industrial tests, where Reynolds numbers approach that of real flights. Large-scale PIV can boost innovation in aircraft design, for instance, helping to identify the roots of drag increase, and providing means to investigate aircraft stability through the analysis of flow structures.

The proof of concept for applying HFSB tracers for quantitative measurements has been presented at laboratory level (Bosbach et al. 2009, Scarano et al. 2015, Morias et al. 2016). However, the control of the fundamental HFSB properties, namely, the production regime, the production rate, the bubble size and density, has not been rigorously researched. Further developing HFSB to the point of technological maturity has the potential to set large-scale PIV as a standard measurement technique for industrial tests.

In addition, PIV measurements using helium-filled soap bubbles offer the potential to provide accurate velocity information over much wider observation volumes for CFD validation of relevant cases, covering domains of interest not usually feasible with other techniques. In this respect, the measurement accuracy and quantification of uncertainty

become crucial and a systematic assessment of HFSB slip velocity is required.

1.3 Scope and methodology

Although there have been several important developments lately on the use of HFSB in wind tunnels (e.g. development of the first HFSB seeding rake for wind tunnels and first measurements of HFSB time

Topic	Method	Reference / Length Scale/ Flow velocity	Parameters under investigation
Generation and control	Shadowgraph experiments.	Generator nozzle *O*(1) mm N/A	Production regime, production rate and bubble size.
Tracing fidelity (potential flows)	PIV experiments (comparisons with DEHS[1]).	Cylinder *O*(1) cm 30 m/s	Density and time response.
	Numerical simulations / PIV experiments (comparisons with DEHS).	Airfoil *O*(10) cm 15-70 m/s	Slip velocity.
Tracing fidelity (wall-bounded turbulence)	PIV experiments (comparisons with DEHS and AFSB[2]).	Boundary-layer *O*(1) cm 30-50 m/s	Slip velocity and velocity fluctuations.
Industrial application	PIV experiments.	Tiltrotor aircraft *O*(1) m 15-60 m/s	System adequacy.

[1]DEHS: Di-Ethyl-Hexyl-Sebacat [2]AFSB: air-filled soap bubbles

Table 1-1. Scope and Methodology.

response), most of which can be found in the PhD thesis of Caridi (2018), there are still important research questions to be addressed. A systematic control of HFSB generation is still lacking, the limits of the technique in terms of tracing accuracy have not been established, and there is no simple and accurate way of assessing and predicting the accuracy of PIV errors using HFSB. The work presented in this thesis addresses these topics, bringing the technology closer to maturity. The investigations herein performed can be divided in the following topics regarding HFSB: generation and control, tracing fidelity in potential flows and in wall-bounded turbulence, and industrial application (table 1-1).

1.4 Goals

The goal of this project is to further advance the reliability of HFSB systems for large-scale PIV towards the point of industrial applications. This relevant objective, however, requires first tackling a number of scientific questions at the foundation of HFSB physics that will indicate the conditions of proper use of such tracers for accurate measurements. To this end, the following objectives are pursued:

1. Characterize the HFSB generation process and provide guidelines for the control of the most relevant bubble properties.
2. Identify and model the physical processes governing the tracing behaviour of submillimetre soap bubbles. In what respect do they differ from conventional PIV tracers?
3. Evaluate experimentally the HFSB tracing accuracy under flow conditions relevant for industrial aerodynamics (e.g. high Reynolds number and turbulent flow regime).
4. Demonstrate the feasibility of integrating HFSB systems in a large-scale wind tunnel for applications of industrial aerodynamics.

1.5 Outline

The research reported in this manuscript is structured as follows:

- Chapter 2 – “Particle Image Velocimetry” provides the reader with the relevant background on the fundamental and technical aspects of PIV.
- Chapter 3 – “Flow tracers” discusses the optical and mechanical behaviour of flow tracers typically used for PIV in air flows and gives an introduction to the physical modelling of particle motion.
- Chapter 4 – “Generation and control of HFSB” analyses the process that leads to the production of small bubbles by controlled streaming of air, helium and soap. Shadowgraph visualizations are used to define the relevant production regimes and to quantify the relation of bubble size and production regime with the input fluid flow rates.
- Chapter 5 – “Density and time response” quantifies experimentally the dependence of HFSB density and time response on the input flow rates of helium and soap.
- Chapter 6 – “Slip velocity modelling”: model developed based on numerical simulations for estimating the HFSB slip velocity.
- Chapter 7 – “Tracing fidelity in turbulent flows”: mean velocity and Reynolds stresses measurements in a turbulent boundary-layer with HFSB, air-filled soap bubbles and DEHS.
- Chapter 8 – “Industrial application: tiltrotor aircraft”: Demonstration of the technique in an industrial measurement, part of the NEXTTRIP project (HORIZON 2020).
- Chapter 9 – “Conclusions and outlook” summarizes the main findings of the research and give the author’s outlooks for the future of HFSB and large-scale PIV.

2

PARTICLE IMAGE VELOCIMETRY

2.1 Introduction

Particle Image Velocimetry is a widespread technique of measuring flow velocity from the displacement of particles within a given time interval (Raffel et al. 2018). It is the most practiced technique that allows instantaneous flow velocity measurements in a plane or a volume. The scope of PIV capabilities range from simple statistical analysis of average flow velocity and Reynolds stresses, from which vorticity and pressure (van Oudheusden, 2013) can be extracted, to the study of the dynamics of coherent turbulent structures (Westerweel et al. 2013).

2.2 Operational principle and image acquisition

Particle image velocimetry aims at recording the spatial displacement of particles flowing within an observation plane or volume, during a pre-defined time interval. The main components and conditions for a PIV measurement are:

- homogeneous distribution of particles tracers that faithfully follow the flow and scatter sufficient light;
- high-power double/multi-pulse illumination sources;
- optical arrangements for light delivery;
- sensitive, low-noise, high-resolution double-frame or high-speed image recording devices;
- synchronization, timing, data storage and processing units.

An example of a PIV setup, where two cameras record images from different directions (stereo-PIV), retrieving the three velocity components in a measurement plane, is shown in figure 2-1. In case a single camera is used, the camera optical axis must be perpendicular to the laser sheet, and only the two velocity components orthogonal to the imaging direction (in-plane motion) are measured. The principles discussed below are applied to both cases (as viewed per each camera). The combination of images acquired by each camera in stereo-PIV to render the three velocity components is discussed in section 2.5.

The particles are illuminated by two laser pulses of very short width δt (10-100 ns), separated by a short time interval $\Delta t \gg \delta t$. Typically Δt is about 10-100 μs for external aerodynamic measurements. The illumination source (usually lasers) and cameras exposure time are controlled by a synchronization unit. The cameras exposure time is also considerably larger than δt.

In case of *single-exposure* recording, the laser is pulsed a single time within one camera exposure. Thus, each particle is only illuminated once

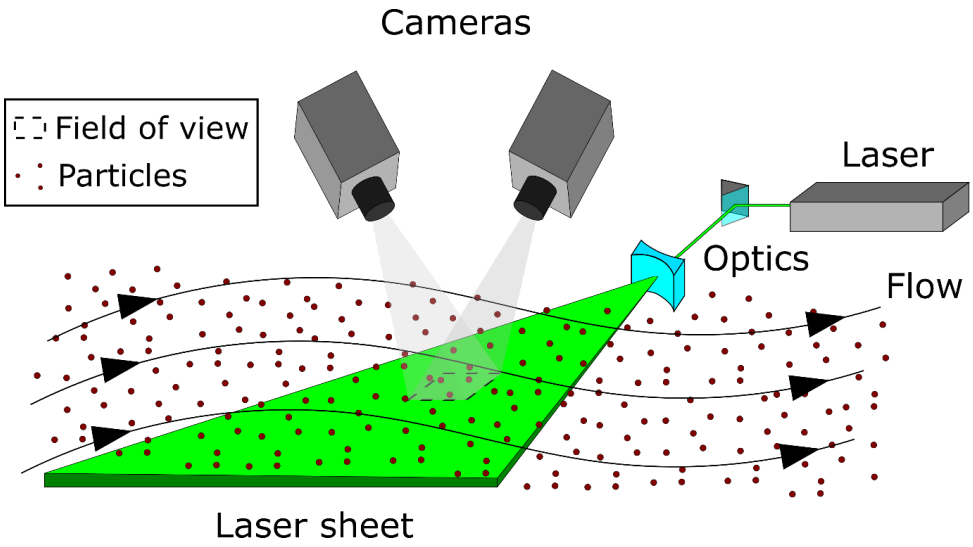

Figure 2-1. Schematic layout of an experiment conducted by stereo-PIV.

per frame. In *multi-exposure* recordings the laser is pulsed more than once during the camera exposure, and the particle displacement may be obtained from a single frame. However, at the cost of direction ambiguity.

There are two important characteristics from the PIV hardware that allow single exposure recordings on separate frames, separated by a short Δt (*double-frame*), that is independent and may be considerably smaller than the acquisition frequency $f = 1/\Delta T$ (figure 2-2, top). Digital cameras for PIV have the advantage of an electronic structure that allows recording two separate frames temporally spaced by a microsecond or less. In addition, PIV lasers are designed as double oscillator systems (two resonators), allowing to adjust the time separation between the two laser pulses independently of pulse strength. In case of time-resolved PIV, however, the images must be recorded in *single frame* (figure 2-2, bottom).

An illustration of a double-frame single-exposure PIV recording is

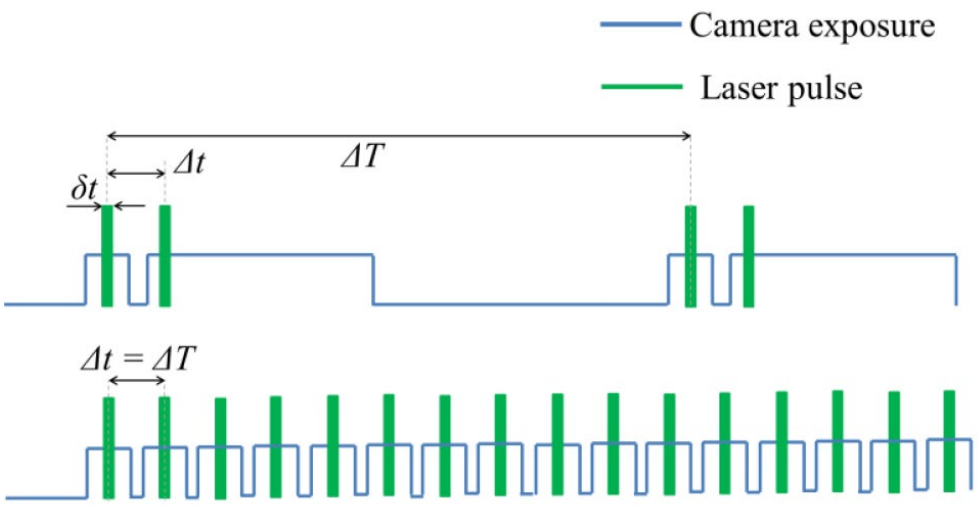

Figure 2-2. Timing synchronization of camera and laser. Top: double-frame single-exposure recording. Bottom: single-frame single-exposure recording. Reproduce from Caridi (2018).

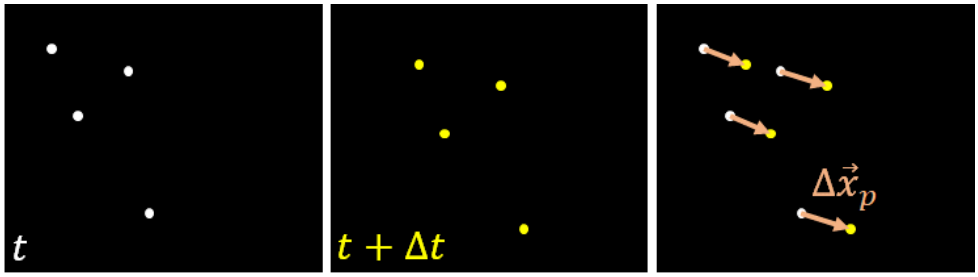

Figure 2-3. Illustration of a double-frame single-exposure PIV recording. The frame on the right is a superposition of the two measured frames, showing the particle displacements.

shown in figure 2-3. In this case the particle displacements may be tracked by eye due to the low concentration of particles and uniform displacement. This is not usually the case and sophisticated image processing algorithms are required (section 2.4). The flow velocity is obtained by assuming that the flow acceleration during Δt is negligible:

$$\vec{u}(t) \approx \vec{u}_p(t) \approx \frac{\vec{x}_p(t+\Delta t) - \vec{x}_p(t)}{\Delta t}, \tag{2.1}$$

where $\vec{u}$ and $\vec{u}_p$ are the fluid and particle velocities, respectively, and $\vec{x}_p$ is the particle position. In the latter, it is also assumed that the particles follow the flow faithfully, i.e. $\vec{u}_p(t) - \vec{u}(t) \ll \vec{u}(t)$. The time separation Δt must be sufficiently small to avoid particles moving out of the laser sheet plane, and to minimize errors due to flow acceleration (Raffel et al. 2018). The effect of acceleration can be taken into account if the particle image is captured three or more times by either performing multi-exposure or single-frame time-resolved measurements (Malik et al. 1993).

2.2.1 Particles

Particles are introduced into the flow homogeneously with minimum intrusiveness as possible, either locally or by seeding the entire tunnel flow (in the case of closed-circuit wind tunnels). They might be introduced either after the test section (in the latter case), or immediately

after the fan, or downstream of the tunnel turbulence screens. Typical particles used for PIV in air are shown in table 2-1. With exception of soap bubbles, particle diameters of about 1 μm are commonly used.

Type	Material	Diameter (μm)
Solid	Titania TiO2	0.1-5
Droplet	Di-ethyl-hexyl-sebacat (DEHS)	0.5-1.5
Bubble	Helium-filled soap bubbles (HFSB)	300-2000

Table 2-1. Typical particles used for PIV in air

2.2.2 Illumination and image recording devices

The illumination of particles is usually provided by high-power lasers, such as Nd:YAG (neodymium: yttrium aluminium garnet) and Nd:YLF (neodymium: yttrium lithium fluoride), coupled with frequency doublers to produce light of wavelengths within the visible part of the spectrum (532 nm and 526 nm, respectively), Lasers provide high energy monochromatic light (typically up to 400 mJ per pulse), allowing illumination of large volumes or planes (laser sheets) through properly manipulating the light with optical lenses and mirrors (Raffel et al. 2018).

The most common electronic sensors used for digital PIV cameras are charge coupled devices (CCD), complementary metal oxide semiconductor (CMOS) devices, and scientific CMOS (sCMOS) devices (Raffel et al. 2018).

2.3 Particle imaging

In the section above, the displacement of particles has been considered directly on the object plane for simplification. In reality, the displacement is measured by illuminating particles on the object plane, where the light scattered (or simply reflected) towards the camera, travels through a lens, and impinges onto the image sensor (image plane). The displacement recorded on the image plane must then be translated back to the object plane before the velocity is calculated. From the thin lens

approximation, the lens focal length relates the distance between the image and the lens planes (z_i) to the distance between the object and lens planes (z_o) as follows (figure 2-4):

$$\frac{1}{f} = \frac{1}{z_i} + \frac{1}{z_o}. \tag{2.2}$$

The particle position on the object plane at time t is obtained as follows:

$$\vec{x}_p(t) = -\frac{\vec{X}(t)}{M}, \tag{2.3}$$

where $\vec{X} = (X, Y)$ is the position of the particle image, i.e. the projection of the particle position $\vec{x}_p = (x_p, y_p, z_p)$ onto the image plane, and M is the image magnification:

$$M = \frac{z_i}{z_o}. \tag{2.4}$$

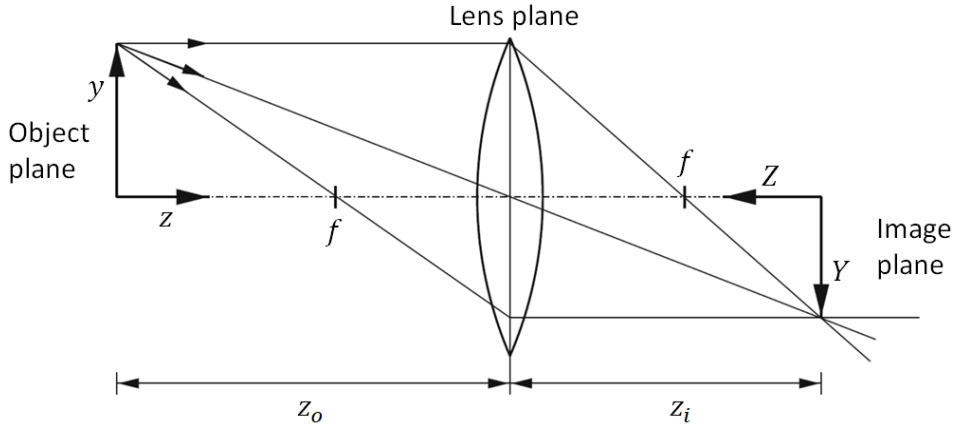

Figure 2-4. Geometric image reconstruction. Adapted from Raffel et al. (2018)

Consider a particle initially at $\vec{x}_p(t) = (x_p, y_p, 0)$, where $z = 0$ is the centre of the laser sheet, moving to $\vec{x}_p(t + \Delta t) = (x_p + \Delta x_p, y_p + \Delta y_p, \Delta z_p)$ (figure 2-5). Assuming the camera is focused on the object plane ($z = 0$), the displacement perceived by the camera $(\Delta x'_p, \Delta y'_p, 0)$ is different than the real displacement $(\Delta x_p, \Delta y_p, \Delta z_p)$. If the measurement is performed using a single camera, the true displacement $\Delta\vec{x}_p$ is not recovered, and the experimental results are given by the apparent in-

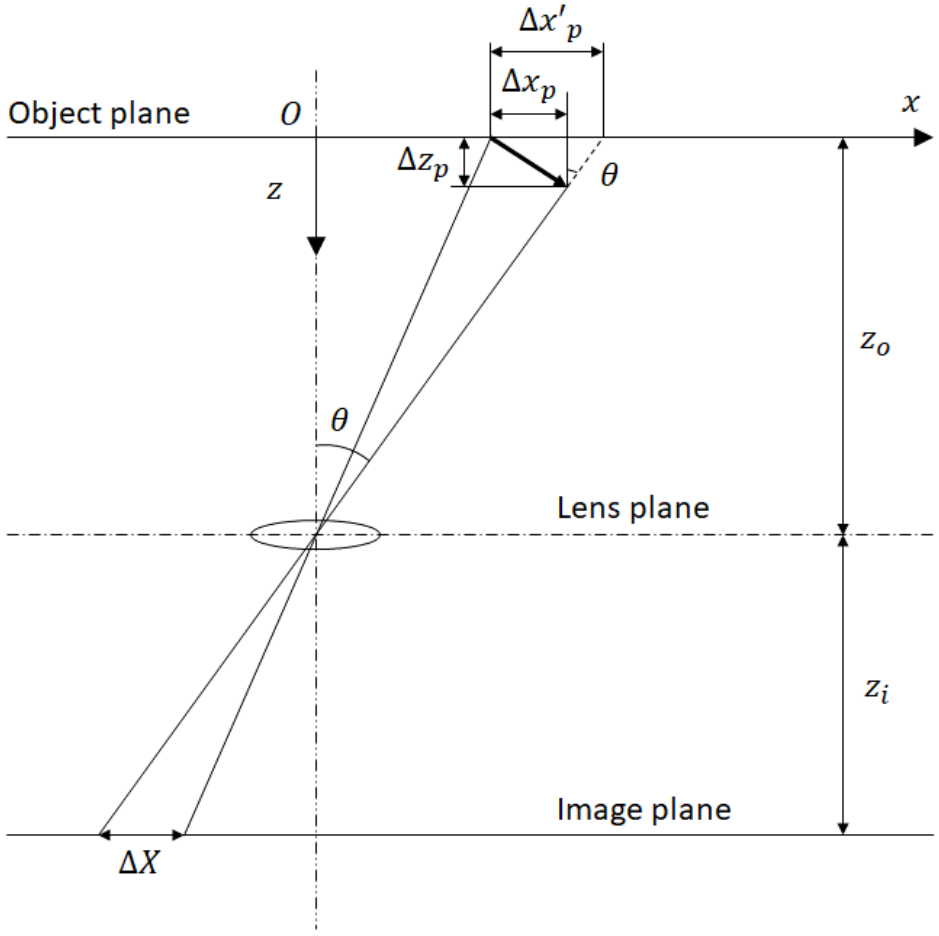

Figure 2-5. Schematic showing the translation of particle displacement from the object plane to the image plane. Adapted from Prasad (2000).

plane displacement $\Delta\vec{x}_p'$:

$$\Delta\vec{x}_p' = -\frac{1}{M_n}(\Delta X, \Delta Y, 0). \tag{2.5}$$

The true in-plane displacements are related to the apparent displacements as:

$$\begin{aligned} \Delta x_p &= \Delta x_p' - tan\,\theta_x\,\Delta z_{p,} \\ \Delta y_p &= \Delta y_p' - tan\,\theta_y\,\Delta z_p, \end{aligned} \tag{2.6}$$

where θ_x and θ_y are projections of θ onto the x-z and y-z planes, respectively. Consequently, the *perspective errors* relative to the in-plane displacements are given as:

$$\begin{aligned} \epsilon_x &= \frac{\Delta x_p'}{\Delta x_p} - 1 = \frac{\Delta z_p}{\Delta x_p} tan\,\theta_x\,, \\ \epsilon_y &= \frac{\Delta y_p'}{\Delta y_p} - 1 = \frac{\Delta z_p}{\Delta y_p} tan\,\theta_y. \end{aligned} \tag{2.7}$$

The perspective error can be significant for large θ and relatively large Δz. For instance, $\epsilon_x = 10\%$ for $\theta = 6°$ and $\Delta z = \Delta x$. In flows where $\Delta x_p \gg \Delta z_p$ and $\Delta y_p \gg \Delta z_p$ (predominantly two-dimensional), and z_o is much larger than the FoV length (small θ), the perspective error is negligible. Otherwise, stereoscopic PIV section (2.5) can be used to retrieve the out-of-plane displacement Δz_p, eliminating the perspective error.

2.3.1 Imaging of small particles

The planning of a PIV experiment requires the proper choice of the camera lens focal length f and the aperture diameter D_a. The latter is defined in practice by setting the objective f-number:

$$f_{\#} = \frac{f}{D_a}. \tag{2.8}$$

The choice of f and $f_{\#}$ defines the particle image diameter D and the depth of field δ_Z for a given image magnification M and light wavelength λ.

To obtain the image diameter of a small particle, it is necessary to consider light diffraction. The light scattered by a small particle forms a diffraction pattern on the camera sensor, even if an aberration free lens is used. The diffraction-limited image diameter is given by (Adrian and Yao, 1985):

$$d_{diff} = 2.44 f_{\#}(M + 1)\lambda. \tag{2.9}$$

Neglecting lens aberrations and considering particles imaged in focus, the particle image diameter becomes:

$$D = \sqrt{\left(M d_p\right)^2 + d_{diff}^2}. \tag{2.10}$$

The diffraction-limited image diameter usually determines the effective particle diameter for particles in the micrometre regime. For instance, if d_p = 2 μm, M = 0.5, $f_{\#}$ = 5.6 and λ = 532 nm, then $d_{diff} \approx$ 11 μm, while $M d_p$ = 1 μm. Instead, if $M d_p$ > 100 μm, then d_{diff} is negligible. The particle images should encompass at least 2 pixels to avoid *peak-locking*—a biasing of the measured displacement towards integer values of the displacement in pixel units (Westerweel, 2000).

Furthermore, if all particles are to be in-focus, the depth of field δ_z must be greater or equal than the depth of the illuminated volume (laser sheet thickness in planar PIV). The depth of field gives the distance along the camera axis between the two extreme out-of-focus positions, based on d_{diff}, that still yield an acceptable particle diameter (up to 20% variation with respect to image diameter at in-focus condition, Adrian 1991). The depth of field is given as (Raffel et al. 2018):

$$\delta_z = 4.88\lambda\, f_{\#}^2 (M^{-1} + 1)^2 \tag{2.11}$$

2.3.2 Imaging of helium-filled soap bubbles in air

When large helium-filled soap bubbles (0.3-1 mm diameter) floating in air are illuminated, the light rays reflected on the bubble soap film towards the recording medium form two glare points, resultant from reflections occurring externally and internally of the bubble (figure 2-6).

If the bubble diameter is resolved in several pixels (large magnification factor), the two bubble glare points are plainly visible (figure 2-7). The bubble centre is given by the midpoint between the two glare points. The distance between them can be used to calculate the bubble diameter. Since the refractive index of helium and air are approximately the same, and the shift of light ray direction within the soap film is negligible (the film thickness of a neutrally buoyant HFSB of 0.5 mm is about 80 nm, section 3.6), refraction can be neglected. Thus the spherical bubble diameter can be obtained from geometric considerations:

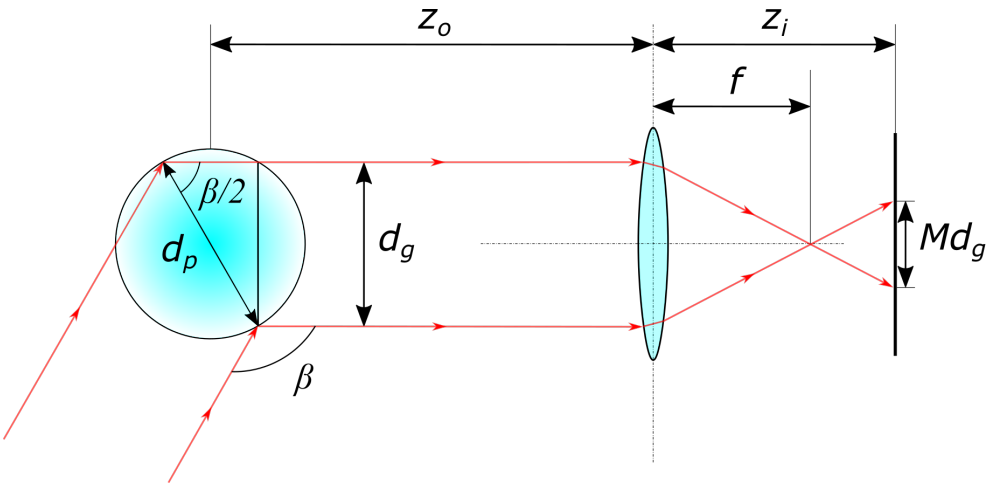

Figure 2-6. Schematic representation of bubble glare points image formation. Only the main two light rays from the parallel laser illumination are considered, that reflect directly towards the imager.

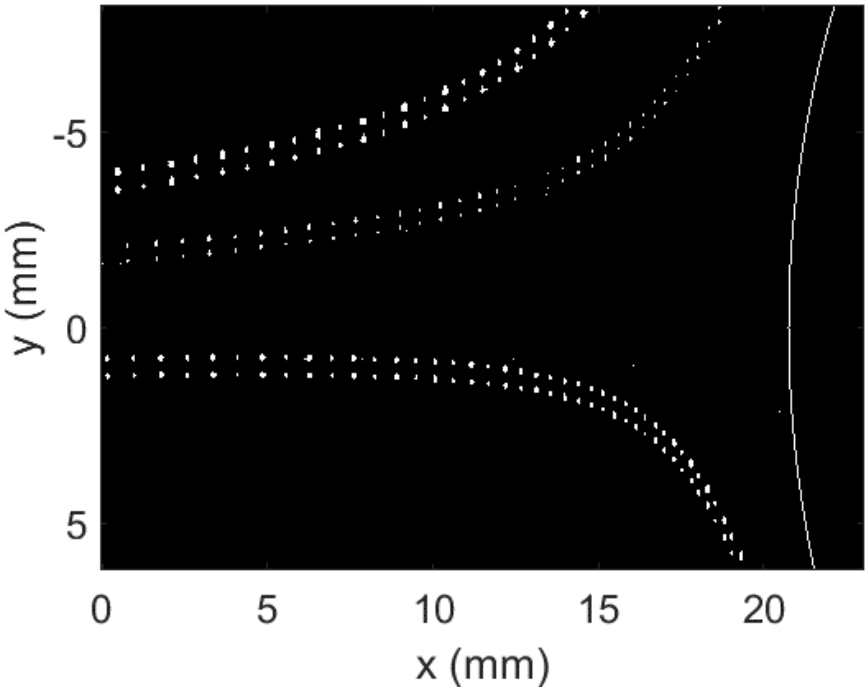

Figure 2-7. Example of raw image from a multi-exposure measurement of helium-filled soap bubbles (d_p~0.55 mm) trajectories around a cylinder of 5 cm diameter. Each bubble is visualized by its two glare points. The image magnification factor is 0.44. Details of the experiment are given by Faleiros et al. (2018).

$$d_p = \frac{d_g}{cos\left(\frac{\pi - \beta}{2}\right)}, \tag{2.12}$$

where d_g is the distance between the bubble glare points and β is the angle between the incoming light and the imaging direction. If the camera is positioned perpendicularly to the laser light sheet ($\beta = 90°$), as in a typical planar PIV setup, then eq. (2.12) reduces to:

$$d_p = \sqrt{2} d_g. \tag{2.13}$$

2.3.2.1 Glare point size

The size of a glare point δ_g can be obtained geometrically as a function of the bubble size and imaging conditions. Consider the case of a bubble being illuminated at a straight angle relative to the imaging direction ($\beta = 90°$, figure 2-8). For simplicity, the centre of the glare point is positioned at the lens symmetry axis. The distance from the glare point to the lens is z_o. The angle φ subtended by the illuminated area on the bubble surface (figure 2-9), corresponding to the glare point, is half the angle subtended by the aperture diameter (figure 2-8). For $z_o \gg D_a \gg d_p$ ($\tan\varphi \approx \varphi$), the angle φ is given as:

$$\varphi \approx \frac{D_a}{2z_o} \tag{2.14}$$

The glare point size is obtained geometrically from figure 2-9 ($\sin\varphi/2 \approx \varphi/2$):

$$\delta_g = \frac{a}{\sqrt{2}} \approx \frac{1}{2\sqrt{2}}\, d_p\varphi \tag{2.15}$$

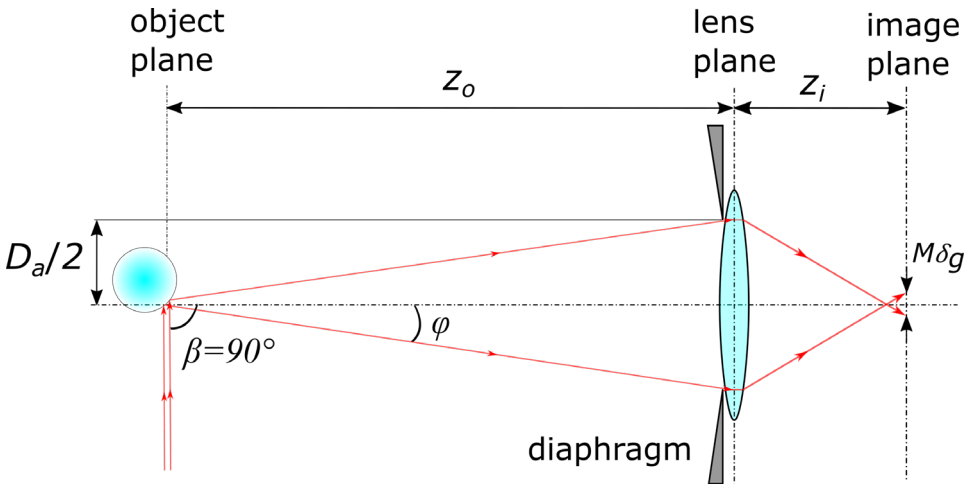

Figure 2-8. Glare point size of a bubble imaged at $\beta = 90°$ relative to the illumination direction.

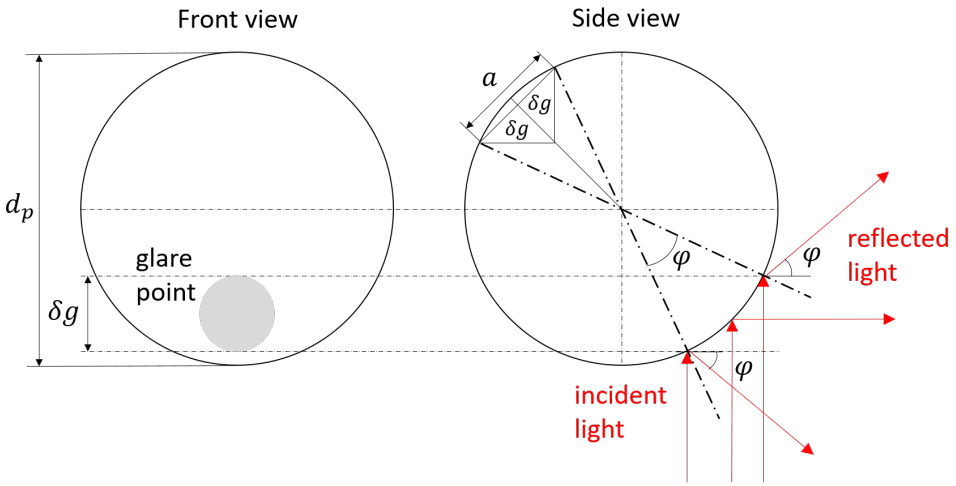

Figure 2-9. Angle subtended by the illuminated surface area corresponding to the imaged glare point.

Substituting eq. (2.14) and $D_a = f/f_\#$ into eq. (2.15), yields the glare point size in the object plane:

$$\delta_g \approx \frac{1}{4\sqrt{2}} \frac{d_p f}{z_o f_\#}. \tag{2.16}$$

Additionally, considering diffraction effects, the glare point size in the image plane is:

$$\Delta_g = \sqrt{\left(M\delta_g\right)^2 + d_{diff}^2}, \tag{2.17}$$

where d_{diff} is given by eq. (2.9). In fact, diffraction effects become dominant. For instance, for $d_p = 0.5$ mm, $z_o = 1$ m, $f = 100$ mm and $f_\# = 8$, then $M\delta_g = 1$ µm and $d_{diff} = 11$ µm. Therefore, the glare point image diameter Δ_g can be estimated from eq. (2.9).

2.3.2.2 Merging of glare points at large-scale

For large-scale PIV (small M), the glare points merge, forming a single particle image. The merging of glare points of a half-millimetre bubble within a laser light sheet ($\lambda = 526$ nm), imaged at a straight ($\beta =$

90°), is analysed by comparing the glare points distance in the image plane Md_g to the diffraction-limited-image diameter d_{diff} for $f\#$ = {5.6, 8, 16, 32} (figure 2-10). For this purpose, the magnification is calculated as $M = \sqrt{A}S/L_{FoV}$, where A is the camera sensor area [px^2], S is the sensor pixel-pitch [m/px] and L_{FoV} is the FoV side length [m].

For instance, when using an sCMOS camera (A = 2160 × 2560 px^2, S = 6.5 µm/px) and aperture diameter $f/16$, the glare points merge for $L_{FoV} > 25$ cm (figure 2-10, left). Instead, for a high-speed CMOS camera (A = 1000 × 1000 px^2, S = 20 µm/px), this occurs for $L_{FoV} > 33$ cm (figure 2-10, right).

The HFSB particle image area after merging, considering only diffraction, may be approximated to the area of an ellipse, extended along the axis passing through both glare points, i.e. $\pi(Md_g + d_{diff})d_{diff}$. For $f\#$ = 16, which is feasible with HFSB, d_{diff} is

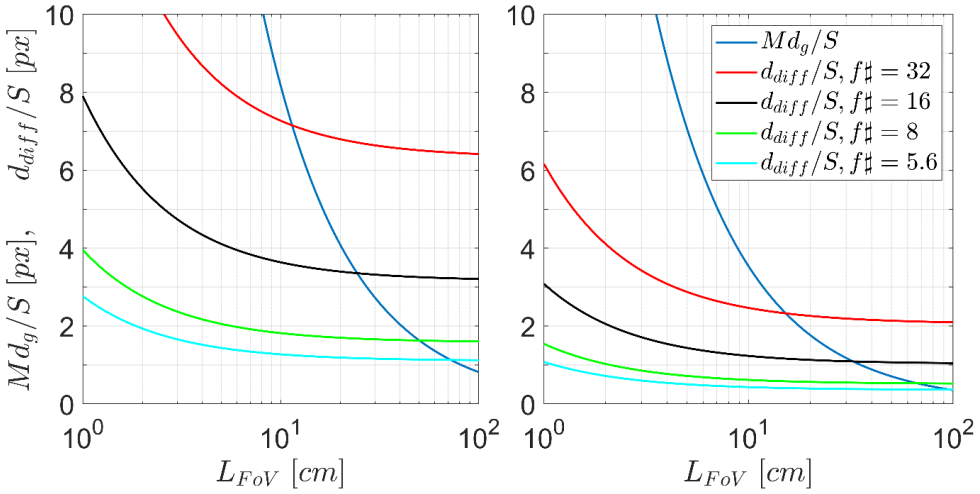

Figure 2-10. Comparison of HFSB glare point distance d_g with the diffraction-limited-diameter d_{diff} formed by each glare point for several FoV side lengths L_{FoV} and $f\#$. Laser light wavelength is λ = 526 nm. Left: sCMOS camera ($A = 2560 \times 2160$ px^2, S = 6.5 µm/px). Right: high-speed CMOS camera ($A = 1000 \times 1000$ px^2, S = 20 µm/px).

approximately threefold of Md_g for $L_{FoV} = 1$ m. Therefore, for narrow apertures at meter-scale FoV, the particle image diameter may be approximated to d_{diff}.

2.4 Image processing

The technique of tracking particles individually (figure 2-3) is referred as particle tracking velocimetry (PTV) or Lagrangian particle tracking (LPT), while the term PIV is often associated to the analysis by division of the image into small areas, namely, interrogation windows (IW), followed by cross-correlation of the particle intensity. Since most of the principles applied to one technique is usually applied to the other, the term PIV is used in this thesis with a broader meaning, involving both techniques. A clear distinction is only made when discussing in details the image processing techniques. In this section the main concepts involved in image processing for both PIV and PTV are given. For more details see Raffel et al. (2018).

2.4.1 Particle displacements via cross-correlation

Consider the intensity distribution I_a at time t on the image plane within one interrogation window due to the light scattered by particles positioned at $\vec{x}_{p,i}$ for $i = \{1, 2, \dots, N_I\}$, where N_I is the number of particles within the IW. After a short time interval Δt the intensity will have changed to I_b due to the particle displacements $\Delta\vec{x}_{p,i}$ and some measurement noise N (effects due to recording noise, three-dimensional flow, etc.). With both I_a and I_b known, the aim is to estimate $\Delta\vec{x}_{p,i}$ while excluding the effects of N (Raffel et al. 2018). This is accomplished by finding the particle displacements in a statistical sense, through the use of the discrete cross-correlation function (figure 2-11):

$$C(m,n) = \sum_{i=1}^{D_I}\sum_{j=1}^{D_I} I_a(i,j)I_b(i+m, j+n), \qquad (2.18)$$

where D_I [px] is the IW size, assuming it to be a square, and m and n are discrete pixel shifts around the initial IW position. For each shift (m,n), the sum of products of the overlapping pixel intensities is registered as the cross-correlation value $C(m,n)$. For instance, if all shift possibilities are considered, combining m = {-2, -1, 0, 1, 2} and n = {-2, -1, 0, 1, 2}, then a 5 × 5 correlation map is formed. When the discrete shift is the closest to the true average displacement of the particles within the IW, the closest match of I_a and I_b is found and C is the largest. The highest value in the correlation plane is therefore used to obtain the integer particle displacement.

Sub-pixel accuracy is obtained by fitting a smooth curve to the correlation map. The most common applied fit is the one-dimensional 3-point Gaussian fit (figure 2-12), calculated using the highest correlation value and its two neighbouring values. For a cross-correlation peak

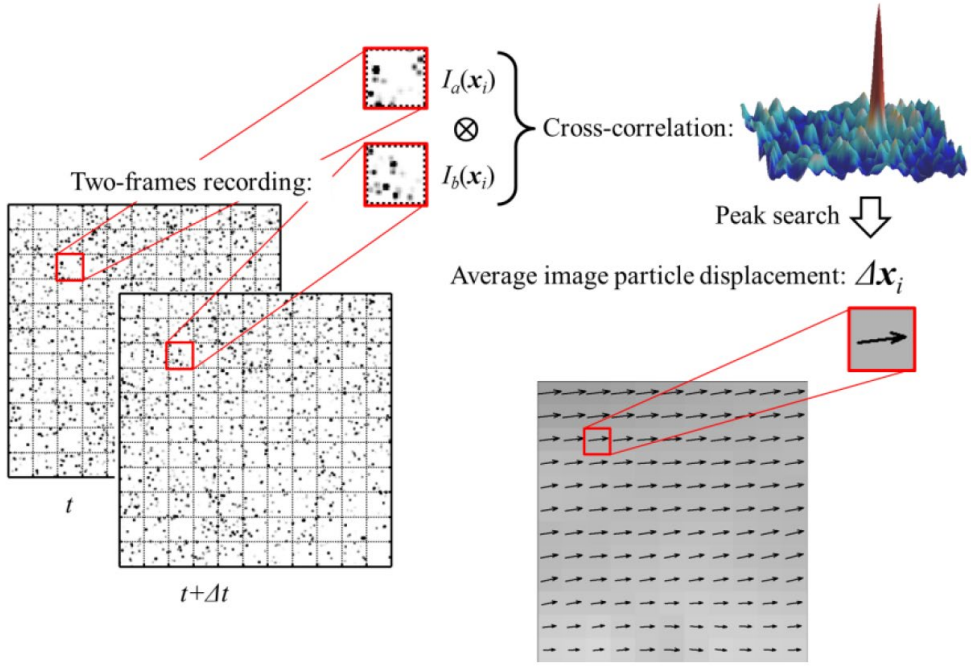

Figure 2-11. Determination of particle displacement through cross-correlation. Reproduced from Caridi (2018).

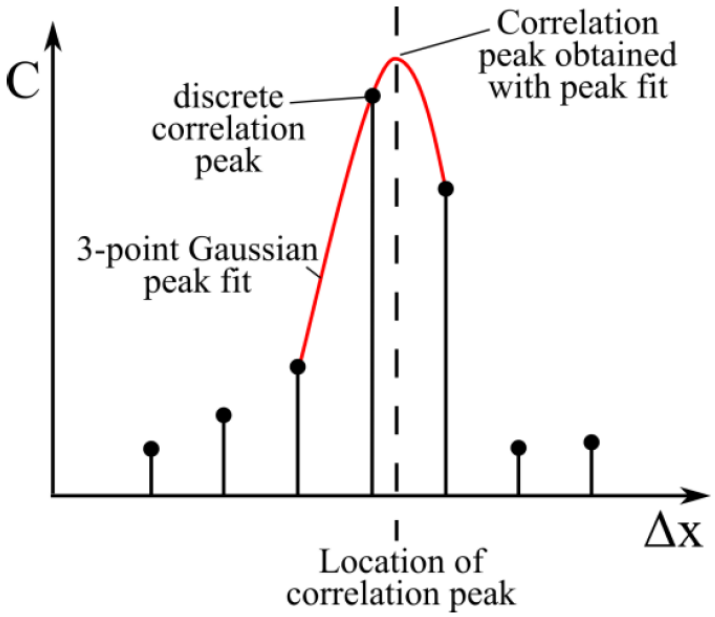

Figure 2-12. Representation of the one-dimensional 3-point Gaussian fit to the cross-correlation map for obtaining sub-pixel accuracy of particle displacements (Reproduced from Sciacchitano 2014).

$C(i,j)$, the horizontal displacement with subpixel accuracy is (Raffel et al. 2018):

$$\Delta x = j + \frac{ln\, C(i,j-1) - ln\, C(i,j+1)}{2\, ln\, C(i,j-1) - 4\, ln\, C(i,j) + 2\, ln\, C(i,j+1)}. \quad (2.19)$$

Likewise, the vertical displacement is obtained as:

$$\Delta y = i + \frac{ln\, C(i-1,j) - ln\, C(i+1,j)}{2\, ln\, C(i-1,j) - 4\, ln\, C(i,j) + 2\, ln\, C(i+1,j)}. \quad (2.20)$$

2.4.1.1 Maximum particle displacement

It is also worth noting that the interrogation window size must be larger than the particle displacement. For FFT-based correlation algorithms, the data within one interrogation window is assumed to be

periodic, restricting the displacement to maximum half of the interrogation window ($\Delta x = D_I/2$) due to the Nyquist sampling criterion (Willert and Gharib, 1991). However, $\Delta x = D_I/2$ yields poor signal to noise ratios, especially if velocity gradients within the IW are not negligible. Willert and Gharib (1991), recommended a maximum displacement of $\Delta x = D_I/3$, while Keane and Adrian (1990) recommended $\Delta x = D_I/4$. The latter, became well-known as the *one-quarter-rule*.

Current PIV algorithms, however, use multiple-pass grid-refining interrogation schemes (Raffel et al. 2018) that relax this restriction. The procedure starts with larger interrogation windows, successively estimating particle displacements via cross-correlation for window-shifting (and possibly window deformation), while also reducing the IW size, down to the desired resolution. In this case, the one-quarter-rule needs only to be observed in the first pass.

2.4.1.2 Minimum number of particles

Under ideal conditions, the value in the correlation map corresponding to the average particle displacement within IW is the highest, and clearly distinct from the random noise peaks in the correlation map. In case the displacement peak in the cross-correlation map is not the highest, an incorrect displacement is obtained. If the number of spurious vectors are limited to a few percent, they can be detected and removed by, for instance, applying spatial filters that compare the displacement obtained with neighbouring vectors (universal outlier detection, Westerweel and Scarano 2005). Keane and Adrian (1992) recommended the effective particle image density $N_I F_I F_O > 7$ to ensure a 95% valid detection probability (VDP) for cross-correlation of single-exposure and double-exposure images, where

$$F_I = \left(1 - \frac{\Delta x}{D_I}\right)\left(1 - \frac{\Delta y}{D_I}\right), \tag{2.21}$$

$$F_O = \left(1 - \frac{\Delta z}{z_0}\right),$$

represent the fraction of particles that remained within the IW after Δt. The particle displacements Δx and Δy are along the laser sheet, while Δz is the out-of-plane displacement.

However, a recent investigation (Scharnowski et al. 2019) has shown that the product $N_I F_I F_O$ is not sufficient to characterize VDP. F_I and F_O affect mainly the width of the displacement height distribution. The second highest peak, however, is mainly affected by D_I, the particle

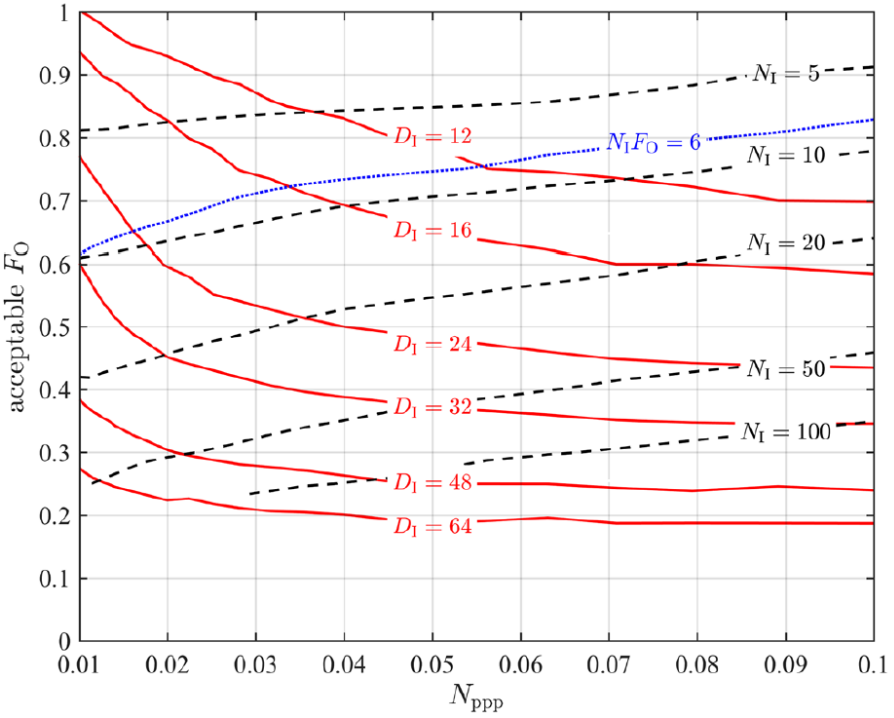

Figure 2-13. Isolines with VDP = 0.95 showing the level of acceptable FO with respect to the particle image density N_{ppp} for different interrogation window sizes (red solid lines). The dashed black lines indicate the required number of particle images within the interrogation window. Reproduced from Scharnowski et a. (2019).

image diameter D and N_{ppp} (number of particles per pixel). For a given N_{ppp} and F_O (with $F_I \approx 1$), the minimum N_I (or D_I) for VDP = 95% may be estimated using figure 2-13. For instance, for $N_{ppp} = 0.01$ and $F_o = 0.8$, N_I should be at least 5.

Another reason to increase N_I is to reduce the uncertainty of the measured displacement, as the random error of the instantaneous particle displacement calculated through cross-correlation analysis scales with $1/\sqrt{N_I}$ (Sciacchitano et al. 2013).

2.4.2 Particle tracking velocimetry

If the particle concentration is sufficiently low, such that the distance between the particles is large enough to minimize errors of particle identification or incorrect particle pairing, the displacement of particles may be calculated directly from the distance travelled by individual particles. The usual steps for PTV analysis are:

1. identification of particle images;
2. particle pairing;
3. velocity calculation.

2.4.2.1 Identification of particle images

Particle detection typically requires image pre-processing to minimize image background noise, followed by identification of local maxima, yielding the pixels containing the particle centres, followed by a 3-point Gaussian fit, given by eq. (2.19) and (2.20), to obtain the particle centre with subpixel accuracy (Raffel et al. 2018).

An issue for particle identification is the overlapping of particle images, which reduces the accuracy of the Gaussian fit. Mass (1992), as cited by Cierpka et al. (2013), has derived an expression for the number of overlapping images N_o, assumed to be of circular shape and randomly distributed on an image sensor with area A [px^2]:

$$N_o = (N_p - 1) + \frac{A}{\pi R_{min}^2}\left(e^{-(N_p-1)\frac{\pi R_{min}^2}{A}} - 1\right), \quad (2.22)$$

where $N_p = AN_{ppp}$ is the number of particle images within A, and R_{min} is the minimum distance between the particle images that still allow distinct identification of their centre position. Lei et al. (2012) have shown that the detection of the particle image centre is possible up to $R_{min} = D/2$ (50% overlap). Thus, eq. (2.22) may be rewritten in non-dimensional form as:

$$\frac{N_o}{N_p} = \frac{(N_p - 1)}{N_p} + \frac{1}{\pi(D/2)^2 N_{ppp}}\left(e^{-\pi\left(\frac{D}{2}\right)^2\left(N_{ppp}-\frac{1}{A}\right)} - 1\right). \quad (2.23)$$

In addition, observing that $(N_p - 1)/N_p \approx 1$ and that N_{ppp} (0.001-0.1) is much larger than $1/A = O(10^{-7})$, eq. (2.23) may be simplified to:

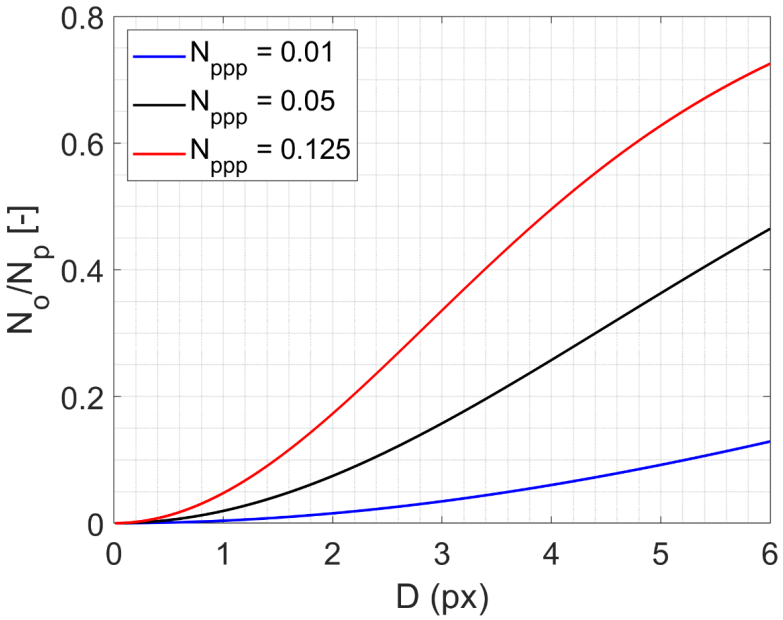

Figure 2-14. Fraction of overlapping images as a function of particle density and image diameter.

$$\frac{N_o}{N_p} = 1 + \frac{1}{\pi(D/2)^2 N_{ppp}}\left(e^{-\pi\left(\frac{D}{2}\right)^2 N_{ppp}} - 1\right), \qquad (2.24)$$

yielding, therefore, the fraction of overlapping images as a function of particle density and image diameter (figure 2-14). For instance, when D = 3 px, the fraction of overlapping particle images is less than 5% for N_{ppp} = 0.01, while reaching about 35% for N_{ppp} = 0.125.

2.4.2.2 Particle pairing

Matching particle images to obtain the displacement between two frames, or to form trajectories, involve algorithms that make assumptions based on the particles motion within the flow, predictors obtained from theory or through the use of data obtained from other measurements, and use of spatial and/or temporal data from neighbouring particles.

The simplest algorithm is the *nearest neighbour* (Malik et al. 1993). As the name suggests, this criterion bases the pairing upon the nearest particle on the next frame to form a pair. Starting from a particle image i on the first frame, it searches for the particle j on the second frame that minimizes $\left|\vec{x}_{p,i}(t) - \vec{x}_{p,j}(t + \Delta t)\right|$. The procedure may be repeated by reversing the temporal order, starting from the second frame instead. If the particle pairing changes when the temporal order is reversed, the particles are discarded. This may occur, for instance, if a particle leaves or enters the laser sheet in between the 1st and 2nd frames. This simple and intuitive approach is ideal for (and restricted to) measurements with low particle concentration.

Malik et al. (1993) defines the *particle spacing displacement ratio, p,* to enable assessing the difficulty of successfully matching the correct images pairs:

$$p = \frac{d_0}{u'_{rms}\Delta t}, \qquad (2.25)$$

where $d_0 = 1/\sqrt[3]{C}$ [m] is the mean interparticle distance, C [m^{-3}] is the particle concentration, and $u'_{rms}\Delta t$ [m] is the distance moved by particles during one imaging time step Δt due to turbulent velocity fluctuation u'_{rms}. The use of u'_{rms} instead of the mean velocity is justified if a predictor accounts for the mean velocity. Suppose for instance that the mean velocity is known through theoretical estimations, through the use of the law of the wall in a boundary layer (Schlichting 1979), for instance, or through cross-correlation analysis prior to the particle tracking. In this case, the *expected position* of the particle in the second frame $\vec{e}_{p,j}(t + \Delta t)$, which should be a good approximation of the mean particle displacement at that location, is used as initial guess. Possible matches for the particle pairing, referred as *particle candidates*, are then searched around $\vec{e}_{p,j}(t + \Delta t)$, within a *search window* of side scaling with $u'_{rms}\Delta t$. In this case the *nearest neighbour* algorithm looks for the particle j on the second frame that minimizes $\left|\vec{x}_{p,j}(t + \Delta t) - \vec{e}_{p,j}(t + \Delta t)\right|$.

The accuracy of the *nearest neighbour* algorithm may be improved by increasing temporal information, i.e. by following the particle through more than two frames. Malik et al. (1993) developed an algorithm that tracks the particles during four frames, through a procedure, illustrated in figure 2-15, as follows:

- Find the particles on frame one.
- Estimate particle candidates on the next frame using a predictor.
- Search for particle candidates around the expected position in the area delimited by the search window.
- From the particle candidates found, predict the expected positions for the next frame, and so on, until all possible trajectories are formed.
- Select the correct trajectory using a physics-based criterion

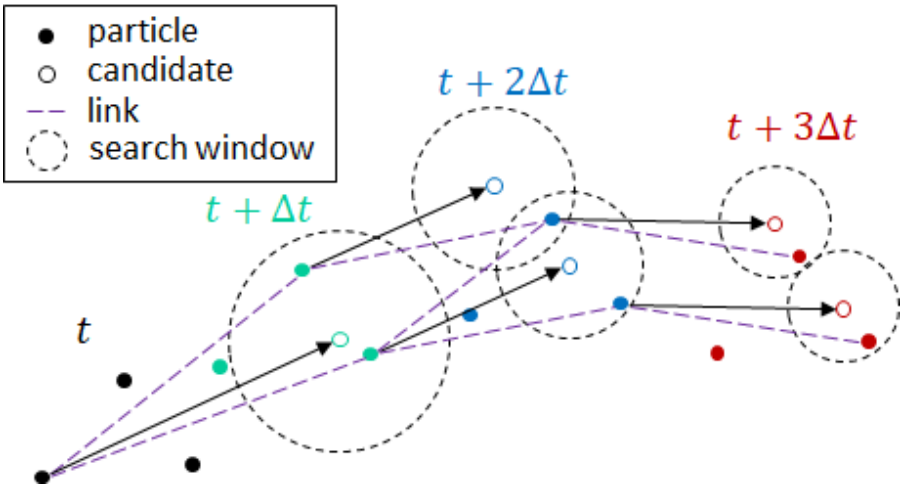

Figure 2-15. Illustration of four-frame particle tracking algorithm.

The criterion used by Malik et al. (1993) to select the correct trajectory is based on the assumption of uniform acceleration, selecting the trajectory in which the acceleration change is minimum. The acceleration obtained with a three point-scheme is:

$$\vec{a}_p(t+\Delta t) = \frac{\vec{x}_p(t) - 2\vec{x}_p(t+\Delta t) + \vec{x}_p(t+2\Delta t)}{\Delta t^2} \quad (2.26)$$

The difference in acceleration to be minimized $\Delta\vec{a}_p = \vec{a}_p(t+2\Delta t) - \vec{a}_p(t+\Delta t)$ is:

$$\Delta\vec{a}_p = \frac{-\vec{x}_p(t) + 3\vec{x}_p(t+\Delta t) - 3\vec{x}_p(t+2\Delta t) + \vec{x}_p(t+3\Delta t)}{\Delta t^2}. \quad (2.27)$$

The trajectory may also be selected assuming uniform velocity, and minimizing eq. (2.26) instead. Malik et al. (1993) report that both of sorting criteria give a similar yield of links, but the criterion of minimum change in acceleration consistently gives fewer errors.

In case of high particle concentration (small p), there are more sophisticated algorithms available that make use of the information from neighbouring particles. Examples of algorithms of this kind are the

spring-force method of Okamoto et al. (1995), the iterative *relaxation method* of Ohmi and Li (2000) and the non-iterative method of Fuchs et al. (2017). These are not reviewed here as they are not relevant for the understanding of this thesis.

2.4.2.3 Velocity calculation

The particle velocity in double-frame PTV is obtained from eq. (2.1), whose error is $O(\Delta t)$ for uniformly accelerated flows. In case of three frames, the more accurate quadratic scheme can be used:

$$\vec{u}(t) = \frac{\vec{x}_p(t + 2\Delta t) - \vec{x}_p(t)}{2\Delta t} + O(\Delta t^2) \tag{2.28}$$

Furthermore, if more frames are available, the particle positions along the trajectory may be fitted using a 2nd or 3rd degree polynomial function (Cierpka et al. 2013). The velocity and acceleration are then obtained as the 1st and 2nd time-derivatives of $\vec{x}_p(t)$. This not only reduces the error, but also allows for reallocation of the vector position halfway of the trajectory more accurately, as the trajectory fit is able to reconstruct the path curvature.

2.5 Stereoscopic PIV

Stereoscopic PIV makes use of a second camera for measuring the particle displacements from two different angles, which allows reconstruction of the three-components of the velocity vector. This is not only of interest to eliminate the perspective error (section 2.3), but also to obtain the in-plane and out-of-plane motion simultaneously, e.g. in the study of trailing vortices in the wake of an airfoil (Willert, 1997).

There are two main systems used for stereo-PIV, namely, *translational* and *rotational* systems (Willert, 1997). The off-axis angle θ (figure 2-17) is limited in the translation configuration, implying that the accuracy of the out-of-plane velocity component is restricted (Prasad, 2000). Therefore, rotational systems are usually preferred, where the image plane is rotated with respect to the object plane (figure 2-16). The

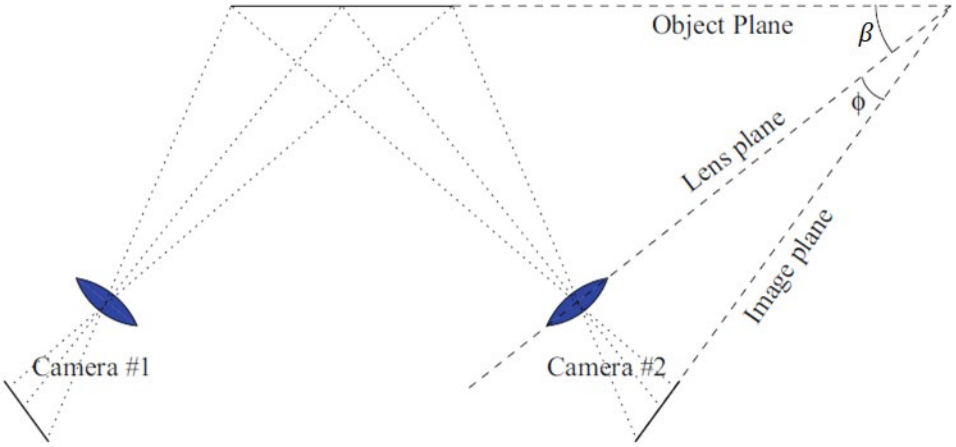

Figure 2-16. Rotational stereoscopic-PIV system. Adapted from Willert (1997).

lens plane is also usually rotated with respect to the image plane, such that the image, lens and object planes intersect at a line (Scheimpflug condition), enabling the entire field of view to be focused. This requirement can be overcome if large depth-of-focus can be achieved, e.g. by increasing the f-stop (eq. (2.11)).

2.5.1 Stereoscopic geometric reconstruction

The method presented here for the reconstruction of the three velocity components is similar to that of Brücker (1996). Consider two cameras, whose optical axes form the angles θ_1 and θ_2 with the plane perpendicular to the object plane ($z = 0$) (figure 2-17), and whose projections onto the x-z and y-z are distinguished with the subscripts x and y, respectively. The laser sheet is aligned with the object plane, with centre at $z = 0$. The cameras are considered sufficiently far away, so that the light rays scattered by a particle moving from $\vec{x}_p(t)$ to $\vec{x}_p(t + \Delta t)$, reaching one camera, are approximately parallel, i.e. $\delta\theta_1 \approx \delta\theta_2 \approx 0$. In this case, it is obtained on the x-z plane:

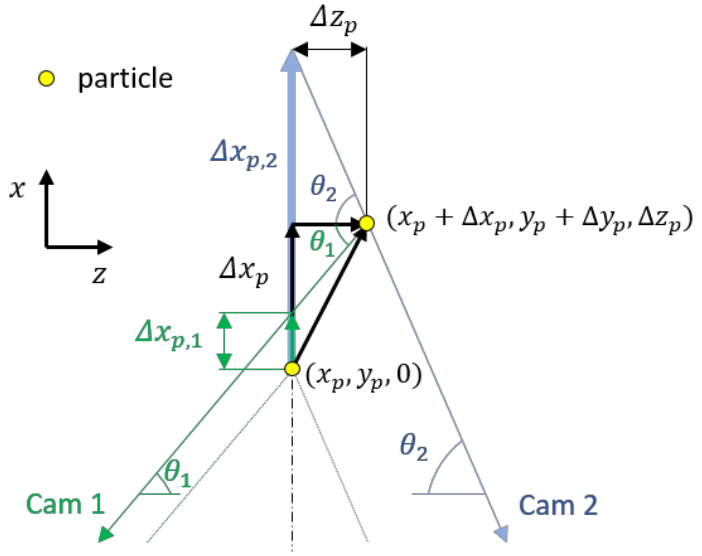

Figure 2-17. Stereoscopic geometric reconstruction. Cameras on opposite sides of the object plane.

$$tan\,\theta_{1,x} = \frac{\left(x_p + \Delta x_p\right) - \left(x_p + \Delta x_{p,1}\right)}{\Delta z_p},$$
$$tan\,\theta_{2,x} = \frac{\left(x_p + \Delta x_{p,2}\right) - \left(x_p + \Delta x_p\right)}{\Delta z_p}. \tag{2.29}$$

Solving eq. (2.29) for Δz_p, the in-plane displacement Δx_p is obtained:

$$\Delta x_p = \frac{\Delta x_{p,2}\, tan\,\theta_{1,x} + \Delta x_{p,1}\, tan\,\theta_{2,x}}{tan\,\theta_{1,x} + tan\,\theta_{2,x}} \tag{2.30}$$

Instead, solving eq. (2.29) for Δx_p, the out-of-plane displacement Δz_p is obtained:

$$\Delta z_p = \frac{\Delta x_{p,2} - \Delta x_{p,1}}{tan\,\theta_{1,x} + tan\,\theta_{2,x}} \tag{2.31}$$

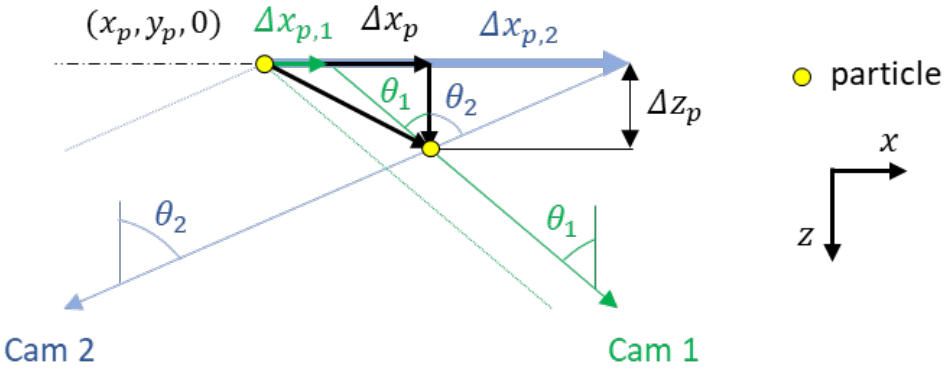

Figure 2-18. Stereoscopic geometric reconstruction. Cameras on the same side of the object plane.

Likewise, on the y-z plane the in-plane and out-of-plane displacements are obtained as:

$$\Delta y_p = \frac{\Delta y_{p,2}\, tan\, \theta_{1,y} + \Delta y_{p,1}\, tan\, \theta_{2,y}}{tan\, \theta_{1,y} + tan\, \theta_{2,y}}$$
$$\Delta z_p = \frac{\Delta y_{p,2} - \Delta y_{p,1}}{tan\, \theta_{1,y} + tan\, \theta_{2,y}} \tag{2.32}$$

Note that there are three unknowns and four measured values, resulting in an overdetermined system, which can be solved in a least-square sense (Raffel et al. 2018).

Finally, observe that, although the cameras on figure 2-17 are on opposite sides of the object plane, the same equations presented above can be used in case the cameras are placed on the same side (figure 2-18).

2.5.2 Image remapping

Rotating the image plane with respect to the object plane leads to non-uniform magnification (figure 2-19). This has to be dealt with using a mapping function that takes into account the local magnification to remap the particle positions to world coordinates (object plane).

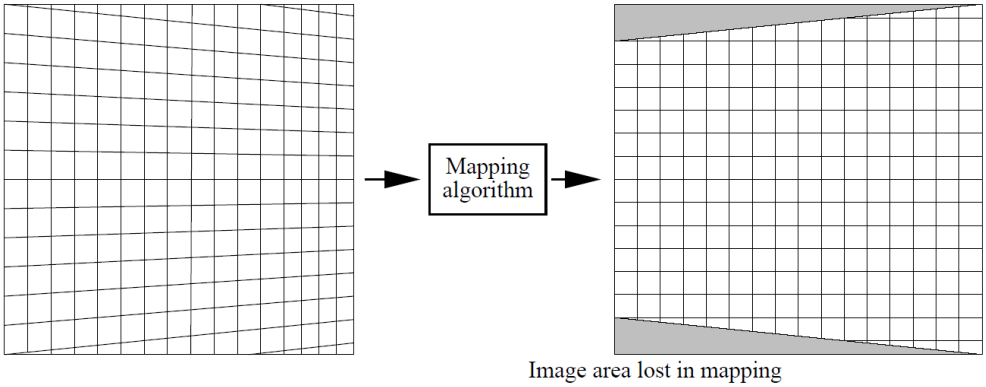

Figure 2-19. Remapping of the recorded image (left) to the reconstructed image (right). Reproduced from Willert (1997).

Geometric back-projection based on geometrical optics is possible if the following imaging parameters are known: the focal length, the angles between the object, lens and image planes, the exact position of the lens plane and the nominal magnification factor. However, this procedure does not account for nonlinearities such as lens distortions and are sensitive to small variations in each of the parameters (Willert, 1997).

Mapping can also be realized without directly applying the laws of geometric optics. For instance, the reconstruction of images can be done through projection equations based on perspective projection, which maps a rectangle into a general four-sided polygon (Willert, 1997):

$$x_p = \frac{a_{11}X + a_{12}Y + a_{13}}{a_{31}X + a_{32}Y + 1}, \qquad y_p = \frac{a_{21}X + a_{22}Y + a_{23}}{a_{31}X + a_{32}Y + 1}, \quad (2.33)$$

which can be extended to higher order to account for geometric distortions due to imperfect imaging optics (Willert, 1997).

The coefficients of eq. (2.33) are obtained through a calibration procedure (Willert 1997, Soloff et al. 1997, Prasad 2000, Raffel et a. 2018) that usually involves acquiring images of a multi-level calibration plate (figure 2-20) or by translating a planar calibration target. The

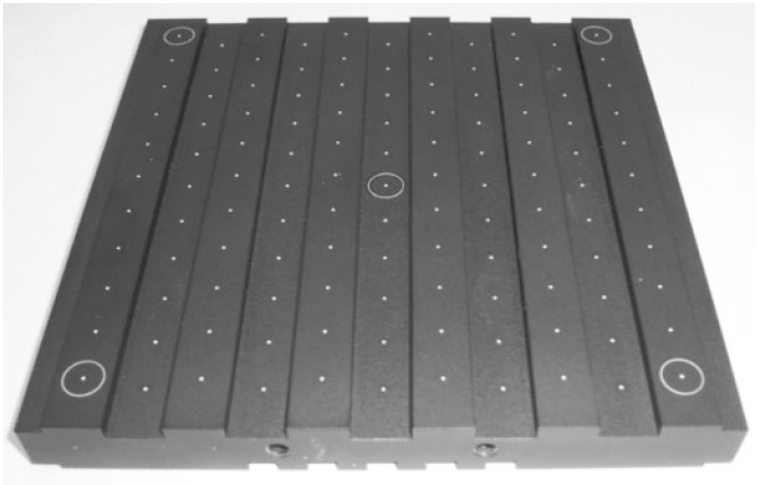

Figure 2-20. Precision-machined dual level calibration target with dot pattern for stereo PIV calibration. Levels are separated by 2 mm, dots are equally spaced on a 10mm grid. Reproduced from Raffel et al. (2018).

calibration performed in this manner requires a perfect alignment between the calibration plate and the light sheet.

A correction scheme (*self-calibration* procedure, Wieneke 2005) based on disparity maps, computed from cross-correlation between recorded particle images with both cameras (after reconstruction to world coordinates), provides accurate mapping functions, even when the calibration plate is shifted or tilted relative to the light sheet.

2.6 Volumetric PIV

Volumetric PIV consists on the imaging of an illuminated seeded volume. Usually it is performed by obtaining 2D images from multiple viewing directions (typically using 3 to 6 cameras, figure 2-21). The processing algorithms usually follow one of these two paths:

1. reconstruction of the three-dimensional position (x_p, y_p, z_p) of the particles from 2D particle image positions (X, Y) (3D-triangulation Mass et al. 1993, Iterative Particle Reconstruction, Wieneke 2013), followed by 3D particle tracking (Malik et al. 1993, Schanz et al. 2016);

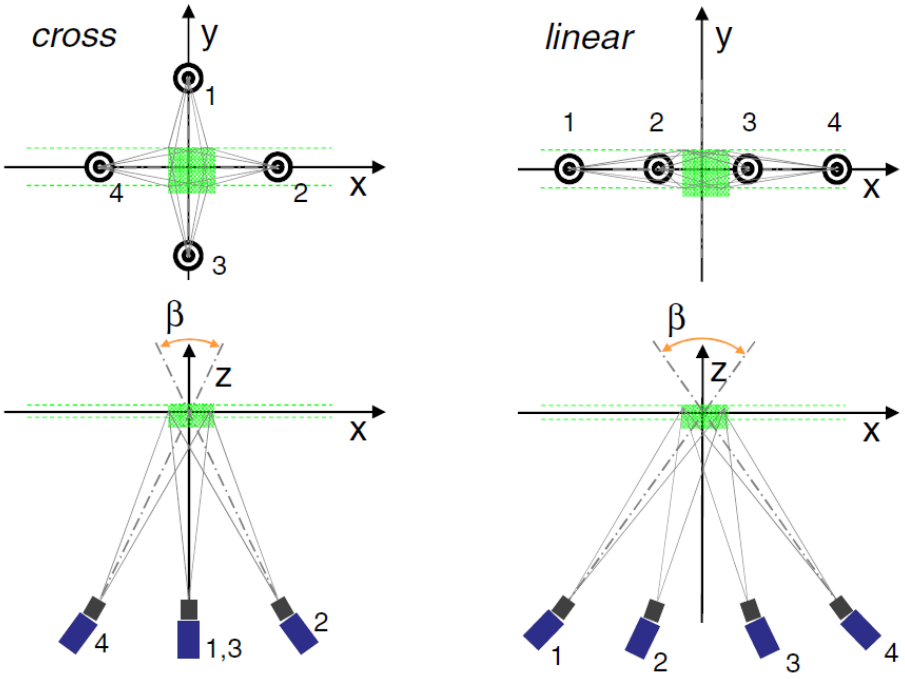

Figure 2-21. Cross-like and linear imaging configurations of tomographic PIV systems based on four cameras. Reproduced from Scarano (2013).

2. reconstruction of the 3D intensity field $E(x, y, z)$, an array of voxels (volumetric pixels), based on the 2D intensity fields $I(X, Y)$, followed by 3D cross-correlation of interrogation volumes (tomographic PIV, Elsinga et al. 2006, Scarano 2013).

A detailed description of volumetric PIV is, however, beyond the scope of this thesis.

2.7 Performance of a PIV system

A PIV system is usually characterized by its accuracy and spatial resolution. The uncertainty of the velocity vector σ_u is mainly dictated by the RMS error of the measured particle displacement $\sigma_{\Delta x}$, while the uncertainty in Δt is negligible for flows up to a few hundred meters per second (Adrian, 1997). Thus,

$$\sigma_u = \frac{\sigma_{\Delta x}}{\Delta t}. \tag{2.34}$$

Another important characteristic of a PIV system is the *dynamic velocity range* (DVR), which is the ratio of the maximum to the minimum resolvable velocities, that is (Adrian, 1997):

$$DVR = \frac{\Delta u_{max}}{\sigma_u} = \frac{\Delta x_{max}}{\sigma_{\Delta x}}. \tag{2.35}$$

The DVR of the system will determine the range of the velocity spectra measurable by the instruments.

It is also important to quantify the range of measurable length scales, which is given by the *dynamic spatial resolution* (DSR). Considering that the minimum length scale is smaller than Δx_{max}, the DSR is at least (Adrian, 1997):

$$DSR = \frac{l_{max}}{\Delta x_{max}}, \tag{2.36}$$

where l_{max} is the linear size of the FoV.

The ability of a system to measure simultaneously large range of velocity and length scales is quantified by the product of DVR and DSR (Adrian, 1997):

$$DSR \times DVR = \frac{l_{max}}{\sigma_{\Delta x}} = \frac{L_{max}}{\sigma_{\Delta X}}, \tag{2.37}$$

where $L_{max} = l_{max}M$ is the camera sensor linear dimension and $\sigma_{\Delta X} = \sigma_{\Delta x}/M$ is the uncertainty of the particle image displacement. L_{max} is only a hardware limitation, while $\sigma_{\Delta X}$ is both a hardware limitation (e.g. the determination of the centroid depends on the particle image size, which per se depends on the sensor pixel pitch) and an algorithm limitation, which will be significant on how accurate the particle displacement is determined.

3

FLOW TRACERS

3.1 Introduction

Particle Image Velocimetry is generally deemed as a non-intrusive technique for measuring the instantaneous flow velocity, in contrast to probe-based techniques. However, the tracer particles must follow the flow faithfully for accurate measurements, a crucial requirement often taken for granted.

In this chapter, the techniques used for the seeding of air flows are presented; the main equations governing spherical particle motion are given; and results from experimental investigations of particle tracing fidelity are reviewed.

3.2 Typical seeding particles for PIV in air

Seeding of air flows may be classified into three main groups: solid particles (powders), liquid droplets and soap bubbles. Powders and liquid droplets of small diameters (about 1 μm) are usually good flow tracers irrespectively of their weight, but have poor optical properties. Alternatively, if the particle density is carefully controlled to match the air density, then the particle size may be increased, increasing light scattering, while retaining good flow tracing capabilities. As shown in figure 1-6, the use of soap bubbles of about 500 μm diameter (10,000 times brighter than micrometre particles, Caridi 2018) has led to an increase of three orders of magnitude of the observation volume, allowing large-scale 3D PIV.

Nevertheless, for small scale measurements, especially for planar PIV, micrometre particles remain the best alternative. Droplet seeding is usually preferred to powder-based seeding when applicable. Liquid droplets are easier to be homogenously distributed at high concentrations, and allow for global seeding (seeding of the entire wind tunnel flow). Vegetable oils and DEHS are the preferred choice, since vegetable oils are believed to be less harmful to human inhalation and DEHS tracers evaporate in the long term. Powder-based seeding is usually employed in high-temperature (e.g. combustion) or high-enthalpy flows (e.g. compressible regime).

3.2.1 Powder-based seeding

Metal oxide powders are usually the preferred material due to their inertness, high melting point and low cost (Raffel et al. 2018). Typical examples are titanium dioxide, alumina and silica powders. Solid particles tend to agglomerate, requiring special seeding devices. For instance, cyclone separators have been used to breakup or remove these agglomerates prior to delivering the seeding particles into the flow. Another approach is to aerate the powder within a vertical tube, creating a fluidized bed, where the flow is forced through a sonic throat prior to reaching the test section, in order to remove particle clusters (Raffel et al. 2018).

3.2.2 Droplet seeding

The use of Laskin atomizers with oil as seeding material is the most common method of producing micrometre droplets for PIV. In the sketch of figure 3-2, one air-pressurized input pipe, connected to the top of the container, drives the generated particles through an output pipe, reaching the wind tunnel. In addition, a second air-pressurized input pipe, with about 0.5-1 bar overpressure (with respect to the other input pressure), connects to four Laskin nozzles, dipped within the oil in the container.

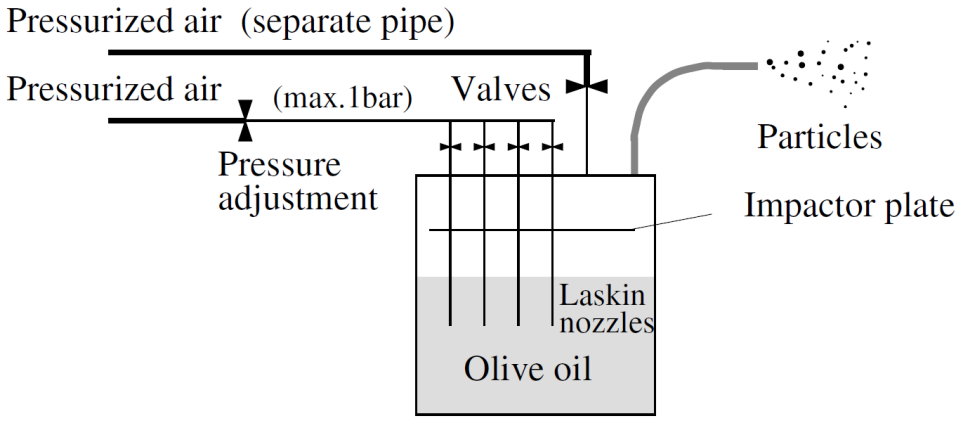

Figure 3-2. Sketch of a Laskin atomizer. Reproduced from Raffel et al. (2018).

The nozzles (figure 3-1) are pipes of approximately 5 mm inner diameter with closed ends and four or more holes of about 1-2 mm diameter, symmetrically distributed along the pipe circumference (Kähler et al. 2002). The air jets, exiting laterally from the pipes within the oil,

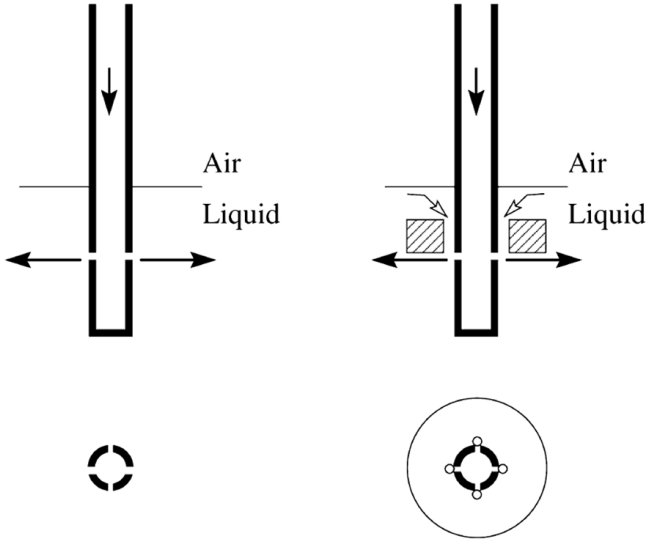

Figure 3-1. Left: Simplified version of a Laskin Nozzle (without a feed-hole ring). Right: Laskin Nozzle. Reproduced from Kähler et al. (2002).

form air bubbles containing micrometre entrained droplets. As the air bubbles reach the oil surface, bursting in the process, the entrained droplets are released into the main air stream. Optimizing the pressure inputs and the geometry, a median droplet (DEHS) diameter of 1 μm can be obtained (Kähler et al. 2002).

3.2.3 Soap bubble seeding

The use of soap bubbles for aerodynamic measurements dates back to 1938, when the French inventor Henry Redon from the "Société Provençale de Constructions Aéronautiques" registered the first bubble generator for use in wind tunnel measurements in the patent "Means for materializing the streamlines of a fluid". In Redon's design (figure 3-3),

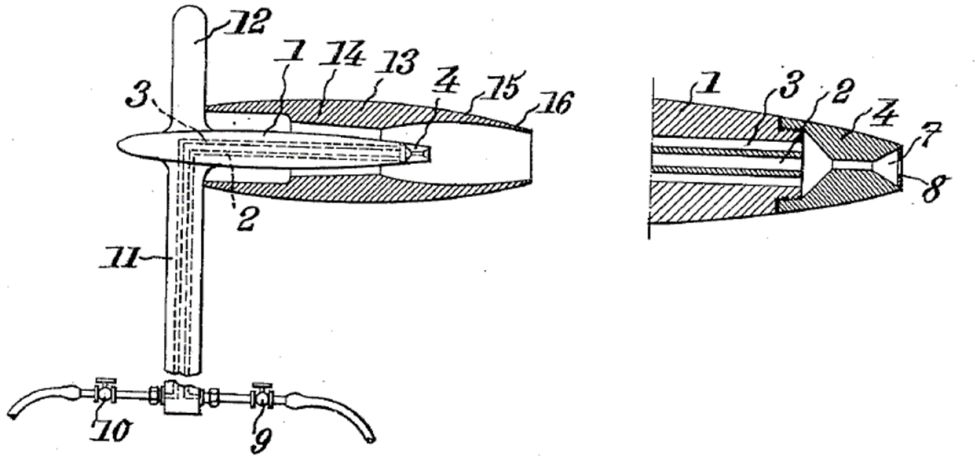

Figure 3-3. Redon's soap bubble generator invention in 1938. Left: The full system of bubble generation, including valves for the input fluids (9 and 10) that flow through the conduits (2 and 3) to the main body (1), a funnel (16) used to prevent dispersion of the bubble streamlines, and a nozzle (4), used to control the bubble formation. Right: Details of the attachment point of the nozzle (4) to the main body (1). The inner-gas flows through the conduit (2). The soap solution flowing through the conduit (3) creeps along the walls of the convergent-divergent nozzle up to the outlet (8), where the bubble is formed. Reproduced from Redon (1938).

a soap bubble is formed through the control of two concentric flows, an inner gas and a soap solution involving it. The fluids meet at a convergent-divergent nozzle, forming a soap bubble at the tip of the nozzle outlet. Redon added a funnel involving the nozzle, through which the air flow from the wind tunnel would pass through, releasing the bubble from the nozzle tip.

Admittedly without knowledge of Redon's device, Sage Action Inc. began their developments of a soap bubble generator for aerodynamics in 1967, as reported by Hale et al. (1969, 1971). Sage Action's bubble generator (figure 3-4) is very similar to that from Redon, with exception that the convergent-divergent nozzle was eliminated, the tip of the intermediate pipe of soap solution was extended further downstream of the inner gas (helium) pipe, and, instead of using the wind tunnel flow to blow the bubbles off the tip, a tertiary outer gas was introduced

In 1993, Okuno et al. introduced the orifice-type bubble generator (figure 3-5, sketch from Bosbach et al. 2009). The concept is very similar to that of Sage action's, however the annular jet of soap filled with helium is forced through an orifice, where the surface tension forces acting on the soap film cause the jet to break-up, forming helium-filled soap bubbles. The orifice ultimately defines the bubble size, allowing for generation of smaller bubbles—from a manufacturing point of view, it is simpler to reduce the orifice size than to miniaturize the entire nozzle. This led to a significant increase of bubble production rate, which is inversely proportional to the bubble volume. The orifice-type bubble generator introduced by Bosbach et al. (2009) was the first to produce

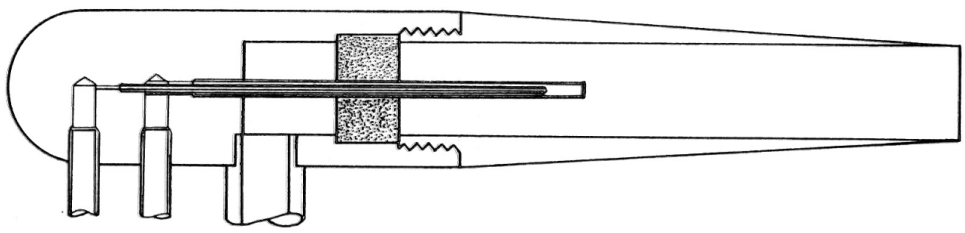

Figure 3-4. Sage Action's bubble generator (Hale et al. 1971).

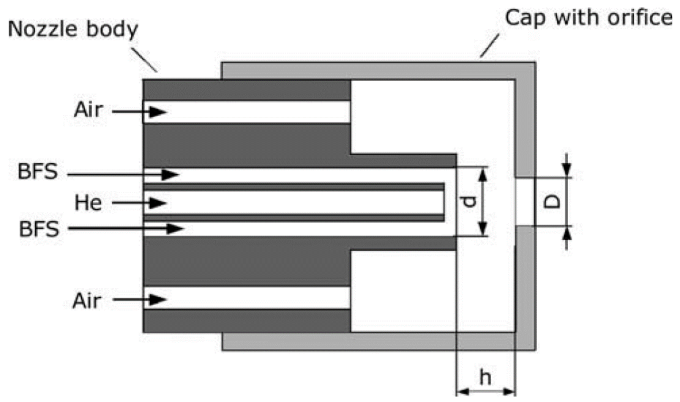

Figure 3-5. Orifice-type bubble generator (d = 2 mm, D = 1 mm and h = 1 mm). BFS stands for bubble fluid solution. Reproduced from Bosbach et al. (2009).

submillimetre bubbles (200 μm diameter), making it possible to reach production rates in the order of 10^4 bubbles/s from a single nozzle.

The use of a single nozzle, however, is insufficient to achieve the required particle concentration for wind tunnel measurements, and further developments have been directed towards the assembly of seeding rakes. The first HFSB seeding rake used in wind tunnels (figure 3-6, Caridi et al. 2016) comprised a single bubble generator that accumulated the bubbles temporarily within a reservoir, and, subsequently, the seeded air volume was driven into the flow through a piston driven by a linear actuator. Currently, HFSB systems for wind tunnels containing hundreds of nozzles has become standard (figure 3-7, Jux et

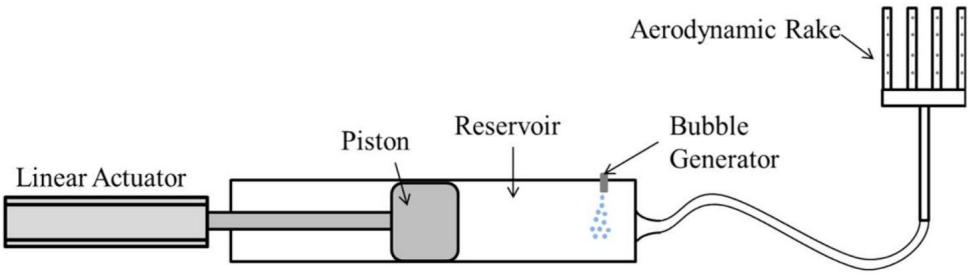

Figure 3-6. Schematic description of HFSB seeding storage and transient injection system. Reproduced from Caridi et al. (2016).

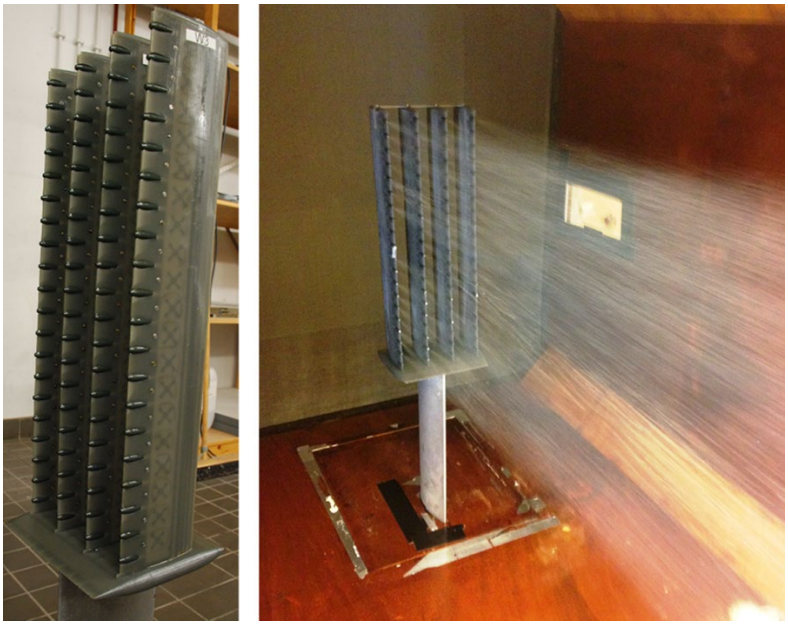

Figure 3-7. TU Delft's HFSB seeding rake of 80 nozzles (50 cm × 15 cm). Reproduced from Jux et al. 2018.

al. 2018).

Given their relatively large size, the bubbles must be introduced into the flow downstream of the tunnel turbulence screens to avoid contaminating them. Preferably, they should be introduced in the settling chamber, so that most of the flow interference caused by the rake decays along the wind tunnel contraction (flow contraction reduces anisotropy from grid generated turbulence, which, prior to the contraction, is highest in the streamwise direction, Comte-Bellot et al. 1976).

If installed in the settling chamber, the bubble concentration (particles/m³) may be calculated as follows:

$$C = \frac{nf}{U_\infty}\frac{A_{ratio}}{A_{rake}}, \tag{3.1}$$

where n is the number of nozzles, f is the bubble production rate per nozzle, U_∞ is the free stream velocity in the test section, A_{rake} is the

cross-section area seeded by the rake and A_{ratio} is the tunnel area contraction ratio.

3.3 Particle light scattering

3.3.1 Mean exposure of an individual particle

The mean light intensity of a single particle, averaged over the particle image cross-sectional area $\pi(D/2)^2$, where D [m] is the particle image diameter from eq. (2.10), and integrated over the duration of the light pulse δt, yields the mean exposure for an individual particle image $\langle\epsilon\rangle$ [J/m^2] (Adrian and Yao 1985,):

$$\langle\epsilon\rangle = \frac{I_0 P_s}{\pi(D/2)^2 k^2} \tag{3.2}$$

where I_0 [J/m^2] is the illuminating intensity, P_s [-] is the scattering power (dimensionless), $k = 2\pi/\lambda$ [m^{-1}] is the wave number, and λ [m] is the light wavelength.

For a homogeneous spherical particle, the scattering power, calculated from Mie-scattering theory, depends on the illumination angle with the imaging direction, on the ratio of the refractive index of the particle to the refractive index of the fluid, and on the normalized particle diameter $\pi d_p/\lambda$ (Adrian and Yao, 1985).

Adrian and Yao (1985) performed Mie-scattering calculations (figure 3-8) for the light energy collected by a camera lens in side-scatter (see below). Particles in the micrometre range (1-10 μm) scatter 2-3 orders of magnitude more light than in the submicrometre range (0.1-1 μm). Adrian (1991) gives an approximation for $\langle\epsilon\rangle$ for particles in the range of 1-10 μm:

$$\langle\epsilon\rangle \sim \frac{I_0\left(d_p/\lambda\right)^3 D_a^4}{z_o^2 z_i^2}, \tag{3.3}$$

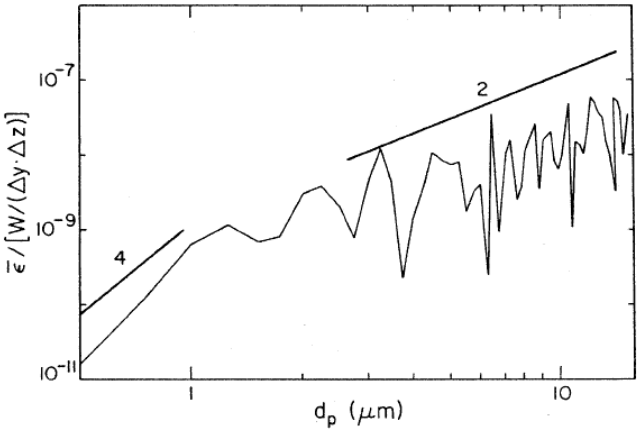

Figure 3-8. Mean-exposure dependence on particle size ($f_\# = 22$), non-dimensionalized by the input light intensity $I_0 = W/\Delta y \Delta z$, where W is the total energy per pulse, Δy and Δz are the laser-sheet width and thickness, respectively. Reproduced from Adrian and Yao (1985).

where z_o and z_i are the distances to the lens plane from the object and image planes, respectively, and D_a is the camera aperture. Furthermore, as the particle size increases into the geometric limit, $\langle \epsilon \rangle$ becomes independent of the particle diameter (Adrian 1991):

$$\langle \epsilon \rangle \propto \frac{I_0 D_a^2}{z_o^2 M^2}. \tag{3.4}$$

Hence, after reaching the geometric limit, increasing the particle size does not increase the mean exposure. However, the mean energy integrated over the particle image cross-section $\pi(D/2)^2\langle \epsilon \rangle$ increases with d_p^2—in the geometric limit $D \sim M d_p$. Thus, the total energy captured by one sensor element of the camera, impinged by the scattered light, increases with d_p^2 while D remains smaller than one pixel.

3.3.2 Backward, forward and side scattering

The influence of the observation angle relative to the direction of the incident light is shown in figure 3-10 for a 1 µm oil particle in air. The intensity of the scattered light varies with direction. At 90° degrees

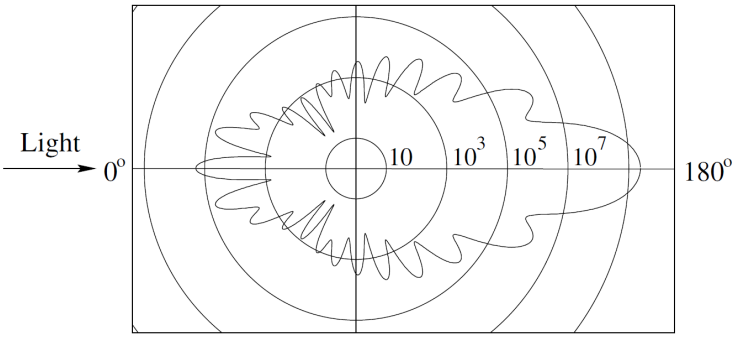

Figure 3-9. Light scattered by a 1 μm oil particle in air. Reproduced from Raffel et al. (2018).

observation angle (*side scattering*), the light intensity is the weakest (10^3), *backward scattering* (0°) is two orders of magnitude stronger than side scattering, reaching 10^5, and *forward scattering* (180°) is the most advantageous, reaching 10^9, six orders of magnitude larger than in side scattering.

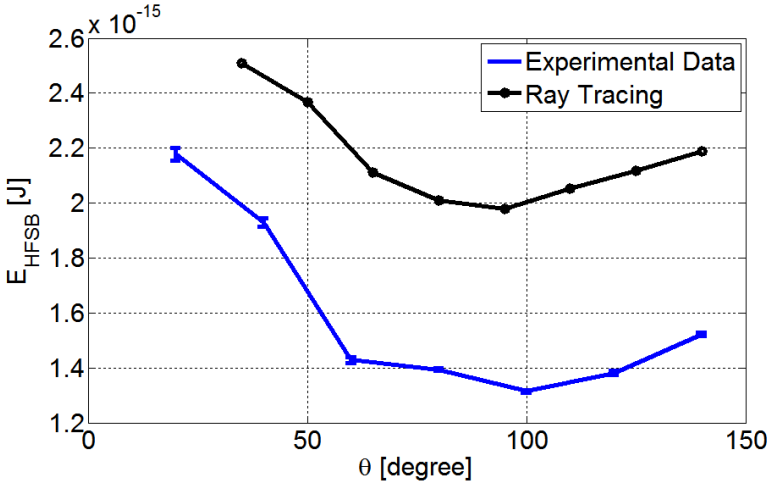

Figure 3-10. Simulation and experimental results of the light scattered by a 300 μm HFSB (Reproduced from Caridi 2018). In the notation of this graph, θ is the angle between the incident light and the recording medium, with θ = 0° being forward scattering and θ = 180° being backward scattering (opposite to what shown in figure 3-10).

In the case of a 300 μm HFSB, however, Caridi (2018) have shown via simulation and experiments that although forward scattering is still higher than side scattering, the differences are small with forward scattering reaching about twofold (inferred from extrapolation of the experimental data in figure 3-9) of the energy from side scattering.

3.4 Physics of spherical particle motion

Analysis of particle tracing accuracy originates from the pioneering work of Stokes (1851), in which he derived the equation for the drag force of a rigid sphere in a viscous uniform flow at very small particle Reynolds number values (creeping flow), the so-called Stokes' drag law:

$$\vec{F}_D = -3\pi\mu d_p \, \vec{u}_{slip}. \tag{3.5}$$

where μ is the fluid dynamic viscosity and $\vec{u}_{slip} = \vec{u}_p - \vec{u}$ is the slip velocity (particle relative velocity with respect to the fluid velocity). Stokes went further and analysed the particle terminal velocity in the case of a particle slowly falling in a quiescent fluid ($\vec{u} = \vec{0}$), in which the drag force is in equilibrium with the buoyancy force:

$$\vec{F}_B = \frac{\pi d_p^3}{6}\left(\rho_p - \rho\right)\vec{g}, \tag{3.6}$$

where ρ_p and ρ are the particle and fluid densities, respectively, and $\vec{g}$ is the gravitational acceleration. When in equilibrium, $-\vec{F}_D = \vec{F}_B$, and the particle terminal velocity becomes:

$$\vec{u}_p = \frac{d_p^2}{18\mu}\left(\rho_p - \rho\right)\vec{g} \tag{3.7}$$

A few decades later, Boussinesq (1885a; 1885b) and Basset (1888a; 1888b) expanded the Stokes' analysis to the more general case of unsteady motion, with the particle velocity being an arbitrary function of time, however, still under creeping flow conditions. Following Boussinesq and Basset, Maxey & Riley (1983) provided a more generic

equation for a small rigid sphere, including the forces due to non-uniform flows. There have been several works attempting to relax the assumption of creeping flow to achieve a more general dynamic equation that would describe the motion of particles with small, yet finite, particle Reynolds number. However, most accurate equations up to date still rely on semi-empirical corrections (especially for the drag coefficient), resultant from experiments, simulations and analytical expansions of asymptotic solutions (Mei 1996; Magnaudet 1997; Michaelides 1997; Loth & Dorgan 2009). The full unsteady equation of motion as proposed by Mei (1996), per particle volume $\pi dp^3/6$, is given as:

$$\rho_p \frac{d\vec{u}_p}{dt} = \overbrace{(\rho_p - \rho)\vec{g}}^{Buoyancy\ force} + \overbrace{\rho \frac{D\vec{u}}{Dt}}^{Undisturbed\ fluid\ stresses} + \overbrace{\frac{\rho}{2}\left(\frac{D\vec{u}}{Dt} - \frac{d\vec{u}_p}{dt}\right)}^{Added-mass\ force} - \overbrace{\frac{18\mu}{d_p^2}\phi(Re_p)\vec{u}_{slip}}^{Quasi-steady\ Drag} - \overbrace{\frac{18\mu}{d_p^2}\int_{-\infty}^{t} K(t-\tau)\frac{d\vec{u}_{slip}}{d\tau}d\tau}^{History\ force}, \quad (3.8)$$

where $\phi(Re_p)$ is an empirical relation to correct for deviations from the Stokes' drag law due to a finite particle Reynolds Number, $Re_p = d_p|\vec{u}_{slip}|/\nu$, ν is the fluid kinematic viscosity, and $K(t-\tau)$ is the history force kernel. The time derivatives $d/dt = \partial/\partial t + \vec{u}_p \cdot \nabla$ and $D/Dt = \partial/\partial t + \vec{u} \cdot \nabla$ are evaluated, respectively, on the particle trajectory and on the trajectory of fluid elements around the particle. Eq. (3.8) returns to eq. (3.7) when $d\vec{u}_p/dt = \vec{0}$ (force equilibrium), $D\vec{u}/Dt = \vec{u} = \vec{0}$ (quiescent flow), $\phi(Re_p) = 1$ (creeping flow, $Re_p \ll 1$), and after a sufficient time after force equilibrium is achieved, so that the history force may be considered negligible ($K(t-\tau)$ decays as $(t-\tau)^{-1/2}$ at short times and as $(t-\tau)^{-2}$ at long times, Mei 1996).

The history force kernel may be calculated using the approximation by Mei (1994):

$$K(t-\tau) \approx \left\{ \left[\frac{4\pi(t-\tau)\nu}{d_p^2} \right]^{\frac{1}{4}} + \left[\frac{\pi(t-\tau)^2 Re_p^3 \nu^2}{\left(0.75 + 0.105 Re_p\right)^3 d_p^4} \right]^{\frac{1}{2}} \right\}^{-2}, \quad (3.9)$$

where Re_p is evaluated at $(t-\tau)$.

3.4.1 Drag correction

Several empirical relations have been proposed for the drag correction term $\phi(Re_p) = C_d/C_{d0}$ (Clift et al. 1978), where C_d is the particle drag coefficient, and $C_{d0} = 24/Re_p$ is the drag coefficient of a rigid sphere given by the Stokes' law ($Re_p \ll 1$). A commonly used expression given by Schiller and Naumann (1933) for which the drag coefficient, accurate within 5% for $Re_p \leq 800$, is given as:

$$\phi(Re_p) = 1 + 0.15 Re_p^{0.687}. \quad (3.10)$$

More accurate approximations were compiled by Clift et al. 1978, for different Re_p ranges:

$$\begin{aligned}
&\phi = 1 + \frac{3}{16} Re_p && Re_p \leq 0.01 \\
&\phi = 1 + 0.1315 Re_p^{0.82-0.05w} && 0.01 < Re_p \leq 20 \\
&\phi = 1 + 0.1935 Re_p^{0.6305} && 20 < Re_p \leq 260 \\
&\phi = 1.8335 Re_p^{0.1558w-0.1242} && 260 < Re_p \leq 1500 \\
&\phi = 1.45 \times 10^{-4} Re_p^{3.5558-0.9295w+0.1049w^2} && 1500 < Re_p \leq 12{,}000
\end{aligned} \quad (3.11)$$

where $w = \log(Re_p)$. Notice that there are different expressions for the drag coefficient in the case of a clean bubble (the flow slips along the surface) or due to particle deformation (Clift et al. 1978; Magnaudet &

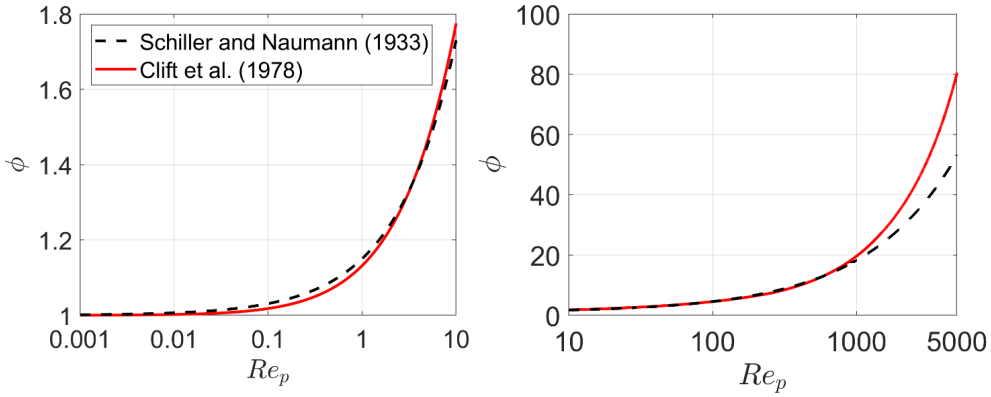

Figure 3-11. Comparison of drag correction given by Schiller and Naumann (1933), eq. (3.10), with more accurate corrections compiled by Clift et al. (1978), eq. (3.11).

Eames 2000; Loth 2008), which may be neglected for HFSB (see section 3.4.4).

Comparison of eq. (3.10) and (3.11) (figure 3-11) shows that, up to $Re_p = 800$, the corrections differ less than 5% from each other. However, when Re_p surpasses this limit, eq. (3.10) underestimates drag significantly, with the estimate from eq. (3.11) being 50% larger than that given by eq. (3.10) at $Re_p = 5000$. In most PIV applications. eq. (3.10) is sufficient, since $Re_p = 800$ represents a slip velocity of 24 m/s for a half-millimetre particle in air. Furthermore, it is evident from figure 3-11 that the assumption of $\phi(Re_p) = 1$ is limited to low speed flows and small particles. The correction term is already twice this value ($\phi(Re_p) \approx 2$) for a slip velocity of 0.4 m/s under the same conditions, and, hence, it needs to be accounted for HFSB.

3.4.2 Faxén terms

Strictly speaking the flow velocity and acceleration should be calculated as averages along the particle surface $\langle \vec{u} \rangle_S$ and over its volume $\langle D\vec{u}/Dt \rangle_V$, respectively. Faxén (1922), as cited in Michaelides (1997), derived approximations to these averages using a Taylor series expansion

in the particle limit $d_p \to 0$ for $\vec{u} \approx \vec{u}_p$, resulting in extra terms that contain the Laplacian of the velocity (Mei 1996), the so-called Faxén terms. In an incompressible ($\nabla \cdot \vec{u} = 0$) and irrotational ($\nabla \times \vec{u} = \vec{0}$) flow, the Laplacian of the velocity is equal to zero. In fact, even in rotational flows the Faxén terms are usually negligible in comparison to the remaining terms (Mei 1996), only becoming relevant when the slip velocity approaches zero, and the effect of drag and history force have the least impact on the net force (Calzavarini et al. 2009). Therefore, they have been omitted from equation (3.8).

3.4.3 Lift force

The lift force has also been neglected. Lift is the most complex force to be modelled and is still topic of active research (Shi & Rzehak 2020). As the presence of a wall influences lift significantly, there are different approximation methods, depending if the wall is in the *inner* or in the *outer region*—a definition that compares the significance of inertial terms to the viscous term (Shi & Rzehak 2020). The wall is in the outer region if the particle distance to the wall is at least of the order of the Oseen length or the Saffman length (Shi & Rzehak 2020), in other words, if the inertial terms are larger than or comparable to the viscous term. However, in the case of shear flow in the outer region (the most relevant for the current study), there is no accurate model available for the lift force that extends over a wide range of parameters and is supported by data. In a comparison given by Shi & Rzehak (2020), the best model according to the authors, given by Zeng et al. (2009), exhibits discrepancies of up to 350% when compared to DNS data (Lee & Balachandar, 2010). Furthermore, the models reported in literature are only valid for a narrow range of values of the particle Reynolds Number (up to 250 in the model of Zeng et al. 2009).

3.4.4 Bubble deformation

Bubble fluid solutions are obtained by addition of surfactants to water, which reduces its surface tension to about 1/3 of the initial value, allowing bubbles to form. Surfactants contaminate the bubble surface altering the fluid dynamics of a bubble. Studies on bubble deformation and drag make clear distinction on the type of bubble depending on the amount of contaminants on the surface. According to Loth (2008) bubbles can be classified in *clean*, *partially-contaminated* and *fully-contaminated.* Roughly speaking, bubbles can be considered clean if the contaminant concentration is less than 10^{-7} g/l, and fully-contaminated if larger than 10^{-2} g/l. The amount of surfactants used to produce soap solutions is far greater than this threshold (e.g. Hale et al. 1971). Thus, HFSB can be safely considered to be fully-contaminated.

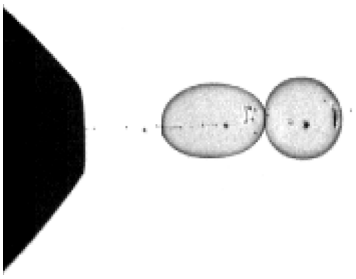

Figure 3-12. Image of a large HFSB being deformed right after generation.

The interaction between fluid-dynamic stresses acting on the bubble surface (causing deformation) and the counteracting surface tension stresses (resisting deformation) are responsible for changes of the bubble shape. When these changes are small, the bubble takes the shape of a spheroid. The deviation from spherical shape is quantified by the bubble aspect ratio, i.e. the ratio between the diameter along the axis of symmetry and the diameter about the axis of symmetry ($E = d_{||}/d_{\perp}$). Spheroids are classified as oblates if $E < 1$, and as prolates, otherwise.

For Re_p within 1-10,000 the deformation is governed by the Weber number (Loth, 2008):

$$We_p = \frac{\rho \left|\vec{u}_{slip}\right|^2 d_p}{\sigma} \tag{3.12}$$

where σ is the surface tension between the bubble surface and the surrounding fluid. If $We_p \ll 1$, particles tend rapidly to spherical geometry. When $We_p \sim 1$, the bubbles suffer moderate deformation. If $We_p \gg 1$, the bubble may deviate significantly from a sphere. The theoretical onset of ellipsoidal condition ($E \leq 0.9$) of a clean bubble occurs at We_p = 0.64 (Taylor and Acrivos 1964, as cited by Loth 2008). This occurs at $\left|\vec{u}_{slip}\right| \approx$ 5.4 m/s for d_p = 0.5 mm, ρ = 1.2 kg/m^3 and σ = 27.5 mN/m (*SAI 1035* from Sage Action, Inc., Faleiros et al. 2019). For contaminated bubbles, however, this onset occurs at higher We_p. Based on experimental data, Loth (2008) suggests this limit at $We_p \approx 2$, that is, $\left|\vec{u}_{slip}\right| \approx$ 9.5 m/s for the same conditions above. Therefore, HFSB can be safely assumed to be rigid particles in subsonic flows. For instance, on experiments with HFSB, with densities varying from 70% to 160% of the air density (Faleiros et al. 2019), We_p remains below 0.1 (figure 3-13).

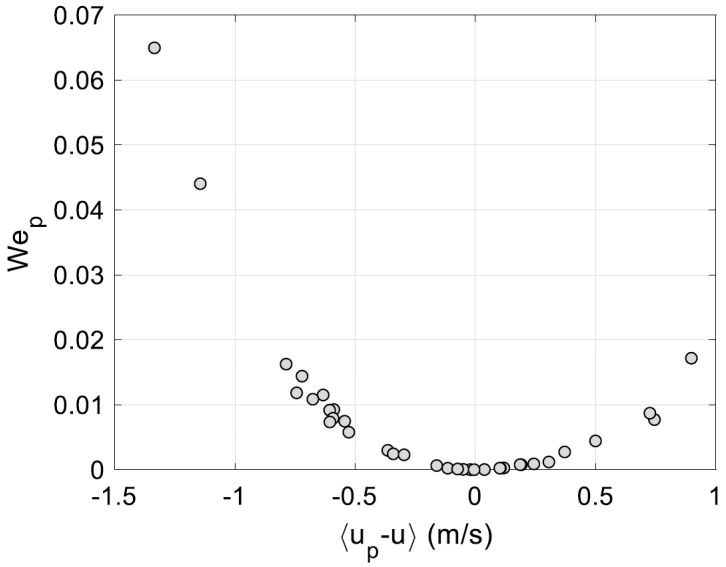

Figure 3-13. HFSB Weber numbers in the stagnation region of a cylinder for $U_\infty = 30$ m/s, $a_p \sim 7000$ m/s^2, $\rho_p/\rho = [0.7, 1.6]$. Reproduced from Faleiros et al. 2019.

3.5 Particle time response

3.5.1 Time response of micrometre heavy particles

Usually in external aerodynamics, the buoyancy force is insignificant, given that the acceleration due to the flow kinematics substantially exceeds the gravitational term. If $\rho_p \gg \rho$ then the undisturbed fluid stresses and the added-mass force also become negligible in comparison to the drag force. In addition, for d_p = 1 μm and $\left|\vec{u}_{slip}\right| < 10$ m/s, then $1 \leq \phi \lesssim 1.1$, so that ϕ is assumed to be equal to 1. When the history force can also neglected in comparison to the drag force, then eq. (3.8) is greatly simplified to:

$$\vec{u}_{slip} = -\tau_p \frac{d\vec{u}_p}{dt} \tag{3.13}$$

where $\tau_p = \rho_p d_p^2/18\mu$ is the particle time response, defined for micrometre heavy particles. Usually eq. (3.13) is normalized using a reference velocity U_0 and length L_0, resulting in:

$$\hat{\vec{u}}_{slip} = -S_k \frac{d\hat{\vec{u}}_p}{d\hat{t}} \tag{3.14}$$

where $\hat{.}$ is used for representing normalized variables, and $S_k = \tau_p U_0/L_0$ is the Stokes number. According to Samimy and Lele (1991), velocity measurements with micrometre heavy particles for $S_k < 0.02$ result in errors smaller than 2%.

The time response of micrometre heavy particles may be determined experimentally by measuring the normal component of the particle velocity $u_{p,n}$ across a shockwave. Assuming that the particle initially follows the flow perfectly ($u_{p,n1} = u_{n1}$), the particle relaxation time τ_p is given by the time it takes for the particle relative velocity with respect to the velocity upstream of the shock $\left|u_{p,n2} - u_{n1}\right|$ to be reduced to $1/e$ (36.8%) of the flow velocity jump $|u_{n2} - u_{n1}|$ (Melling, 1997), that is:

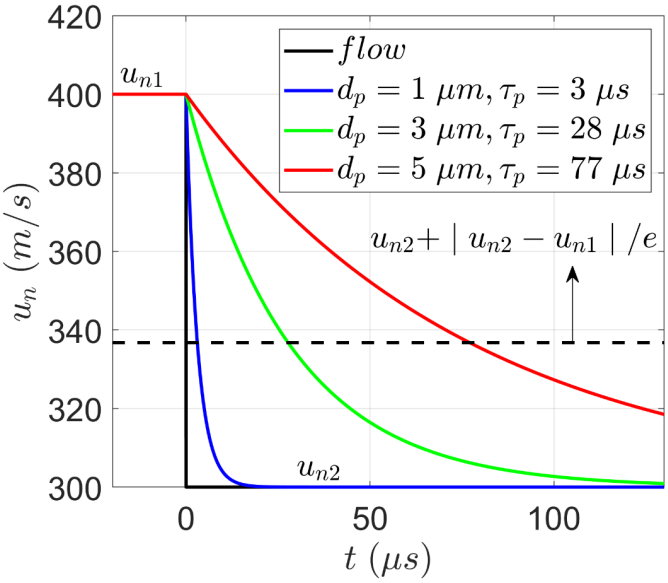

Figure 3-14. Micrometre heavy (ρ_p = 1000 kg/m3) particle time response across a shock wave.

$$\left|u_{p,n2} - u_{n1}\right| = \left|u_{n2} - u_{n1}\right| e^{-\frac{t}{\tau_p}}, \tag{3.15}$$

where n indicates normal component, 1 indicates the state upstream of the shockwave and 2 the state downstream of the shockwave. The relaxation time for particle sizes d_p from 1 to 5 µm and density ρ_p = 1000 kg/m^3 are illustrated in figure 3-14.

3.5.2 Time response of nearly-neutrally-buoyant bubbles

Neutrally buoyant particles are particles whose density approaches that of the surrounding medium. For nearly-neutrally-buoyant bubbles ($\rho_p \approx \rho$), the full equation (3.8) should be used to evaluate their tracing fidelity. However, if measurements are performed in a flow, where $d\vec{u}_p/dt \approx D\vec{u}/Dt$, and $\vec{g} \ll D\vec{u}/Dt$, then the slip velocity may be approximated as (Scarano et al. 2015):

$$\vec{u}_{slip} \approx -\tau_p^* \frac{d\vec{u}_p}{dt} \approx -\tau_p^* \frac{D\vec{u}}{Dt}, \tag{3.16}$$

where $\tau_p^* = (\rho_p - \rho) d_p^2 / 18\,\mu\phi(Re_p)$. Respecting the conditions above, τ_p^* may be used as an indicator of the HFSB tracing fidelity.

3.5.3 Measurements of particle time response

Experiments across shock waves with submicron TiO2 particles by Scarano & van Oudheusden (2003) (supersonic regime) and by Schrijer et al. (2006) (up to Mach 7), returned particle response times in the range of 2 μs. Ragni et al. (2010), reported a time response of 2 μs for di-ethyl-hexyl-sebacat (DEHS) droplets of 1 μm median diameter. Based on the study of Samimy & Lele (1991), it can be inferred that velocity measurements with micrometre particles of 2 μs time response result in

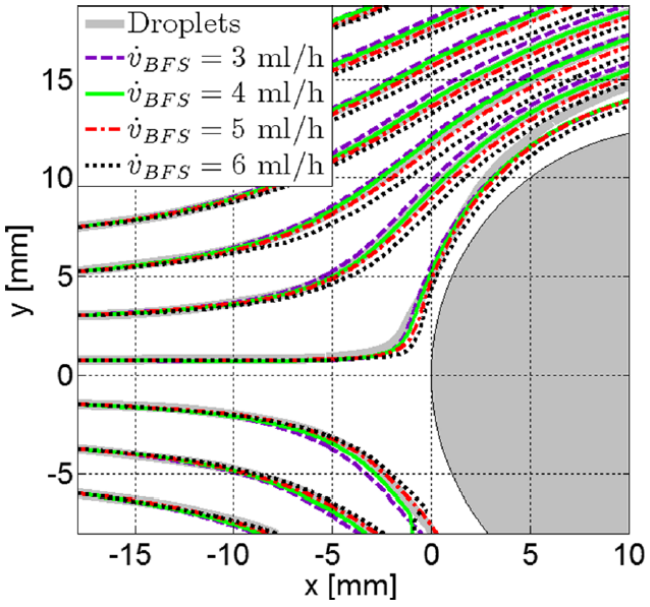

Figure 3-15. Time averaged streamlines at U_∞ = 30 m/s obtained with micron-size droplets and HFSB for different combinations of helium ($\dot{v}_{He}$ = 4 l/h) and soap ($\dot{v}_{BFS}$ = 3-6 ml/h) volume flow rates. Reproduced from Scarano et al. (2015).

errors smaller than 2% for flow frequencies up to 100 kHz.

Scarano et al. (2015) quantified the time response of helium-filled soap bubbles experimentally, by measuring the velocity and acceleration of HFSB, and the velocity of fog droplets (used as reference for estimating $\vec{u}_{slip}$), around the stagnation streamline of a cylinder (figure 3-15). They reported time responses within 10-40 μs depending on the volume flow rates of helium and soap. It is stressed, however, that the concept of the time response can only be used for comparing the tracing fidelity of bubbles in flows where $d\vec{u}_p/dt \approx D\vec{u}/Dt$. It is most useful to estimate the bubble density. However, the measured value of time response cannot be used to estimate slip velocity when the particle acceleration deviates significantly from that of the flow acceleration.

3.6 Soap bubble density and thickness

The soap bubble density can be obtained from mass conservation:

$$\begin{gathered} \rho_p V_p = \rho_{in} V_{in} + \rho_{soap} V_{soap} \\ \frac{\pi}{6} d_p^3 \rho_p = \frac{\pi}{6} \left(d_p - 2t\right)^3 \rho_{He} + \frac{\pi}{6} \left(d_p^3 - \left(d_p - 2t\right)^3\right) \rho_{soap} \end{gathered} \tag{3.17}$$

where $V_p = \pi d_p^3/6$ is the bubble volume, t is the bubble thickness and the subscript in stands for the *inner gas*. Eq. (3.17) can be rearranged to yield the bubble thickness:

$$t = \frac{d_p}{2} \left(1 - \sqrt[3]{\frac{\left(\rho_p - \rho_{soap}\right)}{\left(\rho_{in} - \rho_{soap}\right)}} \right) \tag{3.18}$$

Figure 3-16 (left) shows the thickness variation for neutrally-buoyant HFSB at NTP (20° C and 1 atm), that is, for $\rho_p = \rho_{air} = 1.205$ kg/m^3, $\rho_{in} = \rho_{He} = 0.1664$ kg/m^3 and $\rho_{soap} = 1124$ kg/m^3 (Faleiros et al. 2019). The shaded area represents 10% of density variation. The

absolute thickness variation increases with diameter as a consequence of t scaling with d_p. For fixed fluid densities, the ratio t/d_p is constant.

Figure 3-16 (right) compares the different choices of inner gas: helium, hydrogen ($\rho_H = 0.0899$ at NTP) and air. Since an air-filled soap bubble (AFSB) cannot be neutrally-buoyant in an air flow, which would require a zero film thickness, the thickness lines for soap bubbles twice as dense as air are also included. Three important conclusions can be drawn:

1. Helium and hydrogen yield similar t/d_p. Thus, with respect to this criterion, the two gases are equivalent.
2. AFSB with similar density of helium- or hydrogen-filled soap bubbles present significantly thinner soap films.
3. An AFSB with similar thickness as a neutrally buoyant HFSB

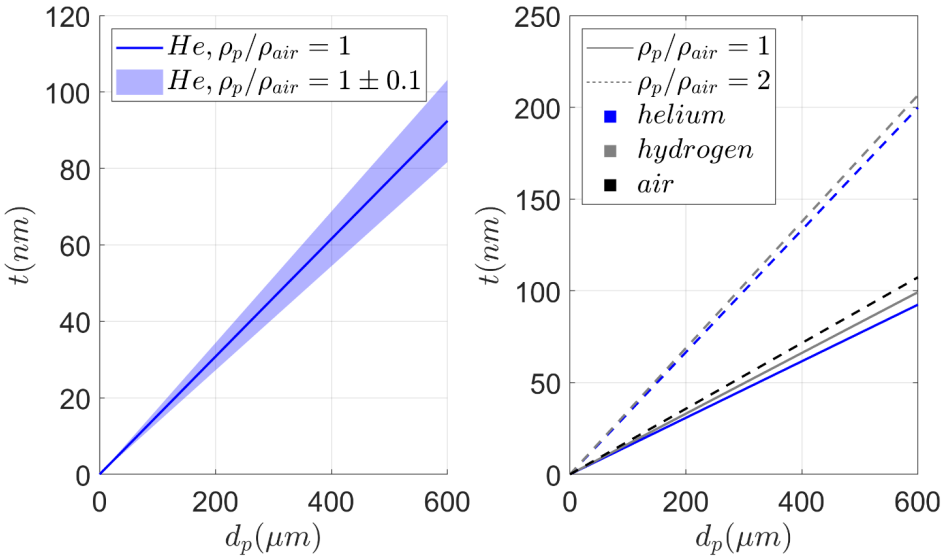

Figure 3-16. Bubble thickness versus diameter at NTP (20° C and 1 atm). Left: The thickness of a neutrally-buoyant HFSB (solid line) and the thickness changes for 10% of density variation (shaded area). Right: Bubble thickness comparison using different inner-gases. Solid and dashed lines represent neutrally-buoyant and twice as heavy as air, respectively. Blue, grey and black represent helium, hydrogen and air as inner gas, respectively.

is twice as heavy. The slip velocity, being approximately proportional to density difference, is one to two orders of magnitude larger.

4

GENERATION AND CONTROL OF HFSB

This chapter comprises a detailed study of the generation of helium-filled soap bubbles, regarding the control of the bubble size, the production rate, and the bubble production regime. The control of bubble density is considered in the next chapter. The material presented has been published in Experiments in Fluids (*Generation and control of helium-filled soap bubbles for PIV*, Faleiros et al. 2019).

4.1 Introduction

The control of the bubble generation process is essential for performing accurate PIV measurements. As discussed in section 2.3, the amount of light scattered by bubbles increases with their cross-sectional area d_p^2. In addition, it has been shown through a simplified model (3.5.2) that the particle time response is also proportional to d_p^2. Therefore, the choice between producing 425 μm or 600 μm particles, for instance, means a twofold difference in the recorded particle signal and in velocity errors. Larger bubbles might be preferred for exceedingly large volumes in low speed flows, while smaller bubbles are more suited for high speed (subsonic) applications. As will be demonstrated in this chapter, such choice is available for the same nozzle geometry by properly tuning the input volume flow rates of air, soap and helium.

The particle size distribution should be monodisperse (small deviations in size with respect to the mean), especially if the images are to be subdivided in interrogation windows and processed via cross-correlation. Brighter particles usually dominate the results in cross-correlation, leading to a bias error, in the case of a polydisperse size distribution, that emphasizes the displacement of larger particles. Morias et al. (2016) have reported that the bubbles may be generated in two different *production regimes* (modes of bubble generation): *bubbling* and *jetting*. During bubbling, the bubbles are formed within the bubble generator orifice, establishing a stable and periodic formation. In the jetting regime, the cylindrical soap film extends beyond the nozzle exit and eventually breaks up into bubbles in a less regular process. The authors also reported that in the bubbling regime the bubble diameter standard deviation was within 10% of the mean value, however, as the air flow rate was increased, the size dispersion approximately doubled. This was ascribed, although not confirmed, to a transition to the jetting regime. The production regimes are methodically analysed in this chapter.

Finally, controlling the production rate will determine the particle concentration, and, consequently:

- the vector resolution for PIV cross-correlation (5 particles or more are required per interrogation volume);
- the number of images required for statistical convergence in PTV measurements—together with the desired resolution and quantity of interest, i.e. mean velocity, turbulent stress, vorticity, among others.

Guidelines for HFSB generation using an orifice-type nozzle of 1 mm orifice diameter have been given in literature to some extent. Bosbach et al. (2009), Scarano et al. (2015) and Morias et al. (2016) used a similar device and reported similar flow rates of soap and helium (5 ml/h and 5 l/h, respectively), resulting in the production of neutrally buoyant HFSB. The flow rate of air was varied more broadly from 60 l/h (Bosbach et al.

2009) up to 160 l/h (Morias et al. 2016), although only a few conditions were tested. The reported bubble diameters vary from 0.23 mm (Bosbach et al. 2009) up to 0.55 mm (Morias et al. 2016). Bubble production rates range from 50,000 bubbles per second (Morias et al. 2016; Caridi et al. 2016) to 200,000 bubbles per second (Bosbach et al. 2009). The literature lacks, however, a systematic characterization of the relation between the fluid supply rates and the bubble properties.

A thorough description of HFSB generation is hereby realized. For a given generator geometry, the input parameters affecting the HFSB production are the fluid properties and volume flow rates of air, helium and soap. The system output is monitored in terms of production regime production rate and particle size. The knowledge of such parameters is a prerequisite for a well-designed PIV experiment and estimation of the experimental uncertainty.

4.2 Bubble size and production rate

The bubble size and production rates are obtained from shadow visualization close to the bubble generator exit, where the production regime is also detected. Shortly after their release, the bubbles are not spherical yet but of ellipsoidal shape, being slightly elongated along the jet axis direction. Assuming axisymmetric flow, the bubble shape is approximated by that of an ellipsoid, whose volume is obtained by measuring the semi-major and semi-minor axes, a and b, respectively, of the bubble elliptical cross-section, yielding:

$$V_b = \frac{4}{3}\pi a b^2. \tag{4.1}$$

The subscript b for *bubbles* is used in this chapter, as most properties discussed are exclusive of this seeding type.

Eventually, due to surface tension forces, the bubbles reach spherical shape. The bubble diameter is, therefore, estimated for this equilibrium condition as:

$$d_b = \left(\frac{6}{\pi} V_b\right)^{\frac{1}{3}}. \tag{4.2}$$

Assuming constant flow rate of helium, no helium leakage during the bubble formation, and neglecting the soap film thickness, V_b can also be determined by integrating the helium volume flow rate Q_{He} (assumed to be constant) during the bubble formation time (1/*f*):

$$V_b = \frac{Q_{He}}{f}. \tag{4.3}$$

The bubble production rate f is defined by the number of bubbles crossing a given target per the unit time. The production rate can also be estimated as the ratio of bubble velocity and the separation length λ (figure 4-1) right after their formation:

$$f = \frac{u_b}{\lambda}. \tag{4.4}$$

The parameters f, u_b and λ are measured independently by counting and tracking the bubbles and measuring the distance between them via high speed flow visualization.

4.3 Experimental Setup and Procedures

4.3.1 Bubble generation

The main bubble generator employed in the experiments (figure 4-1, left), of 1 mm orifice diameter, is a CNC-manufactured generator designed by NLR. The main dimensions (table 4-1) are based on the 3D printed HFSB-GEN-V11 generator developed at TU Delft. Another bubble generator geometry (figure 4-1, right) based on the DLR design (Bosbach et al. 2009) was also tested for comparison. The scaling properties of the bubble generation were investigated adopting three different values of the orifice diameter d_o, namely, 0.75, 1 and 1.5 mm. The main difference of the NLR design in comparison to the DLR

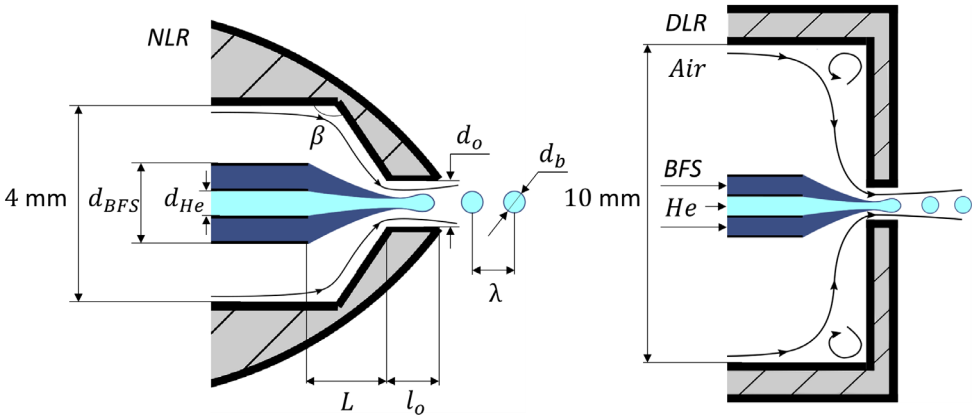

Figure 4-1. Schematic sectional view of the bubble generators used in the experiments (not to scale). Dimensions are given in table 4-1. BFS stands for bubble fluid solution.

nozzle consists in a conical contraction region upstream of the orifice ($\beta > 90°$). This modification is intended to avoid flow separation at the junction between the cylindrical part and the end wall, where residues of recirculating soap fluid accumulate under specific conditions.

Nozzle	NLR	DLR
β	125°	90°
d_{BFS}	2	2
d_{He}	0.6	0.5
d_o	1	{0.75, 1, 1.5}
L	2	2
l_o	1	1

Table 4-1. Dimensions (mm) of NLR and DLR bubble generators (figure 4-1).

Fluid	Density ρ (kg/m³)	Dynamic viscosity μ (Pa.s)	Surface tension σ (mN/m)
Air	1.20	1.8×10^{-5}	-
Helium	0.17	2.0×10^{-5}	-
BFS	1124	8.0×10^{-3}	27.5

Table 4-2. Fluid properties at 20° C and 1 atm.

The gases and soap mass flows are set, respectively, using *El-Flow Select* and *Mini Cori Flow* mass flow controllers from Bronkhorst. The bubble fluid solution (BFS) used is the *SAI 1035* from Sage Action, Inc. The properties of the fluids used are given in table 4-2.

4.3.2 Visualization Technique

The production regimes and the production rate were investigated via bubble shadow visualization at the exit of the generator. The images were recorded with a LaVision HighSpeedStar 5 CMOS camera (1024×1024 pixels, 12 bits, 20 µm pixel pitch), equipped with a lens of 200 mm focal length, placed perpendicular to the bubble stream and opposite to a continuous LED light source (figure 4-2). Recordings at 70 kHz frame rate with an exposure time of 1 μs provided images of HFSB resolved in time and space. The image sensor was cropped to 320×192 pixels with a magnification factor of 0.78, resulting in a FoV of 8×5 mm². The image resolution was 40 px/mm.

The volume flow rates of helium Q_{He} (4-17 l/h), air Q_{air} (20-180 l/h) and soap Q_{BFS} (3.5-11 ml/h) were systematically varied, resulting in a total of 530 measurement conditions. Most of the results presented (310 recordings) are based on the NLR bubble generator. The DLR generator is only included in the bubble size and production rate analysis (section 4.5). Each recording comprises ten uncorrelated cycles of 500 images realized with a time interval of 200 ms from each other.

A detection and tracking in-house algorithm renders the bubble size, the bubble velocity and counts the number of bubbles produced during each cycle. The bubble size is obtained from equations (4.1) and (4.2) by fitting an ellipse to the bubble boundary recorded in the shadowgraph images. The bubbles are tracked from the nozzle exit until they leave the frame. The production rate in a single cycle is then calculated as:

$$f_c = \left(\frac{n_b}{n_{im} - 1}\right) f_{ac}, \tag{4.5}$$

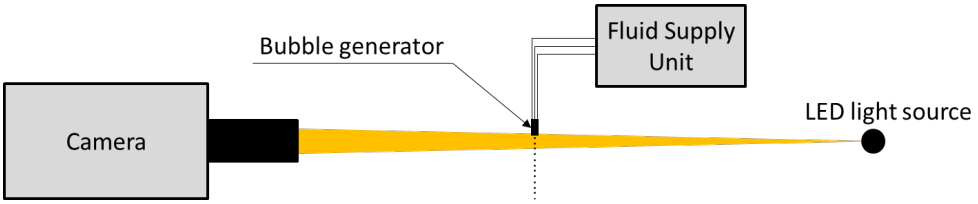

Figure 4-2. Schematic illustration of the experimental set-up for bubbles shadow visualization.

where n_b is the number of bubbles generated in one cycle, n_{im} is the number of images per cycle and f_{ac} is the camera acquisition frequency. Given that each measurement is performed for n_c = 10 cycles, the average bubble production rate f is then obtained as:

$$f = \frac{1}{n_c}\sum_{i=1}^{n_c} f_{c,i}. \tag{4.6}$$

4.4 Production regimes

4.4.1 Shadow visualization of production regimes

For a given generator geometry and fixed fluid properties, the combination of the fluids volume flow rates determines the type of bubbles that are produced. A qualitative classification of the regimes of bubble production (figure 4-3) facilitates the discussion of the different phenomena involved in bubble formation. The main distinction is based on whether the bubble forms inside or outside of the nozzle. Exterior bubble formation is here defined as *jetting*, where the bubble is formed and detaches from the jet at least one bubble diameter downstream of the nozzle exit. If the bubble is formed closer to the nozzle (normally within the orifice) the production regime is defined as *bubbling*.

Other distinctions are based on whether the production of bubbles is monodisperse, i.e. periodic formation of bubbles with constant size, or visibly polydisperse. Monodisperse generation of bubbles is mainly obtained in the bubbling regime, however, with a few exceptions. A specific regime is recognized when alternated production of two distinct populations of monodisperse bubbles coexist (*double-bubbling*). *Merging* of bubbles has also been observed during double-bubbling or polydisperse production. Another observed phenomenon is the formation of *satellite bubbles* between the detachment point of bubble formation and

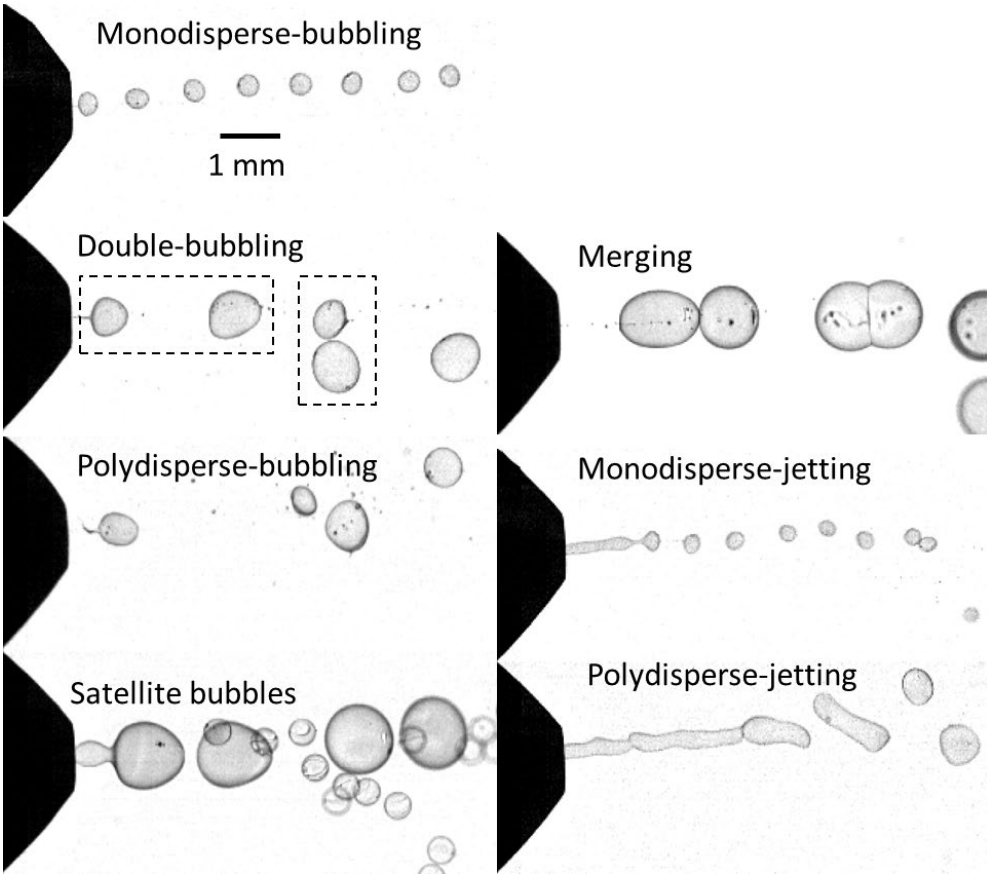

Figure 4-3. Shadow visualization of production regimes and their classification.

the envelope of helium and soap. In most cases satellite bubbles are significantly smaller than the main bubbles and can be neglected. For ease of communication, double-bubbling, polydisperse-bubbling, large satellite bubbles and merging will be altogether referred to as *polydisperse-bubbling*, and monodisperse periodic bubble production will be referred to simply as *bubbling*. Although monodisperse bubble formation may occasionally occur in the jetting regime, such condition is often unstable and turns into irregular (polydisperse) production by a slight change in the inputs.

Guidelines for avoiding the jetting regime may be derived from observations of its occurrence in relation to the imposed flow rates. The effects of volume flow rate variation are observed for independent increase of air, helium and soap volume flow rate, while keeping the flow rates of the other two fluids constant (figure 4-4).

Low volume flow rates of air result in the generation of large bubbles in the bubbling regime. By increasing the air flow rate, the bubbles reduce in size, and consequently the distance between them, suggesting an increase in the production rate. At Q_{air} = 129 l/h, a jet extending about two bubble diameters away from the nozzle is formed, yet a rather monodisperse bubble size distribution is observed (monodisperse-jetting). As the volume flow rate of air is increased to Q_{air} = 145 l/h, the jet extends to about four bubble diameters downstream of the nozzle and the soap film breaks up irregularly, yielding a polydisperse distribution of bubbles.

Low volume flow rates of helium yield monodisperse bubbles. Increasing the helium flow rate, increases the bubble size. The distance between the bubbles, however, seems independent of the helium flow rate. Transition to jetting occurs by increasing the volume flow rate to Q_{He} = 11.8 l/h. The transition is more abrupt in this case, and a longer jet of about six bubble diameters is observed. It is noted that the smaller jet length in the snapshot shown for Q_{He} = 15 l/h relative to the case of Q_{He}

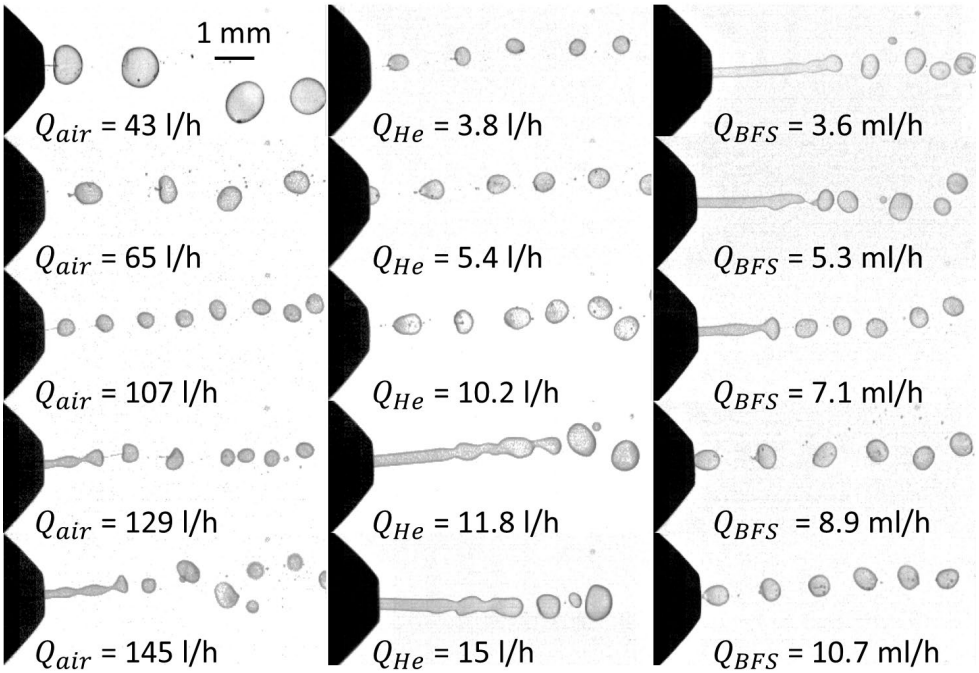

Figure 4-4. Effect of input flow rate increase (from top to bottom) on the bubble generation modes. Left: Air flow rate effect (Q_{BFS} = 8.9 ml/h and Q_{He} = 7 l/h). Middle: Helium flow rate effect (Q_{BFS} = 8.9 ml/h and Q_{air} = 75 l/h). Right: Soap flow rate effect (Q_{He} = 8.6 l/h and Q_{air} = 86 l/h).

= 11.8 l/h should not be interpreted as a reduction in the jet size, as it is an instantaneous representation of a very dynamical and unsteady state.

Changes in soap flow rates yield opposite effects on the production regime to that of air and helium. Low flow rates of soap are likely to yield jetting regime. By increasing the soap flow rate, the bubble production becomes less disperse and eventually transitions to bubbling (Q_{BFS} = 8.9 ml/h). Moreover, changes in soap flow rates do not seem to affect either the bubble size or the frequency of bubble formation.

4.4.2 Production regime envelopes

A systematic procedure is implemented to map the production regimes. First, the volume flow rates of soap and helium are fixed

while Q_{air} is increased from the first working condition till beyond the transition point from bubbling to jetting. This process is repeated for different helium and soap flow rates until a complete mapping of the production regimes is obtained. The resulting mappings (figure 4-5) are given at fixed values of Q_{BFS}.

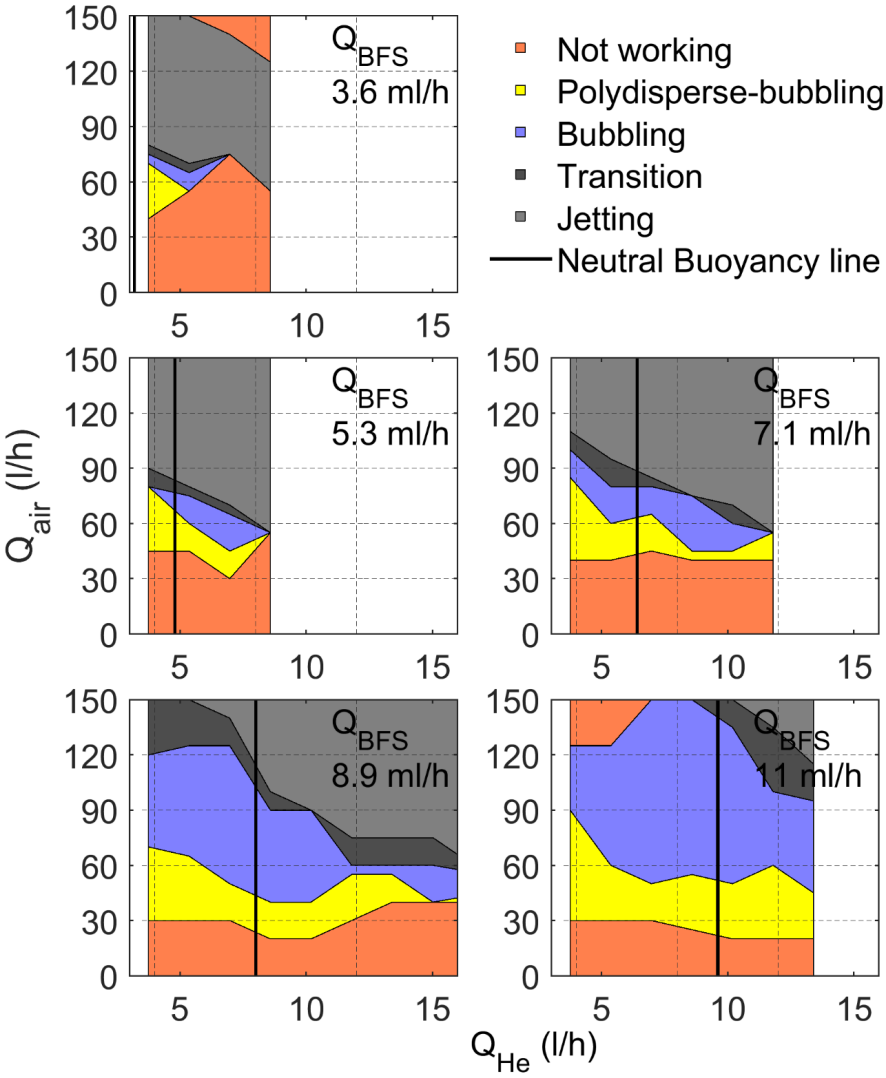

Figure 4-5. Two-dimensional maps of production regimes for varying flow rates.

For low values of Q_{BFS}, the blue region, where the combination of air and helium flow rates yield bubbling regime, is limited to small ranges. Larger values of Q_{BFS} offer significantly wider operational ranges within the bubbling regime. The previous observation that jetting is present for high gas flow rates and low BFS flow rates (section 4.4.1) is evident in these maps. Polydisperse-bubbling occurs mostly for low air flow rates and can be easily avoided through increasing the air flow rate. The intersection of the bubbling region with the vertical black lines (neutral buoyancy condition, $Q_{He}/Q_{BFS} = 900$, derived in chapter 5), shows the desired working region. Imposing simultaneously these two criteria significantly restricts the choice of flow rates.

Although from these maps it appears that increasing soap flow rates is always beneficial, a more frequent occurrence of intermittent bubble production has been observed for $Q_{BFS} \geq 11$ ml/h at high air volume flow rates, i.e. the bubble generator works only a fraction of the time, reducing the bubble production rate and increasing soap spitting. If the flow rates of soap are increased even further, the annular jet collapses and the bubble production ceases entirely.

4.5 Bubble production rate and size

The inverse proportionality of the bubble volume and the production rate of bubbles for a monodisperse production of bubbles (bubbling regime) is confirmed experimentally (figure 4-6) for the NLR (d_o = 1 mm) and DLR (d_o = 0.75, 1.00 and 1.50 mm) bubble generators. The good agreement of the data indicates that eq. (4.3) holds independently of bubble generator geometry.

From the flow visualizations (section 4.4.1), it was observed that the distance between the bubbles, and, consequently, the production rate changes almost independently with Q_{air}. This is confirmed by analysing f while varying the flow rates of air, helium and soap (figure 4-7). For instance, while fixing the helium and soap flow rates, f increases linearly with Q_{air}. In the interval $40 < Q_{air} < 120$ l/h, f increases from 10 kHz

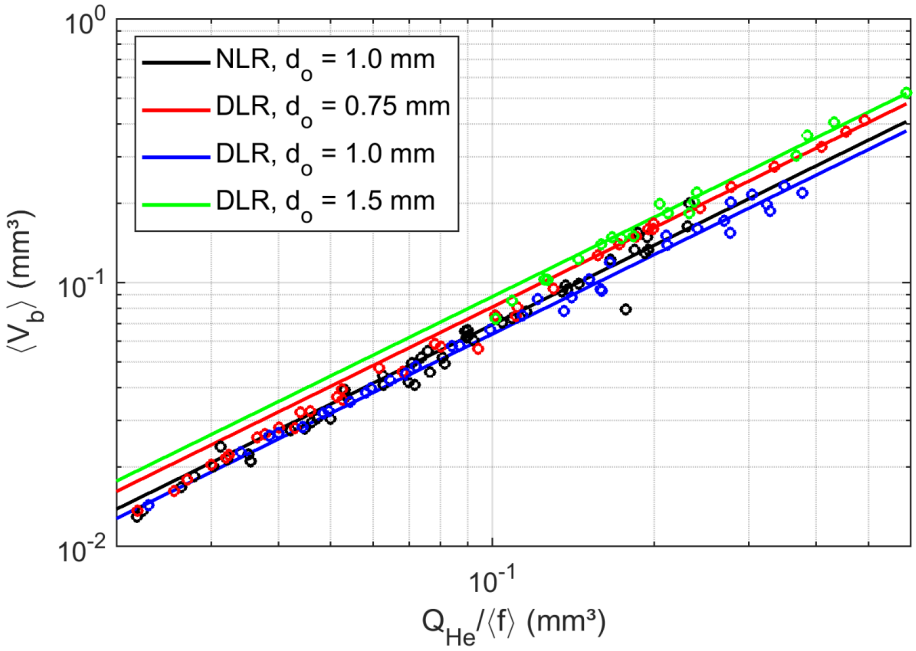

Figure 4-6. Bubble volume vs. production rate.

to 50 kHz, almost independently from helium and soap (figure 4-7, right). The linear correlation between Q_{air} and f for all measurements with the NLR generator in the bubbling regime is 0.91.

The dependence of f on Q_{air} is attributed to the parameters governing annular jet instability (Shen and Li, 1996). When Q_{air} is increased, there is a reduction in the cross section area of the helium-filled soap jet, combined with an increase in the jet velocity. The former enhances curvature effects on the soap film, reducing therefore the wavelength of the fastest growing mode of instability, which determines the wavelength of bubble formation. A decrease in the wavelength or an increase in the jet velocity results in higher production rates (eq. (4.4)).

One reason Q_{air} is the main parameter governing the HFSB production rate is that Q_{air} encompasses the broadest available range (40-120 l/h). In fact, incremental changes of soap and helium flow rates result in larger incremental changes of f. Increasing Q_{air} by 1 l/h yields less than

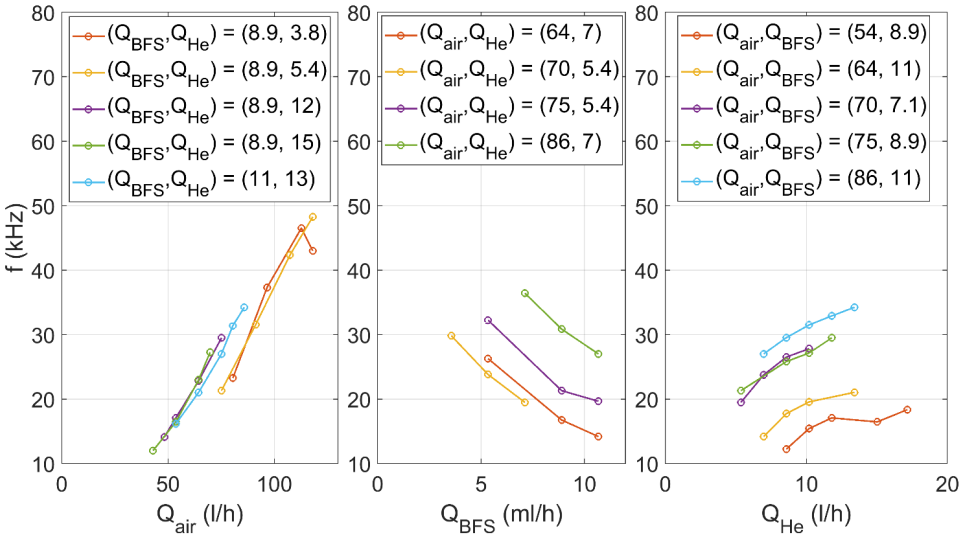

Figure 4-7. Influence of Q_{air} (l/h), Q_{He} (l/h) and Q_{BFS} (ml/h) on the HFSB production rate.

0.5 kHz increase of f, while increasing Q_{He} in 1 l/h or Q_{BFS} in 1 ml/h yields about 1.5 kHz increase and 2.5 kHz decrease, respectively. However, having more restricted working condition ranges ($3 < Q_{BFS} < 11$ ml/h and $4 < Q_{He} < 16$ l/h), the absolute impact of varying soap and helium flow rates on the production rate is less significant than that of air. Most importantly, as the focus is to generate neutrally buoyant bubbles, where Q_{He}/Q_{BFS} must be kept constant (chapter 5), the effects of helium and soap on the production rate counteract each other, further emphasizing the influence of Q_{air}.

A comparison of the HFSB production rate dependence on Q_{air} obtained with different bubble generator geometries is shown in figure 4-8. A linear relation between f and Q_{air} is observed for all configurations. The root-mean-square deviation of the least square fits is about 4 kHz, which is attributed mainly to the influence of helium and soap. The production rate measured with the NLR generator shows a similar trend to that obtained with the DLR generator of smaller orifice size (0.75mm).

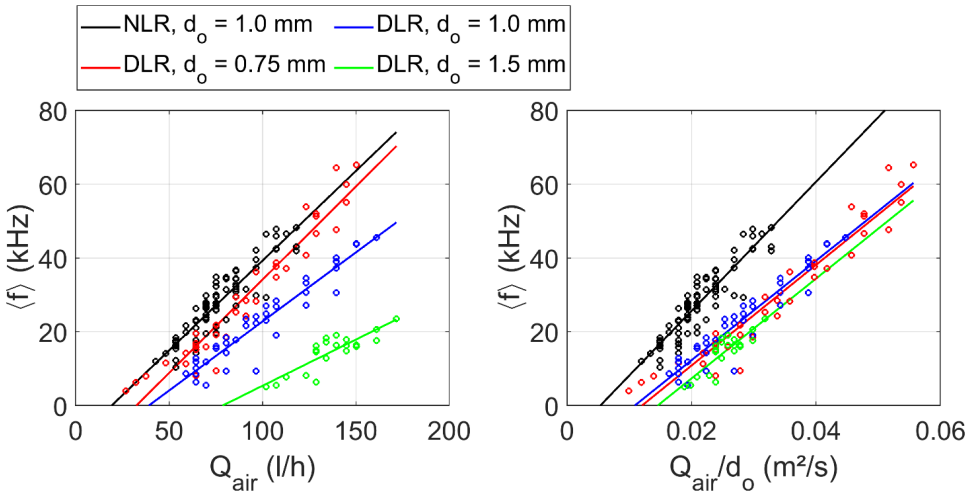

Figure 4-8. Bubble production rate dependency on air flow rate. Helium flow rates varied in the range of 4 to 16 l/h for all generators, except for the DLR of 1.5 mm orifice diameter, for which it varied from 6 to 14 l/h. Soap flow rates varied between 3 to 11 ml/h for the NLR generator and were kept constant at 8.9 ml/h for the DLR generators.

This can be explained by the phenomenon of *vena contracta* (Torricelli, 1644, Reader-Harris, 2015), where the effective orifice area is smaller than the geometric area. This effect is geometry dependent, and it is conjectured that the resultant effective area of the NLR generator compares to the DLR generator of 0.75 mm orifice diameter. Furthermore, the data strongly indicates that when considering different orifice diameters for the same nozzle (DLR generator), the relation between f and Q_{air}/d_o collapses into a single curve (figure 4-8, right).

The bubble velocity after detachment u_b (streamwise component), being proportional to the production rate (eq. (4.4)) is also investigated (figure 4-9). The HFSB velocity is typically between 20 and 40 m/s. Thus, when the bubble generator is installed in the settling chamber, where the typical speed in subsonic wind tunnels is below 10 m/s, the external flow is not expected to influence significantly the bubble production. For instance, at 5 m/s free stream velocity in the settling

chamber, the bubble relative velocity with respect to the free stream flow velocity changes in 10-30%. Furthermore, it is noted that, likewise the production rate, the bubble velocity approximately scales as $u_b \sim Q_{air}/d_o$ (figure 4-9, right). At the orifice, the area of the annular cross section occupied by air is expected to scale with the orifice area $A_{air} \sim A_o$, and the air velocity, therefore, to scale as $u_{air} \sim Q_{air}/d_o^2$. This result contradicts the initial expectation that $u_b \sim u_{air}$. In case the assumption $A_{air} \sim A_o$ holds, then $u_b \sim u_{air} d_o$. A complete analysis of the non-dimensional parameters governing this dependence is subject of further investigation.

From eq. (4.3) and the empirical analysis above, it follows that the bubble volume is proportional to the ratio of helium and air flow rates and to the orifice diameter. The bubble diameter, consequently, scales as:

$$d_b \sim \left(\frac{d_o Q_{He}}{Q_{air}}\right)^{\frac{1}{3}}. \tag{4.7}$$

The measured diameters collapses well with linear curves following this proportionality (figure 4-10) up to about $(d_o Q_{He}/Q_{air})^{1/3} = 0.5$ mm$^{1/3}$.

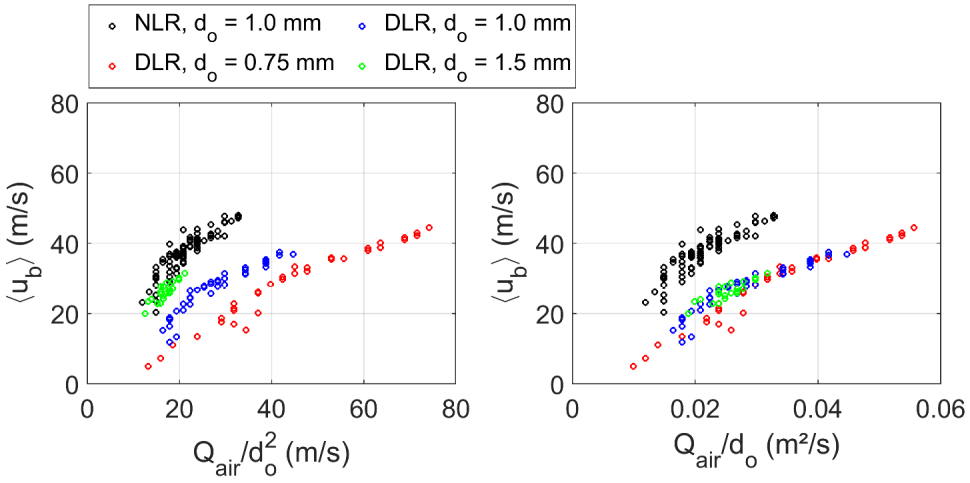

Figure 4-9. Bubble velocity dependency on air flow rate.

For larger values, the data spread increases in particular for the DLR nozzles of 0.75 and 1.5 mm orifice diameters. For the 1.5 mm diameter case, the bubble generator needs high Q_{air} to work properly since the orifice area has more than doubled in comparison to the reference d_o = 1 mm. Moreover, larger bubbles are more prone to deformation and they deviate from the spherical shape for a longer time after detachment, affecting the accuracy to which the bubble size is determined.

From the perspective of PIV application, it is useful to summarize these results by showing frequency and bubble diameter together as a function of air and helium volume flow rate isolines (figure 4-11), which is herein illustrated for the NLR nozzle (d_o = 1 mm). This diagram enables the selection of air and helium flow rates for a desired diameter and production rate. The optimal soap flow rate then follows from the neutral-buoyancy relation ($Q_{He}/Q_{BFS} = 900$, chapter 5). The region

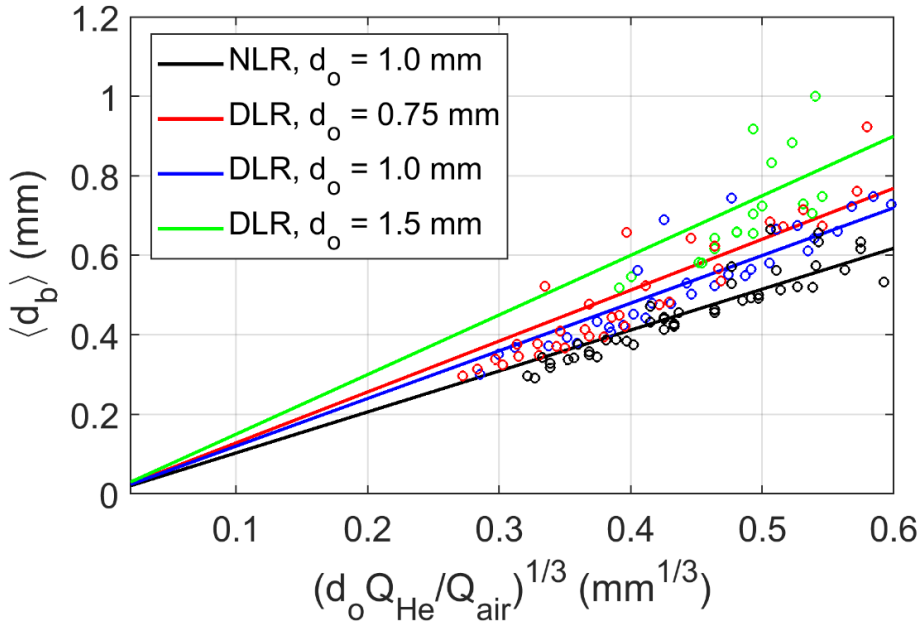

Figure 4-10. HFSB diameter relation to the ratio of air and helium flow rates.

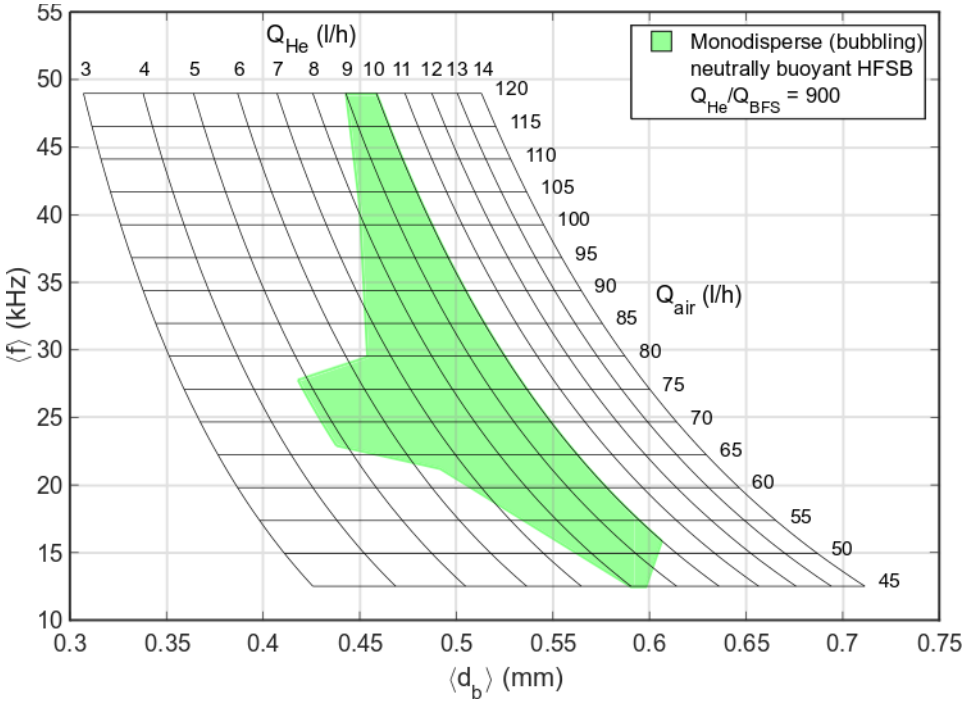

Figure 4-11. HFSB production rate and diameter as a function of air and helium flow rates. Production rate and bubble diameter dependency on the flow rates of air and helium were determined from the fitted curves to the NLR bubble generator data (figure 4-8 and figure 4-10). The green region of monodisperse bubbles was obtained from the mapping of production regimes (figure 4-5). The ratio of neutral buoyancy is obtained in chapter 5 from the measured time response (figure 5-4).

where the bubbles are simultaneously neutrally buoyant and monodisperse (produced in the bubbling regime) is included for completeness.

4.6 Conclusions

Depending on the combination of fluid flow rates, different production regimes exist: polydisperse bubbling, bubbling and jetting. The production of HFSB in the bubbling regime is periodic and stable. Polydisperse bubbling occurs mainly for low air flow rates and can be easily avoided. Transition from bubbling to jetting was found to occur

when increasing the flow rates of air and helium or when decreasing the flow rate of soap.

The bubble production rate and diameter dependence on the fluid flow rates and orifice diameter were investigated for generation in the bubbling regime. The bubble production rate is mostly controlled by changes in the air volume flow rate, increasing linearly with the latter. Furthermore, f reduces linearly with increases in the orifice diameter d_o. The investigations also show that the bubble volume is proportional to the ratio of helium and air volume flow rates and to the orifice diameter, i.e. $V_b \sim d_o Q_{He}/Q_{air}$.

Complying with the restrictions on the flow rates that yield the generation of monodisperse neutrally buoyant bubbles, the NLR bubble generator of 1 mm orifice diameter is able to produce 10 to 50 thousand bubbles per second, of 0.42-0.60 mm diameter.

5

DENSITY AND TIME RESPONSE

The time response and the neutral buoyancy condition are investigated experimentally in this chapter. The polydispersity of HFSB diameter and time response are also quantified. The material here presented has been published in Experiments in Fluids (*Generation and control of helium-filled soap bubbles for PIV*, Faleiros et al. 2019).

5.1 Introduction

The inertial response of helium-filled soap bubbles to the presence of a cylinder is investigated, with emphasis on the flow region where the particle acceleration is sufficiently large for a distinguishable measurement of the slip velocity, but still approximately equal to that of the flow, following the approach devised for time response estimation by Scarano et al. (2015), described in section 3.5.2. This investigation allows for the estimation of bubble density, and, therefore, to empirically determine the combination of input flow rates of helium and soap that leads to the neutral buoyancy condition, where the bubble density equals that of the flow. The dependency of the time response on the bubble diameter is also discussed for the case of finite Re_p.

In addition, measurements of the bubble diameter through the distance between the glare points are used to investigate the bubble diameter dispersion. The quantitative data obtained is associated with the production regimes visualized in chapter 4. The dispersion of the time

response distribution is also investigated, as the latter may affect measurements of velocity fluctuations performed with HFSB.

5.2 Time response and neutral buoyancy

In the ideal case of no soap spillage or helium leakage during the bubble formation process, the following relation can be obtained imposing mass conservation:

$$fV_b\rho_b = Q_{He}\rho_{He} + Q_{BFS}\rho_{BFS}, \tag{5.1}$$

where ρ_{He}, ρ_{BFS} and ρ_b are the helium, soap and bubble densities, respectively. Substituting $V_b \approx Q_{He}/f$ into (5.1) yields:

$$\rho_b = \rho_{He} + \frac{Q_{BFS}}{Q_{He}}\rho_{BFS}. \tag{5.2}$$

Thus, the neutral buoyancy condition ($\rho_b = \rho_{air}$) at normal temperature and pressure is satisfied when $Q_{He}/Q_{BFS} \cong 1{,}080$.

When shape deformation is negligible, a bubble experiences the same drag of a solid spherical particle. As mentioned in section 3.5.2, when the particle acceleration is approximately equal to that of the flow, the slip velocity may be approximated by eq. (3.16). Consequently, the particle density relative to the fluid density $\bar{\rho} = (\rho_p - \rho)/\rho$ may be estimated as:

$$\bar{\rho} = \frac{18\,\nu\phi}{d_p^2\tau_p^*}, \tag{5.3}$$

where ϕ is obtained from eq. (3.10) for $Re_p < 800$ (hereafter, * used to differentiate the time response of nearly-neutrally-buoyant particles with respect to that in the Stokes regime is dropped).

The time response is obtained through the ratio of slip velocity and particle acceleration (Scarano et al. 2015), which in the streamwise direction is:

$$\tau_p = \frac{\left|u_{slip}\right|}{\left|u_p \frac{\partial u_p}{\partial x}\right|}. \tag{5.4}$$

The Stokes number is calculated by selecting a proper flow time scale. For the experiment described in this chapter, $S_k = \tau_p U_\infty / D$, where D is the cylinder diameter.

5.3 Experimental Setup and Procedures

5.3.1 Instrumentation

The bubble generator employed in the experiments is the NLR design (figure 4-1, left) of 1 mm orifice diameter. The gases and soap mass flows are set, respectively, using *El-Flow Select* and *Mini Cori Flow* mass flow controllers from Bronkhorst. The bubble fluid solution used is the *SAI 1035* from Sage Action, Inc. The properties of the fluids used are given in table 4-2. The images were recorded with a LaVision HighSpeedStar 5 CMOS camera (1024×1024 pixels, 12 bits, 20 µm pixel pitch). The laser used during PIV measurements is a diode pumped Litron Nd:YLF *LDY304* (2×30 mJ/pulse at 1 kHz).

5.3.2 PIV/PTV acquisition

HFSB size and time response were measured in the deceleration region in front of a cylinder with HFSB and DEHS (reference flow field) to obtain slip velocity and particle deceleration. Measurements were performed in the small anechoic wind tunnel KAT of the Royal Netherlands Aerospace Centre (NLR) using a cylinder of 50 mm diameter, spanning the 38×51 cm² test-section. A 300 mm splitter plate connected to the cylinder's rear end (figure 5-1) prevents the formation of the von Kármán vortex-street and the consequent unsteady motions that would also be present upstream of the cylinder. The wind tunnel speed was set at 30 m/s. The resulting deceleration ahead of the cylinder is in the order of 7,000 m/s² (~700g). A total of 35 combinations of

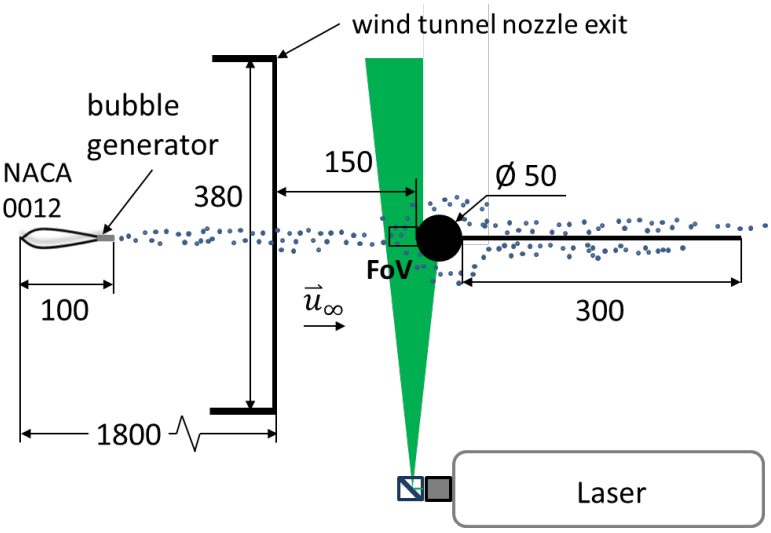

Figure 5-1. Top-view of experimental setup for cylinder flow. HFSB were not produced during the PIV experiment with DEHS, but the NACA0012 wing was always in place. Dimensions are in millimetres.

volume flow rates of air (65 - 160 l/h), helium (4 – 21 l/h) and soap (3.5 - 11 ml/h) were tested.

Planar PIV measurements with DEHS were performed in frame straddling mode at 50 Hz on a laser sheet thickness of 3 mm. A total of 3,500 images were acquired. For the measurements with HFSB, the laser was operated at 20 kHz and 10,000 multi-exposure images per condition were recorded at a rate of 100 Hz with exposure time of 0.01 s. The camera sensor was cropped to 512×320 pixels, resulting in a field of view of 23×14 mm². The lens focal length was 200 mm, resulting in a magnification of 0.44 and an image resolution of 22.15 px/mm. The bubbles were imaged in about 10 pixels, allowing the pair of glare points to be resolved.

5.3.3 Image processing

DEHS images were analysed by cross-correlation, performed with the *DaVis* 8.4 software from LaVision, which provided an accurate reference for the velocity field of the air flow.

The HFSB images were processed through an in-house tracking algorithm. The glare points were found as local maxima. Their centre position was obtained with subpixel accuracy by fitting a Gaussian function to their intensity distribution. The coupling of glare points was straightforward as the image particle concentration was sufficient low. The distance d_g and orientation between the glare points were both taken into account for this purpose. A minimum d_g = 3 px (0.13 mm) was used as a filtering criterion. The bubble centroid was obtained as the midpoint between the glare points. Polynomial fitting was then applied to the centre of the particles along the trajectories captured in the multi-exposure images rendering particle velocity and acceleration.

5.4 Bubble size

5.4.1 Mean HFSB diameter

The bubble size was calculated by eq. (2.13), i.e. $d_p = \sqrt{2} d_g$. The mean HFSB diameter measured from the cylinder experiment and from shadow visualizations (chapter 4) are plotted against one another for comparison (figure 5-2). No significant difference is observed between the two methods, demonstrating control and repeatability in both experiments. A direct comparison of 10 data points obtained with both techniques at precisely the same flow rates shows that the shadow visualization measurements consistently underestimates the bubble size in about 10% in comparison to the glare point method. The latter is deemed to be less prone to errors, since the bubbles are free from nozzle exit effects.

5.4.2 Uncertainty on the measured bubble size

The uncertainty of the measured diameter was verified by checking the variation of bubble diameter along bubble trajectories, where physical variations of bubble size are negligible and occur mainly due to the method itself. This has been done for each tested condition, using

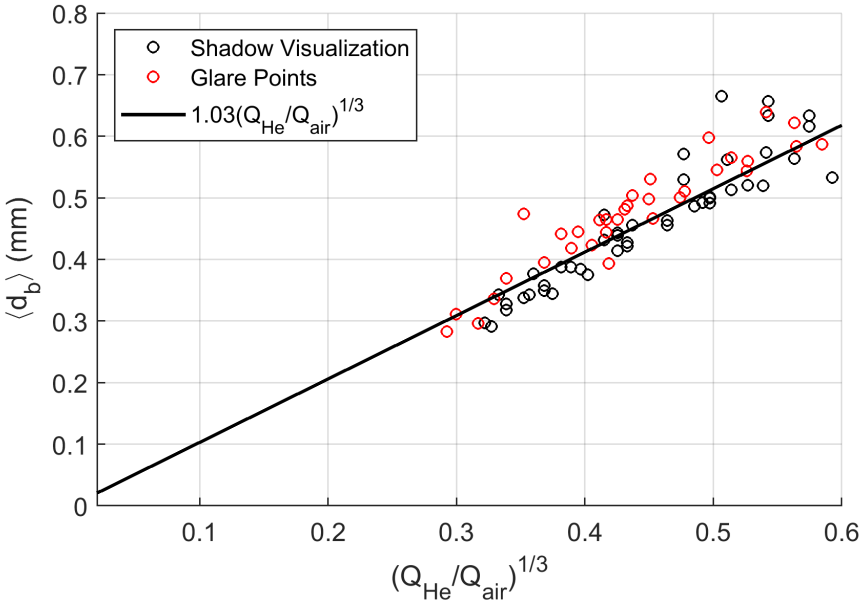

Figure 5-2. Comparison of bubble diameter obtained from the distance between bubble glare points with the shadowgraph measurements performed in the bubble generator exit (chapter 4).

1,000 trajectories with more than ten bubbles each. The diameter standard deviation relative to the mean along a trajectory was larger for smaller bubbles, and consisted of 2% for $\langle d_p \rangle$ = 0.3 mm, decreasing as the mean diameter increased, down to 1.2% for $\langle d_p \rangle$ = 0.8 mm.

The uncertainty of the mean bubble diameter of all samples is smaller. Assuming a normal distribution, the uncertainty may be calculated as $3\sigma_d/\sqrt{N}$, where σ_d is the diameter standard deviation, N is the number of samples and the factor three means it is computed at 99.7% confidence level. This is less than 0.3% of the mean bubble diameter for all tested conditions.

5.5 Neutral buoyancy condition

The effect of deviations from the neutral buoyancy condition can be observed qualitatively through the streamlines in front of the cylinder

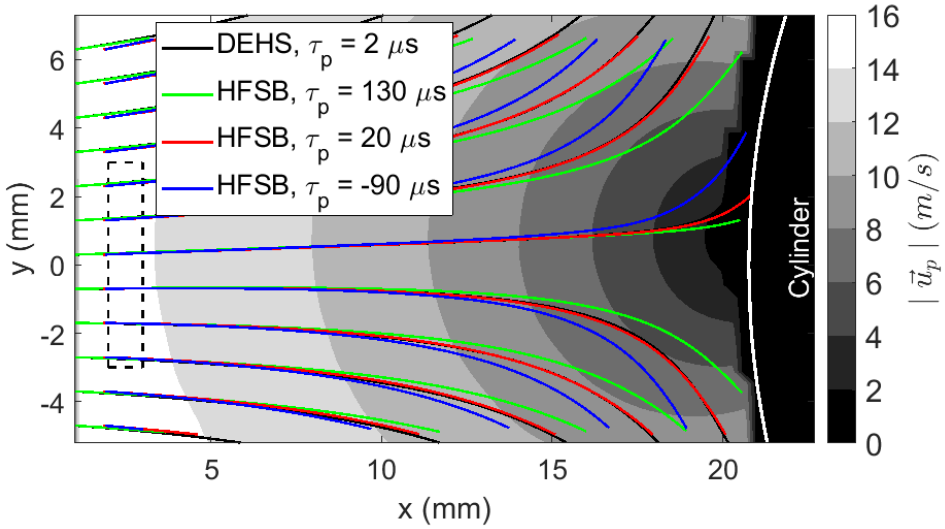

Figure 5-3. Flow field ahead of the circular cylinder obtained from PIV measurements (velocity contours and solid black lines as streamlines). Trajectories followed by neutrally buoyant (red), heavier-than-air (green) and lighter-than-air (blue) HFSB tracers. Dashed region is used for the calculation of quantitative data on HFSB time response, density and diameter.

(figure 5-3). The black streamlines show the reference measurements obtained using DEHS. Nearly neutrally buoyant HFSB ($\langle\bar{\rho}\rangle$ = 0.05, $\langle\tau_p\rangle$ = 20 μs) follow closely the reference streamlines. Heavier-than-air bubbles ($\langle\bar{\rho}\rangle$ = 0.5, $\langle\tau_p\rangle$ = 130 μs) take longer to respond to the deceleration caused by the pressure gradient due to their inertia, and therefore the particles approach closer to the cylinder before turning sideways. Lighter-than-air bubbles ($\langle\bar{\rho}\rangle$ = -0.2, $\langle\tau_p\rangle$ = -90 μs), negative sign indicating lighter than air), respond in a shorter distance (to a lower threshold of pressure drag) than air itself, as a result of their lower inertia force.

The theoretical HFSB density, estimate from eq. (5.2), and the calculated ratio Q_{He}/Q_{BFS} leading to neutrally buoyant bubbles are verified by estimating the bubble density from eq. (5.3), based on the

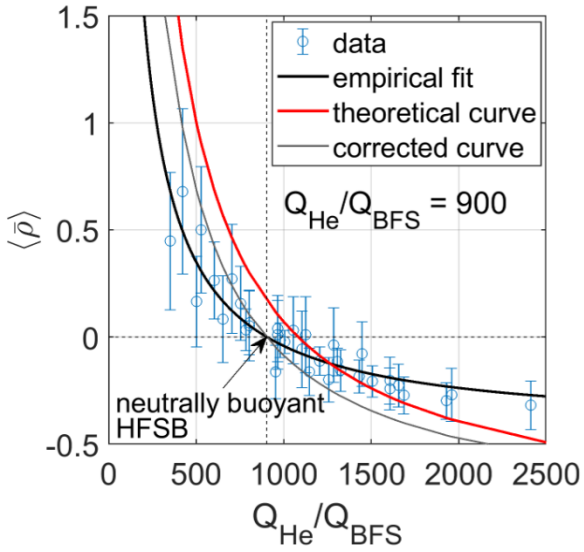

Figure 5-4. HFSB density difference as a function of helium and soap flow rates, measured using the NLR generator. The empirical curve fit is given by $\langle\bar{\rho}\rangle = -0.434 + 392.2(Q_{He}/Q_{BFS})^{-1}$. The error bars represent one standard deviation.

experimentally measured diameter and time response. The dependency of the normalized density difference $\bar{\rho}$ upon the ratio Q_{He}/Q_{BFS} is shown in figure 5-4. The empirical curve fit has a similar shape as the theoretical curve. The point where it crosses the neutrally buoyant line ($\bar{\rho} = 0$), gives the ratio of helium and soap volume flow rates, $Q_{He}/Q_{BFS} = 900$, that results in HFSB with shortest time response.

The standard deviation of the neutral buoyancy ratio is obtained by a Monte Carlo simulation. For each combination of mass flows tested (35 in total), the entire distribution of $\bar{\rho}$ values, containing data from all the recorded bubbles, is considered. In every iteration of the Monte Carlo simulation, a single $\bar{\rho}$ value is randomly selected from each distribution, forming a curve of 35 data points ($\bar{\rho}, Q_{He}/Q_{BFS}$). A least-square fit is applied and the ratio Q_{He}/Q_{BFS} leading to $\bar{\rho} = 0$ (found through extrapolation) is recorded. This procedure is repeated 10,000 times and the standard deviation of the optimal ratio is calculated. From the simulation it is then obtained that the neutral buoyancy ratio is within $Q_{He}/Q_{BFS} = 900 \pm 50$, where the limits are given as $\pm$ one standard deviation.

The difference in the empirically determined to the theoretically calculated ratio of helium-to-soap flow rates leading to neutral buoyancy is attributed to spillage of soap in the bubble formation process, which causes the neutral buoyancy condition to be achieved at slightly lower helium flow rates. It is therefore suggested to introduce a correction to the theoretical density curve (eq. (5.2)) to account for the violation of soap mass conservation:

$$\rho_p = \rho_{He} + K\frac{Q_{BFS}}{Q_{He}}\rho_{BFS}, \qquad K = 900\frac{(\rho_{air} - \rho_{He})}{\rho_{BFS}}, \tag{5.5}$$

where $\rho_p = \rho_{air}$, when $Q_{He}/Q_{BFS} = 900$. The factor $K \cong 0.84$ is interpreted as a correction for the soap that does not end up into bubbles, but is discarded via tiny droplets naturally occurring during bubble production.

5.6 HFSB time response

According to eq. (5.2) and (5.3), the HFSB time response should vary linearly with Q_{BFS}/Q_{He}. This assumption is verified in figure 5-5. The Pearson correlation coefficient $r_{x,y} = cov(x,y)/\sigma_x\sigma_y$, where $cov(x,y)$ is the covariance and σ the standard deviation, shows a linear correlation

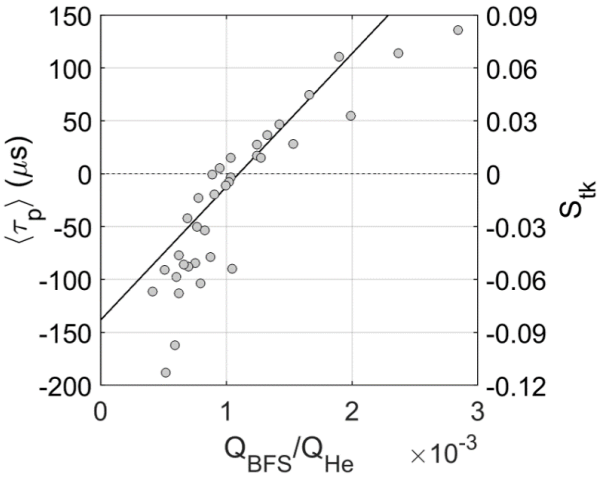

Figure 5-5. HFSB time response as a function of helium and soap flow rates, measured using the NLR generator. Linear fit of $\langle\tau_p\rangle$ is enforced to include the neutrally buoyant condition τ_p $(Q_{He}/Q_{BFS} = 900) = 0$, emphasizing the deviation from the predicted linear relation between τ_p and $\bar{\rho}$ given by eq. (5.3).

of 0.88. Deviations from a linear dependence are observed especially for large $\langle \tau_p \rangle$. Particles with longer relaxation times result in larger particle Reynolds numbers. Consequently, the correction factor $\phi(Re_p)$ becomes more significant, affecting the linearity between τ_p and $\bar{\rho}$. This is a consequence of $\phi(Re_p)$ increasing with $|u_{slip}|$, which, per se, increases with τ_p. Furthermore, variations in the particle diameter contributes significantly to the observed scatter in figure 5-5 and the large negative τ_p values ($d_p \sim \sqrt[3]{Q_{air}/Q_{he}}$, affecting τ_p).

The relation between particle time response and diameter, which have been simultaneously measured, is shown for different HFSB densities (figure 5-6). To avoid biasing the results, instead of using the density values that were estimated from eq. (5.3), which would enforce τ_p to be proportional to $\bar{\rho}$, the density is estimated from eq. (5.5). As reference, theoretical curves of time response τ_t obtained from eq. (5.3) are included for fixed density values. In the theoretical curves, $\phi(Re_p)$ is

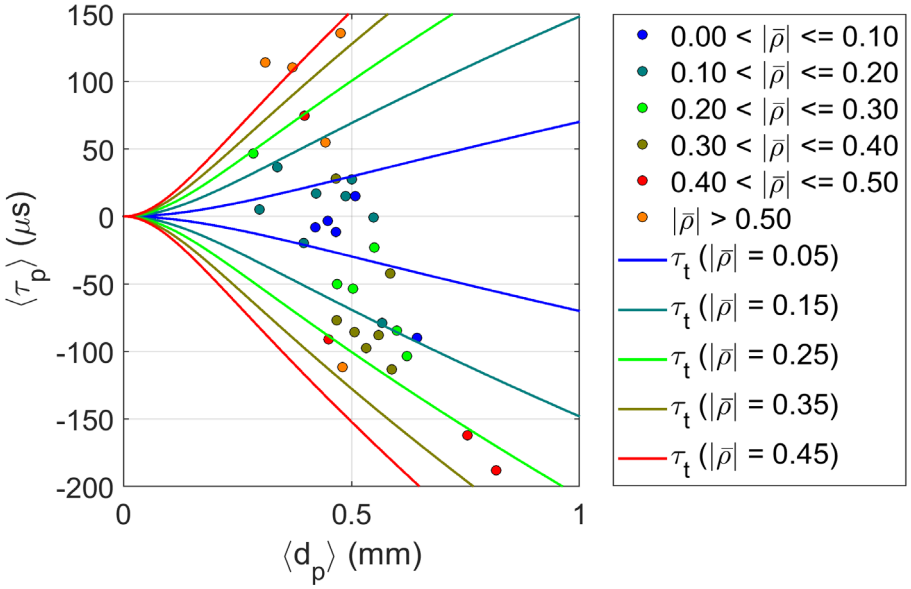

Figure 5-6. HFSB time response in relation to bubble diameter.

estimated by assuming $u_{slip} \approx a_p \tau_p$. A constant particle deceleration of 7000 m/s² is assumed for this purpose. It is noted that $\phi(Re_p) = 1 + 0.15 Re_p^{0.687}$ influences the dependence of τ_p on d_p, showing an approximately linear relation for $d_p > 0.1$ mm. From eq. (5.3), one can see that if $Re_p \ll 15$, then $\phi \approx 1$ and $\tau_p \sim d_p^2$. Instead, if $Re_p \gg 15$, then $\phi \approx 0.15 Re_p^{0.687}$ and $\tau_p \sim d_p^{0.8}$ (assuming $u_{slip} \approx a_p \tau_p$). For instance, if a_p = 7000 m/s², d_p = 0.5 mm, τ_p = 100 μs and ν = 15 mm²/s (air at NTP), then Re_p = 23. It is not surprising, therefore, that the curves become approximately linear as the time response increases in figure 5-6. In addition, note that the theoretical curves are in general larger than the measured values. This is most likely due to the assumption of equal acceleration between the particle and the fluid, which implicitly neglect the unsteady forces.

5.7 Time response and diameter dispersion

The measurements of HFSB time response and diameter (from the glare points distance) are compared to visualizations of the HFSB production regimes (chapter 4), at the same volume flow rates, for analysis of the relation between size and time response dispersions and the regime of production. For this evaluation the diameter coefficient of variation is introduced:

$$CV_d = \frac{\sigma_d}{\langle d_p \rangle}, \tag{5.6}$$

where σ_d and $\langle d_p \rangle$ are, the standard deviation and average of the HFSB diameter, respectively.

The diameter coefficient of variation CV_d is analysed from the PIV measurements, performed for 35 combinations of Q_{air}, Q_{He} and Q_{BFS}, is shown in figure 5-7. In comparison to the shadow visualization technique, the latter method does not suffer from nozzle exit effects and a larger number of images were recorded, leading to a better convergence

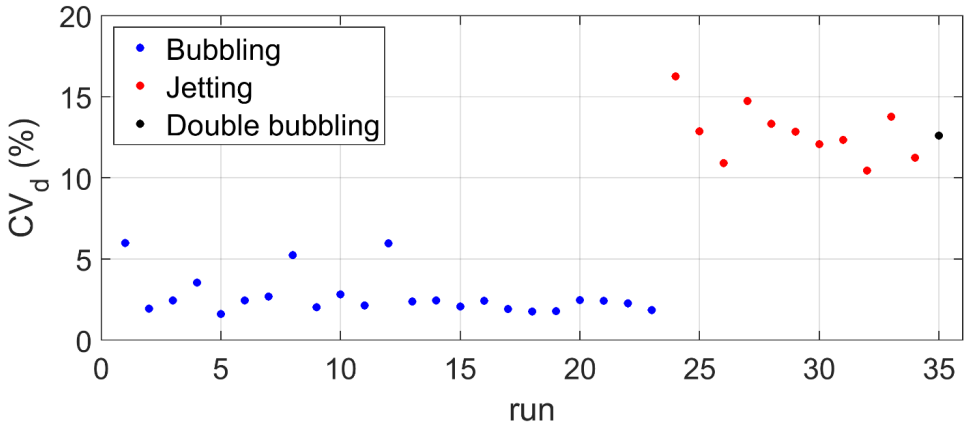

Figure 5-7. Variance coefficient of HFSB diameter. Volume flow rates of air (65 - 160 l/h), helium (4 – 21 l/h) and soap (3.5 - 11 ml/h) were tested.

of σ_d. Through comparison with the shadow visualizations, it is inferred that the bubble generator was operating in the bubbling regime for 23 cases, in the jetting regime for 11 cases, and in double-bubbling for one condition. When working in the bubbling regime small variations of bubble diameter were observed, with CV_d between 2% and 3%, with exception of three cases of low helium volume flow rates ($Q_{He} = 3.5\ l/h$), in which it was approximately 6%. In the jetting or double bubbling regime, CV_d was about 13%. The consistency of the results confirms quantitatively the dependency of the HFSB diameter dispersion on the production regime.

For the particle time response the variance is shown in dimensional units as the coefficient of variation loses significance when τ_p approaches zero. The relation of σ_τ with bubble size and density (through the ratio Q_{BFS}/Q_{He}) is shown in figure 5-8. The time response standard deviation σ_τ seems uncorrelated with Q_{BFS}/Q_{He} and d_p. The τ_p fluctuations appear to be in the order of 40 μs irrespective of bubble size. Furthermore, no clear difference in the time response dispersion is observed between bubbles produced in either bubbling or jetting regimes.

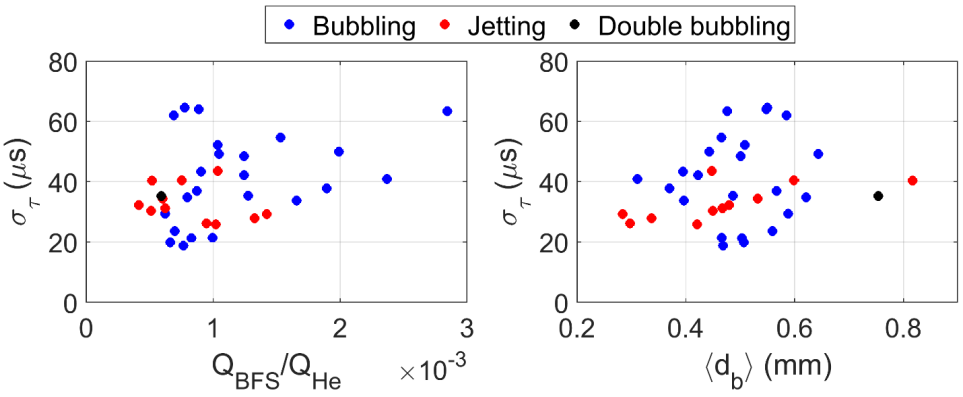

Figure 5-8. Standard deviation of HFSB time response.

In conclusion, neither the mean bubble size, nor the mean density (represented by Q_{BFS}/Q_{He}), nor the dispersion of the bubble size influences significantly the fluctuations of time response. It is hypothesized that the observed dispersion of the time response is mainly a result of variations of the soap film thickness, leading to variations of bubble density.

Additionally, the streamwise velocity fluctuation u'_{rms} measured with our reference DEHS was of 0.1 m/s. In a flow of 7,000 m/s² deceleration, this implies that even a population of ideal tracers would exhibit a minimum σ_τ of 15 μs.

5.8 Conclusions

The neutral buoyancy condition, which guarantees that HFSB behave as an ideal flow tracer, can be met setting the helium and soap flow rates. Although a theoretical prediction yields $Q_{He}/Q_{BFS} \cong$ 1,080, it is found from experiments that the condition closest to neutral buoyancy is achieved when Q_{He}/Q_{BFS} = 900 $\pm$ 50. This indicates that a fraction of soap is spilled off in form of droplets in the real process.

The HFSB time response was quantified in the laminar steady flow in front of a cylinder of 50 mm diameter (U_∞ = 30 m/s). This was found to be about 10 to 20 µs when the bubble density is within 10% of the

density of the surrounding air. For differences in the range of 10% to 20%, the time response is within 20 and 50 μs. The time response dependency of nearly-neutrally-buoyant bubbles with the bubble diameter was shown to change from $\tau_p \sim d_p^2$ to approximately $\tau_p \sim d_p$ as the particle slip velocity increases. The particle time response only scales with d_p^2 when $Re_p \ll 15$.

The production of HFSB in the bubbling regime results in the lowest variation of bubble size with a variance coefficient of bubble diameter CV_d as small as 3%. In the jetting regime the generation of bubbles is more chaotic and the bubble size distribution is polydisperse with a typical CV_d of 13%.

The time response dispersion σ_τ was quantified to be approximately 40 μs. The dispersion of the time response was found to be uncorrelated with bubble size, production regime and mean bubble density. It is hypothesized, therefore, that the time response dispersion results from variations of the bubble film thickness (dispersion of bubble density).

6

SLIP VELOCITY MODELLING

The slip velocity of nearly-neutrally-buoyant bubbles around objects is studied in this chapter, numerically and experimentally. The material presented is under review for publication in Experiments in Fluids (*The slip velocity of nearly-neutrally-buoyant tracers for large-scale PIV*, Faleiros et al. 2021).

6.1 Introduction

Kerho & Bragg (1994) were the first to attempt to characterize the tracing fidelity of HFSB for aerodynamic experiments, measuring the slip velocity along bubble trajectories in the flow around an airfoil. Errors of up to 10% of U_∞ were ascribed to a bubble generation process biased towards lighter-than-air particles. Scarano et al. (2015) have shown that accurate results may be obtained by properly controlling the soap and helium flow rates. They measured the HFSB time response in the stagnation region of a cylinder (section 3.5.2), obtaining a mean time response of approximately 10 μs. Following the same methodology, the HFSB tracing fidelity has been assessed by many authors (Morias et al. 2016; Gibeau & Ghaemi 2018; Gibeau et al. 2020), including the present author (Faleiros et al. 2019), as discussed in chapter 5.

In most PIV experiments it is desirable to know the expected particle slip velocity for estimating the measurement uncertainty. Although the method devised by Scarano et al. (2015) is adequate for time response estimation, when the particle acceleration does not depart significantly

from that of the surrounding fluid, this assumption does not hold for most practical situations. For instance, in the work of Morias et al. (2016), when a 30% heavier-than-air HFSB approaches the cylinder stagnation point (within 10% of the cylinder diameter from the leading edge), the mean particle deceleration is up to twice as large as that of the air flow. The HFSB slip velocity has not been investigated when the particle acceleration deviates considerably from that of the flow.

In this chapter, a generalized model for obtaining the slip velocity around objects is provided, covering the particle-flow parameter space that is typical of large-scale PIV experiments conducted with HFSB. The approach expands from simple predictions of HFSB flow tracing accuracy based on the Stokes regime, or other similar simplifications that neglect the unsteady forces, towards a model that incorporates the latter and allow for large acceleration differences.

The analysis of the motion of nearly-neutrally-buoyant particles is performed through numerical simulations using the full equation of motion (3.8). First, the analysis is performed in a rectilinear oscillatory flow, followed by simulations around an airfoil, with focus on the high-acceleration region in the vicinity of the leading edge. Although the slip velocity can be promptly calculated by realizing a numerical simulation, similar to that carried out in this chapter, the intention here is to enable the assessment and prediction of experimental velocity errors without the need of time-consuming computations.

The potential of the proposed model to assess HFSB slip velocity is demonstrated via application to experimental data. A set of experiments are conducted in a large-scale aerodynamic wind tunnel at high Reynolds numbers, under similar conditions than the simulations. The method allows for estimation of the mean and fluctuations of the HFSB density from the measured slip velocity, helping to identify the source of velocity errors. DEHS is used for obtaining a reference flow field.

In addition, the slip velocity distribution dependency on the HFSB density dispersion, as proposed in section 5.7 for the cause of the measured time response dispersion, is also investigated, based on simulations and experiments. The slip velocity dispersion induce errors in the 2nd moments of velocity, which can lead to incorrect measurements of turbulent stresses.

6.2 Background

6.2.1 Normalization of the equation of particle motion

The study of nearly-neutrally-buoyant bubbles requires considering the full equation of spherical particle motion (3.8), given in section 3.4. In the study of aerodynamic flows, normalization of the equation of particle motion is usually based on a chosen characteristic velocity U_0 and length L_0, with the reference timescale being derived from the latter. For instance, in airfoil flows the free stream velocity and the airfoil chord (or airfoil thickness) are typical choices. Such normalization is convenient in eq. (3.14) for the study of heavy microparticles, as it results in a single non-dimensional parameter, the Stokes number S_k. Normalization of eq. (3.8) based on U_0 and L_0 leads, however, to three non-dimensional parameters, S_k, $\hat{\rho}$ and Re_p, increasing the complexity of the particle tracing fidelity analysis. Alternatively, eq. (3.8) may be normalized based on a chosen reference velocity U_0 and the viscous timescale $t_0 \equiv d_p^2/\nu$. Neglecting the buoyancy force it is given as:

$$\hat{\rho}\frac{d\vec{\hat{u}}_p}{d\hat{t}} = \overbrace{\frac{D\vec{\hat{u}}}{D\hat{t}}}^{\substack{Undist.fluid\\ stresses}} + \overbrace{\frac{1}{2}\left(\frac{D\vec{\hat{u}}}{D\hat{t}} - \frac{d\vec{\hat{u}}_p}{d\hat{t}}\right)}^{\substack{Added-mass\\ force}} - \overbrace{18\phi\left(Re_p\right)\vec{\hat{u}}_{slip}}^{Quasi-steady\ Drag} - \overbrace{18\int_{\hat{t}^-}^{\hat{t}} K(\hat{t}-\hat{\tau})\frac{d\vec{\hat{u}}_{slip}}{d\hat{\tau}}d\hat{\tau}}^{History\ force}, \quad (6.1)$$

where the history force kernel may be calculated using the approximation (Mei 1994):

$$K(\hat{t}-\hat{\tau}) \approx \left\{[4\pi(\hat{t}-\hat{\tau})]^{\frac{1}{4}} + \left[\frac{\pi(\hat{t}-\hat{\tau})^2 Re_p^3}{\left(0.75+0.105Re_p\right)^3}\right]^{\frac{1}{2}}\right\}^{-2}, \quad (6.2)$$

with Re_p evaluated at $\hat{t}-\hat{\tau}$. Rigorously, the lower limit of integration of the history force is -∞. For simulation purposes, t^- is the instant right before the particle is introduced into the flow. Notice that $\hat{\rho}$ and Re_p are the only non-dimensional parameters in equations (6.1) and (6.2). Furthermore, although Re_p represents the actual particle Reynolds number, often it is desirable to specify a reference Reynolds number that is independent of the slip velocity. For this purpose, a diameter based Reynolds Number $Re_d \equiv U_0 d_p/\nu$ is defined, such that $Re_p = Re_d\left|\vec{\hat{u}}_{slip}\right|$.

6.2.2 The slip velocity in an oscillating flow field

It is instructive to first consider the case of a spherical particle immersed in a rectilinear oscillating flow field. The respective velocities are given by $u_p(t) = \tilde{u}_p(\omega)e^{-i\omega t}$ and $u(t) = \tilde{u}(\omega)e^{-i\omega t}$, where $\tilde{u}_p(\omega)$

and $\tilde{u}(\omega)$ are the particle and flow amplitudes of the oscillation, and $\omega = 2\pi f$ is the angular frequency.

For the sake of the discussion, eq. (3.8) is studied under different assumptions. Notice, however, that in the numerical simulations presented in section 6.3, eq. (6.1) is used in its complete form, as presented. Neglecting buoyancy, added-mass and history forces, and assuming $\phi(Re_p) = 1$, which is acceptable for low Re_p, eq. (3.8) becomes:

$$\hat{\rho}\frac{d\vec{u}_p}{dt} = \frac{D\vec{u}}{Dt} - \frac{18\nu}{d_p^2}\vec{u}_{slip}. \tag{6.3}$$

Substitution of the particle and flow oscillating velocity and acceleration in eq. (6.3) gives:

$$-i\omega\tilde{u}_p\hat{\rho} + \frac{18\nu}{d_p^2}\tilde{u}_p = -i\omega\tilde{u} + \frac{18\nu}{d_p^2}\tilde{u}. \tag{6.4}$$

From eq. (6.4), the particle tracing fidelity can be analysed from the ratio of the slip velocity to the flow velocity amplitudes:

$$u_R \equiv \frac{(\tilde{u}_p - \tilde{u})}{\tilde{u}}, \qquad u_R(\omega, \tau_p, \hat{\rho}) = \frac{i(\hat{\rho}-1)\omega\frac{d_p^2}{18\nu}}{1 - i\omega\frac{\hat{\rho}d_p^2}{18\nu}}. \tag{6.5}$$

Following Mei (1996), $u_R(\omega, \tau_p, \hat{\rho})$ may be rewritten as a function of $\hat{\rho}$ and ϵ only,

$$u_R(\epsilon, \hat{\rho}) = \frac{i\frac{4}{9}(\hat{\rho}-1)\epsilon^2}{1 - i\frac{4}{9}\hat{\rho}\epsilon^2}, \tag{6.6}$$

where ϵ is a non-dimensional parameter with similar significance to the Stokes number:

$$\epsilon \equiv \sqrt{\frac{\omega d_p^2}{8\nu}}. \tag{6.7}$$

It can also be easily verified that if the added-mass had been included in eq. (6.3), then the amplitude ratio becomes:

$$u_R(\epsilon, \hat{\rho}) = \frac{i\frac{4}{9}(\hat{\rho} - 1)\epsilon^2}{1 - i\frac{4}{9}\left(\hat{\rho} + \frac{1}{2}\right)\epsilon^2}. \tag{6.8}$$

Lastly, the analysis can be expanded by considering an approximation to the history force in the oscillating flow field for $\epsilon \gg 1$ (Mei 1996):

$$\frac{18\nu}{d_p^2}\int_{t^{-1}}^{t} K(t-\tau)\frac{d\left(\vec{u} - \vec{u}_p\right)}{d\tau}d\tau \approx \frac{18\nu}{d_p^2}\epsilon(1-i)\left(\tilde{u} - \tilde{u}_p\right)e^{-i\omega t}. \tag{6.9}$$

Including added-mass and history force, the amplitude ratio becomes:

$$u_R(\epsilon, \hat{\rho}) = \frac{i\frac{4}{9}(\hat{\rho} - 1)\epsilon^2}{1 - i\frac{4}{9}\left(\hat{\rho} + \frac{1}{2}\right)\epsilon^2 + \epsilon(1-i)}, \tag{6.10}$$

where the history force is represented by the term $\epsilon(1-i)$.

For the purpose of illustration, the tracing behaviour is modelled on the basis of eq. (6.6), which neglects both added-mass and history forces, and eq. (6.10), in which both forces are included. Figure 6-1 shows the flow instantaneous velocity as a sinusoid of unit amplitude, at a frequency f = 100 Hz, flow kinematic viscosity of air at NTP, i.e. ν = 15 mm²/s, and tracer particle diameter d_p = 0.5 mm. Lighter and heavier-

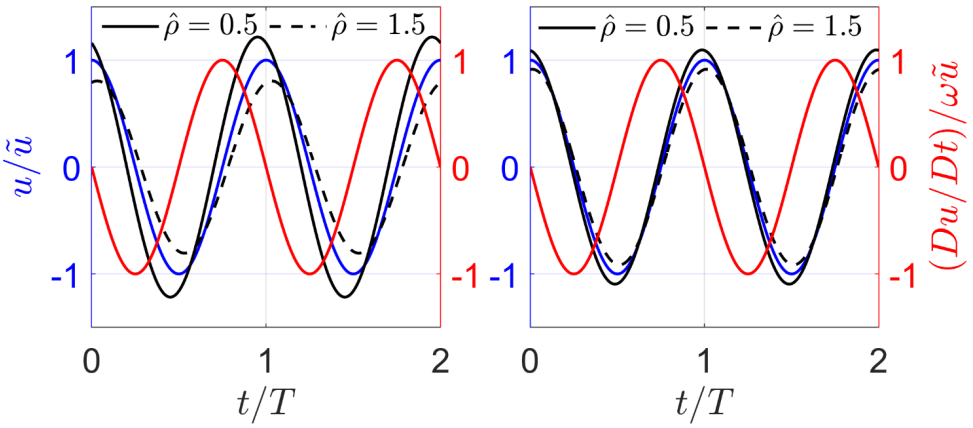

Figure 6-1. Instantaneous velocity of a particle in an oscillating flow field. Left: Eq. (6.6), neglecting added-mass and history-force. Right: Eq.(6.10), including added-mass and Mei's approximation to the history-force for $\epsilon \gg 1$. Fluid velocity: solid blue line, left axis. Acceleration: solid red line, right axis.

than-air particles are considered, with $\hat{\rho}$ = 0.5 and $\hat{\rho}$ = 1.5, respectively. The chosen parameters for the particle and flow conditions are representative of aerodynamic experiments using HFSB, although the density ratio is somehow accentuated to make clear the trend of the particle behaviour.

The particle motion modelled by eq. (6.6) (figure 6-1, left) exhibits a positive phase lag and some degree of amplitude modulation for the heavier-than-air conditions. In the lighter-than-air case, the situation is reversed: the amplitude of velocity oscillations of the particle tracers exceeds that of the flow and a negative phase lag is observed. These observations are in accordance with numerical simulations performed by Müller et al. (2001). The situation remains qualitatively unaltered when the particle motion is modelled by eq. (6.10), including the added-mass and history force term (figure 6-1, right). However, a notable reduction of the discrepancy between the particle and the fluid motion is observed. The amplitude difference and phase lag reduce to approximately half of the previous case for both heavier- and lighter-than-air particles. This is

because the added-mass and history forces are proportional to the slip acceleration and act as restoring forces, reducing the acceleration difference, and resulting in a higher tracing fidelity.

Analysis of the spectral behaviour of the modelled particle motion and the differences arising from the different terms considered in the physical interaction between the fluid flow and the particle gives an overview of the role of the unsteady forces. For this purpose, the normalized slip velocity amplitudes given by equations (6.6), (6.8) and (6.10) are represented in figure 6-2, spanning a considerable range of frequencies for the flow oscillations, represented by the non-dimensional parameter ϵ. In general, including the added-mass force as well as the history force results in reduced slip velocities for all $\hat{\rho}$ and $\epsilon > 1$.

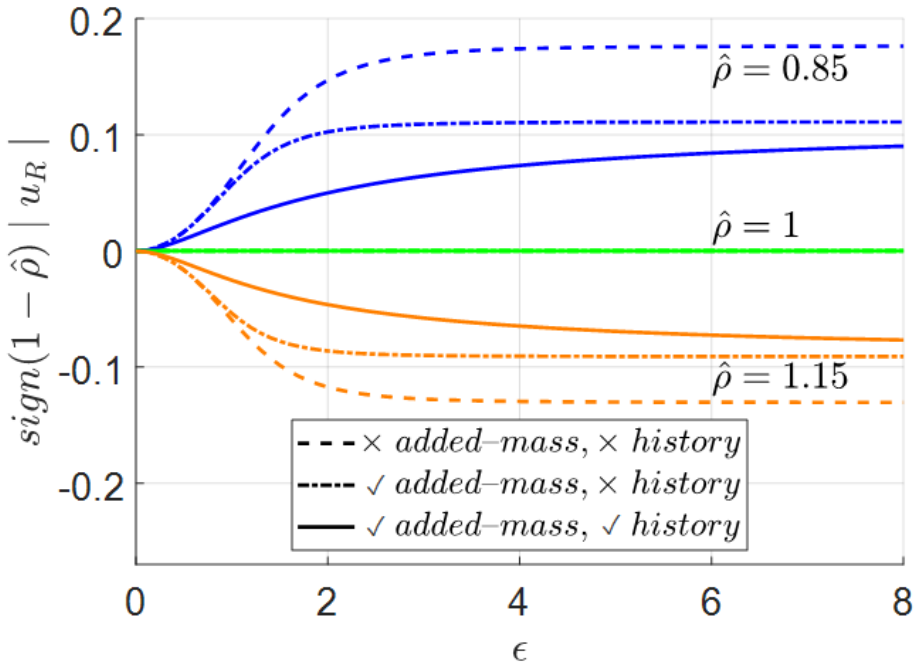

Figure 6-2. Slip velocity amplitude modulation modelled by equations (6.6), (6.8) and (6.10). The absolute value $|u_R|$ is multiplied by $sign(1-\hat{\rho})$ for clarity of visualization. Lighter-than-air particles: positive side of the vertical axis. Heavier-than-air particles: negative side.

Furthermore, note that the slip velocity amplitude of nearly-neutrally-buoyant particles converges to a finite value for large ϵ. This is because at high oscillation frequencies, the acceleration-driven terms are dominant, as $|du/dt|/|u| = \omega$. Therefore, at high-frequencies, the Stokes' drag force, being slip-velocity driven, becomes negligible in comparison to the other forces. When added-mass and history-force are neglected, it is found from eq. (6.6) that when $\epsilon \to \infty$, $|u_R| \to (1-\hat{\rho})/\hat{\rho}$. Additionally, if the added-mass term is included, then $|u_R| \to (1-\hat{\rho})/(\hat{\rho}+\frac{1}{2})$. In fact, this is true for both eq. (6.8) and (6.10). The history force scales with ϵ, while the other forces scale with ϵ^2. Therefore, as ϵ tends to infinity, the influence of the history force on $|u_R|$ becomes negligible. The latter cannot be observed in figure 6-2 due to the short range of ϵ that is plotted.

This analysis shows the importance of including the unsteady forces in the study of nearly-neutrally-buoyant particle motion. Estimates of tracing fidelity based only on Stokes' drag become increasingly conservative as the frequency of the flow fluctuation increases, yielding overestimated predictions of the slip velocity. In addition, the estimates from eq. (6.10) should also be considered conservative due to the assumption of $\phi(Re_p) = 1$. The slip velocity is further reduced when drag correction is considered.

6.3 The slip velocity: from sinusoids to the flow around an airfoil

In the case of a particle moving around an object, the analysis of the slip velocity becomes geometry dependent. It is possible to deal with such problem taking into account the geometry, but the analysis becomes case-specific. The problem can be generalized by making an analogy between the velocity modulation of a particle along its trajectory and that occurring in a sinusoidal flow. Particle trajectories represent finite oscillations that can be approximated by a sinusoid of defined amplitude

and frequency, within a finite time interval. This can be visualized in figure 6-3 for the flow around a cylinder. As the particle moves around the object, the streamwise component of velocity oscillates from a minimum value upstream, to a maximum on top of the cylinder, returning to the same minimum value downstream. In addition, the transverse component fluctuates in a similar fashion, but out of phase, that is, the transverse component is maximum/minimum while the streamwise component is zero, and vice versa.

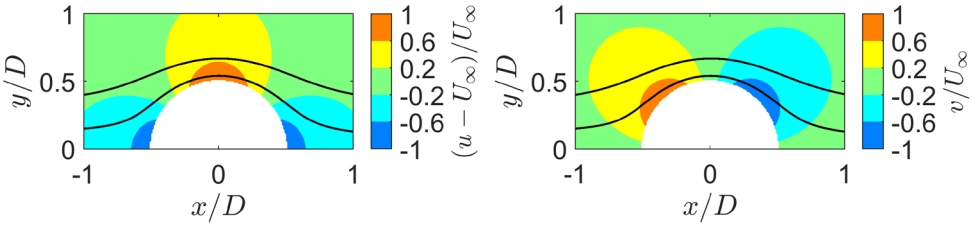

Figure 6-3. Flow streamlines around a cylinder. The cylinder diameter D is used for normalization.

Since the two components of velocity are orthogonally out of phase, the dynamics experienced by a particle traveling around an object are analogous to that in a complex sinusoid flow. The streamwise and transverse components of velocity can be thought of as the "real" and "imaginary" parts of the flow. Following this analogy, the angular frequency may be obtained locally through the ratio of the absolute values of acceleration and velocity. Thus, a local frequency f and phase β are defined as:

$$f = \left|\frac{D\vec{u}}{dt}\right| / 2\pi\tilde{u}, \qquad \beta = atan\frac{v}{u - U_\infty}, \tag{6.11}$$

where $\tilde{u} = \sqrt{(u - U_\infty)^2 + v^2}$ is the amplitude of this oscillation. The free stream velocity is subtracted from the velocity components, to ensure that the velocity oscillates around zero.

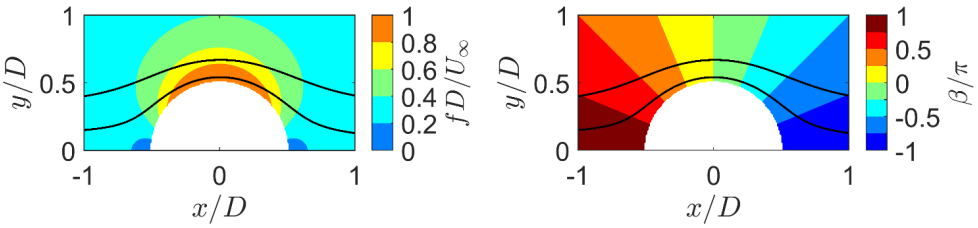

Figure 6-4. Frequency (left) and phase (right) obtained from eq. (6.11).

The flow frequency and phase for the cylinder flow above are shown in figure 6-4. The approximation proposed is most adequate in the region $-\pi/2 < \beta < \pi/2$, where the frequency along a streamline remains approximately constant, as is the cases for a complex sinusoid.

Following the definition above, the slip velocity components are written as:

$$\vec{u}_{slip} = u_{slip}\vec{e}_x + v_{slip}\vec{e}_y,$$
$$u_{slip} = \tilde{u}_p \cos\beta_p - \tilde{u}\cos\beta\,, \qquad v_{slip} = \tilde{u}_p \sin\beta_p - \tilde{u}\sin\beta. \tag{6.12}$$

The slip velocity is, therefore, dependent on the amplitude modulation $\tilde{u}_p/\tilde{u}$ and the phase shift $\beta_s = \beta_p - \beta$.

In summary, the idea set forth here is that, through the calculation of f and β in the flow around an object, easily determined, for instance, by a potential flow calculation, the slip velocity may be estimated from sinusoidal flow results at the same frequency and phase. The benefits of this approximation are demonstrated in the following section.

6.3.1 Numerical simulation set-up

In section 6.2.2, the importance of including the unsteady forces has been demonstrated. So far, however, the drag correction term $\phi(Re_p)$ was not considered and the history force was obtained through an approximation that is valid only for $\epsilon \gg 1$. In this section, the rectilinear oscillating flow field is numerically simulated using the full equation of motion (6.1), with the history-force kernel from (6.2) and $\phi(Re_p)$ from

$\hat{f}$	Re_d	$\hat{\rho}$
[0.05, 100]	[10, 1000]	{0.7, 0.8, 0.9, 0.95, 0.99,
[0.05, 2000]	[2000, 50,000]	1.01, 1.05, 1.1, 1.2, 1.3}

Table 6-1. Input parameters used in the simulations. The frequency range is wider for $Re_d \geq 2000$.

(3.11). The purpose is to obtain empirical relations for assessing the slip velocity of HFSB tracers, depending on $\hat{\rho}$, $\hat{f} = f d_p^2/\nu$ and the Reynolds number based on the particle diameter $Re_d = d_p U_0/\nu$. The latter is more suitable for this task than Re_p, as it does not depend on the slip velocity. Notice that $Re_p = Re_d|\hat{u}_{slip}|$.

The simulations input parameters (table 6-1) include a wide range of applications. For slip velocities from 0.1 to 10% of the reference velocity (wave amplitude), the particle Reynolds number Re_p varies from the Stokes regime ($Re_p = 0.01$) to regions extending that expected for HSFB in subsonic aerodynamics ($Re_p = 5000$). The frequency range is selected such that the asymptotic convergence of the velocity amplitude becomes apparent (see figure 6-2). This occurs at higher frequencies as Re_d increases. The density range covers $\pm$30% density deviations from neutrally buoyant particles, including particles of small density differences, down to 1%, allowing the empirical fits to better capture the particle behaviour near neutral buoyancy.

Neglecting gravity force, and rearranging the terms, eq. (6.1) may be rewritten for a 1D-flow as:

$$C\frac{d\hat{u}_p}{d\hat{t}} + \hat{u}_p = \hat{u} + \hat{a},$$
$$\hat{a} = \frac{1}{\phi}\left(\frac{1}{12}\frac{D\hat{u}}{D\hat{t}} - \int_{\hat{t}-}^{\hat{t}} K(\hat{t}-\hat{\tau})\frac{d\hat{u}_{slip}}{d\hat{\tau}}d\hat{\tau}\right), \qquad C = \frac{2\hat{\rho}+1}{36\phi}, \tag{6.13}$$

where $\hat{u} = e^{-i\hat{\omega}\hat{t}}$. The terms C and $\hat{a}$ are introduced for integration purposes only. The reference velocity U_0 is the wave amplitude, and the

reference time is $t_0 = d_p^2/\nu$. Multiplying equation (6.13) by $\exp(\hat{t}/C)$ and integrating it once yields $\hat{u}_p^{n+1}$, while integrating it twice yields the normalized particle position at $\hat{x}_p^{n+1}$:

$$\begin{aligned} \hat{u}_p^{n+1} &= \hat{u}_p^n e^{-\Delta\hat{t}/C} + (\hat{u}^n + \hat{a}^n)\left(1 - e^{-\Delta\hat{t}/C}\right), \\ \hat{x}_p^{n+1} &= \hat{x}_p^n + \Delta\hat{t}(\hat{u}^n + \hat{a}^n) + C\left(1 - e^{-\Delta\hat{t}/C}\right)\left(\hat{u}_p^n - \hat{u}^n - \hat{a}^n\right), \end{aligned} \tag{6.14}$$

where the initial conditions of the integration are:

$$\hat{x}_p(\hat{t} - \Delta\hat{t}) = \hat{x}_p^n, \qquad \hat{u}_p(\hat{t} - \Delta\hat{t}) = \hat{u}_p^n. \tag{6.15}$$

The simulation is performed until the particle dynamics reach steady conditions. This is achieved when the slip velocity and the phase shift vary less than 0.1% for the duration of half a cycle.

6.3.2 Velocity amplitude modulation and phase shift

Curve fits are applied to the results of the simulation, aiming to provide a simple relation for the velocity amplitude modulation $\tilde{u}_p/\tilde{u}$ and phase shift β_s, and, consequently, the slip velocity from eq. (6.12), as a function of $\hat{\rho}$, Re_d and $\hat{f}$. The amplitude modulation is found to be well described by the following relation:

$$\frac{\tilde{u}_p}{\tilde{u}} = 1 + \left(\frac{1}{\hat{\rho}} - 1\right)\frac{(0.0365|\hat{\rho} - 1|Re_d^{0.25} + 0.56\sqrt{\hat{\rho}})\hat{f}}{0.0163\left|\frac{1}{\hat{\rho}} - 1\right| Re_d - 5\hat{\rho} + 10 + \hat{f}}. \tag{6.16}$$

Although not valid in all limits, this expression does match a few important expectations: no amplitude modulation is observed for neutrally buoyant particles ($\hat{\rho} = 1$) or in the case of zero oscillation ($\hat{f} = 0$), i.e. $\tilde{u}_p/\tilde{u} = 1$ in both cases. Furthermore, similarly to the slip velocity estimations given in section 6.2.2, as $\hat{f} \to \infty$, the amplitude modulation converges to a finite value:

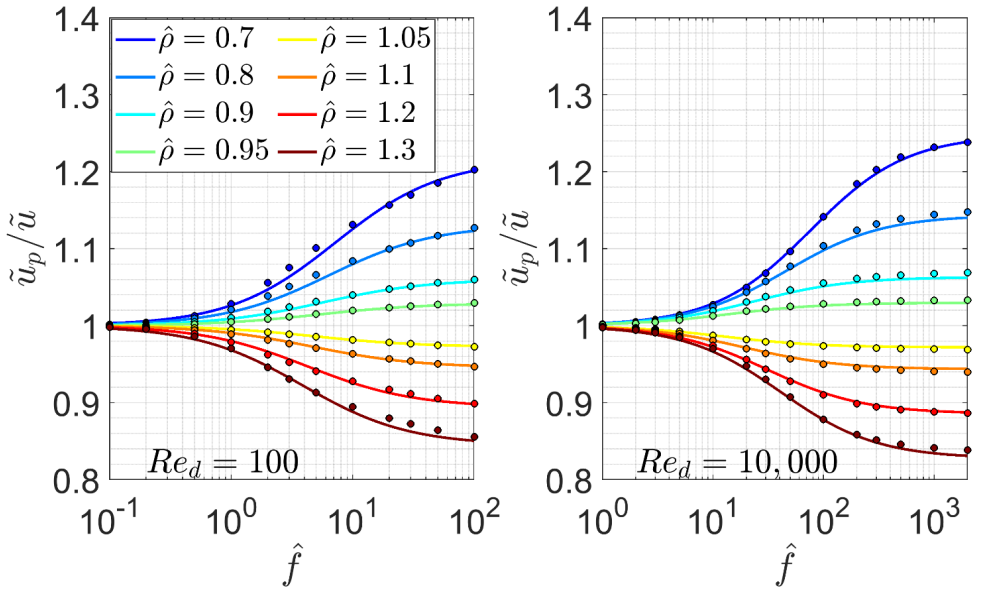

Figure 6-5. Visual demonstration of the accuracy of the estimated amplitude modulation (solid lines), given by empirical relation of eq. (6.16). Markers represent simulated data points.

$$\lim_{\hat{f}\to\infty} \frac{\tilde{u}_p}{\tilde{u}} = 1 + (\hat{\rho}^{-1} - 1)\left(0.0365|\hat{\rho} - 1|Re_d^{0.25} + 0.56\sqrt{\hat{\rho}}\right). \quad (6.17)$$

The results of the simulations for $\tilde{u}_p/\tilde{u}$, including the curve fits given by eq. (6.16) are shown in figure 6-5. The visual agreement of the curve fits and the simulation data suggest that the proposed equation is accurate within the specified conditions (table 6-1). A quantitative measure of the goodness of fit is provided by the statistical coefficient of determination R^2:

$$R^2 \equiv 1 - (SS_{res}/SS_{tot}), \quad (6.18)$$

where the total (SS_{tot}) and residual (SS_{res}) sum of squares are defined as:

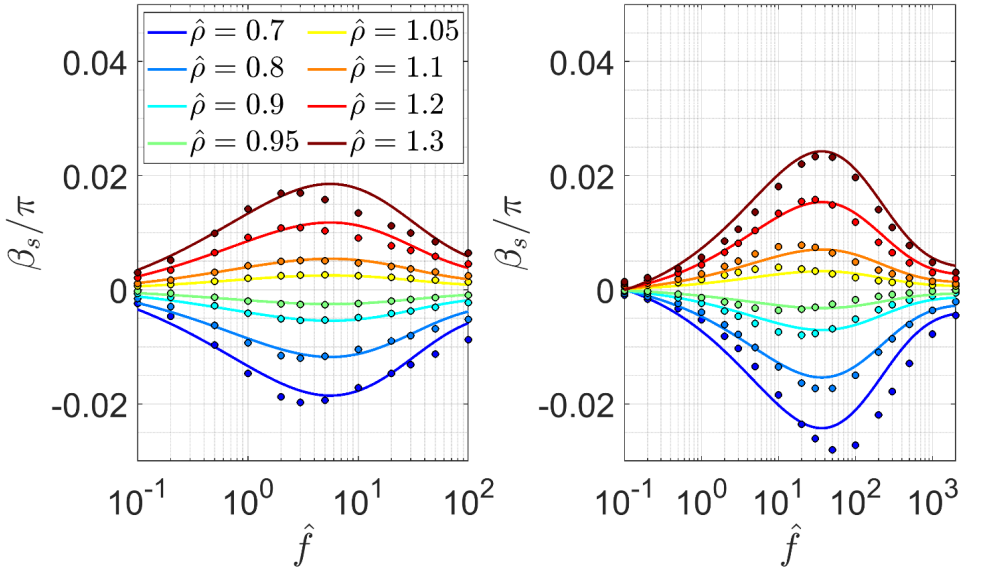

Figure 6-6. Visual demonstration of the accuracy of the estimated phase shift (solid lines), given by empirical relation of eq. (6.20). Markers represent simulated data points.

$$SS_{tot} \equiv \sum_i (z_i - \langle z \rangle)^2 , \qquad SS_{res} \equiv \sum_i (z_i - F_i)^2, \quad (6.19)$$

where z is the data being fitted, and F is the result given by the curve fit. In general, the results demonstrate an accurate prediction of the amplitude modulation with $R^2 > 0.98$.

The phase shift is more challenging to represent with a general empirical relation, and a less accurate fit is accepted to allow generalization (figure 6-6). The empirical relation obtained reads as:

$$\beta_s = (\hat{\rho} - 1)[0.04 - |\hat{\rho} - 1|^{0.15}(e^{(1.9Re_d^{0.035} - 2.9)\sqrt{\hat{f}}} - 0.9e^{-(1.356Re_d^{-0.055} - 0.7)\sqrt{\hat{f}}})]. \quad (6.20)$$

The expression used to estimate the phase shift becomes zero for a neutrally buoyant bubble, and, although it does not converge to proper limits for $\hat{f} \to 0$ or $\hat{f} \to \infty$, it matches the simulated data with reasonable accuracy within the tested range ($R^2 > 0.8$ for most cases).

6.3.3 The slip velocity around an airfoil leading edge

The approach outlined in the beginning of this section is tested by estimating the slip velocity around an airfoil leading edge with the empirical relations presented above. A numerical simulation is performed in the potential flow around an airfoil— a section of the outer wing of Fokker 100 aircraft (model 5-6 with retracted flap in Reinders W 1994)—at incidence α = 14°, obtained using XFOIL (Drela 1989). The same airfoil is used in the experiments of chapter 6.5. The particles are released three chords upstream of the airfoil's leading edge, along a transverse line within y/c = [-0.5, 0.15] at every 0.01c. Fifty particles are released per position, randomly distributed in space within a square of 0.01 c side centred at the reference points, for better resolving the spatial gradients. The particle initial velocity is assumed equal to that of the flow at release.

The Lagrangian simulations are performed for a 20% lighter-than-air bubble ($\hat{\rho} = 0.8$) of 0.5 mm diameter, an airfoil chord of 67.59 cm, $\nu = 15$ mm^2/s and $U_\infty = 70$ m/s, which, with exception of the particle density, simulates the same conditions as in the experiments presented in sections 6.5 and 6.6. The diameter and chord Reynolds numbers are, respectively, $Re_d = 2.3 \times 10^3$ and $Re_c = 3.2 \times 10^6$, where U_∞ is used as reference velocity.

The Lagrangian data is projected on a rectangular grid using square bins of 0.5% chord length. Within each bin, the scattered velocity is fitted using a quadratic function in both spatial coordinates, following the approach discussed in Agüera et al. (2016). The mean velocity is taken as the fitted value at the centre of the bin. For convenience (as it should become clear when other angles of attack are included in the experi-

mental part), the coordinate system in the Eulerian frame of reference is in airfoil coordinates, where x is the chordwise direction and y is the normal-to-chord direction.

The slip velocity obtained from the numerical simulation is shown in figure 6-7-a. In comparison, the slip velocity obtained from eq. (6.12), with $\tilde{u}_p$ and β_s obtained from eq. (6.16) and (6.20), is shown in figure 6-7-b. The close agreement between the approximation and the simulated data supports the validity of the approach. The approximation given in eq. (6.10) (figure 6-7-c), based on Mei's work, overestimates the slip velocity at higher frequencies, as the particle approaches the model surface. In addition, estimating the slip velocity from eq. (3.16), which requires negligible acceleration difference and neglects unsteady forces, leads to an overestimation of up to about 3000% of the simulated value (figure 6-7-d).

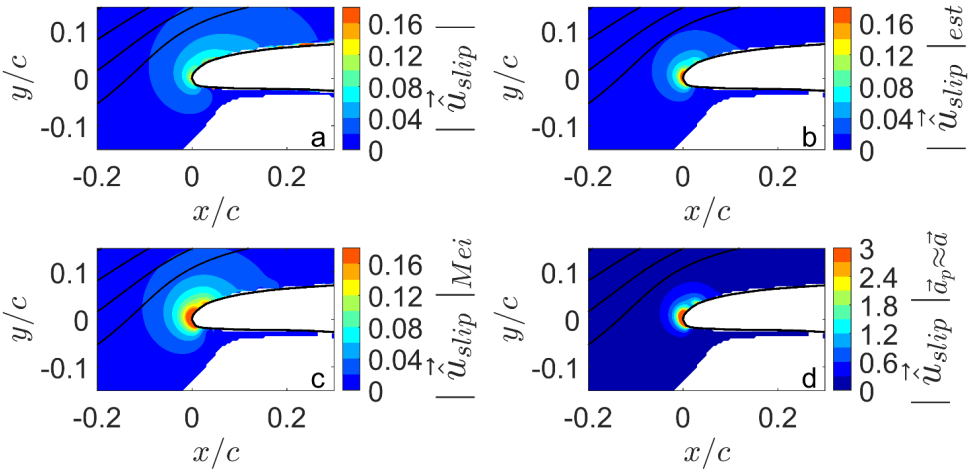

Figure 6-7. Comparison of slip velocity estimations with the numerical simulation results for a light particle ($\hat{\rho} = 0.8$) in the Eulerian frame of reference: a. Numerical simulation; b. Proposed approximation, eq. (6.12), (6.16) and (6.20); c. approximation (adapted) from Mei (1996) in a rectilinear oscillating flow, eq. (6.10) d. No-slip acceleration assumption, eq. (3.16). Notice that the colour scale is different in the latter case.

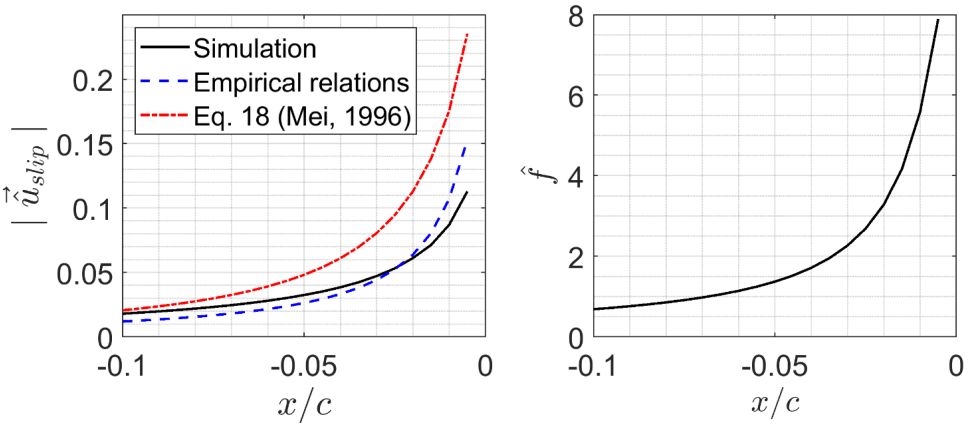

Figure 6-8. Left: Comparison of slip velocity estimates, given by empirical relations obtained in this study, eq. (6.12), (6.16) and (6.20), and from eq. (6.10), adapted from Mei (1996). Right: The increase of the normalized frequency as the particle approaches the model.

A closer comparison of the empirical estimations herein developed with Mei's work is performed along the line $y/c = 0$ in figure 6-8. The empirical expressions (6.16) and (6.20) give accurate estimations for $\hat{f} > 1$, being within 20% of the simulated value for $1 < \hat{f} < 5$. The errors from the estimations given by eq. (6.10) continuously increase as $\hat{f}$ increases, reaching about 100% of the actual $|\vec{\hat{u}}_{slip}|$ at $\hat{f} = 5$. This is most likely because eq. (6.10) does not account for drag corrections and, therefore, should become less accurate as Re_p increases.

6.3.4 Density estimation

Usually in a PIV experiment with HFSB, the bubble density is tuned using mass flow controllers set at appropriate flow rates that have been obtained through controlled experiments (Faleiros et al. 2019). However, it is good practice to verify this information during the measurements for an assessment of the errors. Hence, a procedure is defined to retrieve the bubbles' density from HFSB measurements for which a reference flow is available (e.g. DEHS measurements). The steps involved are outlined

below by considering numerical simulations of HFSB tracers of given density in a reference potential flow solution around an airfoil.

A least-square optimization is used to retrieve the particle density from the equations (6.12), (6.16) and (6.20) presented above, by estimating the slip velocity for several density values within $\hat{\rho} = [0.5, 1.5]$, and comparing with the numerical simulation for $\hat{\rho} = 0.8$. The best match with the simulated particle velocity is obtained by minimizing the sum of squares:

$$SS(|\vec{\hat{u}}_{slip}|) = \sum \left(|\vec{\hat{u}}_{slip}| - |\vec{\hat{u}}_{slip}|_{est}\right)^2, \qquad (6.21)$$

where the subscript *est* stands for estimated value. This procedure is applied within $fc/U_\infty > 3$ (figure 6-9, left) and $\pi/4 < \beta < \pi/2$ (figure 6-9, right), which is deemed well modelled by the proposed approximation.

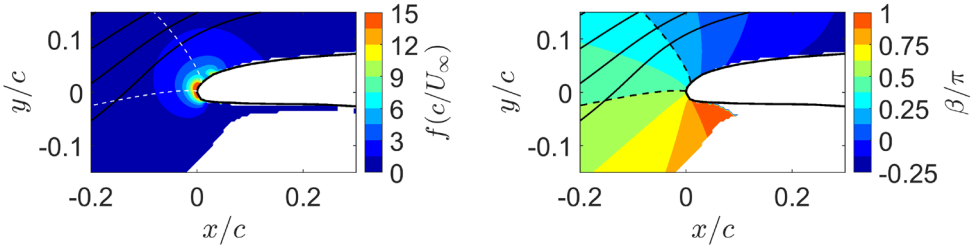

Figure 6-9. Flow frequency (left) and phase angle (right).

The $SS(|\vec{\hat{u}}_{slip}|)$ value has two local minimums (figure 6-10), one for $\hat{\rho} < 1$ and another for $\hat{\rho} > 1$. The correct local minimum is selected by considering the minimum sum of squares of the streamwise slip velocity, $SS(\hat{u}_{slip})$. Although the density estimate from the latter is less accurate than given by $SS(|\vec{\hat{u}}_{slip}|)$, it evidently distinguishes between lighter- and heavier-than-air particles. From the minimum $SS(\hat{u}_{slip})$, it is obtained that $\hat{\rho} < 1$. The local minimum $SS(|\vec{\hat{u}}_{slip}|)$ in the lighter-than-air part yields an estimated density ratio of $\hat{\rho}_{est} = 0.81$, accurate within 1.25%

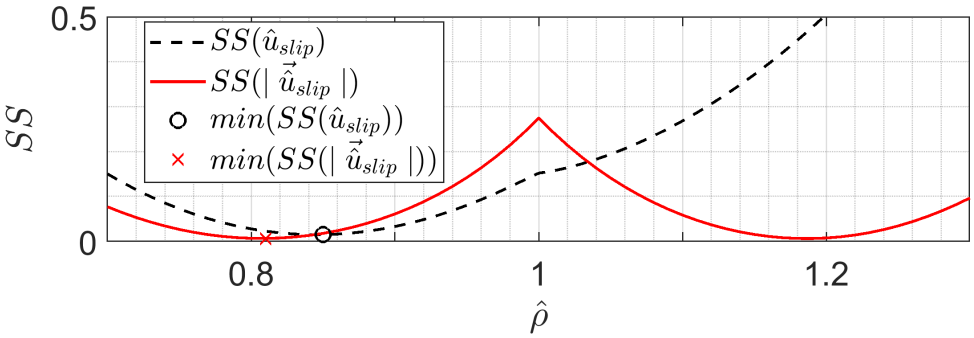

Figure 6-10. Sum of squares of the difference between the slip velocity from the simulation ($\hat{\rho} = 0.8$) and the estimated slip velocity for $\hat{\rho} = [0.5, 1.5]$. The local minimum of $SS(|\vec{\hat{u}}_{slip}|)$ for $\hat{\rho} < 1$ is found when $\hat{\rho}_{est} = 0.81$.

of the simulated value. This result indicates that this method can be used for relatively accurate estimation of particle density from measurements of the slip velocity.

6.4 Velocity fluctuations due to density dispersion

The consequences of HFSB slip velocity dispersion, which was experimentally quantified (Morias et al. 2016; Faleiros et al. 2019) through the standard deviation of τ_p^* (~40 μs), are herein considered.

6.4.1 Sources of time response dispersion

The two main particle parameters affecting the slip velocity are ρ_p and d_p, whose standard deviations σ_ρ and σ_d, respectively, are the main sources of dispersion. The generation of HFSB in the bubbling regime is crucial to guarantee low diameter dispersion. The coefficient of variation of the HFSB diameter $CV_d = \sigma_d/\langle d_p \rangle$ is 3% in the bubbling regime, but as large as 13% in the jetting regime (Faleiros et al. 2019). However, no correlation between diameter and time response dispersions has been observed, with measurements of σ_τ in both regimes being of the same order. This may be understood through Reynolds averaged decomposition of the time response as defined in eq. (3.16), assuming $\phi(Re_p)$~1

for simplicity without losing generality. Notice that the measurements reported by Morias et al. (2016) and Faleiros et al. (2019) have been performed in regions of low slip acceleration, validating this discussion. Neglecting second-order terms and assuming constant $\hat{\rho}$, it reads as:

$$\langle \tau_p^* \rangle + \tau_p^{*\prime} = \frac{(\hat{\rho}-1)\left(\langle d_p \rangle^2 + 2\langle d_p \rangle d_p'\right)}{18\nu}. \tag{6.22}$$

Subtracting $\langle \tau_p^* \rangle$ from both sides, the time response dispersion is given as:

$$\sigma_\tau = \sqrt{\langle \left(\tau_p^{*\prime}\right)^2 \rangle}, \qquad \sigma_\tau = \frac{(\hat{\rho}-1)\langle d_p \rangle^2}{9\nu} CV_d. \tag{6.23}$$

Therefore, for a neutrally buoyant bubble ($\hat{\rho} = 1$) the diameter dispersion does not affect the time response dispersion. In fact, the diameter dispersion only affects σ_τ if there is a substantial deviation from the neutral buoyancy condition. Even if the mean density of half-millimetre bubble deviates 10% from the fluid density, σ_τ would still be 5 μs in the bubbling regime. In the worst case scenario, where jetting regime is present, then $\hat{\rho} = 1.1$ results in $\sigma_\tau \approx 25$ μs. This supports the experimental observations that HFSB diameter dispersion is not the main drive causing time response dispersion.

Bubble density dispersion may occur independently of bubble size through variations of the soap film thickness. Direct measurements of HFSB density have not been performed so far, only indirectly through measurement of bubble size and time response (Morias et al. 2016; Faleiros et al. 2019). Assuming exclusive density dispersion, the Reynolds average decomposition yields:

$$\sigma_\tau = \frac{\langle \hat{\rho} \rangle d_p^2}{18\nu} CV_\rho, \tag{6.24}$$

where $CV_\rho = \sigma_\rho/\langle\rho_p\rangle$ is the density coefficient of variation. Thus, for a distribution of bubbles with a mean density equal to that of the flow, constant diameter $d_p = 0.5$ mm, and time response dispersion of σ_τ = 40 μs, the density coefficient of variation is $CV_\rho = 0.043$ (in air at NTP).

This effect may be translated to soap film thickness variation through mass conservation analysis (section 3.6). For a neutrally buoyant bubble of $d_p = 0.5$ mm, and for $\rho_{soap} = 1124$ kg/m³, the soap film thickness (eq. (3.18)) is on average 77 nm. Additionally, if the changes in thickness are exclusively responsible for the density dispersion, then the film thickness standard deviation σ_t, estimated as,

$$\sigma_t = t\big(\rho_p + \sigma_\rho\big) - t\big(\rho_p\big), \tag{6.25}$$

is about 4 nm for $CV_\rho = 0.043$, where $t\big(\rho_p\big)$ and $t\big(\rho_p + \sigma_\rho\big)$ are calculated from eq. (3.18). Therefore, a film-thickness coefficient of variation ($CV_t = \sigma_t/\langle t\rangle$) of only 5% is enough to result in 40 μs dispersion of the time response. Although this analysis remains to be verified, it is plausible to assume that the soap film thickness varies during the process of bubble formation with a coefficient of variation in the same order of magnitude as that measured for the bubble diameter.

6.4.2 Velocity fluctuation estimation

The density dispersion results in velocity fluctuations that may be falsely interpreted as turbulence. In a two-component PIV measurement, the flow turbulence intensity,

$$I = \sqrt{\frac{u_{rms}^2 + v_{rms}^2}{2}}, \tag{6.26}$$

is inferred from the root-mean-square (RMS) of the particle velocity fluctuation, whose streamwise component (and similarly the transverse component) reads as

$$u_{p,rms} = \sqrt{\langle u_p'^2 \rangle} = \sqrt{E\left(u_p^2\right) - E\left(u_p\right)^2},$$
$$E\left(u_p\right) = \sum_{i=1}^{k} P_i u_{p,i}, \tag{6.27}$$

where $u_p' = u_p - \langle u_p \rangle$, E is the expected value and P is the probability of the outcome u_p. In steady flows, $u_{p,rms}$ may be rewritten as:

$$u_{p,rms} = \sqrt{E\left(u_{slip}^2\right) - E\left(u_{slip}\right)^2},$$
$$E\left(u_{slip}\right) = \sum_{i=1}^{k} P_i u_{slip,i}. \tag{6.28}$$

For an error assessment of this effect, the slip velocity may be estimated from eq. (6.12), (6.16), (6.20), while the probability P may be obtained by assuming that the slip velocity dispersion is exclusively resultant from the particle density distribution. Assuming a Gaussian distribution $N\sim(\langle \rho_p \rangle, \sigma_\rho^2)$, $P(\rho_p)$ is calculated as

$$P\left(\rho_p\right) \approx F\left(\rho_p + \frac{\Delta\rho}{2}\right) - F\left(\rho_p - \frac{\Delta\rho}{2}\right), \tag{6.29}$$

where $F(\rho_p)$ is the cumulative distribution function:

$$F(\rho_p) = \frac{1}{2}\left[1 + erf\left(\frac{\rho_p - \langle\rho_p\rangle}{\sigma_\rho\sqrt{2}}\right)\right]. \tag{6.30}$$

The accuracy of this approximation for estimating $u_{p,rms}$ is evaluated by repeating the simulation of section 6.3.3 for a particle of normally distributed density with $\langle\hat{\rho}\rangle = 0.8$ and $CV_\rho = 0.1$. As before, the data is gridded into bins by fitting the scattered data with a quadratic function. The velocity fluctuations are then obtained as the difference of the simulated particle velocity to the local fit value. This results in more accurate calculation of $u_{p,rms}$ in comparison to simple subtraction of the bin ensemble average (Agüera et al. 2016).

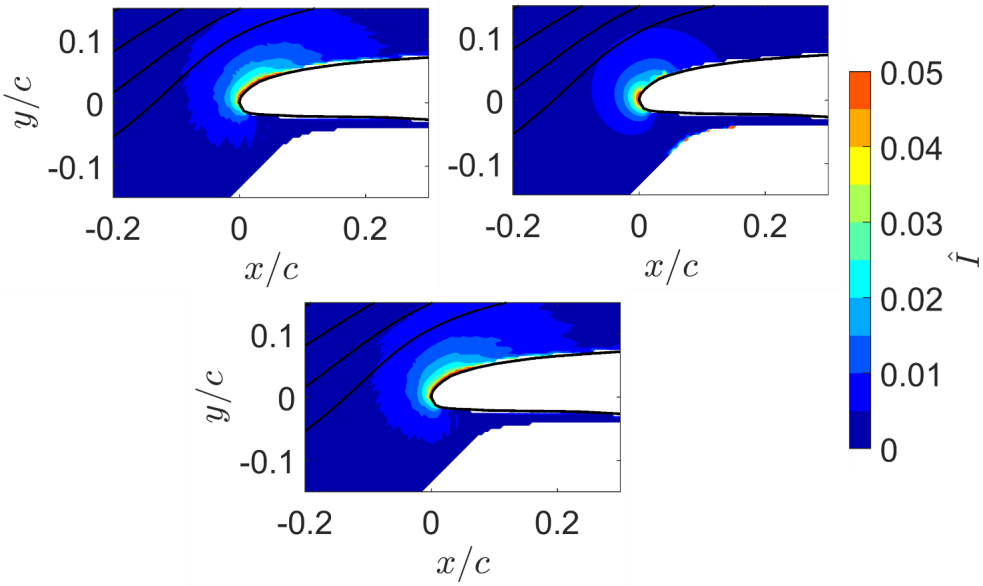

Figure 6-11. Comparison of the velocity fluctuations for $\langle\hat{\rho}\rangle = 1$. Top-left: numerical simulation for $CV_\rho = 0.1$ and $CV_d = 0$. Top-right: approximation from equations (6.26) to (6.30) for $CV_\rho = 0.1$ and $CV_d = 0$. Bottom: numerical simulation for $CV_\rho = 0.1$ and $CV_d = 0.1$.

The normalized turbulence intensity ($\hat{I} = I/U_\infty$) around the airfoil leading edge obtained from the numerical simulation is shown in figure 6-11 (top-left). For the conditions tested, I reaches about 3-4% of U_∞ around the leading edge. There is a good agreement between the simulated $\hat{I}$ levels and that obtained from the proposed approximation (figure 6-11, top-right), with the magnitude of the turbulence intensity error being well captured.

Additionally, if a diameter coefficient of variation CV_d of 10% $\langle d_p \rangle$—dispersion typical of jetting regime—is included in the simulations (figure 6-11, bottom), the results remain virtually unchanged. This supports the arguments given in the discussion of section 6.4.1 that the influence of size dispersion on the slip velocity distribution is negligible in comparison to that of density dispersion.

6.5 Experimental procedure and apparatus

The procedures developed in section 6.3 to estimate slip velocity and in section 6.4 to obtain velocity RMS from density dispersion are applied to evaluate the HFSB tracing fidelity in large-scale PIV measurements.

6.5.1 Set-up of experiments

The experiments are performed in the Low-Speed Tunnel (LST) of the German-Dutch Wind Tunnels (DNW), a closed-circuit tunnel with a closed test section of 3 m (height) × 2.25 m (width) cross-section, area contraction ratio of 9:1, and free-stream turbulence level of approximately 0.03%. The 2D high-lift airfoil represents an outer wing section of the Fokker 100 aircraft (model 5-6, Reinders W 1994) of scale 1:4.96 and chord of 67.59 cm, and was tested with retracted flap. The airfoil was installed vertically spanning the test section height. The measurements were performed at 15, 40 and 70 m/s free stream velocity and at three angles of attack α= {9°, 14°, 17°}.

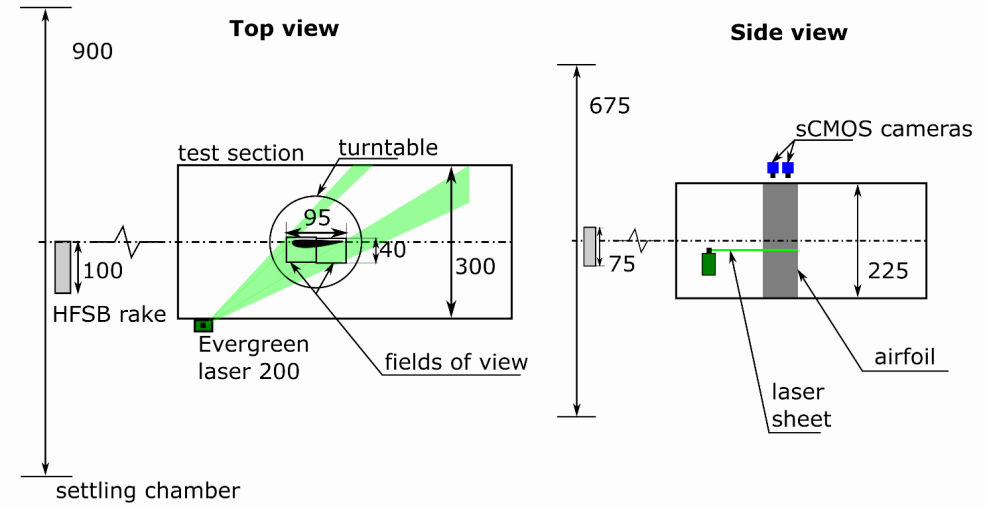

Figure 6-12. Experimental set-up: top view (left) and side view (right). The HFSB are generated in the settling chamber, minimizing flow intrusion. The seeding rake is positioned off centre, enhancing the bubble concentration in the measurement area. The dimensions are given in centimetres.

The planar two-components PIV system (figure 6-12) features two LaVision *Imager* sCMOS cameras (2560 × 2160 px², 16 bit, 6.5 µm pixel pitch) equipped with 50 mm focal length objectives (lens aperture diameter of f/16 for HFSB and f/5.6 for DEHS). The cameras were installed on the top of the test section with their optical axis perpendicular to the laser sheet at a distance of about 1.5 m, yielding an optical magnification of 0.03, a digital imaging resolution of 0.2 mm/px and a combined FoV of 0.95 × 0.4 m², covering the whole airfoil. A Quantel *Evergreen 200* Nd:YAG laser (2×200 mJ/pulse at 15 Hz) was used for the particle illumination. The laser sheet thickness was 10 mm for HFSB and about 4 mm for DEHS. The laser power was set at 40% for the former and at 100% for the latter. As it can be observed, the imaging settings were at the limit in the case of DEHS, in terms of enhancing the optical signal, while the laser power had to be set to low power and the camera aperture fully closed for HFSB to avoid saturation. Thus, the volume achieved with HFSB could have been considerably larger. The

α	U_∞ (m/s)	Re_c (10^6)	Re_d (10^3)	Pulse separation (μs)	N° img. HFSB	N° img. DEHS
9°	15	0.7	0.5	105	2000	2000
	40	1.8	1.3	45	5500	6000
	70	3.2	2.3	30	9500	1000
14°	15	0.7	0.5	105	10,000	5000
	40	1.8	1.3	45	27,000	5000
	70	3.2	2.3	30	20,000	2000
17°	40	1.8	1.3	45	27,000	5000
	70	3.2	2.3	30	37,000	3000

Table 6-2. Test matrix

Seeding	DEHS	HFSB
Camera's sensor size	2560 × 2160 px²	2560 × 2160 px²
Camera's objective focal length	50 mm	50 mm
Combined field of view	0.95 × 0.40 m²	0.95 × 0.40 m²
Image resolution	0.2 mm/px	0.2 mm/px
Lens aperture diameter	f/5.6	f/16
Laser sheet thickness	4 mm	10 mm
Acquisition frequency	15 Hz	15 Hz
Laser pulse energy	200 mJ	80 mJ

Table 6-3. Imaging conditions.

acquisition and optical imaging conditions are summarized table 6-2 and table 6-3.

6.5.2 HFSB generation

The system of HFSB generation is composed of three main components: the fluid supply unit (FSU), the bubble generators and the seeding rake. The in-house built FSU is composed of vessels and valves that can be operated remotely to pressurize and depressurize the fluid supply lines. Pressure flow controllers (coupled with mass flow meters) from Bronkhorst control the flow rates of helium, soap and air. The bubble generators are CNC-manufactured nozzles of 1 mm orifice diameter (Faleiros et al. 2019) designed by the Royal Netherlands Aerospace

Centre (NLR). Flow resistors guarantee equal mass flow to each bubble generator. The seeding rake is a 42-generator array composed of six horizontal segments spaced vertically by 15 cm (figure 6-13). Each segment contains seven bubble generators spaced with a 15 cm pitch. The bubble system, therefore, provides a seeded stream tube of about of 0.75 m (height) × 0.90 m (width) cross-section area, with an injection rate of approximately 1.3 million bubbles/s.

With the seeding rake installed in the settling chamber, the resultant stream tube of HFSB after contraction is 0.25 m (height) × 0.30 m (width). The bubble concentration in the test section is, therefore, 0.24 bubble/cm³ for U_∞ = 70 m/s, 0.42 bubble/cm³ for U_∞ = 40 m/s and 1.1 bubbles/cm^3 for U_∞ = 15 m/s.

The bubble generator dimensions, working principle, regimes of generation and bubble properties are given in chapter 4. In the present experiments, the average volume flow rates per generator were 80 l/h of air, 9.5 l/h of helium and 9.5 ml/h of soap, yielding 30 000 bubbles/s (per generator) of nominal bubble density of 1.1 kg/m^3 ($\hat{\rho}\sim0.9$) and mean

Figure 6-13. NLR's seeding rake of 42 bubble generators.

diameter of 0.5 mm.

6.5.3 Data processing

The data obtained with DEHS was processed using the cross-correlation algorithm from the LaVision software *DaVis 10*. The final interrogation window used is 48 × 48 pixels large (0.96 cm × 0.96 cm in physical space). With an overlap of 75% among adjacent interrogation windows, the vector spacing is 0.24 cm. Vectors whose absolute difference from the mean exceeded two standard deviations were excluded prior to obtaining statistics of the first and second moments of velocity.

The data acquired with HFSB was processed using an in-house algorithm developed with Matlab. Particles were identified based on local maxima and paired to the particles in the next frame according to the nearest neighbour criterion. The particle displacement (2 mm in the free stream) was sufficiently small compared to the average particle distance (about 20 mm at 40 m/s). The FoV was gridded into square bins of 1.5 cm² for statistical analysis. The velocity moments were obtained in the same manner as described in chapters 6.3 and 6.4.

6.6 Experimental results

6.6.1 Slip velocity

The magnitude of the DEHS and HFSB velocities, normalized with the free stream velocity, $|\vec{\hat{u}}|$ and $|\vec{\hat{u}}_p|$, respectively, are shown in figure 6-14 for U_∞ = 40 m/s and α = 14°. The subscript p of particle is here reserved for HFSB, while the reference DEHS is left without a subscript.

The colour contours indicate an apparent good agreement between both measurements. Notice, however, that the measurements at this scale approach the limit of what can be achieved with DEHS. This can be observed in the leading edge region, where the laser illumination is less intense due to the Gaussian shape of the laser beam intensity distribution. The DEHS tracer signal is of the same intensity as that of the background

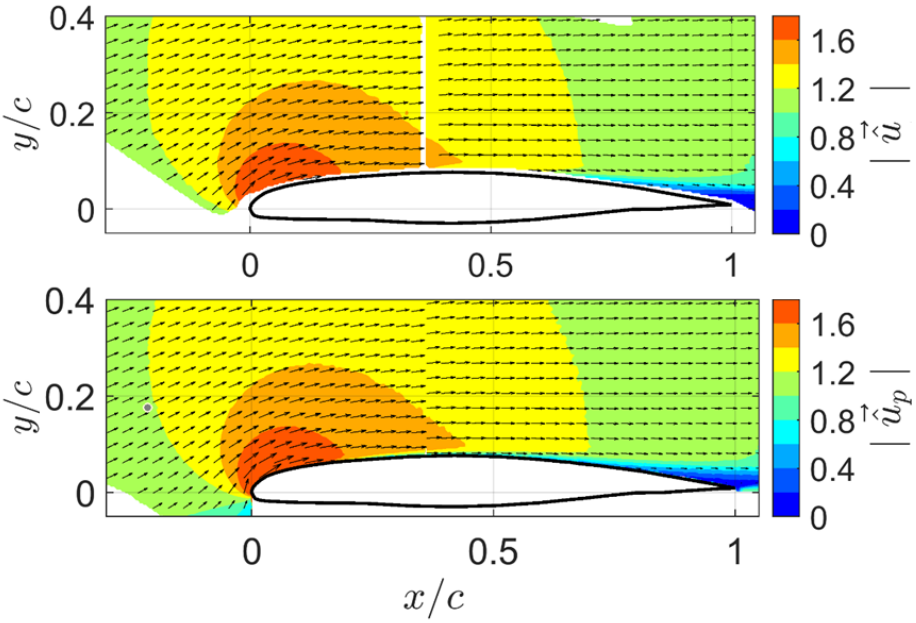

Figure 6-14. Velocity magnitude for U_∞ = 40 m/s and α = 14°, DEHS (top) and HFSB (bottom). Showing 1 every 9 × 9 vectors.

reflections in this region and is corrupted to a larger extent than the HFSB data, which has a signal to noise ratio (SNR) of $O(10^2)$. A more restrictive mask is therefore applied to the DEHS data.

The overall agreement between the two measurements (figure 6-15) is verified by overlaying the HFSB velocity data (colour-filled contours and dashed lines) with the DEHS velocity isolines (solid lines). Two measurement conditions are presented in the discussion for the sake of conciseness: 40 m/s at α = 14° and 70 m/s at α = 17°. The results show a good agreement for the two velocity components in both flow conditions, although with larger deviations at 70 m/s and 17° incidence.

In general, the slip velocity remains within 2% of U_∞ (figure 6-16), with exception of the high-pressure-gradient region around the leading edge and the separated region. In the leading edge region the slip velocity is mostly within 4 to 6%, reaching, in most cases, up to 12% of U_∞ near the surface.In the most extreme case of 70 m/s and 17° incidence, the slip

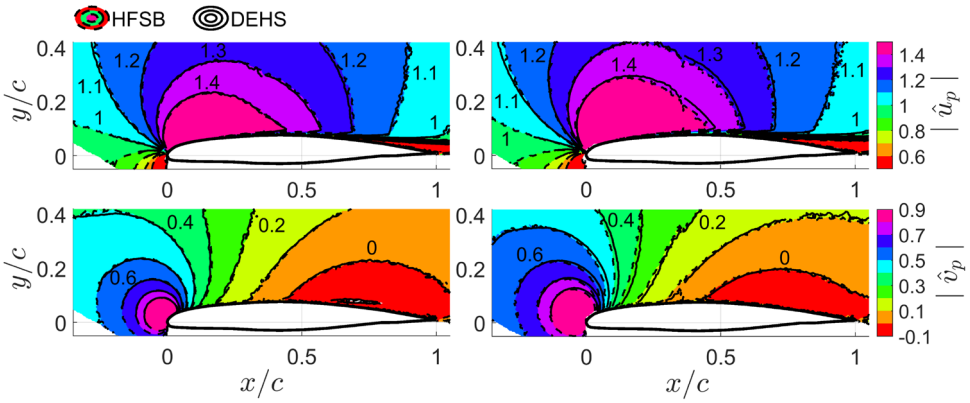

Figure 6-15. Velocity contours of chordwise (top) and normal to chord (bottom) components. Left: $U_\infty = 40$ m/s and $\alpha = 14°$. Right: $U_\infty = 70$ m/s and $\alpha = 17°$.

velocity approaching the surface close to the leading edge reaches up to 20% of U_∞. In addition, it is noted that the slip velocity in the separated region reaches about 10% of U_∞ in some cases.

Close inspection of the data shows that the separation point shifted slightly in some cases between HFSB and DEHS, which could explain these differences. As the transition point has not been fixed through the use of a tripping device, a precise comparison of the slip velocity in the separated region is not possible.

The least square optimization described in section 6.3.4 is used to

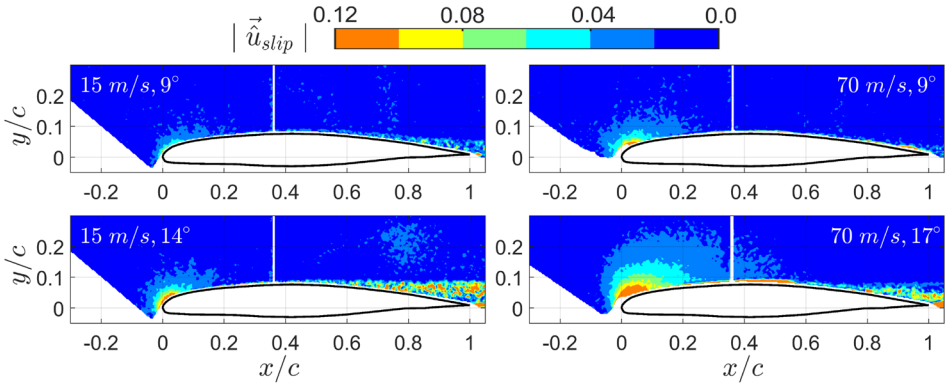

Figure 6-16. HFSB slip velocity with respect to DEHS measurements.

	15 m/s	40 m/s	70 m/s
9°	1.22	0.94	0.81
14°	1.32	1.12	0.81
17°	-	0.90	0.87

Table 6-4. Density ratio $\hat{\rho}$ estimate per measurement condition.

estimate the particle-to-fluid density ratio (table 6-4). A trend is observed which shows the bubble density decreasing with wind tunnel speed. The bubbles are about 20-30% heavier than air at 15 m/s, within 10% difference from the neutral buoyancy condition at 40 m/s, and about 20% lighter than air at 70 m/s. This systematic density variation with wind tunnel speed is not explained by the generation process. Changes in the tunnel total pressure do not affect the mass flow rate of helium, which is mass flow controlled. The pressure-controlled soap input of about 4 bars renders tunnel total pressure variations negligible (<1% of the input pressure). Even though the viscosity of the soap film is sensitive to temperature changes, causing variations in the volume flow rate, those were monitored with a mass flow meter and counteracted by readjusting the helium mass flow for a constant helium-to-soap flow rate ratio (Q_{He}/Q_{soap}~1000).

An alternative explanation is that the HFSB density changed after generation, due to soap film evaporation and diffusion of helium and air through the soap film. Both the tunnel temperature and the bubble residence time (the time from generation until the measurement) influence these physical processes. Shrinking of HFSB, as a result of helium diffusion, and a colour shift from red to blue, attributed to soap film thinning, have both been observed by Huhn et al. (2017), while studying the HFSB lifetime. Unfortunately, it is beyond the scope of this study to validate these conjectures.

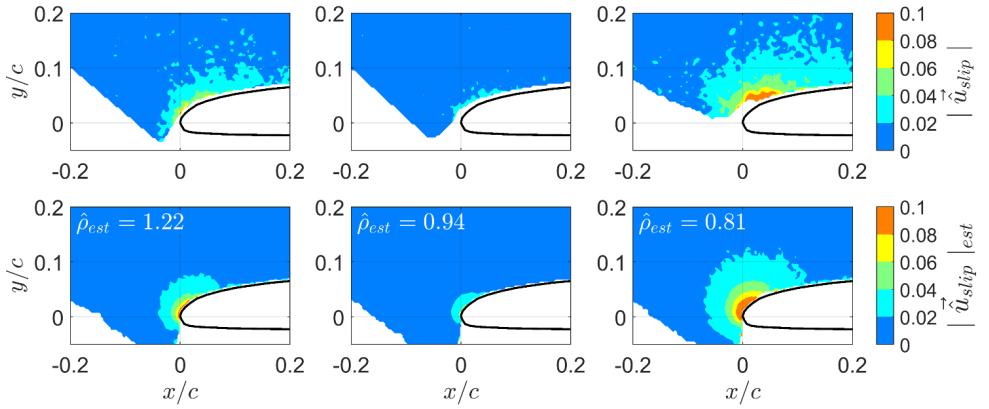

Figure 6-17. Top: Slip velocity (velocity difference between HFSB and DEHS) measured experimentally at 9° angle of attack for (from left to right) $U_\infty = \{15, 40, 70\}$ m/s. Bottom: Slip velocity estimated from HFSB measurements, equations (6.12), (6.16) and (6.20), and estimated density from least square optimization (section 6.3.4).

From the estimated density values, correspondent slip velocity fields are estimated (figure 6-17, bottom), based on the HFSB measurements and equations (6.12), (6.16) and (6.20), and compared to that of the measured slip velocity (figure 6-17, top). Although measurement noise hinders the comparison, there is sufficient agreement between measured and estimated values to support the validity of the density estimation procedure.

6.6.2 Velocity fluctuations

The normalized free stream turbulence intensity $\hat{I}_\infty$, eq. (6.26), is shown in table 6-5. At 15 m/s free stream velocity, the turbulence levels measured with HFSB and DEHS are about the same, while $\hat{I}_\infty$ values measured with HFSB at 40 and 70 m/s consistently exceed the DEHS levels by about 0.5%. This difference is ascribed to the two different processing techniques, namely, cross-correlation analysis and particle tracking. When conducted over two frames, the latter suffers higher uncertainty (Raffel et al. 2018).

	DEHS			HFSB		
	15 m/s	40 m/s	70 m/s	15 m/s	40 m/s	70 m/s
9°	2.0 %	1.4 %	1.7 %	1.9 %	1.9 %	2.2 %
14°	1.7 %	1.6 %	1.6 %	1.7 %	1.8 %	2.1 %
17°	-	1.8 %	1.6 %	-	2.3 %	2.3 %

Table 6-5. Normalized free stream turbulence intensity $\hat{I}_\infty$, taken as the spatial average of $\hat{I}$ within a square of 0.05 chord side length with center at $(x/c, y/c) = (-0.2, 0.3)$.

A few cases are selected for evaluation of the velocity fluctuations measured with HFSB in comparison to DEHS (figure 6-18). First a few comments on the quality of the DEHS data are made. Although used as reference, DEHS tracers are not particularly suitable for large-scale measurements. The DEHS data quality is lower near the leading edge due to the reduced illumination in this region. Additionally, even though

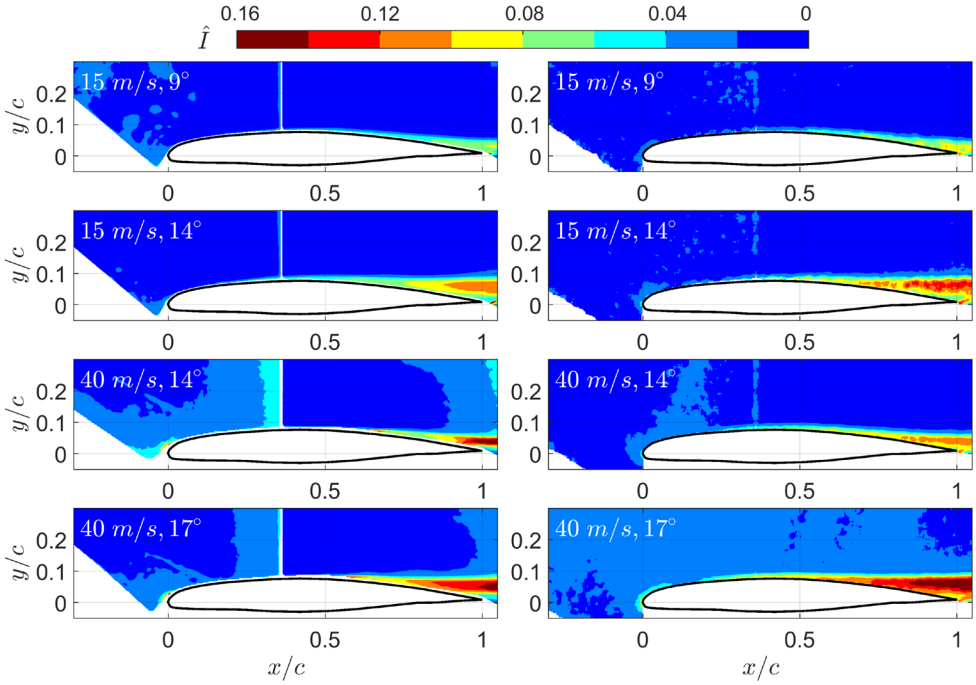

Figure 6-18. Comparison between the velocity fluctuations measured with DEHS (left) and HFSB (right).

the laser sheet is perpendicular to the camera lens optical axis, a small (but significant) component of the scattered light is directed parallel to the optical axis resulting in forward and backward scattering (figure 3-10) from the particles upstream and downstream to the camera axis, respectively—there is a 20° angle between the light rays reaching the camera from the most upstream to the most downstream positions. With light scattered forward being orders of magnitude more intense, a chordwise light intensity gradient is observed in the raw images of both cameras, lowering the quality of the DEHS data in the region within $0.3 < x/c < 0.35$ and downstream of the trailing edge. This can be clearly observed from the $\hat{I}$ values measured with DEHS at 40 m/s (figure 6-18), where the seeding concentration was probably lower than in the other cases (due to seeding evaporation, the DEHS concentration had to be monitored and the atomizers occasionally pressurized).

In general a good qualitative agreement between DEHS and HFSB velocity fluctuations is observed. The separated regions have similar topology, with HFSB measurements of turbulence intensity peak levels exceeding the reference by about 2%, with exception of the 40 m/s and 14° incidence case, where DEHS measurements overestimate the turbulence intensity levels close to the trailing edge. The turbulence levels measured with HFSB close to the leading edge are between 2% to 4% of U_∞ in most cases, except for α = 17°, where it reaches 6%. As discussed in section 6.4, velocity fluctuations in the leading edge region are attributed to bubble density dispersion. It is noted, however, that no significant changes in the velocity fluctuations have been observed between the simulations at 14° and 17° incidence (not shown), posing the question of whether the leading edge fluctuations measured at 17° are indeed exclusively due to bubble density variation or a combination of the latter with existent flow fluctuations that are known to occur at the leading edge in the onset of stall (e.g. Benton & Visbal, 2018).

	15 m/s	40 m/s	70 m/s
9°	0.12	0.15	0.12
14°	0.10	0.10	0.11
17°	-	0.18	0.21

Table 6-6. Density coefficient of variation CV_ρ estimated per measurement condition.

Unfortunately, DEHS cannot be used to determine turbulence levels at the leading edge due to the lower quality in the region.

The density coefficient of variation CV_ρ is estimated via a least-square optimization analogous to the one performed for the mean density estimation. The normalized density dispersion is mostly within 10 and 15% of the mean density (table 6-6), with exception of the data for 17° incidence, where σ_ρ is about 20% of the mean density. The density dispersion at 17° might be overestimated, however, as mentioned above,

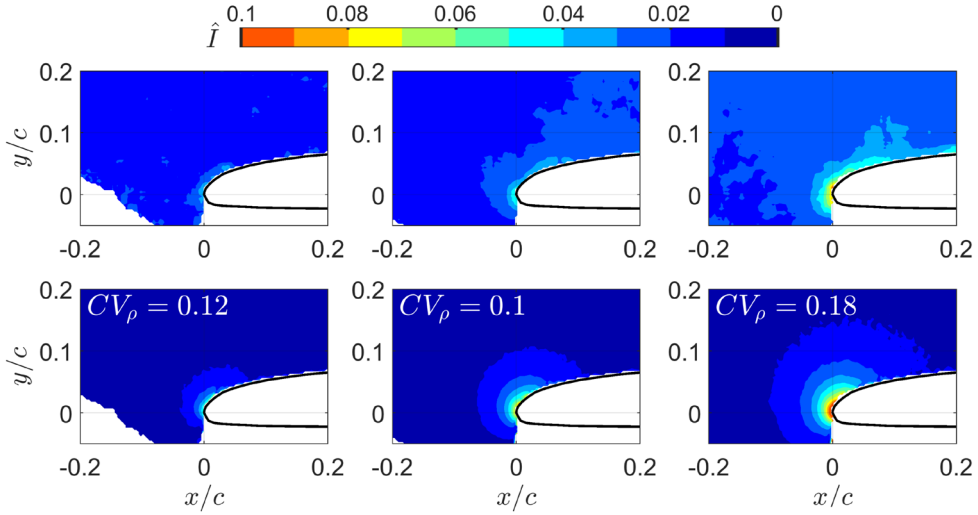

Figure 6-19. Top: turbulence intensity levels measured experimentally for, from left to right, 15 m/s and 9°, 40 m/s and 14°, and 40 m/s and 17°, respectively. Bottom: the correspondent turbulence intensity estimated from eq. (6.26) to (6.30), with slip velocity obtained from eq. (6.12), (6.16) and (6.20), and the density dispersion estimated from a least square optimization.

due to possible extra flow fluctuations that occur in the onset of stall. Overall, the estimated values are at least twice as large as those estimated in section 6.4.1. The larger values might be a result of the extra uncertainties resultant from the simultaneous operation of a multi-nozzle system.

The measured $\hat{I}$ with HFSB in the leading edge region (figure 6-19, top) is compared to estimated values (figure 6-19, bottom) from eq. (6.26) to (6.30), where the slip velocity is obtained from eq. (6.12), (6.16) and (6.20), and the density dispersion from table 6-6. Within the limitations of measurement and processing errors, and of statistical convergence, the estimated values show a good agreement with the experimental data. Furthermore, the extra turbulence intensity caused by HFSB density dispersion is shown to be a localized effect, only occurring within regions of high flow frequency.

6.7 Conclusions

6.7.1 The proposed method for slip velocity analysis

This study has contributed to a more systematic assessment and prediction of the slip velocity of nearly-neutrally-buoyant tracers in typical conditions expected for large-scale PIV measurements in wind tunnels.

It was shown that the slip velocity is governed by three non-dimensional parameters (as opposed to a single Stokes number), namely, the ratio of particle to fluid density, the particle Reynolds number, and the local flow frequency normalized with the viscous timescale d_p^2/ν.

The motion of a particle travelling around an object has been shown to be analogous to that in a sinusoid flow, providing generalization to the analysis of particle slip velocity in external aerodynamics.

Empirical relations for estimation of the slip velocity of bubbles were obtained by means of numerical simulations in a rectilinear oscillatory flow. The use of these relations, coupled with the definitions presented

for the local definition of flow frequency and phase around an object, allowed estimations of the slip velocity around an airfoil within 20% of numerical simulations of lighter-than-air bubbles around an airfoil at $Re_c = 3.2$ million. This is significantly more accurate than other methods available in literature, emphasizing the importance of considering unsteady forces and drag correction for the slip velocity estimation.

The method has also been extended to allow evaluation of bubble density, based on measurements of slip velocity, and of velocity fluctuations. It has been shown that the latter is mainly a consequence of bubble density dispersion, while the effects of diameter dispersion are negligible in comparison.

6.7.2 HFSB slip velocity around an airfoil

PIV measurements with a (nominally) 10% lighter-than-air HFSB around a 70 cm airfoil (95×40 cm^2 FoV), for $U_\infty = \{15, 40, 70\}$ m/s and $Re_c = \{0.7, 1.8, 3.2\}$ million. Prior to this study PIV measurements with HFSB had not exceeded 50 m/s.

The HFSB slip velocity was shown to be overall below 2% of U_∞, with exception of the high acceleration region around the leading edge, where in most cases it is up to 5% of U_∞. Only in the most extreme measurement conditions, as in the onset of stall at 70 m/s, that the slip velocity close to the airfoil surface has reached values up to 20% of U_∞.

Although HFSB had been expected to be 10% lighter-than-air, using the tools developed in this chapter, the HFSB densities have been estimated to be 20-30% heavier than air at 15 m/s, within 10% difference from the neutral buoyancy condition at 40 m/s, and about 20% lighter than air at 70 m/s. Analysis of tunnel temperature and pressure variations, considering the instrumentation used for mass flow rate and pressure control, has not presented any logical explanation to ascribe the density variation to the HFSB generation. Hence, leading to the conclusion that the HFSB densities have changed post-generation. The

main mechanisms responsible for density variations post-generation are evaporation of the soap film and helium diffusion.

In addition, the HFSB density coefficient of variation was quantified to be approximately 10%. This results in velocity fluctuations around the leading edge of up to 5% of U_∞ for most test conditions. In general, the velocity errors were localized and had minor effect on the overall measurement quality.

7

TRACING FIDELITY IN TURBULENT FLOWS

The mean velocity and turbulent stress profiles measured with HFSB and air-filled soap bubbles in a turbulent boundary-layer are assessed in this chapter. Part of the material herein presented has been published in Experiments in Fluids (*Helium-filled soap bubbles tracing fidelity in wall-bounded turbulence*, Faleiros et al. 2018).

7.1 Introduction

The importance of the unsteady forces on the tracing fidelity of nearly-neutrally buoyant bubbles has been demonstrated in a sinusoidal flow (section 6.2.2). Due to the added-mass and history forces the tracing fidelity of these bubbles is markedly better than when considering Stokes drag alone. As shown in figure 6-2, the unsteady forces become more relevant as the frequency of the flow fluctuation increases. The total velocity error converges to a finite value at high frequencies, which depends on the bubble density and Reynolds number (section 6.3, eq. (6.17)).

In turbulent flows, the spectrum of the turbulence kinetic energy covers a broad frequency range. Based on the concept of particle inertia and the analyses made in the previous chapters, neutrally buoyant bubbles are expected to follow the flow accurately within the entire

range, while slightly heavy and light particles are expected to have a finite slip velocity that increases with frequency up to a certain threshold.

However, previous studies on the tracing fidelity of nearly-neutrally-buoyant particles in turbulence indicate otherwise. Experimental studies on this topic include the work of Voth et al. 2002, Volk et al. 2008 and Xu and Bodenschatz 2008 using polystyrene and glass particles in von Kármán water flows, and the work of Qureshi et al. (2008) and Bourgoin et al. (2011), using air- and helium-filled soap bubbles in isotropic turbulent flows. The studies involved mostly inertial particles of normalized density to fluid density in the order of $O(1)$ and $O(10)$ and particle diameters in the submillimetre and millimetre range. In general, for the flows studied and within this particle-parameter space, measurements of the 1st and 2nd moments of velocity yielded virtually the same results for all particles. The influence of the particle properties was only observed through analysis of the acceleration variance, which reduced as the particle size or density were increased.

In this chapter we expand on previous works by analysing the tracing fidelity of HFSB and AFSB in a turbulent boundary-layer. The higher turbulence intensity levels and the non-isotropic nature are expected to contribute for larger errors in velocity and turbulent stresses. The air-filled bubbles used in this study are four times heavier than air. Measurements performed with DEHS are used as reference.

The use of helium-filled soap bubbles close to walls becomes relevant especially for the study of three-dimensional flow phenomena (horse-shoe vortex at wing junction, Belligoli et al. 2020) and for pressure measurements close to surfaces, where pressure taps cannot be installed (e.g. pressure fluctuations over serrations, Lima Pereira et al. 2020). Furthermore, being much brighter than oil droplets, HFSB can be used close to walls as a way of reducing reflections, as the required laser power is extremely reduced, allowing, inclusively, for led light illumination (Schanz et al. 2019).

7.2 Experimental Set-up and data processing

7.2.1 Wind tunnel

The experiments were performed in the small anechoic wind tunnel KAT of the Royal Netherlands Aerospace Centre (NLR). The KAT is an open jet wind tunnel with an area contraction ratio of 10 and an exit cross section of 38.4 cm × 51.2 cm. The test section was enclosed by 90 cm long end plates made of wood, with exception of the upper plate, made of Plexiglas to enable optical access. The free stream turbulence intensity of the tunnel ranges from 0.3% to 0.4% of the free stream velocity, measured from 10 m/s to 70 m/s.

7.2.2 Seeding Particles

DEHS droplets were generated using an aerosol generator from LaVision that produces particles predominantly below 1 μm. The particles are introduced into the wind tunnel far upstream of the turbulence screens to guarantee homogenization of the particle distribution. The bubble generator employed in the experiments is the HFSB-GEN-V11 developed at TU Delft (similar geometry to the NLR bubble generator, figure 4-1, left).

7.2.3 PIV acquisition

Particles were illuminated with an Nd:YLF Litron LDY304 PIV laser (2×30 mJ/pulse at 1 kHz). The images were recorded with a LaVision HighSpeedStar 5 CMOS camera (1024×1024 pixels, 12 bits, 20 μm pixel pitch). The PIV recording parameters are summarized in table 1-1.

7.2.4 Data processing

The DEHS images are processed using a spatial cross-correlation algorithm available in the LaVision software Davis 8.4. The bubble images are analysed in Matlab using an in-house tracking algorithm, based on Malik et al. (1993), using the DEHS data as predictor for particle displacements and search window. Only trajectories where the

Imaging conditions	
Camera objective focal length (mm)	200
Active sensor size (px²)	640 × 640
Field of View (mm²)	30 × 30
Magnification Factor	0.44
Measurements with HFSB and AFSB (Single frame, multi-exposure)	
Camera recording frequency	50 Hz[a] / 500 Hz[b]
Laser frequency	20 kHz
Numerical aperture	f/32
Laser sheet thickness (mm)	5
Exposure time (ms)[a]	0.2 (HFSB) / 0.33 (AFSB)
Exposure time (ms)[b]	2
Measurements with DEHS (Double frame, single exposure)	
Double-frame recording frequency	500 Hz
Pulse separation	30 μs
Numerical aperture	f/4
Laser sheet thickness (mm)	2
Interrogation window (mm)	1.4 (32 px)

Table 7-1. PIV/PTV recording parameters of cylinder experiment.
[a] Cylinder measurements. [b]Boundary Layer measurements.

particle image is detected more than 5 times are considered. A sliding 2nd order polynomial least-squares fit is applied to the discrete particle positions. The kernels are centred at each particle position, encompassing a minimum of 5 samples. If more particle neighbours are available, larger kernels are used up to a maximum of 11 samples. Particle velocity and acceleration are determined from the gradient of the fitted polynomials at the centre of each kernel. The first two and last two vectors in every trajectory are neglected due to the lower accuracy of the polynomial fitting in the trajectory ends. Thus the smallest acceptable trajectory of only 5 points would render a single vector.

7.3 Particle properties

The particle time response and density of HFSB and AFSB are measured in the stagnation region of a cylinder of 50 mm diameter, following the procedure described in section 3.5.2, and with the same experimental setup detailed in section 5.3.2. The wind-tunnel velocity was set to 30 m/s. In total a set of 12,000 image pairs were recorded with DEHS, while sets of 5,000 multi-exposed images were obtained per bubble tracer (HFSB / AFSB).

The pathlines obtained with the three tracers are shown figure 7-1. AFSB particles, due to their higher inertia, clearly deviate from the reference along the curved trajectories in front of the cylinder, penetrating closer to the stagnation region before turning sideways. As previously, HFSB feature streamlines that follow closely the reference

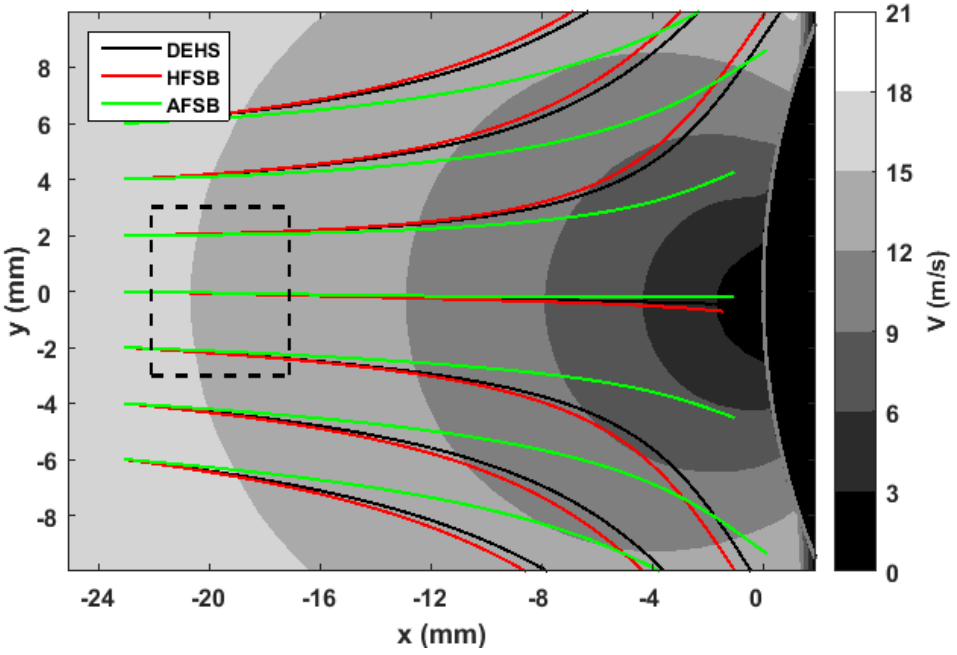

Figure 7-1. PIV and PTV measurements of the flow in front of a cylinder. Velocity contours from the DEHS measurements. The dashed square shows the area used to evaluate the time response.

	Q_{He} (l/h)	$Q_{air,in}$ (l/h)	$Q_{air,ext}$ (l/h)	Q_{BFS} (ml/h)	$d_p \pm \sigma_d$ (mm)	$\tau_p \pm \sigma_\tau$ (μs)	$\rho \pm \sigma_{\bar{\rho}}$ (kg/m³)
DEHS	-	-	-	-	~ 10^{-3}	2	750
HFSB	8.8	-	53	5.5	0.55 ± 0.07	30 ± 20	1.1 ± 0.05
AFSB	-	2.4	62	7.6	0.40 ± 0.06	430 ± 60	4.4 ± 0.7

Table 7-2. AFSB and HFSB volume flow rates, diameter, time response and density difference. The standard deviations of the ensemble averages of the particle diameter σ_d, time response σ_τ and density difference $\sigma_{\bar{\rho}}$ are also indicated.

streamlines (measured with DEHS). Being marginally lighter-than-air in the present case, the streamlines slightly anticipate the air flow deflection.

The particle diameter is estimated from eq. (2.13) by measurements of the glare points distance d_g. The bubble properties are summarized in table 7-2. The slip velocity of the bubbles is calculated using DEHS velocity as reference. The particle slip velocity and the particle Lagrangian acceleration are evaluated in a control region as highlighted in figure 7-1. The deceleration in this region is about 600g (~ 6,000 m/s²). The ratio between the streamwise components of the slip velocity and the particle acceleration yields the particle time response from eq. (5.4). The AFSB tracers exhibit a considerably larger mean time response of 430 μs and standard deviation of 60 μs. The bubble density is obtained from eq. (5.3).

7.4 Turbulent boundary layers measurements

Turbulent boundary layer measurements are performed using a flat plate of 90×51×1 cm³ (length × width × thickness) with a rounded leading edge of 0.5 cm radius. The plate was positioned vertically, spanning the entire test section height. A zigzag trip of 1.6 mm thickness was placed 10 cm downstream the leading edge forcing the transition to the turbulent flow regime. The experiments were performed at free stream velocities of 30 and 50 m/s. The experimental setup is shown

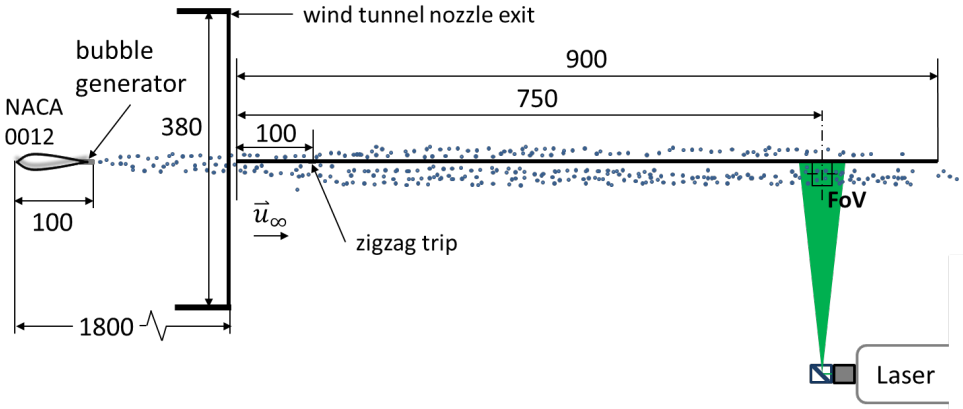

Figure 7-2. Top-view of the turbulent boundary layer experiment. No bubbles were produced during the PIV experiment with DEHS, but the NACA0012 wing was always in place. Dimensions are in millimetres.

schematically in figure 7-2. The PIV settings are described in table 1-1 and table 7-3.

The raw images from PIV (figure 7-3) are interrogated using of 16×16 px^2 windows with 75% overlap are used, resulting in 5.5 vectors per millimetre. The average number of particles per track, after discarding two vectors from each trajectory end, is about 20 at 30 m/s and 12 at 50 m/s. The scattered data from the ensemble is averaged out into bins of 0.9×0.9 mm^2 with 50% overlap, applying radial weighting based on a Gaussian function (figure 7-4). A standard deviation of 0.27 mm is chosen for the Gaussian distribution, so that the weight $w(x, y)$ equals 0.5 at a distance of half grid cell. Every bin includes the contribution of particles within a region of 3×3 grid points, resulting in one vector every 0.45 mm. Weighted time-averaged velocity and turbulent fluctuations are

	DEHS	HFSB / AFSB
Runs per condition	1	5
Images per run	10,000	20,000
Total	10,000	100,000

Table 7-3. Image acquisition for turbulent-boundary-layer measurements

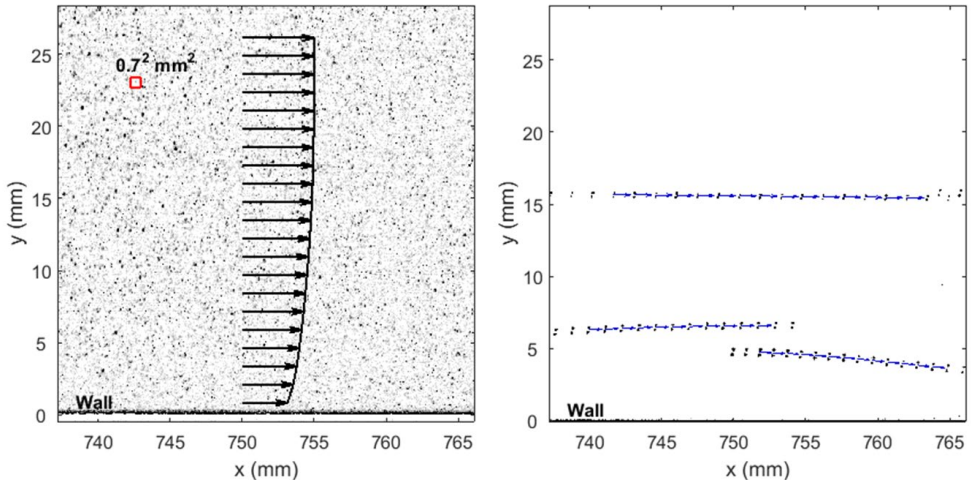

Figure 7-3. Left: Raw image from PIV measurements at $U_\infty = 30\,m/s$ (inverted gray scale). Interrogation window is indicated in the image (red square). Mean velocity profile is plotted showing one in every seven vectors for ease of visualization. Right: single-frame multi-exposure PTV images at $U_\infty = 30\,m/s$. Multiple positions of the bubbles are captured along their trajectories. Each bubble produces two glare points with the velocity vector assigned in the middle.

then calculated for each grid point.

The data is further averaged in the streamwise direction along 18 mm,

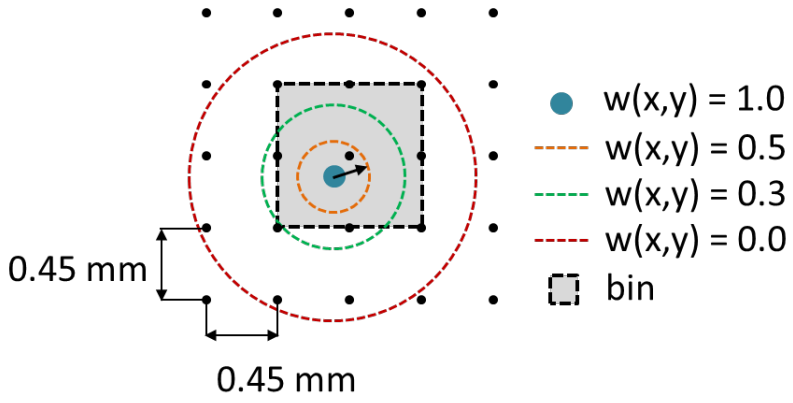

Figure 7-4. Radial weighting of scattered data into a grid. Every vector contributes to a bin of 0.9 mm².

when representing velocity profiles. The data points of the HFSB profiles contain on average 3×10^5 vectors at 30 m/s and 2×10^5 vectors at 50 m/s. The concentration of AFSB was generally lower, containing on average 2×10^5 and 1×10^5 vectors per data point at 30 and 50 m/s, respectively.

7.5 Measurement Uncertainty

The random uncertainty of the mean velocities, velocity fluctuations and turbulent stresses, from the reference measurements with DEHS, are quantified following Sciacchitano and Wieneke (2016). The use of 10,000 image pairs for the reference data guarantees that the mean streamwise velocity and the velocity fluctuations u'_{rms} and v'_{rms} are statistically converged. The uncertainties are computed at 95% confidence level, assuming a normal error distribution. The random uncertainty of velocity does not exceed 0.2% and 0.1% of U_∞ for the streamwise and wall-normal velocity components, respectively. The uncertainty of the streamwise and wall-normal velocity fluctuations reaches, respectively, a maximum of 2% and 1.5% of the respective peak values. The uncertainty of the Reynolds shear stress is approximately 5% of the peak value.

An additional source of uncertainty in this study results from changes of magnification factor across the laser sheet, which was thicker during measurements with bubbles (5 mm). The variation of optical magnification across the depth from the centre plane to the edge of illumination is approximately 0.5%. The latter induces velocity fluctuations of less than 0.5% with respect to the local velocity measured in the middle plane of the laser sheet. The turbulence intensity measured in the free-stream with DEHS is approximately 1%. Therefore, the measurement uncertainty due to magnification changes across the laser sheet can be neglected as it is in the same order of the velocity fluctuations in the free stream.

7.6 Results

7.6.1 Boundary layer integral properties

The Reynolds numbers based on momentum thickness are 3,300 and 5,100 for 30 and 50 m/s, respectively. The boundary-layer thickness δ_{99}, displacement thickness δ^*, momentum thickness θ and shape factor H are shown in table 7-4. The more robust boundary-layer thickness estimated at 90% of the free stream velocity δ_{90} is also included, given the better accuracy of this estimator. A theoretical 1/7 power law profile (Schlichting, 1979) is included for reference:

$$(x) = 0.37 x {Re_x}^{-1/5}, \quad \delta^* = \frac{1}{8}\delta, \quad \theta = \frac{7}{72}\delta. \tag{7.1}$$

A comparison of the integral parameters between measured values with DEHS tracers and those predicted from theory generally indicates a good agreement. The boundary-layer thickness δ_{99} measured with DEHS deviates less than 10% and 20% from the values obtained from theory for 30 and 50 m/s, respectively. However, the boundary-layer thickness δ_{99} measured with DEHS at 50 m/s seems to be overestimated—it differs only 1.5% from that measured at 30 m/s. This difference is 7% when δ_{90} is considered, which is closer to the 10% difference between the δ_{99} obtained from the 1/7 power law for 30 and 50 m/s. Measurements of

	U_∞ (m/s)	δ_{99} (mm)	δ_{90} (mm)	δ^* (mm)	θ (mm)	H
DEHS	30	17.77	9.78	2.30	1.80	1.28
HFSB	30	18.90	10.47	2.50	1.94	1.28
AFSB	30	19.17	10.61	2.47	1.94	1.27
1/7 power law	30	16.33	-	2.04	1.59	1.29
DEHS	50	17.50	9.13	2.11	1.67	1.26
HFSB	50	18.68	9.97	2.28	1.81	1.26
AFSB	50	17.90	9.75	2.25	1.77	1.27
1/7 power-law	50	14.75	-	1.84	1.43	1.29

Table 7-4. Boundary-layer integral values.

displacement and momentum thicknesses with DEHS are about 10% larger than the theoretical values. The shape factors exhibits only small deviations up to 2%. Therefore, DEHS used here as reference, is deemed to be in accordance to what is expected from boundary layer theory.

The boundary-layer integral properties assessed from HFSB measurements are compared to the DEHS values. The parameters δ_{90}, δ^* and θ are overall about 10% larger for HFSB for both free stream velocities, indicating slightly larger mass and momentum flow rate deficits with respect to the inviscid approximations of either uniform flow velocity or momentum. The shape factors deviate less than 0.5%.

Furthermore, no distinctive differences have been observed between HFSB and AFSB, with almost all the integral values agreeing within 2%. These results indicate that the turbulent state of the boundary layer can be reliably established from measurements conducted with HFSB or AFSB, despite the latter being 4 times heavier than air.

The following results present the wall distance normalized with respect to the boundary-layer thickness δ_{90}, based on the reference DEHS measurements. When referring to the boundary-layer edge, however, this is intended as δ_{99} ($\sim 1.8\ \delta_{90}$).

7.6.2 Particle size and concentration

The size distributions obtained during the boundary-layer measurements were very similar to those obtained upstream of the cylinder, strongly suggesting that the same conditions were reproduced. The diameter and standard deviation of each distribution in dimensional units and normalized with boundary-layer thicknesses (d_p/δ^* and d_p/δ_{90}) are summarized on table 7-5. Compared with δ_{90} the mean bubble diameter is two orders of magnitude smaller, indicating their potential ability to follow the most energetic turbulent fluctuations.

Particle	U_∞	d_p (mm)	σ_d (mm)	$d_p/\,\delta^*$	$d_p/\,\delta_{90}$
HFSB	30	0.55	0.06	0.25	0.06
HFSB	50	0.54	0.05	0.28	0.06
AFSB	30	0.42	0.03	0.19	0.04
AFSB	50	0.46	0.05	0.21	0.05
DEHS	30	$\sim 10^{-3}$	-	4×10^{-4}	1×10^{-4}
DEHS	50	$\sim 10^{-3}$	-	5×10^{-4}	1×10^{-4}

Table 7-5. Particle size. The DEHS size is only estimated.

The number of detected particle images n_p is illustrated in figure 7-5 normalized with the number of particles in the free stream $n_{p,\infty}$. The concentration in the outer region of the boundary layer is rather uniform. The relatively large concentration gradient normal to the wall, with the number of particles gradually increasing from the free stream region towards $y/\,\delta_{90} \approx 0.5$, and reaching about $4n_{p,\infty}$, is ascribed to the

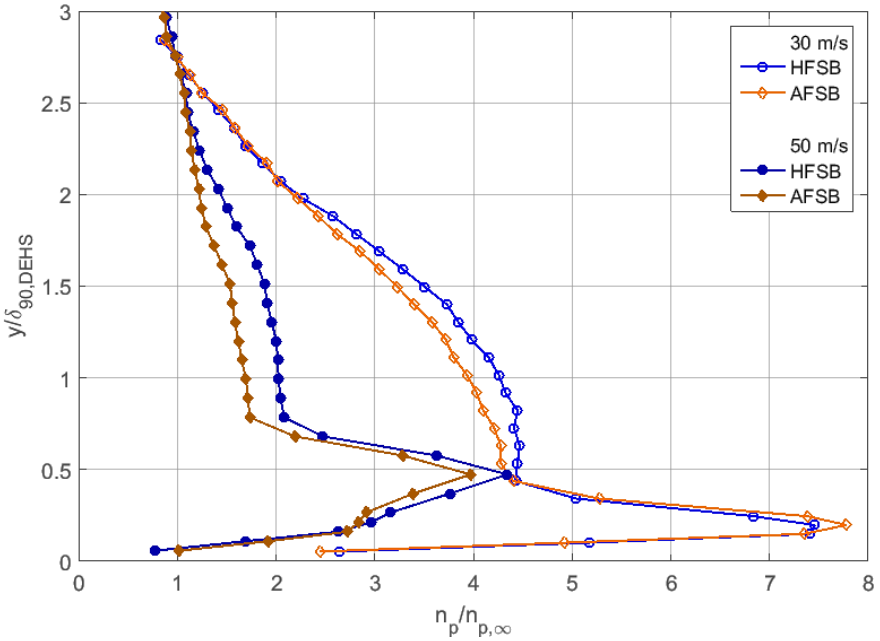

Figure 7-5. Wall-normal distribution of the number of particles per unit area. Values normalized with respect to the free stream.

spatial dispersion of bubbles introduced by the turbulent air jet exiting the bubble nozzle. The particle concentration would likely have been uniform, had more nozzles been used.

The cause of a peak concentration close to wall is unclear and remains to be investigated. As the wall is further approached ($y/\delta_{90} < 0.2$), the bubble concentration decreases dramatically, which is consistent with the hypothesis of bubbles bursting when they enter in contact with the wall.

7.6.3 Mean velocity and turbulent stresses

The mean streamwise velocity profiles measured with the bubbles are in good agreement with the DEHS measurements (figure 7-6). From the free stream flow towards the wall, departures from the reference begin at $2\delta_{90}$. Overall, the bubbles underestimate the mean velocity by approximately 2% of U_∞. The difference between HFSB and DEHS is

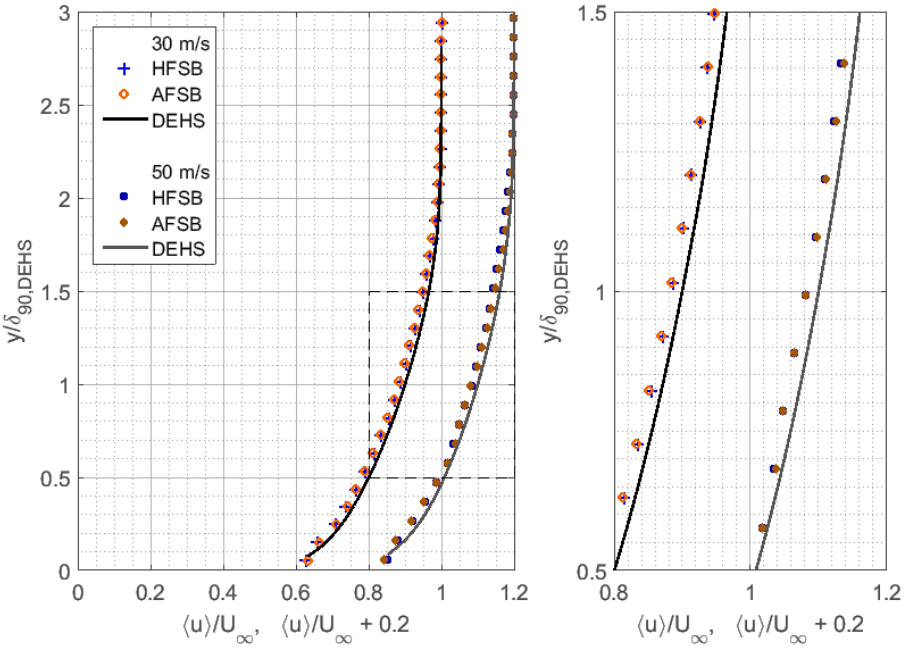

Figure 7-6. Mean streamwise velocity profiles measured with HFSB and AFSB at 30 and 50 m/s (shifted to the right by 0.1). The reference velocity measured with planar PIV and DEHS tracers is given (black solid line).

consistent in the region within $0.5 < y/\delta_{90} < 1.5$, whereas the difference between AFSB and HFSB is negligible. Furthermore, there is no clear trend that would indicate a growing departure closer to the wall.

The mean wall-normal velocity profiles are shown in figure 7-7. The shape of the curves and the magnitude of the mean wall-normal velocity are similar to what was found numerically by Sardina et al. (2012), with particles drifting towards the wall along the boundary-layer and away from it in the free stream. The DEHS particles show a slightly positive mean wall-normal velocity, consistent with the mechanism of boundary-layer growth. It should be remarked, however, that the vertical velocity component here is a small fraction of a percent with respect to the free

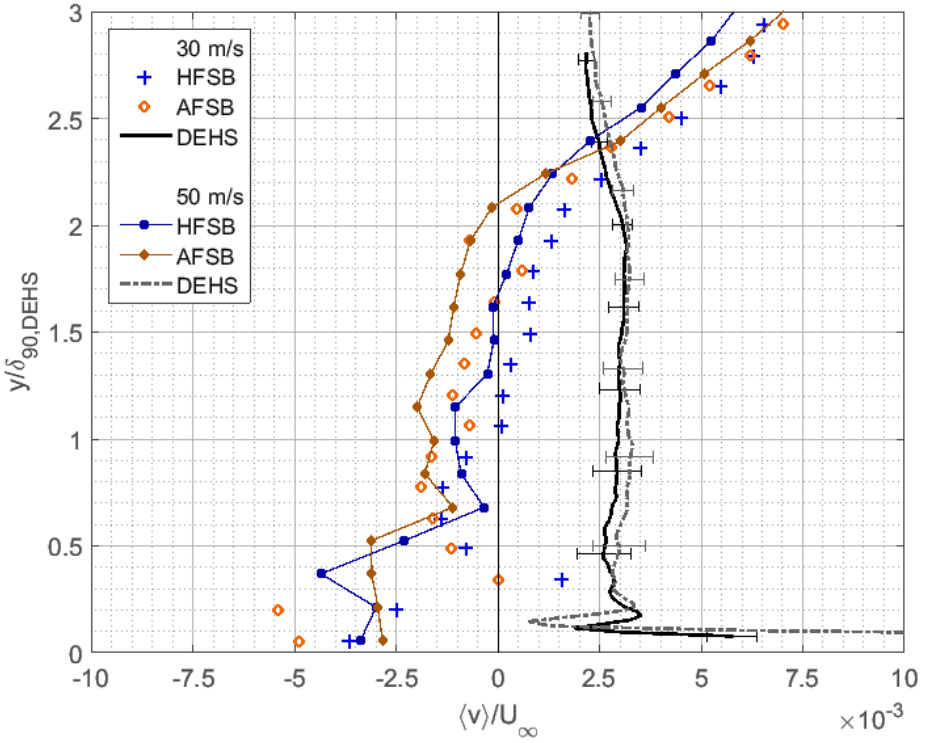

Figure 7-7. Mean wall-normal velocity profiles measured with HFSB and AFSB at 30 and 50 m/s, compared with measurements performed with DEHS tracers.

stream value.

The normal Reynolds shear stress distributions are computed from the root-mean-square of the velocity fluctuations (figure 7-8). The normal stresses are in good agreement with the reference data. The distribution of u'_{rms} and v'_{rms} for both HFSB and AFSB follows that of DEHS with discrepancies of about 0.5% of U_∞. No systematic pattern can be observed for these deviations, indicating that errors are more likely of random type.

The lower values of turbulent fluctuations yielded by HFSB and AFSB at the edge and outside the boundary layer in comparison to the reference data are ascribed to the higher level of random errors associated with the measurements with DEHS tracers. Two-frame cross-

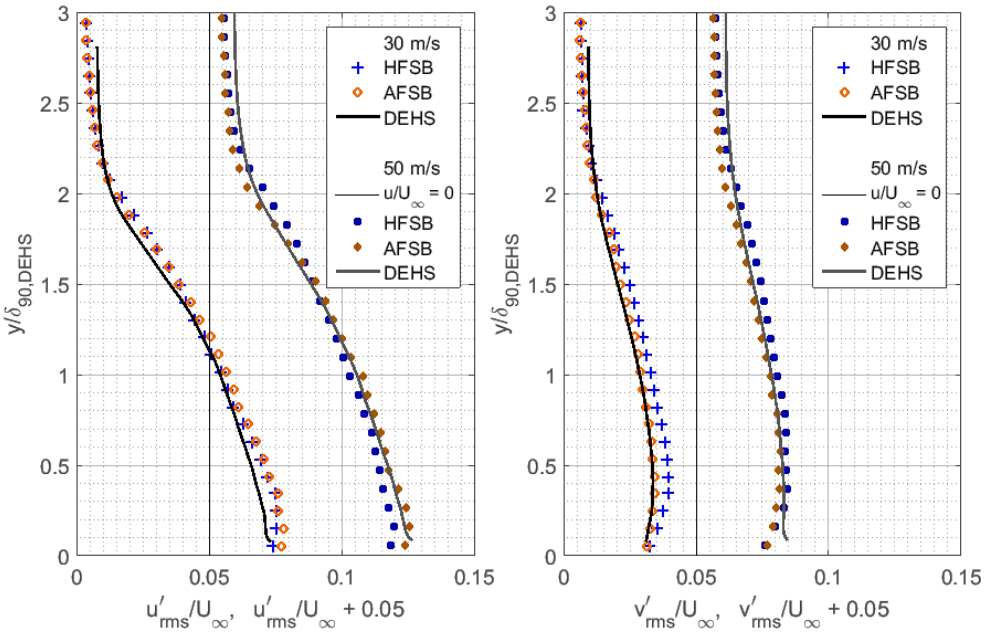

Figure 7-8. Normalized root mean square of streamwise (left) and wall-normal (right) velocity fluctuations measured with DEHS, HFSB and AFSB at 30 and 50 m/s. The 50 m/s profiles are shifted to the right to ease visualization.

correlation systematically overestimates the free stream turbulence intensity by approximately 0.5% of U_∞ (considering a sub-pixel precision of 0.05 px, Raffel et al. 2018).

The normalized Reynolds shear stress profiles (figure 7-9) show a systematic discrepancy with respect to the reference data. The HFSB and AFSB measurements overestimate $\langle u'v' \rangle$ in the region below $y/\delta_{90} = 0.8$. At 30 m/s free stream velocity, the HFSB tracers exhibit a visible deviation from the reference of approximately 10% the local value, with a peak departure of 30% at $y/\delta_{90} = 0.4$. At the same speed, AFSB have a more pronounced deviation, overestimating $\langle u'v' \rangle$ by approximately 20%, and with a maximum difference of 50% at $y/\delta_{90} = 0.15$. The

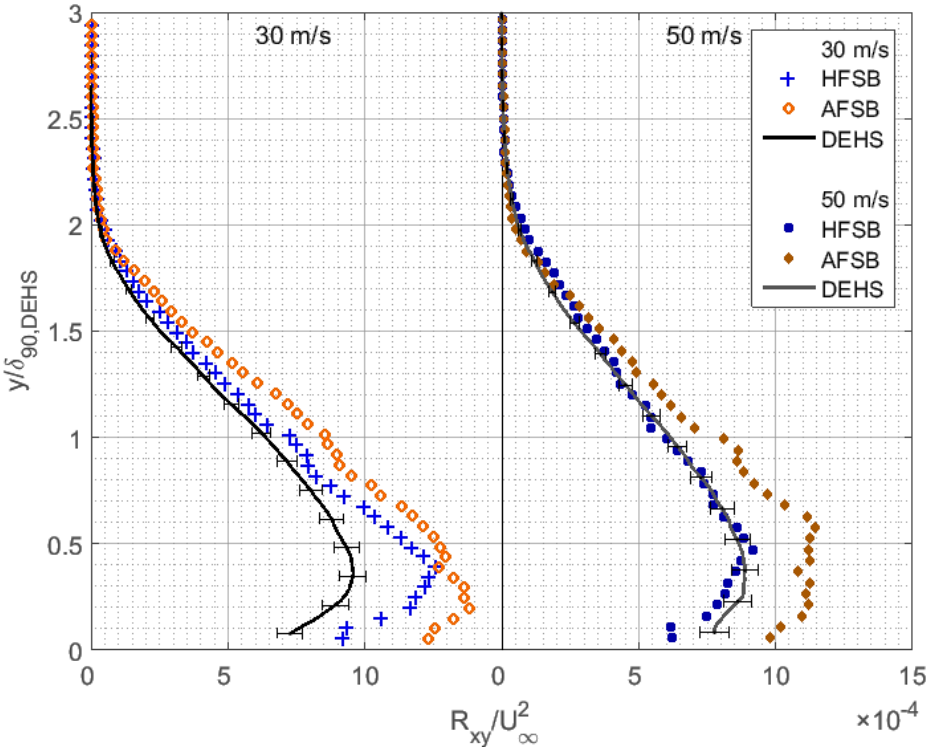

Figure 7-9. Normalized Reynolds shear stress measured with DEHS, HFSB and AFSB at 30 and 50 m/s. The profiles at 50 m/s free stream velocity are shifted to the right to ease the visualization.

cause of the above discrepancy, especially for the HFSB tracers, is not yet understood and should be subjected to further investigation.

At 50 m/s free stream velocity, the discrepancy between HFSB and the reference data is surprisingly small, with only a minor underestimation in the lowest portion of the boundary layer ($y/\delta_{90} < 0.4$). This behavior is somehow in contrast with the expectation that at higher free stream velocity, the measured discrepancy should be exacerbated by the higher level of fluid flow accelerations. The Reynolds shear stress peaks measured with AFSB are also systematically overestimated at 50m/s. The departure to the reference data is in the order of 15% with peak value of 30% around the $y/\delta_{90} = 0.5$.

7.7 Discussion

It was previously hypothesized by the author (Faleiros et al. 2018) that the added-mass force was responsible for the higher tracing fidelity of air-filled soap bubbles in the presence of turbulence. It was argued that the added-mass force, being dominant at high frequencies in comparison to the drag force, was acting to reduce the particle slip velocity. Although, this argument is correct, the effect does not cause the slip velocity to become smaller at lower frequencies, but simply avoids it from becoming even larger than it would in the absence of these forces. As frequency increases, the error eventually converges to a maximum value (figure 6-2). Therefore, the previous hypothesis does not hold, as the added-mass would only limit the slip velocity, but the behaviour of particle inertia acting as a kind of low-pass filter should still be present and it would be evidently larger for AFSB. This, however, is not supported by the data.

Qureshi et al. (2008) offer a more plausible explanation that heavy particles tend to reside longer in the quietest regions of the flow, i.e. regions of the flow of low vorticity and acceleration. This is supported by the work of Coleman and Vassilicos (2009), where they have shown, through simulations in 3D homogeneous isotropic turbulence, that the

sweep-stick mechanism dominates particle segregation for small particles much heavier than the fluid of Stokes numbers of $O(1)$. In such case, particles tend to agglomerate in regions of the flow of zero acceleration. Although not a perfect analogy to the study of soap bubbles in air, one might expect, to a certain degree, a similar behaviour for a heavy bubble.

It would seem that, even though nearly-neutrally-buoyant particles avoid high acceleration events, explaining the dampening of acceleration variance observed by Qureshi et al. (2008) and by the other authors mentioned in the introduction, they still sample the most significant part of the flow to retrieve correct values for the velocity statistics.

7.8 Conclusions

The models of particle slip velocity for laminar flows are not sufficient to describe particle behaviour in turbulence. In general, the velocity statistics obtained with nearly-neutrally-buoyant bubbles in turbulent flows are considerably more accurate than predicted based solely on particle inertia analysis.

Nearly-neutrally-buoyant bubbles retrieve accurate measurements of turbulent boundary-layer properties at Re_θ in the order of 10^3 to 10^4. Relative to measurements with conventional micron-sized tracers (DEHS), HFSB yielded measurements of boundary-layer thickness within 10%, mean streamwise velocity profile within 2% of U_∞, and normal turbulent stresses within 0.5% U_∞. Larger differences were observed in the Reynolds shear stress profiles of up to 30% of the peak value measured by DEHS.

Although air-filled soap bubbles (AFSB) are not able to follow streamline curvatures in the potential flow, in the zero-pressure-gradient turbulent boundary layer, they provide acceptable accuracy for the measurement of mean velocity and normal turbulent stresses.

8

INDUSTRIAL PIV APPLICATION: TILTROTOR AIRCRAFT

8.1 Introduction

Fixed-wing aerial vehicles play a key role in aviation. Driven forward through the use of propellers or jet engines, they achieve higher cruise speeds and mileage than any other aircraft. Helicopters, on the other hand, have lower cruise speeds and flight endurance, but much more flexibility during take-off and landing, and are able to hover at fixed positions. Tiltrotor aircrafts are more versatile vehicles, combining these two concepts to yield high speed cruise and vertical take-off and landing (VTOL). They have three flight modes (figure 8-1): *hover*, *transition* and *cruise*. For these flight modes, various degrees of interference between the prop-rotor and the fuselage appear, affecting the aerodynamic performance and stability of tiltrotor aircrafts (Jung et al. 2014).

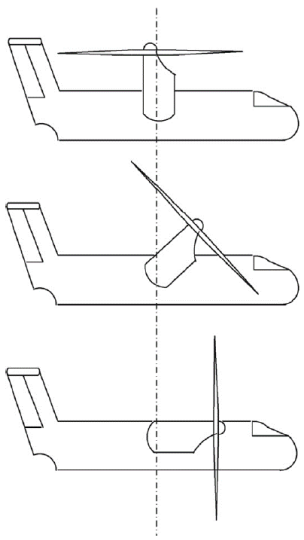

Figure 8-1. Tiltrotor aircraft flight modes: hover (top), transition (middle) and cruise (bottom). Reproduced from Liu et al. (2017).

Within the scope of the NEXT generation civil Tilt Rotor Interactional

aerodynamic tail oPtimisation (NEXTTRIP) project, funded under the HORIZON 2020 EU Research and Innovation programme, large-scale PIV using helium-filled soap bubbles has been applied to study the interaction between the rotor wake and the tail of a tiltrotor. Although the understanding of the fluid dynamics of such an interaction being of extreme relevance to aviation, it is not on the scope of this thesis to give a full presentation of the physics of the problem and comparison to previous investigations on the topic. Instead, the main goal is to demonstrate the capabilities of large-scale PIV using HFSB seeding for aeronautical studies in industrial wind tunnels. Thus, the content of this chapter is of descriptive nature, examining the experimental setup, the quality of the images produced and the results generated.

8.2 Experimental Setup

The experiments were performed in the Large Low-speed Facility (LLF) of the German-Dutch Wind tunnels (DNW). The test-section used for this experiment is 9.5×9.5 m², resulting in an area contraction ratio of about 5:1. The model tested (figure 8-2) is referred to as the NEXTTRIP tiltrotor aircraft. Its design is based on the model developed during the NICETRIP project, which preceded the NEXTTRIP, but with new rotors and tails. The measurement conditions are given on table 8-1.

The stereo-PIV system (figure 8-3) features two LaVision *Imager* sCMOS cameras (2560 × 2160 px², 16 bit, 6.5 μm pixel pitch) equipped with 50 mm focal length objectives (lens aperture diameter of f/16). The FoV was aligned with the streamwise direction, 2.75 m above the test-section floor. The cameras were installed underneath the test section, one

Flight mode	Rotor angle	U_∞ (m/s)	Yaw angle β	N° of planes
Cruise	0°	60 m/s	0°	7
Transition	45°	40 m/s	0°	5
Hover	90°	15 m/s	10°	4

Table 8-1. Test conditions. The aircraft pitch and roll angles were kept at 0° for all conditions.

Figure 8-2. The NEXTTRIP tiltrotor aircraft installed in the DNW-LLF 9.5×9.5 m² test-section.

upstream and another downstream of the FoV centre, at an angle of about 60º with the horizontal plane. The optical magnification was 0.015, yielding a FoV of 1.1 × 1.1 m², spanning from wing to tail. The image resolution was 2.5 px/mm. A Quantel *Evergreen 200* Nd:YAG laser (2×200 mJ/pulse at 15 Hz) was used for the particle illumination. The laser sheet thickness was 10 mm. The recordings were made in frame-straddling mode (double-frame, single exposure). The pulse time separation was set to 280, 110, and 70 µs for 15, 40 and 60 m/s, respectively, yielding about 10 px displacement in the free stream.

The aircraft was moved in the vertical direction, so that different streamwise planes could be sampled with respect to the aircraft vertical position, using a single PIV calibration. The measurement planes were

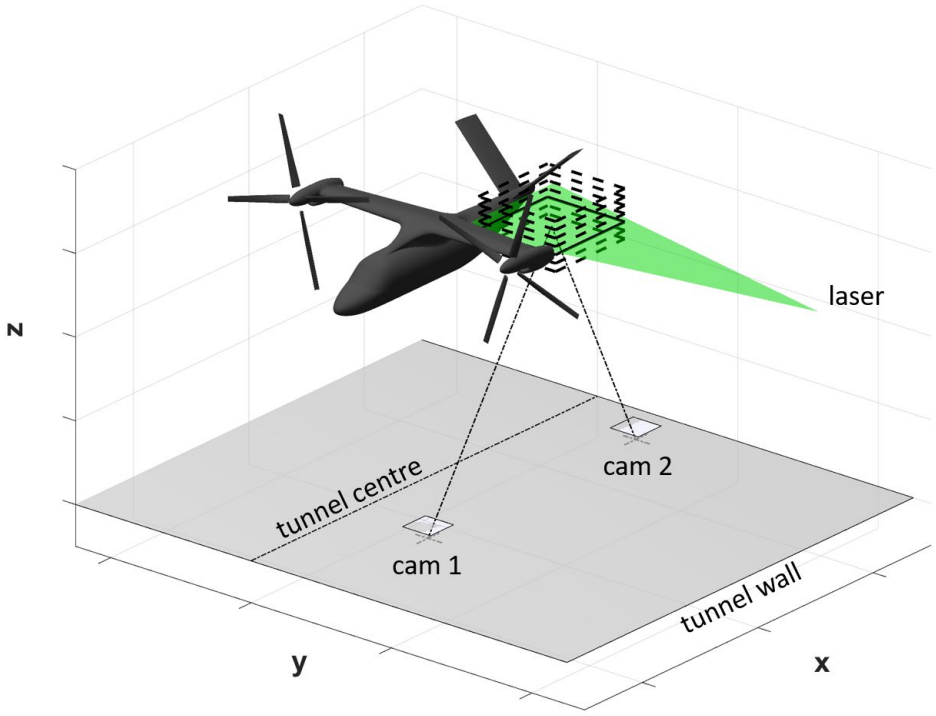

Figure 8-3. Experimental set-up. The square outlined within the laser sheet (black solid line) represents the measured FoV, as positioned with respect to the tunnel. The dashed squares parallel to the FoV represent the measured positions (cruise configuration) with respect to the model (in reality the FoV remains fixed in space, while the model is translated up and down in steps of 10 cm). The cameras are positioned underneath the test section.

spaced 10 cm from each other in most cases. The number of measurement planes per condition is given in table 8-1. A total of 4000 image pairs per camera were obtained per measurement plane. Combining the seven measurement planes in the cruise condition, for instance, the measurement depth is 60 cm, yielding a measurement volume larger than 700 litres.

The HFSB seeding rake (figure 8-4), manufactured by NLR, consists of 400 bubble generators, distributed along 20 vertical wings, and covering an area of 9 m². Considering the tunnel contraction ratio of 5:1, the bubble streamtube cross-section becomes about 2 m² in the test section, covering more than half of the model frontal area (figure 8-5). Figure 8-6 shows the extend of the streamtube of bubbles within the laser sheet.

The fluid supply unit, coupled with a mass flow controller for air, and mass flow meters and pressure controllers for helium and soap, was placed outside of the tunnel. Approximately 25,000 l of air, 3.1 l of soap and 2800 l of helium ($Q_{He}/Q_{soap} = 900$) were supplied to the rake

Figure 8-4. NLR seeding rake of 400 bubble generators, 20 wings and cross-section area of 9m², installed in the DNW-LLF settling chamber.

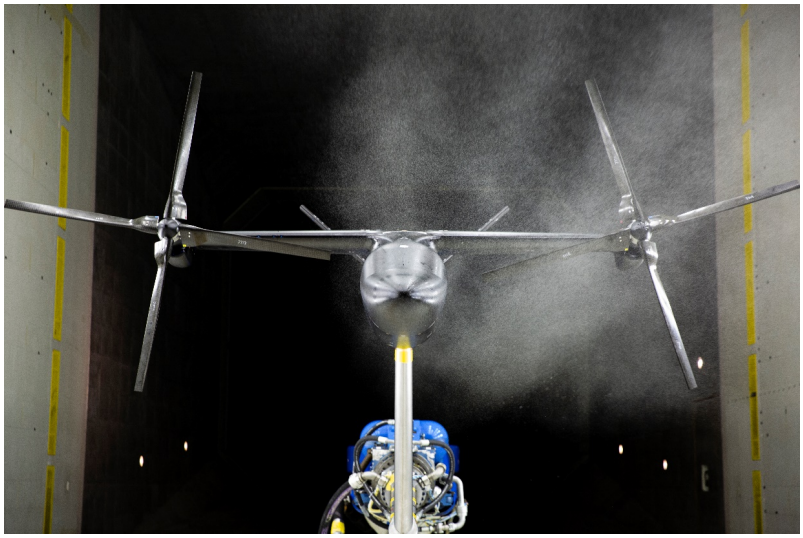

Figure 8-5. HFSB stream tube of 2 m² in the test-section, after contraction, covering about half the model frontal area.

every hour, that is, 70 l/h of air, 7 l/h of helium and 7.75 ml/h of soap per generator. Approximately 25,000 monodisperse neutrally-buoyant HFSB of 0.5 mm diameter were delivered every second per nozzle. The entire

Figure 8-6. The extent of the HFSB stream tube that is captured within the laser sheet. The FoV was 1.1×1.1 m².

rake produced 10 million bubbles per second, resulting in a nominal bubble concentration of 0.09, 0.14 and 0.37 bubbles/cm³ for 60, 40 and 15 m/s free stream velocities.

8.3 Bubble concentration and interrogation window size

A raw image recorded during cruise configuration at 60 m/s is shown in figure 8-7, with the central area (640×640 px²) of the field of view amplified on the right, showing 100 interrogation windows (IW) of 64×64 px² (2.5×2.5 cm²). By visual inspection of the image, it is observed up to eight particles per IW. For cross-correlation algorithms to be applied, a minimum of about five particles per IW is required for 95% valid detection probability, $N_{ppp} = 0.01$ and acceptable $F_o = 0.8$ (figure 2-13).

The particle concentration is quantified by counting the particles in the raw images using an in-house algorithm that identify particles by searching for the local maxima. A total of 500 images per measurement plane is used for this purpose. The concentration values are then interpolated in between planes for visualization of the concentration

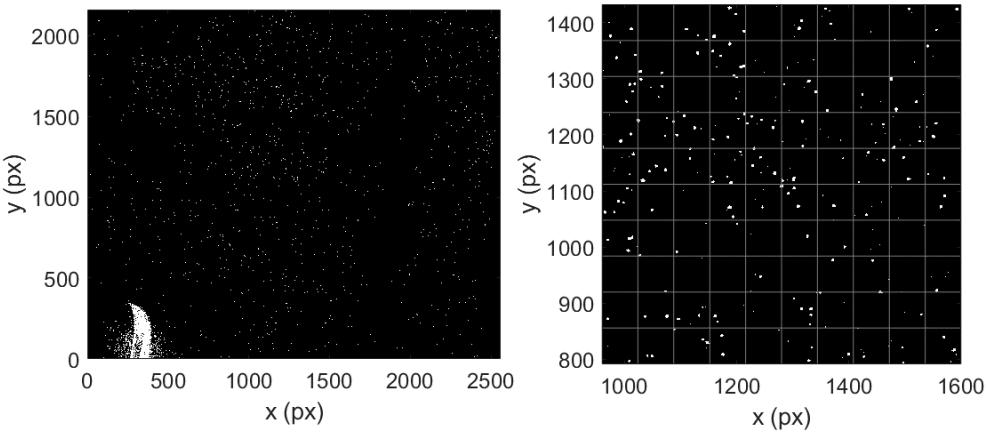

Figure 8-7. Left: raw image recorded in a single time instant by camera-1 in the cruise configuration at 60 m/s free stream velocity. Right: amplified version of the left image, showing 10×10 interrogation windows of 64×64 px².

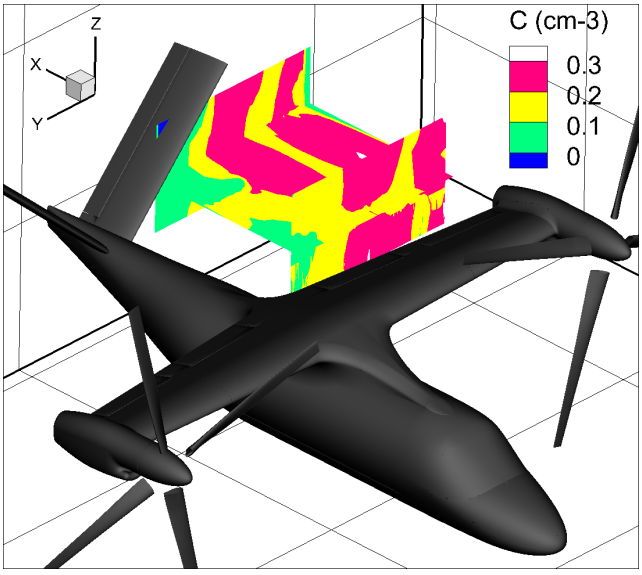

Figure 8-8. Particle concentration at cruise configuration, U_∞ = 60 m/s.

along x-planes (cross-flow).

At 60 m/s free stream velocity (cruise configuration, figure 8-8), $C \sim 0.2$ bubbles/cm³ in the rotor wake. As expected from eq. (3.1), the bubble concentration is higher at lower speeds: $C \sim 0.3$ bubbles/cm³ at 40 m/s (transition, figure 8-9) and 0.4 bubbles/cm³ at 15 m/s (hover, figure 8-10). In the latter case, however, the bubble streamtube is strongly deflected downwards by the downwash flow stemming from the rotor blades. The measured bubble concentration is sufficiently close to the estimated values, considering errors due to particle identification, laser sheet thickness estimation, possible inhomogeneity in the bubble generation across the rake and also due to flow contraction in the propeller wake.

Considering the lowest measured concentration of 0.2 bubbles/cm³, a laser sheet thickness of 10 mm and image resolution of 2.5 px/mm, it is found that $N_{ppp} = 0.0003$. In addition $N_I = 5.2$ and $N_I = 1.3$ for $D_I = 128$ px and $D_I = 64$ px, respectively. The out-of-plane motion is much

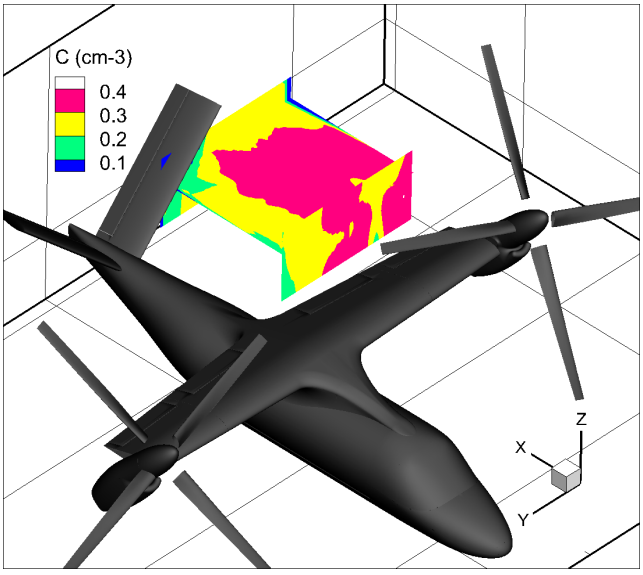

Figure 8-9. Particle concentration at transition configuration, U_∞ = 40 m/s.

smaller than the laser sheet thickness in the cruise configuration ($F_o \sim 1$). In the hover configuration, $\Delta z \sim \Delta x \sim 10$ px (4 mm), yielding $F_o \sim 0.6$.

According to figure 2-13 the rule of thumb of $N_I \geq 5$ (Raffel et al.

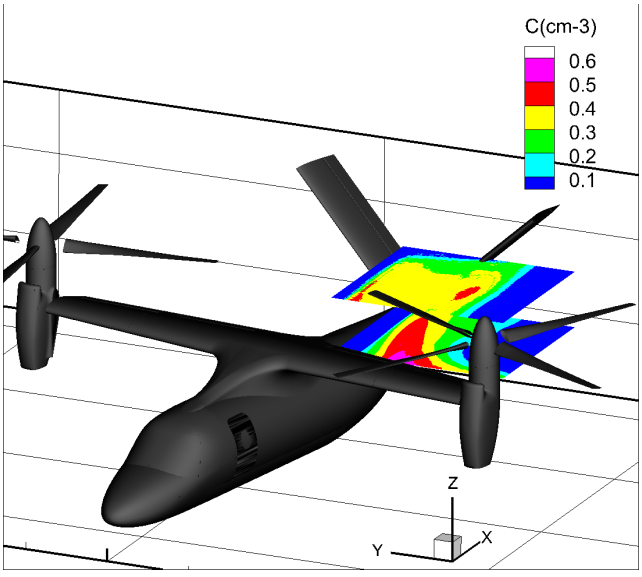

Figure 8-10. Particle concentration at hover configuration, U_∞ = 15 m/s.

2018), seems conservative for a particle density of $N_{ppp} = 0.0003$, especially for the cruise configuration, where the out-of-plane motion is negligible.

An iterative multi-grid interrogation algorithm is used starting from $D_I = 128$ px down to $D_I = 64$ px. Visual inspection of instantaneous velocity fields using different final interrogation window sizes only showed increase in spurious vectors as the final D_I becomes smaller than 64 px. With D_I = 64 px and 75% of IW overlap, the resolution is 1 vector every 6.5 mm. The minimum length scale that can be measured, however, is given by the IW size, not accounting for overlap. Considering the larger size of the camera sensor (2560 px) as the maximum measurable length scale, the dynamic spatial resolution (section 2.7) of the system is $DSR = 40$.

8.4 Results

Mean velocity fields measured in the cruise (figure 8-11) and hover

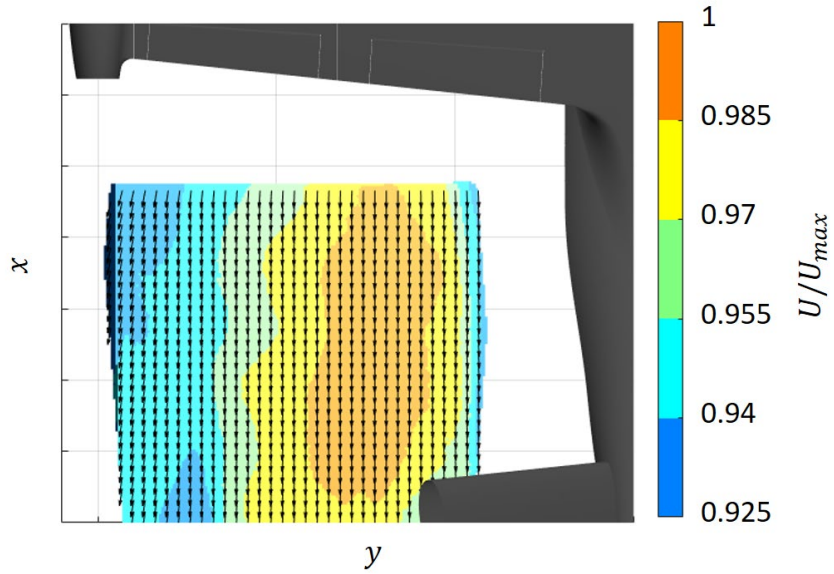

Figure 8-11. Velocity magnitude at cruise configuration. Vectors represent in-plane velocity components. Showing 1 every 25 vectors.

(figure 8-12) configurations show the vector resolution obtained within a single measurement plane. Only 1 every 25 vectors is shown for ease of visualization. Clearly, the vector resolution in streamwise and spanwise directions is sufficiently high to capture the large-scale flow features. Combination of the different z-planes allow interpolation of the data in the transverse direction, and, thus, visualization of cross-flow planes and three-dimensional flow features. The spatial resolution in the transverse direction is, however, significantly lower, and given by the distance between the measured z-planes (about 10 cm in most cases).

Cross-flow planes for the cruise configuration (figure 8-13) show the propeller wake deficit in the streamwise velocity component and its rotational nature reflected in the v and w velocity components, propagating downstream, and sufficiently far from the v-tail. The wing

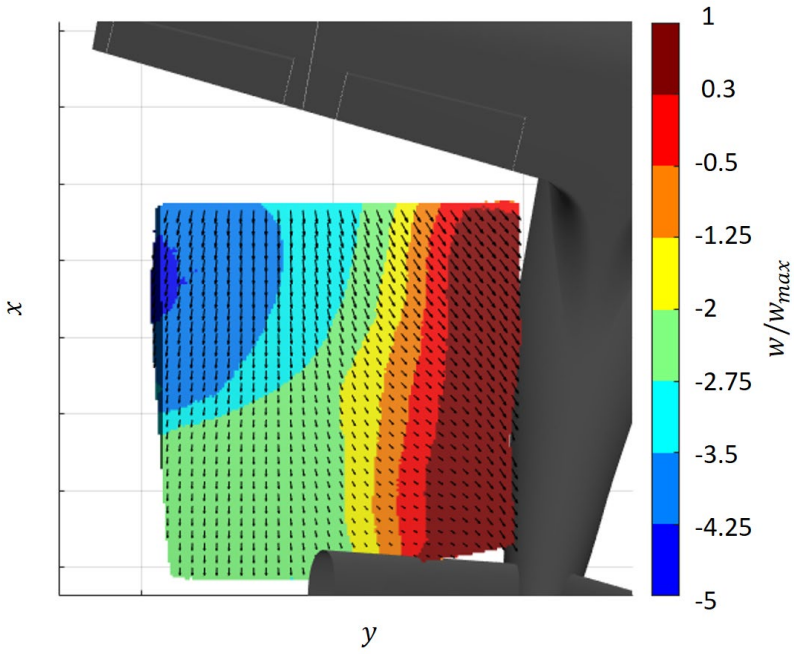

Figure 8-12. Velocity components at hover configuration. Vectors represent in-plane velocity components. Showing 1 every 25 vectors.

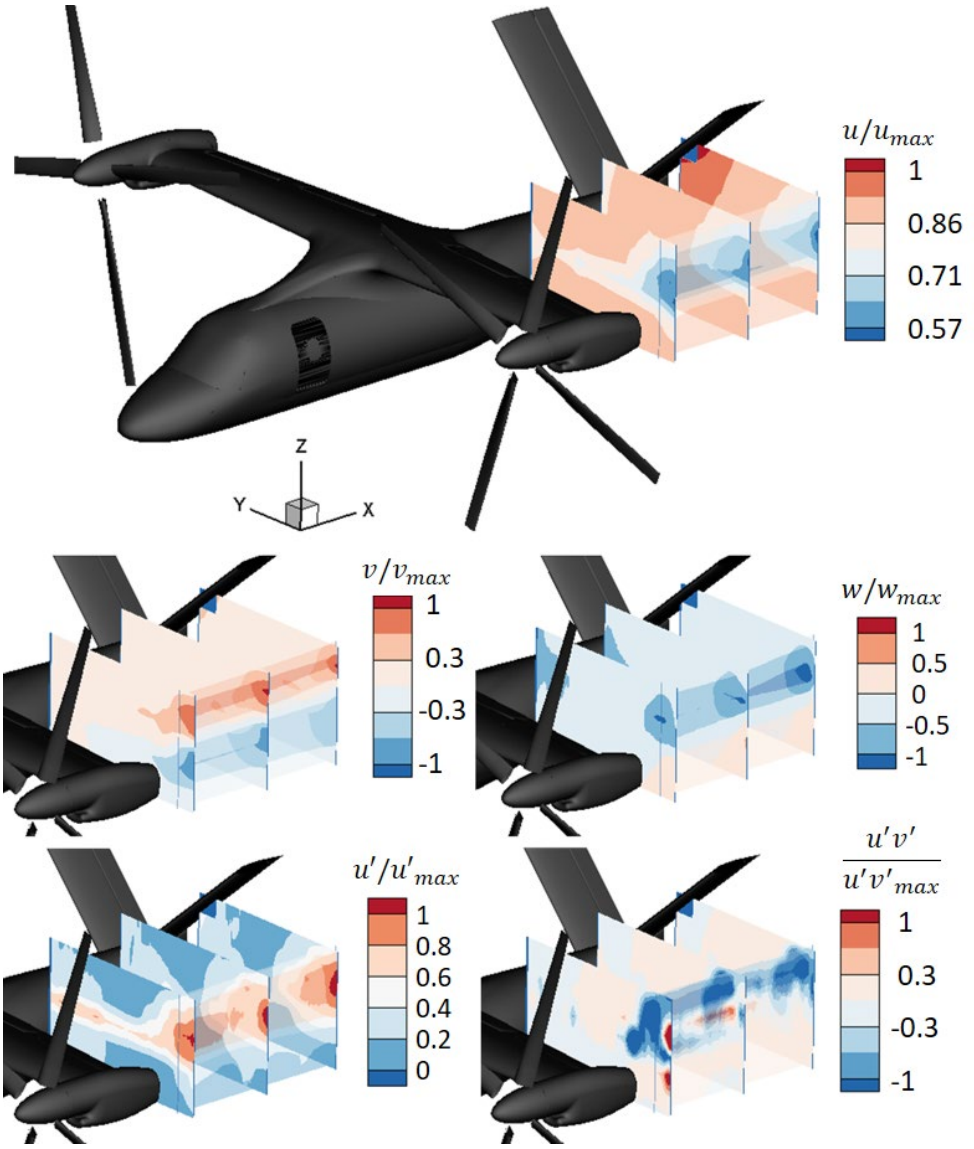

Figure 8-13. Mean velocity and velocity fluctuations in the cruise configuration.

wake is also noticeable in the u component, as well as in the root-mean-square of the streamwise turbulence fluctuation u'. The turbulent-stress

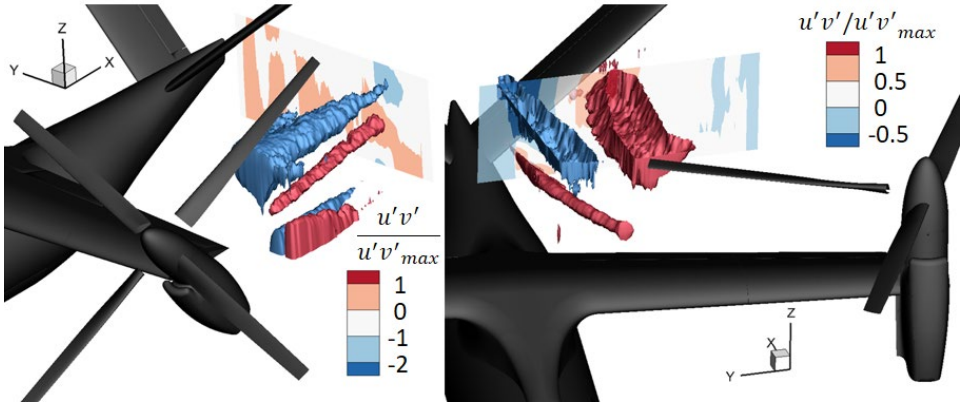

Figure 8-14. Reynolds stress at transition (left) and hover (right) configurations. Isosurfaces of $u'v'/u'v'_{max}$ (blue for negative and red for positive): -2 and 1 (left), and -1.25 and 1 (right).

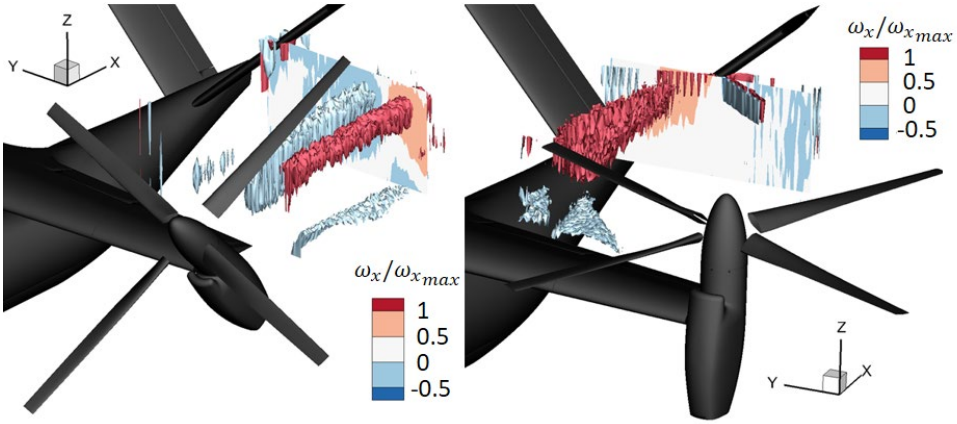

Figure 8-15. Vorticity ω_x at transition (left) and hover (right) configurations. Isosurfaces of $\omega_x/\omega_{x,max}$ = 1 (red) and $\omega_x/\omega_{x,max}$ = -0.3 (light blue).

$u'v'$ is most significant in the propeller wake. Still, only a small fraction of the free stream velocity squared.

Figure 8-14 shows isosurfaces of turbulent stresses $u'v'$ for the transition and hover configurations. The latter had also a yaw angle of 10° (figure 8-12). In the transition configuration, the normalized Reynolds stress is larger but of similar magnitude than in the cruise configuration. With zero yaw angle and propeller at 45° the turbulent

stresses indicate that the propeller wake is propagated downstream without interacting with the tail. The only case where the propeller wake affects the aircraft stability is for the hover configuration. Turbulent stresses, seemingly emanating from the tip of the propeller blades, impinge onto the aircraft v-tail. The normalized $u'v'/U_\infty^2$ is one order of magnitude larger than in the cruise configuration. Wake interaction with the v-tail (positive vorticity) and with the fuselage (negative vorticity) is also observed for the hover configuration by analysing the streamwise vorticity ω_x (figure 8-15).

8.5 Final observations and conclusions

A system for seeding large air flow volumes in a wind tunnel with submillimetre soap bubbles has been engineered, leading to the execution of a successful industrial PIV test around a tiltrotor aircraft, for which only 12 wind tunnel hours have been allocated (including the assembly of the rake in the settling chamber and the PIV calibration). The set of empirical rules that have been developed during chapters 4 and 5 were essential for the controlled generation of HFSB and the success of this test. Not to mention several technicalities that had not been described in this thesis, not being of new scientific value, but that are essential for the equal distribution of fluids to the nozzles internally of the seeding rake, and for the remote and precise control of the mass flow rates of helium, air and soap. These efforts guaranteed homogeneous and stable production across the rake, as observed through the photographs and with the naked eye.

In comparison to using micrometre seeding, the benefits demonstrated are several:

- A relatively large measurement plane is illuminated using a single laser;
- Background reflections are negligible compared to the intensity of the light reflected on the bubbles;
- Particle images of 2-3 pixels are achieved without defocusing;

- The camera aperture may be significantly closed (fully closed in these measurements), yielding large depths of field, which render the use of Scheimpflug adapters unnecessary.

PIV cross-correlation was also shown to be possible, however, at the limit of what is considered acceptable in terms of particle concentration, regarding the minimization of spurious vectors. Increasing the particle concentration by adding more bubble generators is possible, but not practical. The seeding rake used for these measurements, already contained 20 three-meter wings, 15 cm apart. The cost of adding more wings and the wind tunnel blockage that it would result, also indicates that this is close to the limit of the bubble concentration that can be achieved with this technique.

A more elegant solution is to combine HFSB with three-dimensional measurements. When a 3D volume is imaged with a 2D camera sensor, the concentration of the projected images onto the 2D plane increases linearly with the volume depth. For large-scale 3D measurements, the HFSB concentration is already close to the maximum concentration acceptable. For instance, considering a volume of 1 m^3, a particle concentration of 0.25 bubbles/cm^3, and a 5 Mpx camera sensor, the particle image density is 0.05 ppp, which is the limit for a three-camera tomographic PIV measurement (Scarano 2013). Sophisticated 3D PTV algorithms that use the Iterative Particle Reconstruction (IPR, Wieneke 2013) and track particles in time-resolved measurements (Shake-The-Box, Schanz et al. 2016) may reach 0.125 ppp. Hence, the HFSB concentration is ideal for 3D measurements, effectively utilizing the camera sensor. In comparison to plane-scanning schemes, the number of images stored and processed are reduced significantly, and the spatial resolution of average flow fields may be well-resolved for all spatial coordinates, which may be continuously increased by acquiring more images. The minimum length scale that can be resolved is only limited by the particle size (Xu and Bodenschatz 2008).

9

CONCLUSIONS AND OUTLOOKS

9.1 Conclusions

9.1.1 Generation of helium-filled soap bubbles

The generation of HFSB for wind tunnel applications is properly realized using orifice-type nozzles, which are able to provide submillimetre bubbles at sufficiently high production rates for use in low speed aerodynamics, by combining hundreds of nozzles into aerodynamically-shaped rakes.

The generation of HFSB through this type of nozzle is influenced by the nozzle dimensions and the volume flow rates of the input fluids: air, helium and soap solution. Several production regimes of HFSB have been classified qualitatively. Guidelines based on the fluid flow rates have been given to avoid polydisperse and chaotic production, such as, production in the jetting regime, merging of bubbles, double bubbling and satellite bubbles.

The monodisperse production of HFSB, termed as bubbling regime, has been thoroughly studied in terms of bubble size, density and production rate. The bubble volume was found to increase linearly with the ratio of helium-to-air volume flow rates and with the nozzle orifice diameter. The bubble production rate was observed to be mainly dependent on the air volume flow rate, increasing linearly with the latter.

Experiments involving the measurement of HFSB time response, under specific conditions, allowed the estimation of the bubble density.

The latter was demonstrated to decrease approximately linearly with the ratio of helium-to-soap mass flow rates. The optimal ratio of helium and soap flow rates, yielding the generation of neutrally buoyant bubbles, was found to be 900:1. This is higher than the theoretical ratio (1080:1). The difference was attributed to soap spillage during the generation process.

The findings on the generation of HFSB are well summarized in figure 4-11, for a 1 mm orifice diameter nozzle. The optimal region, where the bubbles are simultaneously monodisperse and neutrally buoyant is given as a function of helium and air flow rates, represented by isolines, while the bubble diameter and production rates are given in the horizontal and vertical axes, respectively. Considering the ideal working region (bubbling and neutrally buoyant), there is still a considerable range of choice for the HFSB diameter (0.45-0.6 mm) and production rate (10,000-50,000 bubbles per second).

9.1.2 Tracing fidelity of nearly-neutrally-buoyant particles

9.1.2.1 The time response concept

Large part of the PIV community is familiar with concepts that are only valid for solid powders and heavy droplets. For instance, the concept of characterizing the particle tracing fidelity through a time response. Naturally, as the focus turned to small bubbles, similar concepts and ideas have been applied to characterize the bubble tracing fidelity. The concept of time response for bubbles, however, has to be used with caution; it is only appropriate when the acceleration difference with the flow acceleration is minimal, rendering unsteady forces negligible. In many flows, however, the mismatch between particle and fluid accelerations is considerable, and the unsteady forces must be included for determining the slip velocity of nearly-neutrally-buoyant bubbles (chapter 6). In this case, the bubble tracing fidelity depends on

three parameters: the *normalized particle density*, the *particle Reynolds number* and the *normalized flow time-scale*.

9.1.2.2 The slip velocity of particles travelling around objects

The forces experienced by a particle accelerating around an object were shown to be similar to that experienced in a rectilinear sinusoidal flows (chapter 6). This enabled the particle slip velocity around an object to be estimated, through the simpler analysis of sinusoidal flows. Empirical relations relating the slip velocity to the particle properties, flow frequency and phase were then derived based on numerical simulations that include the effect of unsteady forces and allow for mismatch of acceleration between particle and fluid. The derived relations were applied to assess HFSB slip velocity, mean density and density dispersion. The latter was shown to cause velocity fluctuations in laminar regions of the flow of high acceleration, which was attributed to variations of the soap film thickness during generation. Dispersion of the bubble diameter has been shown to be negligible in comparison to the latter.

9.1.2.3 HFSB tracing fidelity in turbulent flows

The HFSB tracing fidelity has also been studied in wall-bounded turbulence and compared with DEHS and air-filled soap bubbles (AFSB). The mean velocity and fluctuations have been accurately measured with HFSB and, contrarily to the initial expectations, also with AFSB. A plausible explanation is that, while tracing turbulence, the particles tend to concentrate in regions of the flow of low acceleration and vorticity (Coleman and Vassilicos, 2009), where the particles can more easily follow the flow. The velocity statistics are well captured by nearly-neutrally-buoyant particles and mostly dampening of acceleration variance is observed, as the size or density of the particle is increased (Qureshi et al. 2008).

9.1.3 Industrial application

The use of HFSB (3×3 m^2 seeding rake, 400 generators) for large-scale (9.5×9.5 m^2 test section) stereo-PIV measurements (1.1×1.1 m^2 FoV) at relevant speeds (up to 60 m/s) for aeronautical experiments in an industrial facility (LLF wind tunnel of DNW) was successfully demonstrated in the flow around a tiltrotor aircraft. The particle concentration achieved was sufficient for cross-correlation analysis, yielding 1 vector every 6.5 mm (64×64 px^2 IW with 75% overlap) and a dynamic spatial resolution of 40.

9.2 Outlooks

9.2.1 HFSB integration in testing facilities

With HFSB proving itself as the most suitable option for seeding of large-scale air flows, it is not too farfetched to imagine that some research institutions will opt to engineer new HFSB-adapted wind tunnels, including:

- bubble capture devices downstream of the test-section;
- permanently installed and aerodynamically optimized HFSB seeding rakes in the settling chamber, with easy access for maintenance.

Such adaptations may ease the burden of soap contamination, while providing more reliable seeding systems, especially regarding leakages.

9.2.2 HFSB for indoor human-related studies

HFSB will also play a more fundamental role on indoor flow investigations, as already applied, for instance, in aircraft cabin mock-ups (Bosbach et al. 2009) and for cyclist aerodynamics (Spoelstra et al. 2019), but also for the analysis of indoor ventilation in cinemas, restaurants, classrooms, hospitals, among others, for minimizing the indoor concentration of pathogens and the risk of infection. Disregarded until recently, the latter topic was brought up to focus in the COVID-19 pandemic. For instance, air-filled soap bubbles expelled from the mouth

of mannequins was utilized for the analysis of High-Efficiency Particulate Air (HEPA) systems as means for mitigation of indoor airborne transmission of infectious diseases (Bluyssen et al. 2021).

9.2.3 Large-scale 3D PTV with HFSB for high-speed flows and statistical analysis

As discussed in section 8.5, HFSB are ideal for 3D measurements, effectively utilizing the camera sensor (typical HFSB concentrations approach the limit particle image density accepted for a cubic-metre volume). In the last decade, there have been some developments on particle tracking, which shifted away the attention from cross-correlation algorithms for 3D velocimetry (tomographic-PIV, Elsinga et al. 2006, Scarano 2013) to PTV-based approaches:

- the introduction of the iterative particle reconstruction (IPR) technique (Wieneke 2013), which enables tracking-based algorithms to handle seeding densities typical of tomographic PIV;
- the development of a PTV algorithm that combines IPR with temporal information (STB, Schanz et al. 2016), extrapolating particle trajectories in time to find particle locations faster and more accurately, handling large particle image density (0.125 ppp), and reducing the computational burden of applying 3D-triangulation every time step.

The limitation of STB is the requirement of time-resolved measurements, which constraints the technique to low flow speed measurements. In addition, STB is not ideal for statistical analysis, which requires vectors to be uncorrelated in time.

Novara et al. (2019) proposed three multi-pulse (MP-STB) methods, using two double-pulse lasers to overcome this restriction, namely:

1. polarization-based pulse separation (polarization filter);
2. timing-based pulse separation (double-shutter);
3. double-frame double-exposure.

The polarization- and timing-based techniques require two independent 3D multi-camera imaging systems, while the double-frame double-exposure strategy suffers from stricter particle density limitations. The innovation of MP-STB in comparison to similar techniques (Malik et al. 1993, Cierpka et al. 2013), previously applied to time-resolved four-frame measurements, is the use of double-frame measurements (shorter time intervals) and the iterative procedure, which uses the tracking information to reposition particles based on polynomial fits and update the IPR. MP-STB does not benefit, however, from the reduced computational time of time-resolved STB, as particle prediction is not available.

So far, it does not seem that spatial information from neighbouring particles have been applied in combination with IPR. For instance, Cierpka et al. (2013) applied the relaxation method of Ohmi and Li (2000) in combination with the temporal predictor concept, based on Malik et al. (1993), to improve significantly the yield of correctly paired vectors.

Therefore, there is room for innovation on two areas regarding 3D PTV measurements for high-speed flows or statistical analysis:

1. PIV hardware that is able to handle multi-pulse recordings more easily;
2. Computational efficient 3D PTV algorithms that incorporate spatial (from neighbouring particles) and temporal information in combination with IPR for multi-pulse measurements.

REFERENCES

Adrian RJ (1984) Scattering particle characteristics and their effect on pulsed laser measurements of fluid flow: speckle velocimetry vs particle image velocimetry. Appl Opt 23:1690.

Adrian RJ, Yao CS (1985) Pulsed laser technique application to liquid and gaseous flows and the scattering power of seed materials. Appl Opt 24:44.

Adrian RJ (1991) Particle-imaging techniques for experimental fluid mechanics Annu Rev Fluid Mech 23:261.

Adrian RJ (1997) Dynamic ranges of velocity and spatial resolution of particle image velocimetry. Meas Sci Technol, 8:1393.

Adrian RJ (2005) Twenty years of particle image velocimetry. Exp Fluids 39:159.

Adrian RJ (2009) Bibliography of particle velocimetry using imaging methods: 1917-1995. DLR, Göttingen Anniversary Edition.

Agüera N, Cafiero G, Astarita T, Discetti S (2016) Ensemble 3D PTV for high resolution turbulent statistics. Meas Sci Technol 27:124011.

Anderson JD (2010) Brief History of the Early Development of Theoretical and Experimental Fluid Dynamics. Encyclopedia of Aerospace Engineering.

Atkinson C, Coudert S, Foucaut JM, Stanislas M, Soria J (2011) The accuracy of tomographic particle image velocimetry for measurements of a turbulent boundary layer. Exp Fluids 50:1031.

Basset AB (1888a) A treatise on hydrodynamics. Deighton Bell, London.

Basset AB (1888b) On the Motion of a sphere in a Viscous Liquid, Philos T R Soc 179:43.

Benton SI, Visbal MR (2018) Understanding abrupt leading edge separation as a mechanism for the onset of dynamic stall. 2018 AIAA Aerospace Sciences Meeting p. 0356.

Belligoli Z, Dwight R, Eitelberg G, Srikumar S, Faleiros DE, van Nesselrooij M, van Campenhout O (2020) A Review of Numerical and Experimental Studies of the Anti-Fairing. AIAA AVIATION 2020 FORUM, June (virtual event).

Bluyssen PM, Ortiz M, Zhang D (2021) The effect of a mobile HEPA filter system on “infectious” aerosols, sound and air velocity in the SenseLab. Building Environ, 188:107475.

Bosbach J, Kühn M, Wagner C (2009) Large scale particle image velocimetry with helium filled soap bubbles. Exp Fluids 46:539.

Bourgoin M, Qureshi N M, Baudet C, Cartellier A, Gagne Y (2011) Turbulent transport of finite sized material particles. J Phys Conf Ser 318:012005.

Boussinesq (1885a) Applications â l'étude des potentiels (reedition 1969). Blanchard, Paris.

Boussinesq (1885b) Sur la résistance qu’oppose un fluide indéfini au repos . . . C R Acad Sci III 100:935.

Brücker CH (1996) 3-D scanning-particle-image-velocimetry: Technique and application to a spherical cap wake flow. Appl Sci Res 56:157.

Calzavarini E, Volk R, Bourgoin M, Lévêque E, Pinton J-F, Toschi F (2009) Acceleration statistics of finite-sized particles in turbulent flow: the role of Faxén forces. J Fluid Mech 630:179.

Caridi GCA, Ragni D, Sciacchitano A, Scarano F (2016) HFSB seeding for large scale tomographic PIV in wind tunnels. Exp Fluids 57:190.

Caridi GCA (2018) Development and application of helium-filled soap bubbles for large-scale PIV experiments in aerodynamics. PhD thesis, TU Delft, Delft.

Cierpka C, Lütke B, Kähler CJ (2013) Higher order multi-frame particle tracking velocimetry. Exp Fluids 54:1533.

Clift R, Grace J, Webe M (1978) Bubbles, drops and particles. Academic Press, New York.

Coleman SW, Vassilicos JC (2009) A unified sweep-stick mechanism to explain particle clustering in two- and three-dimensional homogeneous, isotropic turbulence. Phys Fluids 21:113301.

Comte-Bellot G (1976) Hot-Wire Anemometry, Annu Rev Fluid Mech 8:209.

DeBonis JR, Oberkampf WL, Wolf RT, Orkwis PD, Turner MG, Babinsky H, Benek JA (2012) Assessment of Computational Fluid Dynamics and Experimental Data for Shock Boundary-Layer Interactions. AIAA Journal 50:891.

De Gregorio F, Pengel K, and Kindler K (2010) Industrial measurement campaign on fully equipped helicopter model. 15th International symposium on applications of laser techniques to fluid mechanics, Lisbon.

Drela M (1989) XFOIL: an analysis and design system for low Reynolds number airfoils. In: Low Reynolds Number Aerodynamics, ed. TJ Mueller. Lect Notes Eng 54. Springer, New York.

Elkins III RE, Jackman GR, Johnson RR, Lindgren ER, Yoo JK (1977) Evaluation of stereoscopic trace particle records of turbulent flow fields. Rev Sci Instrum 48:738.

Elsinga GE, Scarano F, Wieneke B, van Oudheusden BW (2006) Tomographic particle image velocimetry. Exp Fluids 41:933.

Faleiros DE, Tuinstra M, Sciacchitano A, Scarano F (2019) Generation and control of helium-filled soap bubbles for PIV. Exp Fluids 60:40.

Faleiros DE, Tuinstra M, Sciacchitano A, Scarano F (2018) Helium-filled soap bubbles tracing fidelity in wall-bounded turbulence. Exp Fluids 59:56.

Faxén (1922) Der Widerstand gegen die Bewegung einer starren Kugel in einer zähen Flüssigkeit, die zwischen zwei parallelen Ebenen Wänden eingeschlossen ist. Ann Phys (Berl) 4:89.

Favier D (2010) The role of wind-tunnel experiments in CFD validation. In: Encyclopedia of Aerospace Engineering.

Fuchs T, Hain R, Kähler CJ (2017) Non-iterative double-frame 2D/3D particle tracking velocimetry. Exp Fluids, 58:119.

Fukuchi Y (2012) Influence of number of cameras and preprocessing for thick volume Tomographic PIV. 16th International symposium on applications of laser techniques to fluid mechanics, Lisbon.

Ghaemi S, Scarano F (2011) Counter-hairpin vortices in the turbulent wake of a sharp trailing edge. J Fluid Mech 689:317.

Gibeau B, Ghaemi S (2018) A modular 3D-printed helium-filled soap bubble generator for large-scale volumetric flow measurements. Exp Fluids 59:178.

Gibeau B, Gingras D, Ghaemi S (2020) Evaluation of a full-scale helium-filled soap bubble generator. Exp Fluids 61:28.

Hale RW, Tan P and Ordway DE (1969) Experimental Investigation of Several Neutrally-Buoyant Bubble Generators for Aerodynamic Flow Visualization. Sage Action Inc, SAI-RR 6901, AD-717 390.

Hale RW, Tan P, Stowell RC, Ordway DE (1971) Development of an Integrated System For Flow Visualization In Air Using Neutrally Buoyant Bubbles. Sage Action Inc, SAI-RR 7107, AD-756 691.

Hinterwaldner I (2015) Model building with wind and water: Friedrich Ahlborn's photo-optical flow analysis. Stud Hist Philos Sci 49:1.

Hoffmann C (2013) Superpositions: Ludwig Mach and Étienne-Jules Marey's studies in streamline photography. Stud Hist Philos Sci 44:1.

Huhn F, Schanz D, Gesemann S, Dierksheide U, van de Meerendonk R, Schröder A (2017) Large-scale volumetric flow measurement in a pure thermal plume by dense tracking of helium-filled soap bubbles. Exp Fluids 58:116.

Humble RA, Elsinga GE, Scarano F, van Oudheusden BW (2009) Three-dimensional instantaneous structure of a shock wave/turbulent boundary layer interaction. J Fluid Mech 622:33.

Jung YS, You JY, Kwon OJ (2014) Numerical investigation of prop-rotor and tail-wing aerodynamic interference for a tilt-rotor UAV configuration. J Mech Sci Technol 28:2609.

Jux C, Sciacchitano A, Schneiders JFG, Scarano F (2018) Robotic volumetric PIV of a full-scale cyclist. Exp Fluids 59:74.

Kähler C, Sammler B, Kompenhans J (2002) Generation and control of tracer particles for optical flow investigations in air. Exp Fluids 33:736.

Keane RD, Adrian RJ (1990) Optimization of particle image velocimeters. I. Double pulsed systems, Meas Sci and Technol 1:1202.

Keane RD, Adrian RJ (1992) Theory of cross-correlation analysis of PIV images. Appl Sci Res 49:191.

Kerho MF, Bragg MB (1994) Neutrally buoyant bubbles used as flow tracers in air. Exp Fluids 16:393.

Kirmse T (2016) Recalibration of a stereoscopic camera system for in-flight wing deformation measurements. Meas Sci Technol 27:054001.

Kühn M, Ehrenfried K, Bosbach J, Wagner C (2011) Large-scale tomographic particle image velocimetry using helium-filled soap bubbles. Exp Fluids 50:929.

Lee H, Balachandar S (2010) Drag and lift forces on a spherical particle moving on a wall in a shear flow at finite Re. J Fluid Mech 657:89.

Lei YC, Tien WH, Duncan J, Paul M, Ponchaut N, Mouton C, Dabiri D, Rösgen T, Hove J (2012) A vision-based hybrid particle tracking velocimetry (PTV) technique using a modified cascade correlation peak-finding method. Exp Fluids 53:1251.

Lima Pereira LT, Ragni D, Avallone F, Scarano F (2020) Pressure fluctuations from large-scale PIV over a serrated trailing edge. Exp Fluids 61:71.

Liu Z, He Y, Yang L, Han J (2017) Control techniques of tilt rotor unmanned aerial vehicle systems: A review. Chinese J Aeronaut 30:135.

Loth E (2008) Quasi-steady shape and drag of deformable bubbles and drops. Int J Multiph Flow 34:523.

Loth E, Dorgan A J (2009) An equation of motion for particles of finite Reynolds number and size. Environ Fluid Mech 9:187.

Maas HG (1992) Digitale Photogrammetrie in der dreidimensionalen Strömungsmesstechnik. PhD thesis, ETH, Zürich.

Maas HG, Grün A, Papantoniou D (1993) Particle tracking in three dimensional turbulent flows—part I: photogrammetric determination of particle coordinates. Exp Fluids 15:133.

McLachlan BG, Bell JH (1995) Pressure-sensitive paint in aerodynamic testing. Exp Therm Sci 10:470.

Malik N, Dracos T, Papantoniou D (1993) Particle tracking in three dimensional turbulent flows—part II: particle tracking. Exp Fluids 15:279.

Magnaudet J (1997) The forces acting on bubbles and rigid particles. ASME Fluids Engineering Division Summer Meeting, FEDSM, 22.

Magnaudet J, Eames I (2000) The motion of high-Reynolds-number bubbles in inhomogeneous flows. Annu Rev Fluid Mech 32:659.

Maxey MR, Riley JJ (1983) Equation of motion for a small rigid sphere in a nonuniform flow. Phys Fluids 26:883.

Mei R (1994) Flow due to an oscillating sphere and an expression for unsteady drag on the sphere at finite Reynolds number. J Fluid Mech 270:133.

Mei R (1996) Velocity fidelity of flow tracer particles. Exp Fluids 22:1.

Melling A (1997) Tracer particles and seeding for particle image velocimetry. Meas Sci Technol 8:1406.

Michaelides EE (1997) The transient equation of motion for particles, bubbles, and droplets. J Fluids Eng 119:223.

Michaelis D, Bomphrey R, Henningsson P, Hollis D (2012) Reconstructing the vortex skeleton of the desert locust using phase averaged POD approximations from time resolved thin volume tomographic PIV. 16th International symposium on applications of laser techniques to fluid mechanics, Lisbon.

Michaux F, Mattern P, Kallweit S (2018) RoboPIV: how robotics enable PIV on a large industrial scale. Meas Sci Technol 29:074009.

Morias KLL, Caridi GCA, Sciacchitano A, Scarano F (2016) Statistical characterization of helium-filled soap bubbles tracing fidelity for PIV. 18th International symposium on the application of laser and imaging techniques to fluid mechanics, Lisbon.

Müller D, Müller B, Renz U (2001) Three-dimensional particle-streak tracking (PST) velocity measurements of a heat exchanger inlet flow: A new method to measure all three air-flow velocity components in a plane is applied to a steady-state three-dimensional flow. Exp Fluids 30:645.

Novara M, Schanz D, Geisler R, Gesemann S, Voss C, Schröder A (2019) Multi-exposed recordings for 3D Lagrangian particle tracking with Multi-Pulse Shake-The-Box. Exp Fluids 60:44.

Ohmi K, Li H-Y (2000) Particle-tracking velocimetry with new algorithms. Meas Sci Technol 11:603.

Okamoto K, Hassan YA, Schmidl WD (1995) New tracking algorithm for particle image velocimetry. Exp Fluids 19:342.

Okuno Y, Fukuda T, Miwate Y, Kobayashi T (1993) Development of three dimensional air flow measuring method using soap bubbles. JSAE Rev 14:50.

Pickering CJ, Halliwell NA (1984) Laser speckle photography and particle image velocimetry: photographic film noise. Appl Opt 23:2961.

Prasad AK (2000) Stereoscopic particle image velocimetry. Exp Fluids 29:103.

Pröbsting S, Scarano F, Bernardini M, Pirozzoli S (2013) On the estimation of wall pressure coherence using time-resolved tomographic PIV. Exp. Fluids 54:1.

Qureshi NM, Arrieta U, Baudet C, Gagne Y, Bourgoin M (2008) Acceleration statistics of inertial particles in turbulent flow. Eur Phys J B 66:531.

Raffel M (2015) Background-oriented schlieren (BOS) techniques. Exp Fluids 56:60.

Raffel M, Willert CE, Scarano F, Kähler C, Wereley ST, Kompenhans, J (2018) Particle image velocimetry—a practical guide, 3rd ed. Springer, Berlin.

Ragni D, Schrijer F, van Oudheusden BW, Scarano F (2010) Particle tracer response across shocks measured by PIV. Exp Fluids 50:53.

Reader-Harris M (2015) Orifice plates and venturi tubes. In: Experimental fluid mechanics. Springer, Cham.

Redon H (1938) Means for materializing the streamlines of a fluid. United States Patent Office. Patent No. 2,134,890.

Reinders W (1994) Data report of the effect of in-flight icing on the 2D high lift model 5-6 in the low-speed wind tunnel LST. I Royal Netherlands Aerospace Centre (NLR), NLR-CR-1994-551.

Samimy M, Lele SK (1991) Motion of particles with inertia in a compressible free shear layer. Phys Fluids A 3:1915.

Sardina G, Schlatter P, Picano F, Casciola CM, Brandt L, Henningson DS (2012) Self-similar transport of inertial particles in a turbulent boundary layer. J Fluid Mech 706:584.

Scarano F (2013) Tomographic PIV: principles and practice. Meas Sci Technol 24:012001.

Scarano F, Ghaemi S, Caridi GCA, Bosbach J, Dierksheide U, Sciacchitano A (2015) On the use of helium filled soap bubbles for large scale tomographic PIV in wind tunnel experiments. Exp Fluids 56:42.

Sciacchitano A, Wieneke B, Scarano F (2013) PIV uncertainty quantification by image matching. Meas Sci Technol 24:045302.

Sciacchitano A (2014) Uncertainty quantification in particle image velocimetry and advances in time-resolved image and data analysis. PhD Thesis, TU Delft, Delft.

Sciacchitano A, Wieneke B (2016) PIV uncertainty propagation. Meas Sci Technol 27:084006.

Schanz D, Gesemann S, Schröder A (2016) Shake-The-Box: Lagrangian particle tracking at high particle image densities. Exp Fluids 57:70.

Schanz D, Novara M, Geisler R, Agocs J, Eich F, Bross M, Kähler CJ, Schröder A (2019) Large-scale volumetric characterization of a turbulent boundary layer flow. 13th International Symposium on Particle Image Velocimetry, ISPIV 2019, Munich.

Scharnowski S, Sciacchitano A, Kähler CJ (2019) On the universality of Keane & Adrian's valid detection probability in PIV. Meas Sci Technol 30:035203.

Schiller L, Naumann A (1933) Über die grundlegenden Berechnungen bei der Schwerkraftaufbereitung. Z Ver Dtsch Ing 77:318.

Schlichting H (1979) Boundary-layer theory, 7th ed. McGraw-Hill Inc., New York.

Schneiders JFG, Caridi GCA, Sciacchitano A, Scarano F (2016) Large-scale volumetric pressure from tomographic PTV with HFSB tracers. Exp Fluids 57:164.

Schneiders JFG, Jux C, Sciacchitano A, Scarano F (2018) Coaxial volumetric velocimetry. Meas Sci Technol 29:065201.

Schrijer FFJ, Scarano F, van Oudheusden BW (2006) Application of PIV in a Mach 7 double-ramp flow. Exp Fluids 41:353.

Schröder A, Geisler R, Sieverling A, Wieneke B, Henning A, Scarano F, Elsinga GE, Poelma C (2009a) Lagrangian aspects of coherent structures in a turbulent boundary layer flow using TR-Tomo PIV

and FTV. 8th International symposium on Particle Image Velocimetry, Melbourne, Australia.

Schröder A, Pallek D, Geisler R, Lauke T, Herr M, v Geyr H, Dierksheide U (2009b) Particle Image Velocimetry as Validation Tool in Aeronautics. 47th AIAA Aerospace Sciences Meeting Including The New Horizons Forum and Aerospace Exposition, Orlando.

Schröder A, Geisler R, Staack K, Elsinga GE, Scarano F, Wieneke B, Westerweel J (2011) Eulerian and Lagrangian views of a turbulent boundary layer flow using time-resolved tomographic PIV. Exp Fluids 50:1071.

Shen J, Li X (1996) Instability of an annular viscous liquid jet. Acta Mech 114:167.

Shi P, Rzehak R (2020) Lift forces on solid spherical particles in wall-bounded flows. Chem Eng Sci 211:115264.

Soloff SM, Adrian RJ, Liu Z-C (1997) Distortion compensation for generalized stereoscopic particle image velocimetry. Meas Sci Technol 8:1441.

Spalart PR, Venkatakrishnan V (2016) On the role and challenges of CFD in the aerospace industry. Aeronaut J 120:1223.

Spoelstra A, de Martino Norante L, Terra W, Sciacchitano A, Scarano F (2019) On-site cycling drag analysis with the Ring of Fire. Exp Fluids, 60:90.

Staack K, Geisler R, Schröder A, Michaelis D (2010) 3D-3C-coherent structure measurements in a free turbulent jet. 15th International symposium on Applications of Laser Techniques to Fluid Mechanics, Lisbon.

Torricelli E (1644) Opera Geometrica, chap. De Motu Aquarum. Florentiae Typis Amotoris Massae et Laurentij de Landis.

van Oudheusden, B. W. (2013) PIV-based pressure measurement. Meas Sci Technol 24:032001.

Violato D, Moore P, Scarano F (2011) Lagrangian and Eulerian pressure field evaluation of rod-airfoil flow from time-resolved tomographic PIV. Exp. Fluids 50:1057.

Volk R, Calzavarini E, Verhille G, Lohse D, Mordant N, Pinton JF, Toschi F (2008) Acceleration of heavy and light particles in turbulence: Comparison between experiments and direct numerical simulations. Physica D 237:2084.

Voth GA, LaPorta A, Crawford AM, Alexander J, Bodenschatz E (2002) Measurement of particle accelerations in fully developed turbulence. J Fluid Mech 469:121.

Westerweel J (2000) Effect of Sensor Geometry on the Performance of PIV Interrogation. In: Adrian RJ, Durão DFG, Durst F, Heitor MV, Maeda M, Whitelaw JH (eds) Laser Techniques Applied to Fluid Mechanics. Springer, Berlin, Heidelberg.

Westerweel J, Scarano F (2005) Universal outlier detection for PIV data. Exp Fluids 39:1096.

Westerweel J, Elsinga GE, Adrian RJ (2013) Particle image velocimetry for complex and turbulent flows. Annu Rev Fluid Mech 45:409.

Wieneke B. (2005) Stereo-PIV using self-calibration on particle images. Exp Fluids 39:267.

Wieneke, B. (2013) Iterative reconstruction of volumetric particle distribution. Meas Sci Technol 24:024008.

Willert CE, Gharib M (1991) Digital particle image velocimetry. Exp Fluids 10:181.

Willert C (1997) Stereoscopic digital particle image velocimetry for application in wind tunnel flows. Meas Sci Technol 8:1465.

Willert C, Schulze M, Waltenspul S, Schanz D, Kompenhans J (2019) Prandtl's flow visualization film C1 revisited. 13th International Symposium on Particle Image Velocimetry, ISPIV 2019, Munich.

Xu H, Bodenschatz E (2008) Motion of inertial particles with size larger than Kolmogorov scale in turbulent flows. Phys D 237:2095.

Yeh Y, Cummins HZ (1964) Localized fluid flow measurements with an He–Ne laser spectrometer. Appl Phys Lett 4:176.

Zeng L, Najjar F, Balachandar S, Fischer P (2009) Forces on a finite-sized particle located close to a wall in a linear shear flow. Phys Fluids 21:033302.

ACKNOWLEDGEMENTS

First of all, I would like to thank my supervisor Marthijn Tuinstra, copromotor Andrea Sciacchitano and promotor Fulvio Scarano for the opportunity they have given me of pursuing a PhD. I am deeply grateful for their guidance, friendship, patience and for challenging me intellectually on an almost daily basis. They have not only been my mentors, but also a source of great inspiration. I can't thank them enough for sharing with me their enthusiasm for science, for so many long and fruitful discussions, and for teaching me the power of a white board.

I would also like to thank Joost Hakkart, manager of the Vertical Flight and Aeroacoustics (AVVA) department at NLR, who has been supportive of this project and of all necessary activities involved in the PhD programme. I am grateful for having had the opportunity to work at the AVVA department in Marknesse for about 5 years of my life, surrounded by so many bright and friendly colleagues. I would like to thank Anton de Bruin, Mark-Jan van der Meulen and Evert Geurts, for the opportunity they have given me of collaborating in the industrial PIV experiments performed at the KKK (Cologne), AWB (Braunschweig) and LLF (Marknesse) wind tunnels, respectively. Furthermore, I would like to thank Karel Lammers for the cheerful conversations at the coffee machine; Evelien van Bokhorst and Julian Bisheuvel for the interesting conversations we have had on the bus to Zwolle; and Arjan Hanema for the assistance with experiments. In particular, I would like to thank Marco de Boer and Jaap Cornelissen for putting up with all the messes I have left behind in the lab and for all the time they have spent with me in the wind tunnels, helping me arrange the "perfect" setup. I am also indebted to Jaap for improving my experiments by always putting up resistance to my ideas, and helping us designing the bubble generators and seeding rake. In addition, I would like to thank Gert-Jan van Toly from NLR for making the CAD drawings of the seeding rake and all the

colleagues from the workshop, who always delivered work of high quality.

I am also very proud to have been a member of the Aerodynamics section of the Faculty of Aerospace Engineering at TU Delft and have a long list of people whom I would like to thank: Giuseppe Caridi, for bringing me up to speed on the TU Delft developments for HFSB generation; Ferry Schrijer, for his help with designing an experiment to visualize bubbles across a shock wave; Frits Donker Duyvis and Dennis Bruikman for helping me setting up the laser countless times; Peter Duyndam, for helping me creating fancy devices in the workshop; Henk-Jan Siemer for helping me keep my setup safe; Nico van Beek for always supporting me in all IT related issues; Colette Russo, for always being efficient dealing with administrative issues; and all my PhD colleagues, particularly, Constantin Jux, Alex Spoelstra, Alessandro D'Aguanno, Gabriel Gonzales, Edoardo Saredi, Wouter Terra and Sagar Adatrao, for the exchange of ideas in the large-scale group, helping me with my experimental setups at TU Delft and for the time we have spent together in conferences and courses.

I am also thankful for the collaboration with the German-Dutch Wind tunnels (DNW) employees, Baart van Roojien, who was involved in the planning and execution of the first LST experiments with HFSB; Iwan Philipsen, who was the DNW project manager during the experiment we performed at the LLF; and Gerrit Feenstra who helped us setting up the laser at the LLF.

I am also fortunate to have made great friends in Zwolle during the four years I have lived there, who made this journey much more pleasurable and gave me the strength to keep going. In particular, I would like to thank Elisabetta Conti, Carolien Sedee, Flavia Namba, Ádám Tűri and Marco Magliano. Your friendship is priceless to me.

I would like also to thank my good friends from Brazil, Vitor Balieiro, Lucas Betholdi, Pedro Lopes, Caio Peixe, Luis Eduardo Barini, Marcel

Hakime, Gustavo Leite, Felipe Fumachi, Breno Tiburcio, Danilo Froner and Frederico Cassis, and from my masters, David Biro, Gustavo Pescador and Aurélien Jouanneau, who have always been there for me.

Above all, I have my family to thank. I am blessed to have the support and love of my parents Marcos and Lilian, who have given me the best education I could wish for and have always pushed me to follow my dreams, and of my brother Bruno, whose unique personality and way of thinking have always been inspiring to me.

CURRICULUM VITAE

David Engler Faleiros was born on 6 May 1988 in Franca (São Paulo), Brazil. In 2015, he graduated in Sustainable Energy Technology, with specialization in wind energy, at University of Twente, the Netherlands. During this period, he joined the Royal Netherlands Aerospace Laboratory (NLR) for an internship on wind tunnel investigations of trailing edge noise mitigation through the use of serrations, followed up by his graduate assignment on open-jet wind tunnel corrections for measurements of airfoil lift and drag. This project was reported on his MSc thesis "*PIV Investigation of Airfoil Wake in Open-Jet Wind Tunnels*" and on the paper "*Drag, Lift and Effective Angle of Attack from the Wake of an Airfoil in the Open-Jet Wind Tunnel*" (54th AIAA Aerospace Sciences Meeting, 2016, San Diego).

In April 2016, David started his PhD research in a collaboration between NLR and Delft University of Technology (TU Delft). At NLR he worked at the department Vertical Flight and Aeroacoustics (AVVA) under the supervision of Ir. Marthijn Tuinstra. At TU Delft, he worked at the Aerodynamics Section of the Faculty of Aerospace Engineering, under the supervision of Dr. Andrea Sciacchitano and Prof.dr. Fulvio Scarano. David's research focused on the generation, control and tracing fidelity of helium-filled soap bubble tracers for large-scale PIV measurements in industrial wind tunnels.

As of September 2020, David is working as a postdoctoral researcher at the Faculty of Mechanical, Maritime and Materials Engineering (3mE), researching the spread of the virus SARS-CoV-2 (disease COVID-19) in the air through human expiratory activities.

LIST OF PUBLICATIONS

JOURNAL ARTICLES

- [1] Faleiros DE, Tuinstra M, Sciacchitano A, Scarano F (2018) Helium-filled soap bubbles tracing fidelity in wall-bounded turbulence. Exp Fluids 59:56.
- [2] Faleiros DE, Tuinstra M, Sciacchitano A, Scarano F (2019) Generation and control of helium-filled soap bubbles for PIV. Exp Fluids 60:40.
- [3] Faleiros DE, Tuinstra M, Sciacchitano A, Scarano F (2021) The slip velocity of nearly-neutrally-buoyant tracers for large-scale PIV. Under review for publication in Exp Fluids.

CONFERENCE PROCEEDINGS

- [1] Faleiros DE, Tuinstra M, Sciacchitano A, Scarano F (2017) Turbulent boundary layer assessment via PTV using Helium-filled soap bubbles. 12th International symposium on Particle Image Velocimetry, Busan, South Korea.
- [2] Faleiros DE, Tuinstra M, Sciacchitano A, Scarano F (2018) Generation and control of helium-filled soap bubbles for large-scale PIV. 19th International symposium on the application of laser and imaging techniques to fluid mechanics, Lisbon.
- [3] Faleiros DE, Tuinstra M, van Rooijen BD, Scarano F and Sciacchitano A (2019), Soap bubbles for large-scale PIV in industrial wind tunnels, 13th International symposium on Particle Image Velocimetry, Munich.
- [4] Belligoli Z, Dwight R, Eitelberg G, Srikumar S, Faleiros DE, van Nesselrooij M, van Campenhout O (2020) A Review of Numerical and Experimental Studies of the Anti-Fairing. AIAA AVIATION 2020 FORUM, p. 2703.

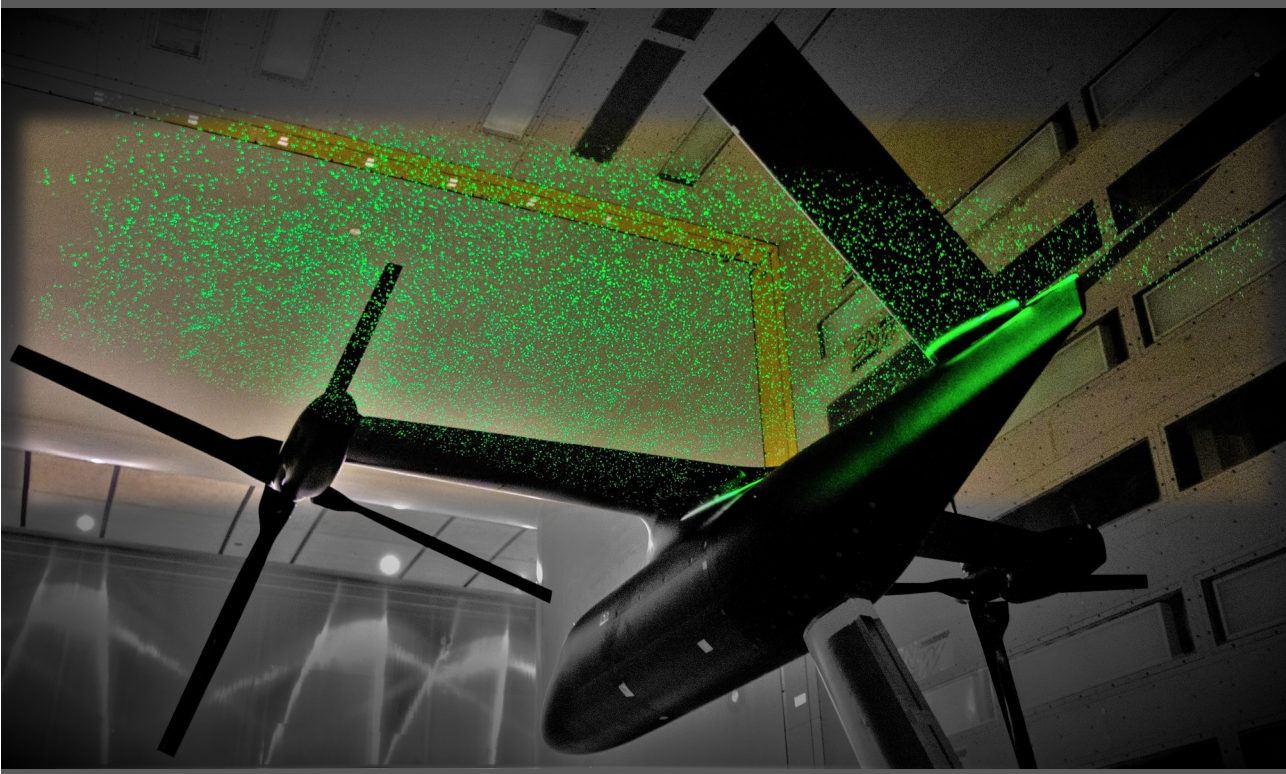

ISBN 978-94-6366-404-2